AWARD NUMBER: W81XWH-14-1-0279

TITLE: Chip-Based Magnetic Imager for Molecular Profiling of Ovarian Cancer Cells

PRINCIPAL INVESTIGATOR: Dr. Hakho Lee

CONTRACTING ORGANIZATION: MASSACHUSETTS GENERAL HOSPITAL

BOSTON MA 02114-2621

REPORT DATE: December 2016

TYPE OF REPORT: Final

PREPARED FOR: U.S. Army Medical Research and Materiel Command

Fort Detrick, Maryland 21702-5012

DISTRIBUTION STATEMENT: Approved for Public Release;
Distribution Unlimited

The views, opinions and/or findings contained in this report are those of the author(s) and should not be construed as an official Department of the Army position, policy or decision unless so designated by other documentation.

Form Approved REPORT DOCUMENTATION PAGE OMB No. 0704-0188 Public reporting burden for this collection of information is estimated to average 1 hour per response, including the time for reviewing instructions, searching existing data sources, gathering and maintaining the data needed, and completing and reviewing this collection of information. Send comments regarding this burden estimate or any other aspect of this collection of information, including suggestions for reducing this burden to Department of Defense, Washington Headquarters Services, Directorate for Information Operations and Reports (0704-0188), 1215 Jefferson Davis Highway, Suite 1204, Arlington, VA 22202-4302. Respondents should be aware that notwithstanding any other provision of law, no person shall be subject to any penalty for failing to comply with a collection of information if it does not display a currently valid OMB control number. PLEASE DO NOT RETURN YOUR FORM TO THE ABOVE ADDRESS. 1. REPORT DATE 2. REPORT TYPE 3. DATES COVERED 1. REPORT DATE December 2016 30 Sep 2014 - 29 Sep 2016 4. TITLE AND SUBTITLE 5a. CONTRACT NUMBER W81XWH-14-1-0279 Chip-Based Magnetic Imager for Molecular Profiling of Ovarian Cancer Cells 5b. GRANT NUMBER W81XWH-14-1-0279 5c. PROGRAM ELEMENT NUMBER 6. AUTHOR(S) 5d. PROJECT NUMBER Hakho Lee 5e. TASK NUMBER 5f. WORK UNIT NUMBER E-Mail: hlee@mgh.harvard.edu 7. PERFORMING ORGANIZATION NAME(S) AND ADDRESS(ES) 8. PERFORMING ORGANIZATION REPORT **NUMBER** MASSACHUSETTS GENERAL HOSPITAL, THE SUSAN ROUDEBUSH 55 FRUIT ST **BOSTON MA 02114-2621** 9. SPONSORING / MONITORING AGENCY NAME(S) AND ADDRESS(ES) 10. SPONSOR/MONITOR'S ACRONYM(S) U.S. Army Medical Research and Materiel Command Fort Detrick, Maryland 21702-5012 11. SPONSOR/MONITOR'S REPORT NUMBER(S)

12. DISTRIBUTION / AVAILABILITY STATEMENT

Approved for Public Release; Distribution Unlimited

13. SUPPLEMENTARY NOTES

14. ABSTRACT

The overall goal of this project is to explore a new, chip-based magnetic sensor that will allow for fast and sensitive molecular analyses of tumor cells. To achieve this goal, we focused on i) implementing a miniaturized Hall (μHall) sensor system and ii) synthesizing magnetic nanoparticles for cell labeling. *Sensor system*. The μHall sensor has a hybrid structure, consisting of an Hall integrated-circuit (IC) chip with a microfluidics on top. The IC chip contains an array of micrometer-scale Hall elements for magnetic detection. To facilitate the system control, we also integrated control electronics in the same chip. By fabricating such ICs through a semiconductor foundry, we could produce a large number of chips (~120 ICs) with tight quality control. *Magnetic nanoparticles (MNPs)*. We have synthesized a panel of MNPs with varying diameters (10, 12, 16 nm); each particle type displayed a unique magnetic property, which will be exploited for multiplexed detection. To make particles water-soluble and amenable for cell targeting, we further coated them with biocompatible polymers. We now plan to apply the developed platforms to detect ovarian cancer cells spiked in the whole blood.

15. SUBJECT TERMS

ovarian cancer, magnetic sensor, magnetic nanoparticles, microfluidics, Hall sensor

			1:	19a. NAME OF RESPONSIBLE PERSON USAMRMC	
a. REPORT	b. ABSTRACT	c. THIS PAGE			19b. TELEPHONE NUMBER (include area code)
Unclassified	Unclassified	Unclassified	Unclassified	149	coue)

Standard Form 298 (Rev. 8-98) Prescribed by ANSI Std. Z39.18

Table of Contents

	<u>Page</u>
1. INTRODUCTION	5
2. KEYWORDS	5
3. ACCOMPLISHMENTS.	5
4. IMPACT	8
5. CHANGES/PROBLEMS	9
6. PRODUCTS	9
7. PARTICIPANTS & OTHER COLLABORATING ORGANIZATIONS	13
8. SPECIAL REPORTING REQUIREMENTS	15
9. APPENDICES	15

1. INTRODUCTION

The overall objective of this pilot project is to to develop a new magnetic platform, named iHD (imaging Hall Detector), that will enable fast and multiplexed molecular analyses of circulating tumor cells (CTCs). The iHD sensing is based on Hall magnetometry: target biological cells are labeled with molecular-specific magnetic nanoparticles (MNPs), and the resulting magnetic field from each cell is detected by micrometer-scale Hall (μ Hall) elements. The sensor can achieve a high signal contrast against extremely low magnetic background in biological samples. Measurements can thus be made without purification steps, minimizing cell loss and potential degradation of biomarkers. In this project, we specifically focus on the following activities. *In Aim 1*, we will implement an array of μ Hall sensors in an IC (integrated circuit) chip to improve the assay throughput. *In Aim 2*, we will synthesize a panel of MNPs with distinct magnetic properties, and use each type of MNPs to target a different molecular marker on cells.

2. KEYWORDS

Ovarian cancer, Magnetic sensor, Magnetic nanoparticles, Microfluidics, Hall sensor

3. ACCOMPLISHMENTS.

What were the major goals of the project?

The major goals of this project are the followings:

Goal 1: Implement a new microHall IC for magnetic detection (100% completion)

Goal 2: Build a data acquisition system (100% completion)

Goal 3: Synthesize magnetic nanoparticles and prepare them for cell labeling (100% completion)

Goal 4: Validate the Hall system for cell detection.

What was accomplished under these goals?

We have accomplished all of our goals. Importantly, we have developed a new μ Hall sensor for single cell analysis and established an optimal protocol for cell labeling.

MicroHall (µHall) IC chip (Goal 1). We have recently implemented a new µHall IC chip for single cell detection (Fig. 1). We designed a sensor IC and used a semiconductor foundry (Electronics and Telecommunications Research Institute, Korea) for the chip fabrication. This strategy significantly improved the performance and the reliability of the system. 1) A large number of sensor chips could be produced with negligible chip-to-chip variations (tolerance < 5%). More than 100 ICs were fabricated in the first batch; further production can be complete in < 2-month turnaround time. 2) The new chip has a denser array (4 × 5) of Hall elements than our homemade prototype, which can improve the overall detection throughout (Fig. 1a). 3) Key electronic components (e.g., switches, amplifiers) were integrated in the same chip (Fig. 1b) to facilitate the array control as well as to improve the signal-to-noise ratio. We characterized the electrical properties of the sensor and designed ancillary electronics for data acquisition. The chip was also packaged with a twostage flow-focusing microfluidics (Fig. 1c).

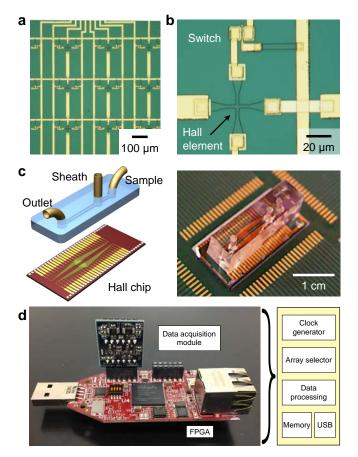


Fig. 1: 2nd generation μ Hall system. (a) A new version of integrated μ Hall chips were manufactured in a semiconductor foundry. The chip has 20 μ Hall elements arranged into a 4 \times 5 array. (b) Other circuit components (e.g., switches, amplifiers) are integrated in the same chip. (c) The new chip was packaged with a microfluidic channel. (d) Data-acquisition module realized on a field-programmable gate array (FPGA) chip.

System-level implementation (Goal 2). We have constructed a custom-designed DAQ (data acquisition) module to interface with the developed IC chip (Fig. 1d). We used a field-programmable gate array (FPGA) chip (Spartan-6, Xilinx) as the core unit, and programmed functional blocks. Specifically, the FPGA generates clock and control signals to sequentially access every µHall element in the chip; processes the output signals from the chip; and communicates with external terminals (computers, smartphones) via a USB2 (universal serial bus2) connection. We are currently implementing graphical, user-friendly software to streamline the system operation.

Different type of magnetic nanoparticles (Goal 3).

We have optimized the synthetic route to produce various ferrite MNPs. In brief, we first synthesized 8-nm core particles through thermal decomposition. We then applied the seed-mediated growth method to increase the magnetic core diameter from 8 nm to 10, 12, or 16 nm (**Fig. 2a**). All ferrite MNPs had crystalline ferrite structure (**Fig. 2b**), and were superparamagnetic at room temperature. Importantly, each type of particles showed a distinct magnetic signature (**Fig. 2c**), which was exploited for magnetic multiplexing (see below).

Universal coating strategy for MNPs (Goal 3). We also developed a new method for MNP-coating and bioconjugation (Fig. 3a). We used dopamine (DOPA) as the affinity ligand, because DOPA can readily attach to metal surface through adsorption. This process, however, is reversible; DOPA can be dissociated from NPs under physiological conditions. To improve coating stability, we thus synthesized PEG polymers containing multiple DOPAs. Specifically, we grafted DOPA and PEG on a polymer backbone, poly(isobutylene-alt-maleic anhydride) (PIMA), creating DOPA-PIMA-PEG. This method did not need additional crosslinkers, and facilitated creation of DOPA-PIMA-PEG with different PEG length and various functional groups for specific bioconjugation (e.g., EDC coupling, bioorthogonal click reaction). We used DOPA-PIMA-PEG to replace hydrophobic capping agents (e.g., oleic acid, oleylamine) on the MNP surface. The polymer-coated MNPs were well dispersed in aqueous media with no aggregation (Fig. 3b). We further tested the colloidal stability of polymer-coated MNPs by subjecting them to heat stress or high salt concentrations. The particles maintained colloidal stability against such challenges. No significant changes in particle distribution were observed after continuous heating at 90° C for 2 h or emersion in 3 M of NaCl. We also monitored the longterm stability of particles; no aggregation was observed up to four weeks in PBS buffer (Fig. 3c).

Molecular detection of ovarian cancer cells. Using the developed $\mu Hall$ system, we profiled individual

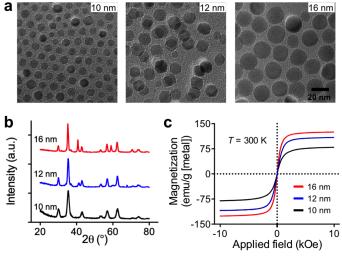


Fig. 2: Different types of magnetic nanoparticles (MNPs). (a) MnFe₂O₄ of different sizes were synthesized through seed-mediated growth. **(b)** X-ray powder diffractograms. All MnFe₂O₄ MNPs exhibited a similar pattern, confirming their ferrite structure. **(c)** The particles were superparamagnetic at 300 K. Importantly, the magnetization increased with particle size, generating a distinct magnetic signature.

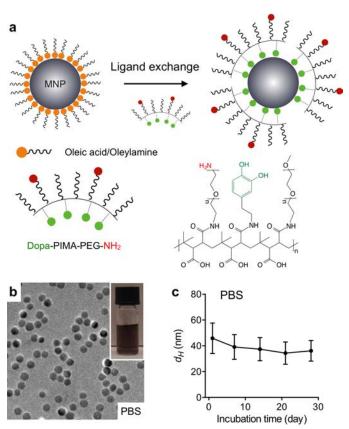


Fig. 3: Generalized coating strategy. (a) Multiple dopamine containing PEG polymers are used to increase the binding affinity between the polymer and the MNPs. (b) MNPs were transferred to aqueous phase through the polymer (PEG length 5k) coating. The particles were well-dispersed without aggregation. (c) No significant changes in particle size were observed during long-term storage in PBS, which confirmed high stability of the polymer coating.

ovarian cancer cells for protein expression. We labeled cancer cells with MNPs; each cell thereby acquired a magnetic moment proportional to the expression level of a targeted biomarker. The µHall sensor was operated in the AC (alternating current) mode (Fig. 4a), measuring magnetic susceptibility of individual cells. We then integrated the measured data to obtain magnetic moments cells (Fig. 4b). This approach allowed us

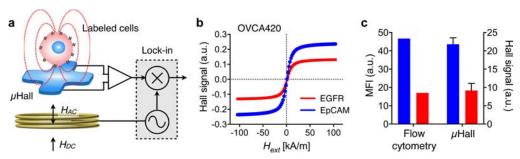


Fig. 4: Cancer cell detection with μ Hall chipT. (a) A panel of ovarian cancer cell lines were screened for protein expression by flow cytometry and μ Hall. The profiling results showed a good match ($R^2 = 96\%$). (b) MNP-labeled tumor cells spiked in PBS or human whole blood were detected by the μ Hall sensor. The detection was insensitive to the biological media.

to achieve high signal-to-noise ratio, accurately measuring MNP counts per cell. The μ Hall profiling data correlated well with those from flow cytometry, which validated the μ Hall's analytical capability (**Fig. 4c**). Note that the interference from biological media was negligible in the μ Hall detection, making it possible to perform the μ Hall assay in native specimens.

What opportunities for training and professional development has the project provided? <u>Training activities.</u>

Practical skill sets for circuit design and microfabrication. With the guidance of the PI and other research fellows, the graduate student (Mr. Changwook Min, MIT) involved in this project has advanced his skills on IC design, microfluidics, and data acquisition. Mr. Min has conducted this project independently. Dr. Huilin Shao (Teal Scholar) was actively involved in the chip design as well as the operation of microfluidic systems.

Nanoparticle development for cellular assay. Dr. Shao and Mr. Min were trained for the synthesis of magnetic nanoparticles, surface modification, and bioconjugation. This learning was expedited through dedicated one-to-one work with expert research fellows (Drs. Yongil Park and Kisoo Park).

Mentorship. Drs. Lee and Castro provided one-on-one mentorship to Mr. Min and Dr. Shao for research. Dr. Min was awarded the prestigious "Lotte Scholarship" scholarship from Korea. Dr. Shao, the Teal Scholar supported by this Pilot Award, has since been selected as a prestigious Junior Fellow at Institute of Molecular and Cell Biology, ASTAR, Singapore, and recentlypromoted to Assistant Professor at National University of Singapore (Bioengineering).

Intern training. Co-PI (Dr. Castro) provided daily mentorship to summer interns (Christina Le, Kerwin Cruz De La Rosa) who were selected from a national pool of underrepresented undergraduate students. These students were trained for essential experiment techniques, including bioconjugation of MNPs, cell labeling, and bioassays. We have also recruited local undergraduate students (Craig Pille and Lucas Rohrer, Northeastern University) for intensive 6-month internship programs. These students were trained to independently perform the device fabrication, system setup, and low-noise electrical measurements.

Professional development.

Course work. The concepts developed in this project (e.g., Hall sensor, IC designs, hybrid system) has been

incorporated into the intramural coursework of *CSB10 – Engineering Biosensors* taught by the PI, that explores key topics in biosensing.

Conferences and workshops. Both Pls and trainees (Dr. Shao, Mr. Min) participated numerous workshops and extramural meetings as summarized in Section 6.

How were the results disseminated to communities of interest? (Fig. 5)







Fig. 5: Community outreaches. (a) Magnetic sensors were exhibited at the Science Museum, London UK. **(b)** Dr. Lee (PI) gave an invited talk at the World Medical Innovation Forum. **(c)** Dr. Castor (Co-PI) presented at ESPN Studios (Bristol, CT).

Our magnetic detection platform was showcased (June 2015) at the <u>Science Museum, London (UK)</u>, as a part of the new exhibit, "Ground-breaking new developments in health diagnostics, from home-testing kits to faster diagnosis times". PI (Dr. Lee) presented the work at the 2016 World Medical Innovation Forum which focused on state-of-the-art and emerging approaches to diagnosing, treating and managing cancer. The audience included CEOs and top executives of dozens of global medical companies (e.g., Novartis, Merrimack Pharmaceuticals), investors, media leaders, and internationally recognized cancer researchers. Co-PI (Dr. Castro) presented research advances in nanosensors to ESPN staff members interested in progress on cancer diagnostics.

What do you plan to do during the next reporting period to accomplish the goals? Nothing to report.

4. IMPACT

What was the impact on the development of the principal discipline(s) of the project?

The developed system introduces a new concept in biosensor design by combining the advantages of semiconductors and microfluidics. In the hybrid system, the IC chip is not just a backend device for signal processing. Rather, the chip takes an active and essential role as a sensor inside the microfluidic network. The hybrid system has the following advantages. • Increased spatial and temporal resolution. Fabricated by the cutting-edge semiconductor technology, the sensors have small footprints to increase the spatial resolution. The IC chips can also be designed to operate in GHz ranges for high speed measurement. By incorporating standard on-chip ADCs and memories, the data sampling rate can be increased, further enhancing the temporal resolution of the measurement. • Parallel and automated measurement. With sensors laid out in an array format, hybrid systems will allow for high throughput, parallel detection. Furthermore, multiplexer circuitry can be integrated into the same chip to control large arrays with a small number of external inputs. The measurement sequences can be easily automated through the programmed control of ICs, which minimizes the need for labor-intensive, potentially error-prone manual procedures. • Robustness and user-friendly interface. One of the significant merits of the hybrid system is its durability and reproducibility. The IC chips are manufactured in a commercial foundry with sophisticated process control. The chip-to-chip variation is maintained minimal, which ensures the consistency in the chip performance. In addition, empowered by integrated control circuits, hybrid ICs can present simple interfaces for external inputs; users can enjoy the same level of the user-friendly interfaces which are now standard in consumer electronics.

What was the impact on other disciplines?

Additional major outcome of this research is the development of new coating/bioconjugation strategies that could be applied to different types of nanoparticles (NPs). A key requisite for rendering NPs useful for biosensing is to stabilize particles' surface with biocompatible and non-reactive coating materials. The surface coating should allow NPs to stay in solution, react with hydrophilic components, and provide functional groups to attach affinity ligands. Without such stabilizing coatings, proteins often absorb non-specifically to the surface, leading to diagnostic interference, high noise levels, or low reactivity. Surface modifications can be particularly challenging for inorganic NPs synthesized via non-hydrolytic thermal decomposition in hydrophobic conditions. During the course of this research, we have advanced a generalizable coating protocol to convert hydrophobic NPs into hydrophilic ones that can be further modified for molecular sensing. This method uses dopamine, which can bind to NP surface with high affinity, as an anchoring group to form stable polymer coated NPs. We tested the method using two representative particles, MNPs and lanthanide NPs. We prepared dopamine-based polyethylene glycol (PEG) polymer and coated hydrophobic NPs with polymer through ligand exchange. The polymer coated NPs displayed excellent colloidal stability at high temperatures and under a wide range of physiological buffer conditions. Furthermore, the conjugates provided facile chemical functionalities to graft various affinity ligands. We used prepared MNPs as sensing agents for Hall sensing; we expect that this coating method could be applied to many different NP types for biosensing.

What was the impact on technology transfer? Nothing to report.

What was the impact on society beyond science and technology? Nothing to report.

5. CHANGES/PROBLEMS

Nothing to report.

6. PRODUCTS

• Publications, conference papers, and presentations

Journal publications.

- 1. Lee K, Shao H, Weissleder R, Lee H (2015) Acoustic purification of extracellular microvesicles. *ACS Nano* 9:2321-2327. PMC4373978, PMID:25672598, Acknowledgement of federal support (yes).
 - This report is indirectly related to the current project. The fluidic system (hardware) developed in this work has been translated to the current project.
- 2. Im H*, Castro CM*, Shao H, Liong M, Song J, Pathania D, Fexon L, Min C, Avila-Wallace M, Zurkiya O, Rho J, Magaoay B, Tambouret RH, Pivovarov M, Weissleder R*, Lee H* (2015) Digital diffraction analysis enables low-cost molecular diagnostics on a smartphone. *Proc Natl Acad Sci U S A* 112:5613-5618. PMC4426451, PMID:25870273, Acknowledgement of federal support (yes).
 - This report is indirectly relevant to the current project. We profiled patient samples suspicious of cervical and ovarian cancer.
- Chen S, Sanjana NE, Zheng K, Shalem O, Lee K, Shi X, Scott DA, Song J, Pan J, Weissleder R, Lee H, Zhang F, Sharp PA (2015) Genome-wide CRISPR screen in a mouse model of tumor growth and metastasis. *Cell* 160:1246-1260. PMC4380877, PMID:25748654. Acknowledgement of federal support (yes).
 - This work is highly relevant to the current project. In this report, we showed that circulating tumor cells
 are more close to cancer metastasis. We also determined the mean size of CTCs (~15 μm), which
 informed the design of our fluidic systems in the current project.
- 4. Im H, Shao H, Weissleder R, Castro CM*, Lee H* (2015) Nano-plasmonic exosome diagnostics. *Expert Rev Mol Diagn* 15:725-733. PMID:25936957, Acknowledgement of federal support (yes).
 - This paper summarizes our results on the protein profiling on a panel of ovarian cancer cell lines (Fig. 8 in the paper). It validates our choice of EpCAM and CD24 for ovarian cancer detection.
- 5. Park YI, Im H, Weissleder R, Lee H (2015) Nanostar clustering improves the sensitivity of plasmonic assays. *Bioconjug Chem* 26:1470-1474. PMID:26102604, Acknowledgement of federal support (yes).
 - The bioconjugation strategy reported in this paper was developed for magnetic nanoparticles in the current project.
- 6. Lee H, Shin TH, Cheon J, Weissleder R (2015) Recent developments in magnetic diagnostic systems. *Chem Rev* 115:10690-10724. PMID:26258867, Acknowledgement of federal support (yes).
 - This work is a comprehensive review on magnetic sensors, including the proposed Hall sensor.
- 7. Park YI, Kim E, Huang CH, Park KS, Castro CM, Lee H*, Weissleder R* (2016) A facile coating strategy to functionalize inorganic nanoparticles for biosensing. *Bioconjug Chem* PMID:27792877, Acknowledgement of federal support (yes).
 - This work describes the surface coating we developed for magnetic nanoparticles.
- 8. Jeong S, Park J, Pathania D, Castro CM, Weissleder R, Lee H (2016) Integrated Magneto-Electrochemical Sensor for Exosome Analysis. *ACS Nano* 10:1802-1809. PMC4802494, PMID:26808216, Acknowledgement of federal support (yes)
 - In this work, we have identified surface protein markers for ovarian cancer detection.
- 9. Min C, Park KS, Weissleder R, Castro CM*, Lee H* (2016), Integrated microHall sensor array for nanoparticle detection. *Manuscript in preparation*, Acknowledgement of federal support (yes)

• This manuscript reports the major outcomes, namely the new Hall sensor and the magnetic detection from the current project.

Presentations

(All of the following presentations acknowledged the federal support.)

Integrated micro-Hall detector for point-of-care molecular diagnostics/ Seminar

Huilin Shao, Changwook Min, Cesar M. Castro, Ralph Weissleder, Hakho Lee, Wilmington, MA; 15-Oct-2014 (Local)

This presentation will review magnetic sensing technologies, specifically focusing on a miniaturized Hall (μHall) cytometer. The μHall system was developed for high-throughput detection and profiling of individual cells in native biological samples. The system is a hybrid microfluidic / semiconductor chip, consisting of an array of microfabricated Hall sensors and a microfluidic channel built on top. For detection by μHall sensors, biological cells are labeled with molecular-specific magnetic nanoparticles (MNPs); individual cells thereby assume magnetic moments proportional to the expression levels of target biomarkers. Subsequent μHall detection not only counts the number of targeted cells but also provides their molecular signature. Furthermore, with their capacity for highly localized magnetic detection, μHall sensors can perform measurements on native biological samples (e.g., whole blood) and without the need to remove excess MNPs. The entire cytometry thus can be carried out in a self-contained, portable chip format. The first μHall prototype could achieve a detection rate of ~100,000 cells/sec with a resolution of 500 MNPs/cell. Clinical potential of the system is demonstrated by molecularly profiling cells for known tumor markers and by detecting as few as ~20 tumor cells in 500 μL of whole blood.

MicroHall sensor for direct CTC detection and profiling in blood/ Seminar

Korean Institute of Machinery and Materials (KIMM), Korea (2014)

Changwook Min

Daejeon, Korea; 11-Nov-2014 (International)

The ability to detect rare cells (<100 cells/ml whole blood) and obtain quantitative measurements of specific biomarkers on single cells is increasingly important in basic biomedical research. Implementing such methodology for widespread use in the clinic, however, has been hampered by low cell density, small sample sizes, and requisite sample purification. To overcome these challenges, we have developed a microfluidic chip–based micro-Hall detector, which can directly measure single, immunomagnetically tagged cells in whole blood. The μ Hall detector can detect single cells even in the presence of vast numbers of blood cells and unbound reactants, and does not require any washing or purification steps. In addition, the high bandwidth and sensitivity of the semiconductor technology used in the μ Hall detector enables high-throughput screening (currently ~107 cells/min). The clinical use of the μ Hall detector was demonstrated by detecting circulating tumor cells in whole blood of 20 ovarian cancer patients at higher sensitivity than currently possible with clinical standards. Furthermore, the use of a panel of magnetic nanoparticles, distinguished with unique magnetization properties and bio-orthogonal chemistry, allowed simultaneous detection of the biomarkers EpCAM, HER2/ neu, and EGFR on individual cells. This cost-effective, single-cell analytical technique is well suited to perform molecular and cellular diagnosis of rare cells in the clinic.

Magnetic sensing technology - a new biosensor platform for medical diagnosis

Material Research Society Fall Meeting, Boston, MA (2014)

Hakho Lee

Boston, MA; 3-Dec-2014 (National)

A major challenge in medicine is the rapid and accurate measurement of protein biomarkers, cells, and pathogens in biological samples. Biosensors based on magnetic detection emerge as a promising diagnostic platform. Due to the intrinsically negligible magnetic susceptibilities of biological targets, magnetic detection experiences little interference from native biological samples; even optically turbid samples will often appear transparent to magnetic fields. Biomolecules or cells of interests, when magnetically labeled, however, can attain a high contrast against complex biological background. This presentation will review such magnetic sensing technologies, specifically focusing on a general detection platform termed diagnostic magnetic resonance (DMR). Similar to clinical MRI, the DMR utilizes magnetic nanoparticles to modulate the spin-spin relaxation time of neighboring water molecules. Various assay configurations and nanoparticles have been

designed to detect a wide range of targets including DNA, mRNA, proteins, enzymatic activity, metabolites, drugs, pathogens, exosomes and tumor cells. With these and on-going advances in system design, the DMR technology holds great promise as a high-throughput, low-cost, and portable platform in clinical and point-of-care settings.

On-chip medical diagnosis

2015 Blavatnik Science Symposium Hakho Lee New York, NY; 5-Aug-2015 (National)

Abstract n/a

Magnetic biosensor for medical diagnosis

The 14th International Conference on Advanced Materials Hakho Lee

Jeju, Korea; 27-Oct-2015 (International)

One of the major challenges in medicine is the rapid and accurate measurement of protein biomarkers, cells, and pathogens in biological samples. Biosensors based on magnetic detection emerge as a promising diagnostic platform. Due to the intrinsically negligible magnetic susceptibilities of biological entities, magnetic detection experiences little interference from native biological samples; even optically turbid samples will often appear transparent to magnetic fields. Biomolecules or cells of interests, when magnetically labeled, however, can attain a high contrast against complex biological background. This presentation will review such magnetic sensing technologies.

New biosensor technologies for cellular and molecular detection (tutorial)

Material Research Society Fall Meeting, Boston, MA (2015)

Hakho Lee

Boston, MA; 3-Dec-2015 (National)

Cancer encompasses a broad family of more than 100 complex diseases that share the phenomenon of cell populations that undergo uncontrolled division and also have the potential to invade other tissues in the body. Our ability to understand the vast complexity of cancer, much less clinically control it, is only as good as the tools we have available to study it. For materials scientists seeking to understand the challenges and opportunities, the tutorial will provide an overview of two important fields of technology development: modeling systems and analysis tools. Materials science is a fundamental feature driving progress in both of these critical fields, yet more is required from the materials science community to further advance capabilities on both fronts. For example, new hydrogel materials for 3D cell culture were integrated in microfluidics for modeling tumor angiogenesis. Novel magnetic nanomaterials were exploited for tumor targeting and biomarker detection. Symposium K will highlight groundbreaking advances that span a broad landscape of emerging molecularand cellular-scale technologies focused on cancer. Part I of the tutorial, presented by Roger Kamm, will discuss the evolution of microsystems for modeling tumor development, progression and metastasis. In particular, descriptions on tumor vascular modeling capturing early stage mechanisms of metastatic potential and characterizing epithelial to mesenchymal transition will provide materials scientists with an understanding of critical events of tumorigenesis, proliferation and progression. Part II, presented by Hakho Lee, will focus on innovative molecular and cellular detection technologies, especially for cancer diagnosis and monitoring. Lee will discuss a broad spectrum of sensor technologies that have been applied towards targeting and tracking molecular markers, circulating tumor cells, and trafficking vesicles used to identify cancer. Both lectures will include a discussion of the role of improved materials science for advancing both novel molecular detection technologies and in vitro modeling systems.

Mobile diagnostics and patient monitoring

Hakho Lee 2016 World Medical Innovation Forum Boston, MA; 25-Apr-2016 (International)

Recent progresses in digital sensors and computational approaches create new opportunities for point-of-care (POC) cancer diagnostics and care delivery. By integrating ideas and techniques embodied in

microelectronics, and nanotechnology, my research focuses on advancing sensitive, fast, and cost-effective diagnostic platforms. This presentation will introduce novel, mobile devices for point-of-care cancer detection.

Magnetic sensors for clinical diagnostics: from nanoscale vesicles to cancer cells Hakho Lee

The 11th International Conference on the Scientific and Clinical Applications of Magnetic Carriers Vancouver, Canada; 3-Jun-2016 (International)

A major challenge in clinical medicine is the rapid and accurate measurement of biomarkers in diverse media. Biosensors based on magnetic detection are promising diagnostic platform for such medical diagnostics. Magnetic detection experiences little interference biological sample because of the inherently negligible magnetic background of biological objects; even optically turbid samples will often appear transparent to magnetic fields. With magnetic labeling, however, biomolecules or cells of interests can attain a high contrast against background. We have been developing different types of magnetic sensors optimized for specific biological targets. Our systems include a miniaturized NMR platform that is ideal for detecting nanoscale objects or molecules (e.g., exosomes, DNA, mRNA); a microHall chip to screen individual cells labeled with magnetic nanoparticles; and iii) a diamond-based magnetometer for ultra-sensitive magnetic imaging. This presentation will review each of these systems, with emphasis on its potential clinical applications. Common key components such as magnetic nanomaterials and labeling strategies will also be discussed.

Nanotechnology platforms for clinical diagnostics (Keynote lecture)

Changwook Min, Huilin Shao, Ralph Weissleder, Cesar M. Castro, Hakho Lee International Society for Nanomedicine (ISNM) Congress Seoul, Korea; 29-Sep-2016 (International)

Biosensors based on nanotechnology are promising platforms for such medical diagnostics. Nanostructures, with their unique size and physical properties, can efficiently recognize biomolecules, and subsequently generate distinctive analytical signals. We have been developing different types of nanotechnology platforms designed for specific clinical applications. This presentation will review some of these platforms that are optimized for high-throughput molecular screening of cells and exosomes. Our data showed promising potential of using these biological targets to monitor the tumor progression and treatment responses. Further clinical investigations are underway to rigorously evaluate their clinical utility for cancer managements.

Advances in proteomics analysis in liquid biopsies

Cesar M. Castro 28th EORTC-NCI-AACR Symposium on Molecular Targets and Cancer Therapeutics Munich, Germany; 1-Dec-2016 (International)

Abstract n/a

Harnessing Nanotechnologies for Innovative Ovarian Cancer Care

Cesar M. Castro Northeastern University IGERT Nanomedicine Lecture Series Boston, MA; 14-Nov-2014

Abstract n/a

• Technologies or techniques.

Nothing to report.

• Technologies or techniques.

The research has produced a library of procedures to make fluidic devices, synthesize magnetic nanoparticles and prepare them for bioconjugation, and perform low-noise magnetic measurements. All data are electronically stored and archived, and will be made available through publications in peer reviewed journals. As in the past, all of these resources will be shared freely with scientific community upon execution of a proper MTA through the Office of Corporate Licensing (MGH).

Other Products

This research led to the following outcomes and products.

- •Hall sensor IC chips for highly sensitive magnetic measurements
- •A poratble, high-speed data acqusition system based on FPGA
- •Magnetic nanoparticles with different magnetic dopings and surface coatings
- •Magnetization and susceptiblity data of various magnetic nanoparticles
- •Biocongugation protocol for nanoparticles
- •Protein screening data on ovarian cancer cell lines

Educational material for intramural coursework of CSB10 – Engineering Biosensors

•New microfabrication facilities (i.e., cleanroom, electronics lab, machine shop), which have significantly expanded our capacities for biosensor development.

7. PARTICIPANTS & OTHER COLLABORATING ORGANIZATIONS

• What individuals have worked on the project?

Name:	Hakho Lee
Project Role:	Principal Investigator
Researcher Identifier	orcid.org/0000-0002-0087-0909
Nearest person month worked:	2
	Dr. Lee supervised the overall research, interacting with investigators and research fellows, and discussing all experimental designs and data.
Funding Support:	

Name:	Cesar M. Castro
Project Role:	Co-Principal Investigator
Researcher Identifier	N/A
Nearest person month worked:	1
Contribution to Project:	Dr. Castro guided the biological research, identifying biomarkers for ovarian cancer detection, and validating the selection through in-vitro assays.
Funding Support:	

Name:	Ralph Weissleder
Project Role:	Investigator
Researcher Identifier	N/A
Nearest person month worked:	1
Contribution to Project:	Dr. Weissleder provided scientific assistance in designing magnetic nanoparticles. He also granted full access to technologies available in his laboratory.
Funding Support:	

Name:	Changwook Min
Project Role:	Graduate student
Researcher Identifier	N/A
Nearest person month worked:	6
Contribution to Project:	Mr. Min designed the Hall IC chip, constructed the electrical measurement setup, and validated the entire system.
Funding Support:	

Name:	Huilin Shao
Project Role:	Research fellow
Researcher Identifier	N/A
Nearest person month worked:	3

	Dr. Shao synthesized magnetic nanoparticles, optimized the surface coating, and validated MNP-conjugation with antibodies.
Funding Support:	

Name:	Yongil Park
Project Role:	Research fellow
Researcher Identifier	N/A
Nearest person month worked:	4
Contribution to Project:	Dr. Park worked with Dr. Shao on the development of magnetic nanoagents for cell labeling. Dr. Park also trained Dr. Shao on these skills
Funding Support:	NIH

Name:	Kisoo Park
Project Role:	Research fellow
Researcher Identifier	N/A
Nearest person month worked:	4
Contribution to Project:	Dr. Park worked with Mr. Min for optimizing the bioconjugation of MNPs for cell labeling. Dr. Park also trained Mr. Min on these skills
Funding Support:	NIH

Name:	Craig Pille
Project Role:	Research intern
Researcher Identifier	N/A
Nearest person month worked:	6
Contribution to Project:	Mr. Pille participated in developing the measurement system, particularly optimizing the operation of molecular dispensers.
Funding Support:	Northeastern University

Name:	Lucas Rohrer
Project Role:	Research intern
Researcher Identifier	N/A
Nearest person month worked:	6
Contribution to Project:	Mr. Rohrer was trained for cellular labeling, and optimized the assay protocol.
Funding Support:	Northeastern University

• Has there been a change in the active other support of the PD/PI(s) or senior/key personnel since the last reporting period?

Nothing to report.

• What other organizations were involved as partners?

Organization Name	Electronics and Telecommunications Research Institute (ETRI)
Location of Organization	South Korea
Partner's contribution to the project	ETRI provided the foundry service for fabricating the IC version of the Hall sensor.
Financial support	In-kind support and Facilities

Organization Name	Yonsei Institute of Basic Science (YIBS)
Location of Organization	South Korea
Partner's contribution to the project	IBS provided a library of magnetic nanoparticles with different magnetic properties. These particles were used to perform magnetic multiplexing with the Hall sensor.
Financial support	Collaboration

8. SPECIAL REPORTING REQUIREMENTS

Not applicable.

9. APPENDICES

Publications listed in **Section 6** are attached.

- Lee H, Shin TH, Cheon J, Weissleder R (2015) Recent developments in magnetic diagnostic systems. Chem Rev 115:10690-10724. PMID:26258867.
- 2. Lee K, Shao H, Weissleder R, Lee H (2015) Acoustic purification of extracellular microvesicles. ACS Nano 9:2321-2327.
- 3. Im H*, Castro CM*, Shao H, Liong M, Song J, Pathania D, Fexon L, Min C, Avila-Wallace M, Zurkiya O, Rho J, Magaoay B, Tambouret RH, Pivovarov M, Weissleder R*, Lee H* (2015) Digital diffraction analysis enables low-cost molecular diagnostics on a smartphone. Proc Natl Acad Sci U S A 112:5613-5618. PMC4426451, PMID:25870273.
- 4. Chen S, Sanjana NE, Zheng K, Shalem O, Lee K, Shi X, Scott DA, Song J, Pan J, Weissleder R, Lee H, Zhang F, Sharp PA (2015) Genome-wide CRISPR screen in a mouse model of tumor growth and metastasis. Cell 160:1246-1260.
- 5. Im H, Shao H, Weissleder R, Castro CM*, Lee H* (2015) Nano-plasmonic exosome diagnostics. Expert Rev Mol Diagn 15:725-733. PMID:25936957.
- 6. Park YI, Im H, Weissleder R, Lee H (2015) Nanostar clustering improves the sensitivity of plasmonic assays. Bioconjug Chem 26:1470-1474. PMID:26102604..
- 7. Jeong S, Park J, Pathania D, Castro CM, Weissleder R, Lee H (2016) Integrated Magneto-Electrochemical Sensor for Exosome Analysis. ACS Nano 10:1802-1809. PMC4802494, PMID:26808216.
- 8. Park YI, Kim E, Huang CH, Park KS, Castro CM, Lee H*, Weissleder R* (2016) A facile coating strategy to functionalize inorganic nanoparticles for biosensing. Bioconjug Chem PMID:27792877.

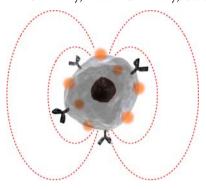


Recent Developments in Magnetic Diagnostic Systems

Hakho Lee,[†] Tae-Hyun Shin,[‡] Jinwoo Cheon,[‡] and Ralph Weissleder**,[†],§

†Center for Systems Biology, Massachusetts General Hospital, and *Department of Systems Biology, Harvard Medical School, Boston, Massachusetts 02114, United States

[‡]Department of Chemistry, Yonsei University, Seoul, 120-749, Korea



CONTENTS	
1. Introduction	10690
2. POC Assay Systems Using Magnetic Nanoparticles	10691
2.1. Magnetic Detection	10691
2.1.1. MicroNMR (μ NMR) System	10691
2.1.2. Magnetic Susceptometers	10691
2.1.3. Magnetoresistance Sensors	10692
2.1.4. Micro-Hall (μ Hall) Sensors	10692
2.1.5. Diamond Magnetometer	10693
2.2. Magnetic Actuation	10693
2.2.1. Magnetic Separation System	10694
2.2.2. Magnetic Manipulation System	10696
3. Key Magnetic Properties of Magnetic Nano-	
particles	10698
3.1. Saturation Magnetization	10698
3.2. Superparamagnetism	10698
3.3. Average Magnetic Moment	10699
3.4. ac Magnetic Susceptibility	10700
3.5. Relaxivity	10700
4. Synthesis of Core Magnetic Nanoparticles	10702
4.1. Ferrite-Based MNPs	10702
4.1.1. Coprecipitation Method	10702
4.1.2. Nonhydrolytic Thermal Decomposition	
Method	10703
4.2. Elemental Iron-Based MNPs	10704
4.3. Iron-Based Bimetallic Alloy MNPs	10704
5. Physical Characterization	10705
5.1. Particle Size	10705
5.2. Crystal Structure	10706
5.3. Composition	10706
5.4. Magnetic Properties	10706
5.4.1. Temperature-Dependent Magnetization	10706
5.4.2. Field-Dependent Magnetization	10708
6. Surface Coating Strategies of Magnetic Nano-	
particles	10708
6.1. Ligand Exchange	10708
6.1.1. Small Molecule Ligand	10708

6.1.2. Polymeric Ligand	10709
6.2. Encapsulation	10709
6.2.1. Amphiphilic Micellar Ligand	10709
6.2.2. Polymeric Matrix	10710
6.2.3. Hydrophilic Inorganic Material	10711
7. Conjugation Chemistries for Magnetic Nano-	
particles	10711
7.1. Covalent Conjugation	10711
7.1.1. Conventional Covalent Linkage Chem-	
istry	10711
7.1.2. Bioorthogonal Chemistry	10712
7.1.3. Amino Acid–Metal Dative Bonding	10713
7.2. Noncovalent Conjugation	10713
8. Clinical Applications	10713
8.1. Infection	10714
8.2. Cancer	10714
8.3. Coagulation	10714
8.4. Other Applications	10715
9. Conclusion and Perspectives	10715
Author Information	10715
Corresponding Author	10715
Notes	10715
Biographies	10715
Acknowledgments	10716
References	10716

1. INTRODUCTION

Rapid point-of-care (POC) diagnostics that enable specific cellular and molecular detection are currently being developed while some have already become clinical reality. These diagnostics are often based on portable, hand-held instruments and reagent-containing test kits. Overall, the development has largely been driven by technological advances, medical needs, and cost-saving initiatives. For example, POC systems allow care providers to obtain test results quicker, which in turn enables immediate clinical management decisions and elimination of costly delays to result in better care. The introduction of POC systems into primary and home care will ultimately preempt unnecessary hospitalization, improve inefficiencies associated with expensive hospital-based medical care, and reduce dependence on large, centralized clinics for routine diagnosis.^{2,3} POC technologies are also expected to have major impacts in resourcelimited settings and low/middle income countries where access to healthcare is often limited.⁴

Special Issue: Nanoparticles in Medicine

Received: December 15, 2014 Published: August 10, 2015

POC technologies were first developed to address basic medical needs. Currently available devices include those for blood glucose testing,⁵ blood gas and electrolyte analysis,⁶ coagulation testing,² cardiac marker diagnostics,^{7,8} drug-abuse screening,⁹ pregnancy testing,¹⁰ fecal occult blood analysis,¹¹ hemoglobin diagnostics, 12 cholesterol screening, 13 and limited infectious disease testing. 14,15 With increasing demands to address more clinical needs, the past few years have seen an explosive growth of different POC sensing approaches 16-19 based on electrical impedance, 20 colorimetric, 21 optical, 22 and magnetic²³⁻²⁵ sensing strategies. Particularly for cellular, molecular, and genetic testings, there remain challenges with many of these techniques. These challenges include further improving sensitivity and specificity, increasing complexity of tests, needs for complicated upfront purification (and possible loss of precious samples), unique issues associated with low volume testing, higher training needs, higher quality control costs, regulatory burden, and expense.

Irrespective of the specific approach, a major limitation to most techniques remains sample purification and enrichment for scarce targets (molecular, genetic, and pathogens). Magnetic sensing offers many advantages as human samples are naturally devoid of ferromagnetic materials (unlike electrical and optical technologies where interferents abound). Magnetic nanoparticles (MNPs) are also extensively used in biomedical separation technologies ^{26–30} and for imaging, ^{31–34} and are generally innocuous to human cells and other samples. Finally, new generations of miniaturized magnetic detectors have recently become available to utilize advanced magnetic nanomaterials for molecular testing. This article reviews recent advances in such magnetic POC devices, requirements for magnetic materials, and advanced conjugation chemistries.

2. POC ASSAY SYSTEMS USING MAGNETIC NANOPARTICLES

Magnetic POC systems exploit the following advantages of MNPs to achieve highly selective and sensitive detection (Figure 1).

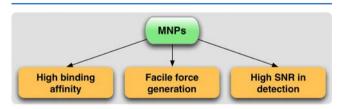


Figure 1. Unique advantages of magnetic nanoparticles (MNPs) in diagnostic applications. Affinity functionalized MNPs can efficiently bind to biological targets. The resultant magnetically labeled targets (cells, proteins, nucleic acids) can be mechanically manipulated by applying external magnetic fields (magnetic actuation), or detected by using magnetometers (magnetic sensing). These operations achieve high contrast against the biological background, and can be performed in native, i.e., nonpurified, clinical specimens.

- (i) By conjugating affinity ligands onto their surface, MNPs can be used to selectively label biological targets. The binding efficiency is higher than that of a single ligand alone, because MNPs offer multiple binding sites.³⁵
- (ii) MNPs can enhance or amplify the analytical signal. By tagging targets with MNPs, one can achieve high contrast against the background, which leads to higher detection sensitivities.³⁶ In nuclear magnetic resonance (NMR) detection where the

relaxation of ¹H protons is measured, each MNP influences millions of surrounding water molecules, a most effective amplification strategy.²³

(iii) MNPs can facilitate selective manipulation and sorting of targets, as only MNP-labeled targets will respond to the external magnetic field and experience mechanical force. This principle is extensively used in MNP-based cell sorting and enrichment.

This section reviews various MNP-based bioassay systems. We broadly categorized them as magnetic sensors and actuators, according to their primary use of MNPs, and discuss representative examples in each category.

2.1. Magnetic Detection

Signals from MNP-labeled biological objects are often measured by magnetometers.³⁷ Based on the detection mechanism, magnetometers can be categorized into volumetric or surfacebased sensors.³⁸ The volumetric sensors measure analytical signals coming from the entire detection volume, which makes assays simple and fast. The sensors' resolving power, however, can be restricted, because the acquired signal is an ensemble average of the whole volume. Representative examples of volumetric sensors include NMR devices, magnetic susceptometors, and conventional superconducting-quantum-interference devices (SQUIDs). Surface-based sensors directly detect individual magnetic objects near the sensing elements. These sensors generally achieve higher sensitivity and finer resolution than volumetric ones, but target samples should be placed in close proximity of the sensor surface. Such an arrangement limits the assay configuration, and typically causes the assays to be more time-consuming. To date, many different types of magnetometers (e.g., magnetoresistance sensors, Hall effect sensors) have been developed as surface-based biosensors.

2.1.1. MicroNMR (μNMR) **System.** NMR detects MNP-labeled targets by measuring the ¹H proton signal. The local dipole fields generated by MNPs perturb the precession of nuclear spins in water protons. Samples containing MNP-labeled targets thus display faster signal decay (higher transverse relaxation rate) than nontargeted samples (Figure 2a).³⁹ Because each MNP can affect a large number of its surrounding water molecules, NMR-based detection benefits from an intrinsic signal amplification to achieve high detection sensitivity.²³

Significant progress has been made toward miniaturizing NMR detection systems for POC diagnostics. Advancements include designing new NMR grade magnets, 40 miniaturizing NMR electronics into integrated circuit (IC) chips,⁴¹ and implementing smaller NMR coils. 42-44 These miniaturized microNMR (μ NMR) systems are not only portable, but also display higher sensitivity than conventional systems. Figure 2b shows a recently developed μ NMR system optimized for clinical operations. 45 The system used disposable tubes (diameter, 1.2 mm) as a sample container to prevent system contamination and to facilitate the sample loading (Figure 2c). The NMR electronics could be programmed to execute many different pulse sequences (Figure 2d). In particular, the system can automatically compensate for drifts in the NMR frequency caused by temperature fluctuations, which enabled robust NMR detection. This system has been used in many clinical trials, detecting various biological entities, including tumor cells, 16,46,4 pathogens, ^{48–52} and extracellular vesicles. ^{43,53}

2.1.2. Magnetic Susceptometers. Magnetic susceptometers measure the responses of MNPs exposed to alternating current (ac) magnetic field. The most widely used sensing scheme is to detect Brownian relaxation of MNPs. ^{54,55} MNPs in

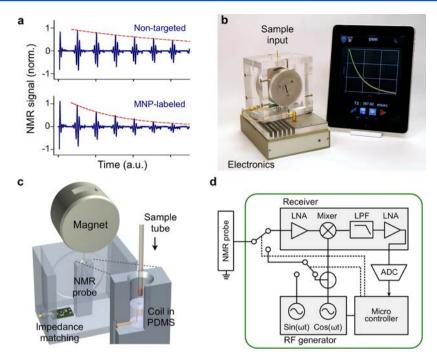


Figure 2. MicroNMR (μ NMR) magnetometer. (a) Sensing mechanism. Samples containing MNP-labeled biological targets have higher transverse relaxation rates of 1 H NMR signals. (b) Prototype portable μ NMR system, developed for clinical applications. This system has a capacity for automatic system tuning and features a user-friendly interface. (c) Magnet assembly and the NMR probe design. The microcoil is embedded in a polydimethylsiloxane (PDMS) substrate. The entire coil bore is accessible by a sample, which maximizes the sample-filling factor. A thin-walled tube is used for sample loading. (d) The NMR electronics is implemented using a field-programmable-gate-array (FPGA) chip that offers standalone operation and high programmability. LNA, low-noise amplifier; LPF, low-pass filter; ADC, analog-to-digital converter. Reproduced with permission from ref 45. Copyright 2011 RSC Publishing.

solution undergo thermal rotation with a time scale (τ_B) that is proportional to the particle's hydrodynamic volume (see section 3.4 for details). This thermal motion affects the ac magnetic susceptibility (χ) of MNPs. Specifically, the quadrature component of χ , which has 90° phase difference with respect to the ac field, has its maximum value when the excitation frequency is equal to $1/\tau_B$. Changes in the hydrodynamic diameter, due to target binding to MNPs, would shift the peak position. Compared to the μ NMR that requires a highly uniform magnetic field, magnetic susceptometry could be performed with a simpler setup. For example, Park et al. implemented a compact magnetic susceptometer to measure Brownian relaxation of MNPs (Figure 3a). The magnetic susceptometry, however, has lower sensitivity than the μ NMR, because the sensing lacks the inherent signal amplification mechanism.

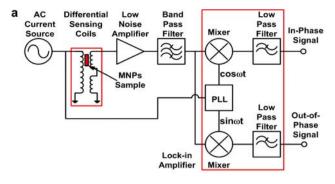
Magnetic susceptometry has been used to detect various biological targets, such as soluble proteins, ⁵⁷ DNA, ⁵⁵ and bacteria, ⁵⁸ with signals measured either by induction coils or SQUID under ac magnetic field excitation. By using ac magnetic susceptibility as a unique signature, the device could differentiate multiple types of MNPs based on their different hydrodynamic sizes (Figure 3b).

2.1.3. Magnetoresistance Sensors. Magnetoresistance sensors detect their changes in electrical resistance when exposed to external magnetic fields. The most widely used magnetoresistance sensor type is the giant magnetoresistance (GMR) magnetometer. The GMR effect is caused by the electron spindependent scattering of conduction electrons in magnetic layers. The phenomenon occurs in an artificial magnetic structure comprising multiple layers of ferromagnetic and nonmagnetic materials (Figure 4a). External magnetic fields change the relative angle between layers' magnetizations.

Accordingly, electrons passing through the layers experience a different level of scattering (Figure 4b). For biosensor applications, GMR sensors are typically used in association with a sandwich assay format, wherein molecular targets are immobilized on the sensor surface and labeled with magnetic probes.

The initial GMR biosensor used micrometer-sized magnetic beads as a probe.⁶⁰ However, the considerable size disparity between the probes and the molecular targets was a limiting factor in the assay speed and sensitivity. 61 The use of MNPs helped overcome such limitations and enabled sensitive detection of low amounts of proteins. 25,61,62 Furthermore, GMR sensor arrays, with each sensor functionalized with different antibodies, were developed for parallel detection. These sensors achieved the detection limit of ~50 aM and displayed high dynamic ranges.²⁵ To provide massively parallel sensing, a hybrid GMR sensor was constructed by juxtaposing two different chips: a 256 GMR array and a complementary metal oxide semiconductor (CMOS) chip for signal processing (Figure 4c). 59 Compared to other magnetic detectors, GMR sensors are usually more difficult to implement, as they require specialized magnetic wafers.

2.1.4. Micro-Hall (µHall) Sensors. When a current-carrying electrical conductor is placed in a magnetic field, a voltage difference is developed across the conductor, transverse to the current direction. This phenomenon, called the classical Hall effect, is caused by the accumulation of the moving charges to the sides of the conductor. Compared to MR-based sensors, the Hall-effect sensors have a lower magnetic-field sensitivity. However, they display an excellent signal linearity at high magnetic fields (>2 T) that can fully magnetize MNPs. Furthermore, the sensor fabrication is compatible with CMOS



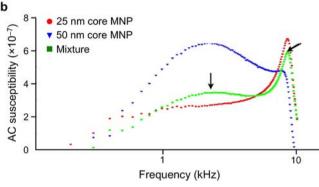


Figure 3. Magnetic susceptometer biosensor. (a) A quadrature detector was developed to sense alternating current (ac) magnetic susceptibility in solution. PLL, phase-locked loop. (b) The peak in the magnetic susceptibility shifts with particle size. The magnetic responses of two differently sized MNPs were measured (red, 25 nm core; blue, 50 nm core). This information was used to distinguish the composition in the mixture (green). Reprinted with permission from ref 56. Copyright 2011 IOP Publishing Ltd.

processing, which enables on-chip integration of a large array of Hall sensors and other auxiliary electronics. Various types of micrometer-scale Hall (micro-Hall; µHall) sensors have been developed and applied for molecular detection. 63-66 Gambini et al. advanced this technology by developing a large (64×160) sensor array via CMOS technology (Figure 5a).⁶⁷ The chip also contained a signal processing circuit and microelectromagnets to temporarily magnetize magnetic beads (Figure 5b). The system measured the remnant magnetic field (B_{bead}) coming from the beads immediately after the polarizing magnetization field (B_0) was switched off (Figure 5c). In this way, the weak B_{bead} from the magnetic beads could be distinguished from much stronger B_0 (10²-10⁵ times larger). In a titration experiment with magnetic beads (Dynabead M280, Invitrogen), the sensor showed the resolution of 25 particles per array, which was equivalent to a 0.1% coverage of the sensing area (0.64 mm²).⁶⁷

More recently, Issadore et al. introduced a new μ Hall system that can profile cells in a flow condition (magnetocytometry). ^{24,69} The sensor detected magnetic fields from MNP-labeled cells. The measured Hall voltage ($V_{\rm H}$) was proportional to the MNP numbers per cell, which in turn enabled quantitative molecular profiling (Figure 5d). For a given number of MNPs, the detection sensitivity was enhanced by using MNPs with high magnetic moments (e.g., doped ferrite, Fe-based particles). Because the sensor measured time-varying signals from flowing cells, it could operate in the ac-coupling mode to block interference from the static external magnetic field (B_0). In addition, eight 8 × 8 μ m² Hall elements were laid out as an overlapping 2 × 4 array (Figure 5e). This arrangement ensured

that cells inside the fluidic channel would be detected by at least two Hall sensors to improve the accuracy. When cancer cells were profiled for surface markers, the μ Hall results agreed well with those from flow cytometry (Figure 5f). The μ Hall detection, however, did not require washing or purification steps, and could be performed in complex biological media. With such a capacity, the μ Hall sensor was ideally suited to detect rare cells in native biological samples. For example, the μ Hall sensor was able to detect circulating tumor cells in cancer patient blood samples, even in those tested negative with clinical standards (CellSearch). Least the contract of the co

2.1.5. Diamond Magnetometer. Magnetometry based on nitrogen—vacancy (N–V) center diamonds is an emerging new technology for ultrasensitive magnetic detection. The N–V center is an association of a nitrogen atom and a vacancy inside a diamond crystal lattice (Figure 6a). The center has a ground-state energy with spin triplet ($m_S = 0$ and ± 1). The $m_S = 0$ state spontaneously split from $m_S = \pm 1$ (zero-field splitting) state, with an energy difference of 2.87 GHz. In the presence of external magnetic fields, the energy levels of $m_S = \pm 1$ would further split according to Zeeman effects (Figure 6b). The energy differences between $m_S = \pm 1$ and $m_S = 0$ can be measured spectroscopically to determine the strength of external magnetic fields.

One readout method is based on continuous optical and microwave excitation.⁷⁴ In this approach, a N–V system is optically polarized, through 532 nm excitation, into the excited state of $m_S = 0$; the spontaneous decay of $m_S = 0$ level from the excited to the ground state generates red fluorescence. A concurrent microwave excitation can induce transition from $m_S = 0$ to $m_S = \pm 1$ at the ground state, and the fluorescence intensity decreases as fewer $m_S = 0$ spins are available. By measuring the florescent intensity at sweeping microwave frequency, the relative change of $m_S = 0$ population can be measured. Without external magnetic fields, only a single dip in the fluorescence intensity is observed due to $m_S = \pm 1$ degeneracy. With external magnetic fields on, the Zeeman effect removes the degeneracy, and splits the single dip into two; the interdip distance is linearly proportional to the field strength (Figure 6c).

N–V diamonds could be an excellent biosensing platform. They assume ultrahigh detection sensitivity (3 nT/Hz^{1/2}),⁷¹ and yet operate at ambient conditions. In addition, standard microscopy is used for signal acquisition, offering a possibility for wide-field imaging. For example, Le Sage et al. used a N–V sensor to magnetically image magnetotactic bacteria (Figure 6d).⁷⁵ Magnetic fields, coming from chains of magnetosomes inside the bacteria, were measured, and their vector maps were generated at a subcellular resolution (400 nm). More recently, N–V diamond sensors have also been adopted as an NMR reader.^{76,77} The sensor demonstrated exquisite sensitivity, detecting NMR signal from 10⁴ nuclear spins from nanometer scale samples.⁷⁷

2.2. Magnetic Actuation

Magnetic actuation uses MNPs as a remote handle to exert mechanical forces on target objects. As in magnetic detection, the operation is highly selective even in complex, turbid samples, ²⁹ due to the inherently negligible magnetic susceptibility of biological objects, and can be performed in a parallel and high-throughput fashion. ^{28,78} Furthermore, by employing microfabrication, magnetic actuators can be integrated with sensing elements into an easy-to-use, microfluidic cartridge. ^{79,80}

Biological objects labeled with MNPs assume an induced magnetic moment (m) when subjected to external magnetic

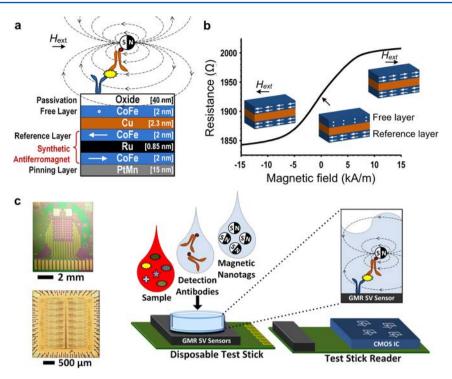


Figure 4. Giant magnetoresistance (GMR) magnetometer. (a) GMR sensors have multiple layers of magnetic and nonmagnetic materials. The magnetization of a reference layer is fixed through indirect exchange coupling in the synthetic antiferromagnet. The magnetization of the free layer, however, can rotate in response to the external magnetic field strength ($H_{\rm ext}$). (b) Due to the spin-dependent electron scattering, the electrical resistance of a GMR sensor changes as a function of the relative magnetization angle between the free and the reference layers. (c) An array of 256 GMR sensors (top) and its interface CMOS chip (bottom) were separately fabricated. The GMR sensor was mounted on a disposable test stick, and interfaces with the stick reader. A sandwich assay was used to detect protein markers. CMOS, complementary metal oxide semiconductor. Reproduced with permission from ref 59. Copyright 2013 IEEE.

fields. The magnetic force \mathbf{F}_{m} due to the external magnetic field induction \mathbf{B}_{0} is given as 81

$$\mathbf{F}_{\mathrm{m}} = \frac{1}{2} \nabla (\mathbf{m} \cdot \mathbf{B}_{0}) \tag{1}$$

For an ensemble of MNPs, the induced magnetic moment can be expressed as $\mathbf{m} = nV\chi_0\mathbf{B}_0/\mu_0$, where n is the particle number, V is the particle volume, χ_0 is the volume magnetic susceptibility, and μ_0 is the vacuum permeability (see section 3.3 for details). Equation 1 can be rewritten as

$$\mathbf{F}_{\mathrm{m}} = \frac{nV\chi_{0}}{\mu_{0}} (\mathbf{B}_{0} \cdot \nabla) \mathbf{B}_{0} \tag{2}$$

The force magnitude ($F_{\rm m} = |\mathbf{F}_{\rm m}|$) therefore can be increased by using MNPs with strong magnetization (hence large χ_0) and optimizing their labeling methods (large n); this topic is further discussed in section 4. On the device level, $F_{\rm m}$ is enhanced by designing magnetic structures that can generate strong (large B_0) as well as highly localized magnetic fields (large ∇B_0).

Various types of micromagnetic structures have been developed and integrated with microfluidic systems to improve the efficiency of magnetic actuation. 26,82,83 For example, lithographically patterned magnets that consist of either ferromagnetic elements $^{84-90}$ (e.g., Ni or Permalloy) or electromagnets $^{79,81,91-93}$ have been implemented. These micrometerscale structures are ideal in producing highly localized magnetic fields ($\nabla B_0 \sim 100~\mathrm{T~m}^{-1}$), and the resulting magnetic forces can be large enough (100 pN to 10 nN on 1 μ m magnetic beads) to enable high-throughput sorting. 88

We discuss two major modes of magnetic actuation in sections 2.2.1 and 2.2.2: magnetic separation and magnetic manipulation. Magnetic separation refers to the sorting operation that identifies and collects target objects, whereas magnetic manipulation is the precise spatial and temporal control of target objects.

2.2.1. Magnetic Separation System. Magnetic separation can be an efficient preparatory tool to enrich biological targets from heterogeneous mixtures.⁹⁴ According to their operation modes, the separation systems can be further grouped as a retention device or an in-flow filter device. 26 In the retention device, magnetically labeled targets are captured and kept in designated areas, while the rest of samples are separated and removed; the captured targets can be subsequently retrieved by removing the external magnetic field. In the in-flow device, spatial trajectories of magnetically labeled targets are deflected through the application of external magnetic fields, and targets are eventually collected in separate fluidic ports. The retentionbased separation is generally fast and easy to operate, although care should be taken not to overwhelm the separation capacity of the device. In contrast, the in-flow filtration can process a large volume of samples without being saturated. The device implementation and operation, however, often require a more sophisticated and balanced coordination between the fluidic flow and the magnetic force.

2.2.1.1. Retention Device. Retention devices should generate large magnetic forces to securely capture targets against the flow. As such, magnets are designed to create short-ranged, large-gradient fields. For example, Tibbe et al. used a combination of macro and microscopic magnets to capture individual cells. The device had a two-stage magnet system consisting of a pair of external magnets and a lithographically patterned array of Ni

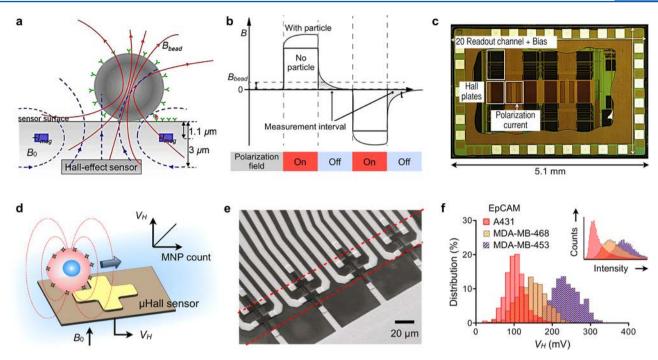


Figure 5. Hall magnetometer. Two types of Hall sensor operation are illustrated. (a) Detection of stationary magnetic beads. A pair of metal wires on both sides of the Hall-effect sensor are used to generate the polarizing field (B_0) that magnetizes the magnetic bead. The magnetic field emanating from the bead is measured. $\pm I_{\text{mag}}$, electrical currents to generate B_0 . (b) The beads are detected via relaxation measurement to eliminate the large offset coming from the polarizing field. The polarization magnetic field is applied, and then switched off. Subsequently, the remnant decaying magnetic field (B_{bead}) from the bead is detected by the Hall sensor. (c) Die photograph of a Hall sensor integrated circuit (IC). The chip contains 10 240 Hall-effect sensors, control electronics, and electromagnets for polarizing field generation. (d) Micro-Hall (μ Hall) sensor for single cell detection in flow condition. Each MNP-labeled cell generates magnetic fields that are detected by the μ Hall sensor. The Hall voltage (V_H) is linearly proportional to the MNP counts per cell. B_0 , external magnetic field. (e) Eight μ Hall sensors are arranged into an overlapping 2×4 array across the fluidic channel width. The dotted lines indicate the location of the sample flow. (f) The μ Hall system measured the expression levels of epithelial cell adhesion molecule (EpCAM) in different cell lines, which agreed with measurements by flow cytometry (inset). Reproduced with permission from ref 67. Copyright 2013 IEEE. Reproduced with permission from ref 68. Copyright 2012 IEEE. Reproduced with permission from ref 24. Copyright 2012 American Association for the Advancement of Science AAAS.

lines (Figure 7a). The external magnets had a wedge shape to produce a field gradient in the vertical direction. The Ni lines were magnetized by the uniform horizontal field from the external magnets, and produced a highly localized magnetic field on the device surface. MNP-labeled cells in the sample chamber would migrate upward due to the global field gradient by the external magnets. When close to the device surface, these cells were trapped between the Ni lines where the magnetic field flux is highly concentrated. As the captured cells aligned along the interstitial space of Ni lines, they could be easily observed by optical systems (Figure 7b). Indeed, the device was further integrated with a translation stage and a compact-disk optics to enable multiplexed single-cell analyses in whole blood.

High magnetic field gradient can also be achieved through the alternating arrangement of magnetic dipoles (Figure 7c). This configuration creates near fields with their maxima tightly confined on top of each dipole. Analytical modeling showed that the field is indeed short-ranged, decaying exponentially away from the dipoles. The leading term in the field magnitude is written as

$$B \approx B_{\rm d} e^{-(2\sqrt{2}\pi/a)|z|} \left| \cos \frac{2\pi}{a} x \cos \frac{2\pi}{a} y \right|$$
 (3)

where a is the pitch between adjacent dipoles and B_d is the field from a single dipole. Equation 3 also shows that the effective distance $\left[\sim a/(2^{1.5}\pi)\right]$ of the field reach can be engineered by controlling a. Issadore et al. used a magnetic self-assembly to

create the desired dipole arrangement (Figure 7d): permanently magnetized materials tend to form antiparallel configuration of moments to minimize magnetic energy. Specifically, NdFeB grains were suspended polydimethylsiloxane (PDMS) polymer, and the mixture was slowly cured (~1 h) to allow for the selfassembly of the NdFeB grains. A microfluidic channel (height 50 μ m) was then directly built on top of the cured magnets (Figure 7e).⁹⁷ The device had two magnetic sections for efficient magnetic capture. At the entry port, the magnetic layer was made of bigger NdFeB particles ($a \approx 125 \,\mu\text{m}$). This layer thus created a magnetic field that extended throughout the microfluidic channel height. Further along the channel, the grain size was reduced ($a \approx$ $8 \mu m$) to firmly trap magnetic objects. The device was used to enrich circulating tumor cells in blood by immunomagnetically depleting leukocytes (Figure 7f). The operation enriched the population of tumor cells to leukocytes by a factor of $>10^3$. The recovery ratio, the fraction of tumor cells that pass through the system, was ~90%.

2.2.1.2. In-Flow Separation Device. In-flow separation is achieved by applying magnetic fields, typically perpendicular to the direction of the fluidic flow. S2,99 The magnetic force changes the trajectories of magnetically labeled targets along the stream lines, continuously separating target objects from others whose trajectories remain unaffected. This scheme has a less stringent requirement for high field gradients, a necessity in the retention systems, and potentially affords higher throughput operation. The device by Inglis et al. used microfabricated Ni lines for cell

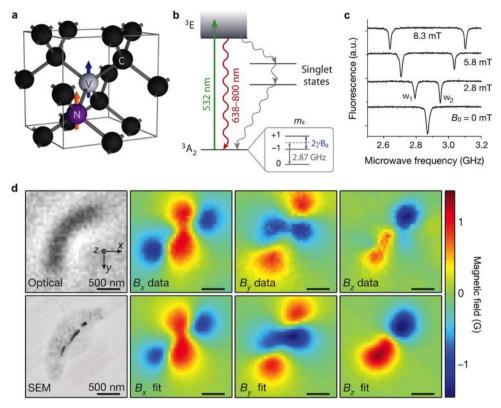


Figure 6. Diamond-based magnetometer. (a) Structure of nitrogen (N) and vacancy (V) inside a diamond lattice. C, carbon. The blue and orange arrows indicate the electron and nitrogen nuclear spins, respectively. (b) Energy state diagram. The N–V center has a spin-triplet ground state (3 A₂) with a 2.87 GHz zero-field splitting between the $m_S = 0$ and $m_S = \pm 1$ spin states. Optical excitation (532 nm) produces the excitation state (3 E) which decays back to the ground state by emitting a photon (638–800 nm wavelength). The $m_S = 0$ spin state has a stronger fluorescence than the $m_S = \pm 1$ states, because the $m_S = \pm 1$ excited states also decay nonradiatively via metastable singlet states. When an external field (B_0) is applied, the $m_S = \pm 1$ states are split by $2\gamma B_0$, where γ is the gyromagnetic ratio of the N–V electronic spin. (c) Optically detected magnetic resonance spectra for a single nitrogen–vacancy. The splitting between w_1 and w_2 is linearly proportional to B_0 . (d) Detection of magnetotactic bacteria with a N–V diamond sensor. Left top and bottom images are from optical microscopy and scanning electron microscopy (SEM), respectively. Measured magnetic field projections of the bacterium along the x (B_x), y (B_y), and z axes (B_z) are shown in the top row. The bottom row shows simulated magnetic field projections, assuming that MNP locations match those in the SEM image. Reproduced with permission from refs 70, 73, and 75. Copyright 2008, 2012, and 2013 Nature Publishing Group.

separation. ⁸⁶ Unlike the trapping system (Figure 7a), the Ni lines were aligned at an angle θ to the flow direction. The net force on a magnetic object is the vector sum of the magnetic force ($\mathbf{F}_{\rm m}$) and the drag force ($\mathbf{F}_{\rm d}$; Figure 8a). If the $\mathbf{F}_{\rm d}$ component perpendicular to the Ni lines is smaller than $F_{\rm m}$, the object will flow along the Ni lines, altering its direction in flow. ⁸⁹ The criterion for such events is $|\mathbf{F}_{\rm d}| \sin \theta < F_{\rm m}$; balanced control on the fluidic flow is thus important. This device was used to separate MNP-labeled leukocytes from whole blood (Figure 8b). The concept has been further extended for differential sorting. ⁸⁸ With a set of magnetic wires, each inclined at a different angle θ , multiple targets could be sorted according to their magnetic moments.

By using Y-shaped fluidic devices, samples can be separated without touching the magnetic structures. These devices have separate fluidic ports for introducing the sample and buffer solution; flow injection generates two laminar streams inside the fluidic channel. The magnets are located on the buffer side to pull MNP-labeled targets and collect them on the buffer outlet. As the magnets are detached from the fluidics, the system is easy to manufacture and cost-effective. The magnetic force can also be controlled in situ by changing the magnet position. Extending from this simple design, Kang et al. developed a blood-cleansing system that removed MNP-labeled pathogens from blood

(Figure 8c). 100 This fluidic system mimicked the architecture of a spleen, consisting of two fluidic channels interconnected with a series of open slits: one channel functioned as an arterial vessel for blood flow, and the other contained slow-flow saline buffer, acting like venous sinusoids. Bacteria targets were labeled by MNPs conjugated with an engineered human opsonin (mannose-binding lectin) that captures a broad range of pathogens (Figure 8c, inset). Under a continuous flow, MNP-labeled bacteria were removed into the venous channel through the magnetic pulling. The device achieved a high separation efficiency (>90%) with the flow rate reaching up to 1.25 L/h.

2.2.2. Magnetic Manipulation System. Magnetic manipulation is an elegant micromanipulation strategy to transport single cells or other small objects to desired locations through dynamic control of the magnetic fields. Lithographically patterned electromagnets are widely used as a field source, and can provide fine spatiotemporal resolution in field control. A planar coil is the most efficient geometry, as it can concentrate the magnetic flux. The field strength produced by electromagnets, however, is much weaker than that by permanent magnets. Most magnetic manipulation is thus performed under static conditions, i.e., without flow.

Several different types of devices have been reported for magnetic manipulation. ^{79,81,85,91,101} In particular, advanced IC

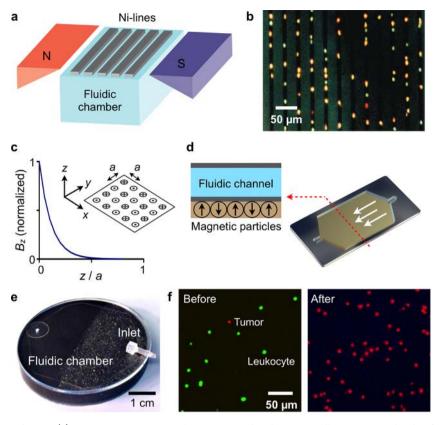


Figure 7. Magnetic retention devices. (a) Magnetic wire system. The separation chamber is optically transparent, but has ferromagnetic lines of nickel (Ni) deposited by lithography. The spacing between these lines is approximately the diameter of one white blood cell. When the chamber is placed between two angular-shaped magnets, the field gradients from the external magnets force the magnetically labeled cells upward to the top of the chamber. When the cells are in close proximity to Ni line, they are subjected to a high local gradient induced by the Ni lines. (b) The device in (a) was used to capture leukocytes that were labeled with CD45-specific MNPs. Because cells are aligned on the edge of Ni lines and counterstained with acridine orange, they can be easily observed by a microscope. (c) Alternating magnetic dipoles. This configuration creates magnetic fields that are tightly confined on the device surface. (d) When magnetic materials are allowed to self-assemble, the magnetic moments align into a similar pattern as in (c). The magnetic structure can easily cover the entire fluidic path to increase the throughput and the capturing efficiency. (e) A prototype device was implemented that consisted of self-assembled layers of 125 μm grain (close to inlet) and 8 μm grain of NdFeB powder. (f) A suspension of leukocytes (stained green) and tumor cells were incubated with a mixture of magnetic beads conjugated with anti-CD45 antibodies and fluorescent antibodies against the tumor (anti-HER2/neu). The suspension was then flowed through the magnetic device shown in (e). Fluorescence micrographs show the enrichment of tumor cells after the negative selection of leukocytes. The initial concentration of tumor cells to leukocytes was 1:10. Reproduced with permission from ref 97. Copyright 2011 RSC Publishing.

chips have been developed by applying the CMOS technology in device fabrication. For example, Dupont et al. implemented a linear array of microcoils integrated with optical detectors (single photon avalanche diodes) at the center of each coil, which allowed for on-chip manipulation and detection of individual magnetic particles (Figure 9a).⁸⁰ Lee et al. implemented an IC chip containing a matrix of microcoils, current sources, and control electronics (Figure 9b); the device was used to control the motion of individual biological cells with microscopic resolution. ¹⁰²

Fluidic droplets represent another technology used for magnetic manipulation. In this strategy, droplets are formed by encapsulating aqueous solution of MNPs in mineral oil. Magnetic particles serve a dual function, both as a force mediator and as a solid substrate for biochemical reaction. By using a two-dimensional microcoil array, implemented in a printed circuit board, Lehmann et al. moved a droplet through a sequence of buffer solutions to purify DNA from cell lysates. Pipper et al. introduced a POC device for avian flu detection (Figure 9c), by combining magnetic actuation with on-chip polymerase chain reaction (PCR). In this system, the magnetic droplets were manipulated by moving the permanent magnet. Sequential

processes were performed on-chip, including viral RNA isolation, purification, proconcentration, and further amplification through real-time reverse transcription PCR (RT-PCR). Because of the small sample volume (<50 μ L), the assay benefited from fast diffusion and low thermal mass, enabling the entire procedure to be completed in less than 30 min.

Magnetic manipulation was also employed to perform key steps in diagnostic assays. ^{105–107} For example, the Magnetotech sensor (Philips) used magnetic actuation to speed up immunomagnetic detection (Figure 9d). ¹⁰⁸ In this system, a pair of electromagnets sandwiched a microfluidic cartridge whose surface was functionalized with antibodies. Samples and immunomagnetic particles were mixed and injected to the cartridge. Activating the bottom electromagnet concentrated magnetic particles to the sensor surface, accelerating their binding kinetics to the surface. Subsequently, the top electromagnet was turned on to remove free and nonspecifically bound particles (magnetic wash). The final particle binding to surface was optically readout through reflection measurements.

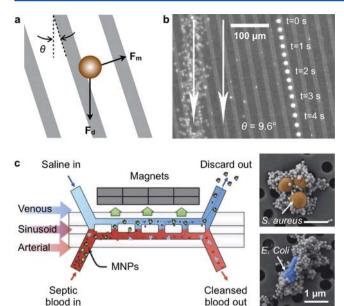


Figure 8. In-flow magnetic separation devices. (a) An array of magnetic lines is used to divert the trajectory of magnetic objects in flow. The magnetic lines are magnetized out of plane, and aligned at an angle θ with respect to the flow direction. The net force on the object is the vector sum of the in-plane magnetic force (F_m) and the fluid drag force (F_d). (b) Time lapse image showing a single magnetically tagged leukocyte. Red blood cells on the left are from a single image. The leukocyte tracks a magnetic line oriented at an angle of 9.6° to the fluidic flow (white arrow). (c) A two-channel microfluidic device to separate MNP-labeled bacteria in blood. The device mimics the structure of the spleen by incorporating a high-flow vascular arterial channel interconnected by open slits to a parallel low- or intermittent-flow venous sinusoid channel. Magnetic particles are mixed with blood sample to label pathogens (inset), and the mixture is introduced to the arterial channel. Reprinted with permission from ref 86. Copyright 2004 American Institute of Physics. Reprinted with permission from ref 100. Copyright 2014 Nature Publishing Group.

3. KEY MAGNETIC PROPERTIES OF MAGNETIC NANOPARTICLES

Table 1 compares key magnetic properties required for different detection modalities. The most important MNP property is the magnetic moment (m_p) . The utilities of MNPs are generally commensurate with their magnetic moment (m_p) , because higher m_p can result in larger force and more pronounced detection signals. m_p is a product of the magnetization (M) and the particle volume (V). Significant efforts thus have been made to synthesize large MNPs using magnetically stronger materials.

3.1. Saturation Magnetization

When a magnetic material has $n_{\rm d}$ atomic magnetic dipoles per unit volume and each dipole has the magnetic moment $m_{\rm d}$, the saturation magnetization M_0 is defined as $M_0 = n_{\rm d} \cdot m_{\rm d}$. This value is an unique material property, and sets a maximum M achievable for a given magnetic material. Table 2 lists the bulk M_0 values of representative magnetic crystals. Element iron, cobalt, and doped ferrite are the most widely used MNP constituents, as the material assumes high M_0 and can be synthesized into MNPs. Magnetization of MNPs increases with particle size, because the surface effect (e.g., spin-canting) is reduced in larger particles (Figure 10a). The saturation magnetization of MNPs, however, is generally smaller than that of bulk material, since the high surface energy of MNPs can hinder the perfect alignment of atomic magnetic dipoles. 110,111 For a spherical MNP, its

saturation magnetization $(M_{\rm p})$ can be estimated as $M_{\rm p}=M_0[(r-\Delta)/r]^3$, where M_0 is the saturation magnetization of the bulk material, r is the particle radius, and Δ is the thickness of magnetically frustrated (spin-canting) surface layer. 112 The surface effect can be reduced by modifying the particle shape. For example, cube-shaped MNPs were shown to have larger $M_{\rm p}$ values than spherical ones with the same magnetic volume, because more magnetic dipoles can align parallel in the cubic geometry (Figure 10b). 113,114

3.2. Superparamagnetism

A unique feature of MNPs is the paramagnetic behavior of an ensemble of MNPs, termed superparamagnetism. ¹¹⁵ Individual MNPs have a single magnetic domain with the magnetization aligned in a particular direction defined by magnetic anisotropy. However, thermal energy can activate the random reversal of magnetization over the anisotropy barrier. ¹¹⁶ Without external magnetic fields, an ensemble of MNPs display negligible remnant magnetic moments, but the magnetic moments grow with increasing external magnetic fields. This property is critical in both magnetic sensing and actuation, as (i) MNPs can be stably suspended in solution without aggregation to enhance their labeling efficiency, and (ii) MNP-labeled biological targets, once collected by external magnets, can be released by removing the external fields.

The superparamagnetism is highly dependent on the particle size. When the external magnetic field is removed, the average magnetic moment of a MNP relaxes to zero through thermal fluctuation. The corresponding relaxation time $(\tau_{\rm N})$ is estimated by the Néel–Brown model: ¹¹⁷

$$\tau_{\rm N} = \tau_0 \exp \frac{KV}{k_{\rm B}T} \tag{4}$$

where τ_0 is a time factor on the order of 10^{-9} s, K is the anisotropy energy constant of the material, $k_{\rm B}$ is the Boltzmann constant, and T is the temperature. MNPs are considered superparamagnetic when $\tau_{\rm N} < 10^2$ s at room temperature, and this condition sets the maximum particle size $(V=25k_{\rm B}T/K)$ for superparamagnetism (Table 2). These values, however, represent a general guideline, as many factors can affect the relaxation behavior of MNPs. For examples, the anisotropy energy constant is affected by the particle size and shape, magnetic interaction among particles could lock their magnetic moments, and electrical charges on the particle surface can exert repulsive force to effectively increase the interparticle distance. Importantly, MNPs in suspension can lose their effective moment through another route, the Brownian relaxation. For a particle with a hydrodynamic volume $V_{\rm h}$, the Brownian relaxation time is given by

$$\tau_{\rm B} = \frac{3\eta V_{\rm h}}{k_{\rm B}T} \tag{5}$$

where η is the fluid viscosity.⁵⁴ Since the magnetic moments can relax through either of these independent mechanisms, the effective relaxation rate is given as $1/\tau_{\rm N} + 1/\tau_{\rm B}$. The effective relaxation time (τ) of MNPs is therefore

$$\tau = \frac{\tau_{\rm N} \tau_{\rm B}}{\tau_{\rm N} + \tau_{\rm B}} \tag{6}$$

Note that $\tau \approx \tau_B$ for larger MNPs, as τ_N is increasing more rapidly than τ_B with the particle size (Figure 11a).

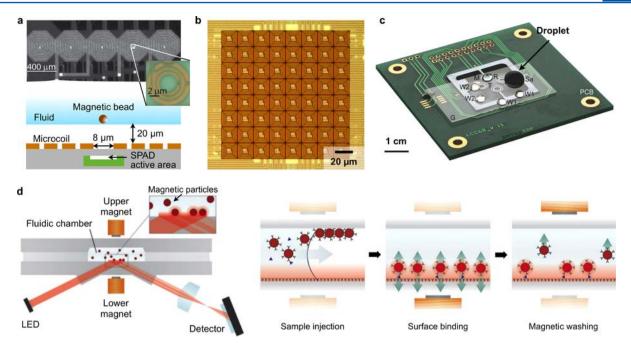


Figure 9. Magnetic manipulator. (a) A linear array of microcoils is implemented in a CMOS chip. Underneath the center of each coil, a single-photon-avalanche diode (SPAD, inset) is placed to detect magnetic beads. Using the combined actuation of adjacent coils, a single bead can be positioned over a SPAD. (b) A two-dimensional matrix of microcoils is integrated in a CMOS chip along with current sources and control electronics. Through dynamic control of electrical current in each coil, versatile magnetic field patterns can be created to trap and move magnetic objects at micrometer resolutions. (c) Magnetic droplet system. A droplet (Sa, 100 μ L) containing biological specimen, magnetic particles, and reagents, is manipulated by a permanent magnet (M). The droplet goes though a series of mixing, splitting, merging, and washing processes to extract RNA from virus. Target RNA is then amplified on chip via RT-PCR. PCB, printed circuit board; G, perfluorinated glass substrate; T, (one of four donut-shaped) miniaturized thermocycler; W1 and W2, washing solutions; R, RT-PCR mixture covered by mineral oil. (d) Magnetic actuation is exploited to facilitate diagnostic assays. (left) A fluidic reaction chamber is placed between a pair of electromagnets. A sandwich-type immunoassay with magnetic particles is performed, and the analytical signal is optically readout. (right) Assay procedure. By sequentially actuating the electromagnets, the immunomagnetic particles are concentrated to the sensor surface for binding, and excess and weakly bound particles are removed. Reprinted from ref 80. Copyright 2010 American Chemical Society. Reprinted with permission from ref 102. Copyright 2007 RSC Publishing. Reprinted with permission from ref 104. Copyright 2007 Nature Publishing Group. Reprinted with permission from ref 108. Copyright 2009 RSC Publishing.

Table 1. Comparison of Magnetic Sensors

mode	sensor type	key MNP requirement	detection limit	disease detection (demonstrated)	note	commercial partner
volumetric detection	μ NMR	high transverse relaxivity	single bacterium; ~10 mammalian cells; ~10 pM proteins	cancer; infection; metabolic disorders	versatile; portable device or desktop system	T2BioSystems
	magnetic susceptometer	Brownian relaxation; colloidal stability; monodispersity	~1 pM DNA (PCR-amplified)	infection	limited to soluble targets; low sensitivity; desktop system	DynoMag
surface sensor	GMR	high magnetic moment; colloidal stability	∼5 fM proteins	cancer; cardiovascular disease	limited to soluble targets; portable device	MagArray
	μ Hall	high magnetic moment	single cell; single bacterium	cancer; infection	CMOS compatible; lower sensitivity than GMR; portable device	
	N-V diamond	high magnetic moment	single MNP	cancer; infection	highest sensitivity; exploratory phase; desktop system	
magnetic actuation	optical sensor	high magnetic moment	∼1 pM proteins	controlled substance; cardiovascular disease	limited to soluble targets; portable device	Philips

3.3. Average Magnetic Moment

At a given temperature and under an external magnetic induction field (B_0) , the magnetization of superparamagnetic MNPs can be expressed using the Langevin function ¹¹⁵

$$M_{\text{avg}} = M_{\text{p}} \left[\coth \left(\frac{M_{\text{p}} V B_0}{k_{\text{B}} T} \right) - \left(\frac{M_{\text{p}} V B_0}{k_{\text{B}} T} \right)^{-1} \right]$$
 (7)

For a MNP population with a size distribution f(r), the magnetic moment of MNPs is obtained through a size-weighted ensemble averaging:¹²¹

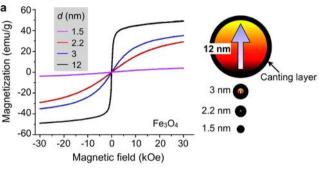
$$m_{\text{avg}} = \left[\int_0^\infty M_{\text{avg}} V f(r) \, dr \right] / \left[\int_0^\infty f(r) \, dr \right]$$
(8)

At low external magnetic fields (\leq 0.1 T), the magnetization of MNPs is linearly proportional to the external fields. The direct current (dc) volume magnetic susceptibility χ_0 for a monodisperse MNPs is given as

Table 2. Magnetic Properties of Selected Magnetic Crystals

material	saturation magnetization a (kA·m $^{-1}$)	anisotropy constant b (kJ·m $^{-3}$)	$d_{\rm sp}^{\ c}$ (nm)
Fe	1752	42	17
Co	1446	410	8
Ni	510	-5.8	32
Fe_3O_4	510	-11	26
$CoFe_2O_4$	475	180	10
$MnFe_2O_4$	560	-2.8	41
$NiFe_2O_4$	300	-5.1	33

^aBulk values at T = 0 K. Adopted from ref 109. ^bThe first order anisotropy constant at room temperature. Adopted from ref 118. ^cCalculated maximum diameter for spherical superparamagnetic MNPs.



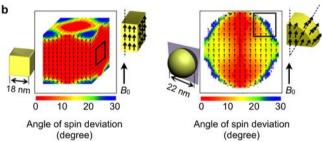


Figure 10. Size and shape dependent magnetization. (a) As the particle size increases, the relative effect of canted spins on the particle surface decreases, which results in an increase of net magnetization. The thickness of the scanted spin layer is \sim 0.9 nm for spherical Fe $_3$ O $_4$ MNPs. (b) Cubic MNPs assume higher saturation magnetization than spherical particles, because the cubic geometry allows more spins to align in the same direction of the applied magnetic fields. Reproduced from refs 111 and 114. Copyright 2011 and 2012 American Chemical Society.

$$\chi_0 = \frac{\mu_0 M_{\text{avg}}}{B_0} \bigg|_{B_0 \to 0} = \frac{\mu_0 M_{\text{avg}}^2 V}{3k_{\text{B}} T}$$
(9)

where μ_0 is the magnetic permeability of vacuum. For a MNP population, χ_{avg} is obtained by ensemble-averaging χ_0 .

3.4. ac Magnetic Susceptibility

When subjected to alternating current (ac) magnetic fields, MNPs may show delayed response due to the finite rate of magnetization changes. This property can be modeled by a complex magnetic susceptibility, $\chi = \chi' + i\chi''$, where χ' and χ'' respectively denote the in-phase and the out-of-phase components with respect to the ac field. For MNPs with the dc susceptibility of χ_0 and the effective relaxation time τ^{54}

$$\chi' = \frac{\chi_0}{1 + (\omega \tau)^2} \tag{10}$$

and

$$\chi'' = \frac{\chi_0 \omega \tau}{1 + (\omega \tau)^2} \tag{11}$$

where ω is the frequency of the applied field (Figure 11b). Note that χ'' has its maximum when $\omega = \tau^{-1}$; the shift in the peak frequency thus can be exploited to measure specific binding of target molecules to MNPs (section 2.1.2).

The out-of-phase component χ'' also has significant implications in magnetic fluid hypothermia, as it represents the energy loss through magnetic relaxation. With the external field strength H_0 , the specific loss power (P) for monodisperse MNPs is given by 122

$$P = \frac{1}{2}\mu_0 H_0^2 \chi'' \omega \tag{12}$$

To achieve maximum heating, MNPs should be monodisperse at the optimum particle size, satisfying $\omega = \tau^{-1}$.

3.5. Relaxivity

In NMR-based sensing, the most important MNP property is the relaxivity. When placed in an external field, each MNP creates a local magnetic field, which efficiently destroys the coherence in the spin—spin relaxation of water protons. The net effect is a shortening of the longitudinal (T_1 , spin—lattice) and transverse (T_2 , spin—spin) relaxation of NMR signal. The capacities of MNPs to decrease T_2 and T_1 are respectively defined as the transverse (T_2) and the longitudinal (T_1) relaxivities. MNPs are mainly used as a T_2 -modulating agent, because $T_2 \ge T_1$. The NPs with higher T_2 are desirable to improve the detection sensitivity.

The r_2 values increase with the particle size (r) and the magnetization $(M_{\rm p})$. The relationship, however, follows a different scaling law, depending on the particle size. When particles are small (e.g., r < 13 nm for MnFe₂O₄ MNPs at the NMR frequency 20 MHz), the diffusional motion of water molecules is fast enough to average out the magnetic fields produced by MNPs. In this regime, called motional averaging, the r_2 value (per metal) is proportional to $M_{\rm p}^2 \tau_{\rm d}^{-126}$ With $\tau_{\rm d} \sim r^2/D$, where D is the diffusion coefficient, $\tau_{\rm d}$ signifies the duration when water protons are under the influence of a MNP. As $\tau_{\rm d}$ increases further with growing particle size, the averaging effect diminishes and MNPs appear to water protons as randomly distributed, stationary objects. The corresponding relaxation mechanism, known as static dephasing, predicts that r_2 relaxivity is only proportional to $M_{\rm p}$.

Figure 11c shows the measured r_2 values of MnFe₂O₄ MNPs. With increasing particle size, the observed r_2 increased as predicted by the motional averaging relaxation. Further improving r_2 in a single-core particle format, however, turned out challenging, as the particles became nonsuperparamagnetic and no longer stable in suspension. Yoon et al. took an alternative approach by assembling small MNPs into a single multicore

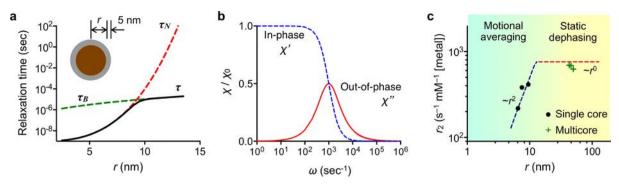


Figure 11. Different magnetic relaxation modes. (a) An ensemble of MNPs in solution can lose net magnetic moments through Néel and Brownian relaxation mechanisms. The Néel relaxation, namely the spontaneous flipping of magnetic moments inside a particle, is dominant for small MNPs. The Brown relaxation, caused by the physical rotation of particles, takes over as the particle size increases. Shown here are the Néel (τ_N) and the Brownian (τ_B) relaxation times calculated for Fe₃O₄ MNPs with 5 nm surface coating. The effective relaxation time (τ) can be obtained from $1/\tau = 1/\tau_N + 1/\tau_B$. (b) The alternating current (ac) magnetic susceptibility has two components: the in phase and the 90° out of phase with respect to the ac excitation source. The out-of-phase component has its maximum when the excitation frequency is close to the relaxation time of the particle. (c) In the NMR detection, MNPs accelerate the transverse relaxation of 1 H signal. The transverse relaxivity (r_2) is the capacity of MNPs to shorten the transverse relaxation time. The r_2 values of single and multicore MnFe₂O₄ MNPs were measured. While the r_2 values of single core MNPs increased steeply with increasing particle size $(\sim r^2)$, the r_2 values for multicore MnPs showed little dependence on particle size $(\sim r^0)$. Theoretical modeling, based on motional averaging and static dephasing, accurately describes the observed r_2 behavior (dotted lines): due to their small particle size, single-core MNPs are in the motional averaging regime (blue line), whereas multicore MNPs fall into the static dephasing regime (horizontal red line).

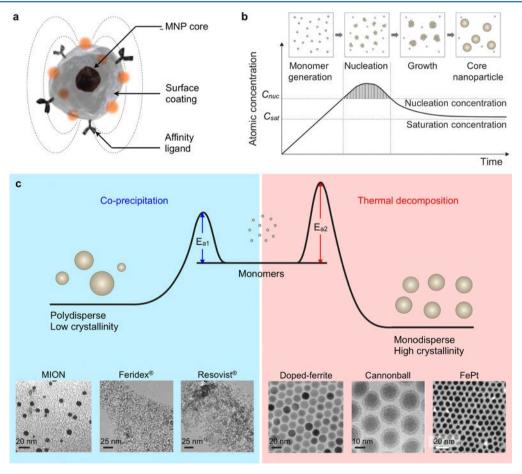


Figure 12. Synthesis of core MNPs. (a) Representative structure of a MNP. (b) Crystal-growth diagram. When the monomers are supersaturated and exceed the nucleation concentration, seed nucleation is induced and monomers are continuously aggregated onto the seeds, leading to crystal growth. C_{nuc} , nucleation concentration; $C_{\text{sa}\nu}$ saturation concentration. (c) Comparison of coprecipitation and nonhydrolytic thermal decomposition methods. The coprecipitation method results in kinetically favored MNPs which generally have a polydisperse size and relatively low crystallinity. Conversely, the thermal decomposition method produces thermodynamically stable MNPs with a monodisperse size and high crystallinity. Examples of transmission electron microscope (TEM) images of MNPs synthesized by coprecipitation (MION, Feridex, Resovist) or thermal decomposition methods (doped ferrite, cannonball, FePt) are shown. Reprinted with permission from ref 155. Copyright 2014 Nature Publishing Group. Reprinted with permission from ref 175. Copyright 2012 American Chemical Society.

particle. ¹²⁸ Such a configuration, akin to that of magnetic beads, allowed particles to remain superparamagnetic, while further increasing r_2 through the static dephasing relaxation mechanism. Indeed, the r_2 values of multicore particles were higher than those of single-core MNPs, and could be fitted to the static dephasing model.

4. SYNTHESIS OF CORE MAGNETIC NANOPARTICLES

MNPs are typically consisted of a magnetic core, surface coating, and versatile targeting molecules at the surface (Figure 12a). Cores can be produced from various materials and have a controlled size, shape, and crystallinity. ^{37,129–133} Generally, core MNPs are either made of pure metals (e.g., Co, Fe, and Ni)^{134–139} or their oxides. Transition-metal-doped oxides and metal alloys, including CoPt₃, FePt, and FeCo, are also good candidates. Among this variety of core MNP libraries, iron-based MNPs are considered to be one of the most attractive candidates for biological application, owing to their biocompatibility. 133,149 In particular, iron oxide MNPs are degraded into nontoxic iron and oxygen components, and their utilization as magnetic resonance imaging (MRI) contrast agents has been approved by the U.S. Food and Drug Administration (FDA) and the European Medicines Agency (EMA) at different time points. 150-155 In this section, representative core MNPs, including ferrite-based MNPs, elemental iron-based MNPs, and iron-based bimetallic alloy MNPs and their synthetic methods, will be discussed.

4.1. Ferrite-Based MNPs

Ferrites are complex magnetic oxides derived from iron oxides such as magnetite (Fe₃O₄) and maghemite (γ -Fe₂O₃), that are chemically combined with one or more metallic elements. ¹⁵⁶ The ferrites have a general composition of MFe₂O₄, where M is a divalent transition metal cation, such as Co²⁺, Mn²⁺, Fe²⁺, Ni²⁺, and Zn²⁺. Ferrite MNPs can be produced by either physical topdown approaches or chemical bottom-up strategies. 157 However, the latter are more adequate for producing highquality MNPs with a controlled size distribution and uniform composition. ^{132,158,159} A variety of colloidal chemical methods, including coprecipitation, thermal decomposition, micelle synthesis, hydrothermal synthesis, and electrochemical synthesis, are directed at the fabrication of MNPs. 159 This section will focus on the coprecipitation and thermal decomposition synthesis because they are the most relevant methods for preparing MNPs for POC applications. The former results in biocompatible MNPs for in vivo use, and the latter results in highly monodisperse MNPs with high magnetic properties, which are generally used for in vitro applications. Other synthetic methods have been reviewed by Laurent et al. 159

4.1.1. Coprecipitation Method. Ferrite MNPs are synthesized by the coprecipitation of stoichiometric amounts of ferrous (Fe²⁺) and ferric (Fe³⁺) salts in an alkaline solution. This technique is usually performed in the presence of water-soluble surface coating materials, such as dextran, ¹⁶⁰ starch, ¹⁶¹ poly(ethylene glycol) (PEG), ¹⁶² poly(acrylic acid) (PAA), ¹⁶³ or poly(vinyl alcohol) (PVA), ¹⁶⁴ to provide colloidal stability and biocompatibility in situ. During this reaction, MNPs are formed by sequential reaction steps, including monomer generation, nucleation, and growth (Figure 12b). According to the LaMer mechanism, a short burst of nucleation followed by a slow growth of particles without any significant additional nucleation is required to produce monodisperse particles. ¹⁶⁵ Therefore, optimizing the reaction conditions to achieve a complete

separation of the nucleation and growth process is critical for generating high-quality MNPs. 166 In coprecipitation synthesis, the reaction can be controlled by adjusting parameters, such as the pH, ionic strength, temperature, types of the iron salts, and $[{\rm Fe}^{2+}]/[{\rm Fe}^{3+}]$ ratio. The influences of these parameters on the size and magnetic properties of MNPs have been extensively explored in a number of studies. $^{167-171}$ However, MNPs synthesized by coprecipitation usually have a large size distribution because the growth of crystal is only governed by kinetic factors (Figure 12c). 159

One unique ferrite MNP, synthesized by coprecipitation method, is monocrystalline iron oxide nanoparticle (MION), which consists of a 3-5 nm magnetite and/or maghemite core surrounded by a biocompatible surface coating material (i.e., dextran). 172 MIONs are synthesized following the addition of concentrated base to an aqueous mixture of di- and trivalent iron chloride salts and dextran. The overall average hydrodynamic size of the MIONs usually falls within the 20-45 nm range. Owing to the biocompatible nature of ferrite and dextran surface coating and adequate hydrodynamic size, MIONs are widely utilized as a platform material for POC diagnostics. 160,172,17 Several variations of mono- or polycrystalline iron oxides have been used as MRI contrast agents (e.g., Feridex I.V., Combidex, and Resovist; though FDA-approved, some of these products have been withdrawn from the market for commercial reasons). 150-154,174,175 In the case of one specific MION-46, the core size is ~4.6 nm, the saturation magnetization value is ~68 emu g⁻¹, and r_1 and r_2 are 16.5 mM⁻¹ s⁻¹ and 34.8 mM⁻¹ s⁻¹ ([Fe], 0.47 T, 37 °C), respectively. Therefore, MIONs generate negative contrast and can be effectively used to image reticuloendothelial system organs, such as the liver and spleen.

However, these ferrite MNPs suffer from dissociation of the surface coating materials under certain biological conditions because of the weaker noncovalent binding interaction between the core ferrite and dextran coating. To prevent such coating dissociation, MIONs are further treated with chemical compounds that promote covalent cross-linkages between surface dextrans. $^{160,176-181}$ Epichlorohydrin is often used as a cross-linker. Upon treatment with base, the hydroxyl groups of dextran are deprotonated into their anions, which act as nucleophiles in an S_N2 reaction with epichlorohydrin. Each epichlorohydrin molecule can react with two molecules of dextran, by S_N2 displacement of the chloride ion and by a basecatalyzed epoxide ring opening reaction. These reactions finally result in cross-linked iron oxide nanoparticles (CLIOs). Followed by treatment with ammonia, primary amine functional groups are easily introduced via opening of the unreacted oxirane ring of epichlorohydrin. The primary amines on the surface of the nanoparticle endow CLIOs with an increased capacity for the conjugation of multiple targeting molecules, additional imaging agents, and therapeutics. 182 Amine-terminated CLIOs (CLIO-NH₂) have an average hydrodynamic size of 25-40 nm, approximately 40-80 amines per nanoparticle, and a r_2 of 50 mM⁻¹ s⁻¹ [Fe]. 160,176 Their unique coating makes CLIOs biocompatible and exceedingly robust for use in many biomedical applications. 182 More recently, alternative carboxymethyl dextran has been used for MION coating because its multiple carboxyl groups exhibit enhanced binding to the surfaces of the MNPs, which results in much higher coating stability. An example of an FDA-approved clinical preparation is ferumoxyol (Feraheme) which can be used not only to treat iron deficiency but also for MR imaging. 34,153

4.1.2. Nonhydrolytic Thermal Decomposition Method.

Although ferrite MNPs fabricated by the coprecipitation method are primarily used for in vivo imaging, the larger size distribution and poor crystallinity are a limitation for their use in POC devices. As a result, nonhydrolytic thermal decompositions methods have been developed. In general, ferrite MNPs synthesized by nonhydrolytic routes have excellent crystallinity and homogeneous size distribution and shape (Figure 12c). 119,141,143,184–186

Two different types of organometallic precursor systems can be used: (i) single source precursors that possess organic ligands and metal—oxygen bonds (e.g., iron cupferronate, iron acetylacetonate, and iron oleate complexes), or (ii) dual source systems where metallic precursors and additional oxidizers (e.g., (CH₃)₃NO)) are introduced for controlled oxidation. The precursors are mixed with nonhydrolytic organic solvents containing stabilizing surfactants and are then heated for thermal decomposition. As a result, monomers are generated and, when their concentration is above a supersaturation level, the nucleation and subsequent growth of crystalline nanoparticles are induced (Figure 12b).¹⁸⁷ The size of MNPs can be finely controlled by varying the reaction condition, such as the types of solvent, heating rate, surfactant, and reaction time, or by a seed-mediated growth process.

In one typical study by Sun et al., the preparation of monodisperse Fe₃O₄ MNPs with an average size of 4 nm (less than 10% standard deviation) is reported. In their study, iron(III) acetylacetonate (Fe(acac)₃) precursors in phenyl ether are decomposed at a high temperature (260 °C) in the presence of a mixture of surfactants (oleic acid and oleylamine) and reducing agent (1,2-hexadecanediol). 188 When the reaction solvent is changed from phenyl ether (boiling point bp = 258 °C) into benzyl ether (bp = $298 \,^{\circ}$ C), larger MNPs with a diameter of 6 nm are obtained. The size of the MNPs can be further increased up to 20 nm through a seed-mediated growth using 3-4 nm Fe₃O₄ MNPs as seeds. Regardless of the size of the MNPs, the heating rate is an important parameter for determining the size distribution of the MNPs. Typically, for highly monodisperse MNPs, the mixture is first heated up to 200 °C, and it remains at that temperature for some time (aging) and is then finally heated up to 260-300 °C. When the mixture is directly heated up to a reflux temperature, the resultant MNPs have a wide size distribution from 4 to 15 nm.

Cheon and colleagues demonstrated size-controlled syntheses of single-crystalline maghemite MNPs by modulating the amount and type of surfactants as well as the reaction times. 186 The size of the synthesized MNPs is increased from 12 to 50 nm by increasing the surfactant-to-metal precursor ratio and reaction time. When sufficiently large amounts of surfactant are introduced, surfactants are reversibly coordinated to the MNP surface, allowing for further growth. The long reaction time provides sufficient opportunity for the Ostwald ripening process during which large MNPs grow larger at the expense of smaller MNPs. 189 The same researchers also showed the surfactant effects on the shape of MNPs. The morphological structure of maghemite is mostly governed by three surfaces: (100), (110), and (111). Therefore, the shape can be controlled by modulating the degrees of truncation along those surfaces. For example, at a low surfactant concentration, surfactants mostly bind to the highest-energy (111) surfaces and growth along the [111] direction is restricted. The resulting (111) truncated MNPs can have diverse shapes, including sphere, diamond, and prism. When the surfactant concentration increases significantly, (111)

and the next-highest-energy (110) surfaces are covered by surfactants providing hexagon-shaped MNPs.

To produce highly monodisperse MNPs, Hyeon et al. took advantage of an iron oleate complex. ^{119,184} First, an iron oleate complex (Fe(oleate)₃) is prepared by reacting iron chloride with sodium oleate; then, the complex is slowly heated up to 310 °C in the presence of organic solvent and surfactants. According to the study, nucleation occurs at 200–240 °C when one oleate ligand is dissociated from Fe(oleate)₃ and growth occurs at about 300 °C by the dissociation of remaining two oleate ligands from the iron oleate complex. Owing to this nature of the iron oleate complex, the nucleation and growth process can be effectively separated, which is a key requirement for preparing uniformly sized MNPs. By modulating the decomposition temperature and aging time, the MNP size is controlled from 5 to 22 nm. Additionally, all of the MNPs are monodisperse with a size distribution of less than 4%.

These nonhydrolytic thermal decomposition approaches can be further extended to the syntheses of transition-metal-doped ferrite MNPs (MFe₂O₄, M = Co, Fe, Ni, Mn, and Zn) simply by using additional divalent transition metal precursors, such as $M(acac)_2$ or MCl_2 (M = Mn, Fe, Co, Ni, and Zn). ^{147,148,185} Such substitution of Fe²⁺ into transition metals offers an opportunity to precisely control the magnetic properties of ferrite MNPs to enhance the saturation magnetization. Ferrite MNPs have an inverse spinel crystal structure with the oxygen anions arranged in a face-centered cubic lattice. ¹³⁰ The tetrahedral (T_d) sites are occupied by Fe^{3+} ions, and octahedral (O_h) sites are filled with Fe³⁺ and Fe²⁺ ions. The magnetic spins of the metal ions at the O_h sites align parallel to each other, while they align antiparallel to those at the T_d sites. Therefore, each magnetic spin of one octahedral Fe3+ and the other tetrahedral Fe3+ is canceled out, and only the magnetic spins of octahedral Fe^{2+} with a high spin d^6 configuration induce a total magnetic moment per unit of 4 $\mu_{\rm B}$ (Bohr magneton; $9.27 \times 10^{-24} \text{ J/T}$). 147,190 In this sense, it is possible to control the net magnetic moment by replacing octahedral Fe²⁺ with divalent transition metal ions.

Following the report on the syntheses of monodisperse metaldoped ferrite MNPs by Sun et al., 185 Lee et al. demonstrated the dopant effects on magnetism of MNPs. 147 A series of 12 nm metal-doped ferrite MNPs, including MnFe₂O₄, FeFe₂O₄, $CoFe_2O_4$, and $NiFe_2O_4$, are fabricated. The reaction is performed by heating an octyl ether solution containing divalent metal chloride (MCl₂, M = Mn²⁺, Fe²⁺, Co²⁺, and Ni²⁺), iron(III) acetylacetonate, oleic acid, and oleylamine. As a result of the electron spin configurations of the metal-doped ferrite MNPs, their net magnetic moments per unit MnFe₂O₄, FeFe₂O₄, $CoFe_2O_4$, and $NiFe_2O_4$ are estimated as 5, 4, 3, and 2 μ_B , respectively. Reflecting those estimations, the saturation magnetization (M_p) values of those MNPs are measured as 110 ($\lceil Mn + 1 \rceil$) Fe]), 101 ([Fe]), 99 ([Co + Fe]), and 85 emu g^{-1} ([Ni + Fe]). Recently, Jang et al. synthesized Zn-doped ferrite MNPs ((Zn_{0.4}Fe_{0.6})Fe₂O₄) and Zn-/Mn-doped ferrite MNPs $((Zn_{0.4}Mn_{0.6})Fe_2O_4)$ with high M_p values of 161 ([Zn + Fe]) and 175 emu g⁻¹ ([Zn + Mn + Fe]). The Zn²⁺ doping level, a key parameter for a high M_p value, is precisely controlled by varying the molar ratio between metal precursors. Another example of metal-doped ferrite MNPs utilizes not only the doping but also the sizing strategies to achieve a high magnetization. Lee et al. synthesized metal-doped ferrite MNPs by reacting the mixture of $Fe(acac)_3$, $Mn(acac)_2$, and 1,2-hexadecanediol at a high temperature of 300 °C. 44 The size of the resultant MnFe₂O₄ MNPs (10 nm) is further increased to 12,

Chemical Reviews Review Review

16, or 22 nm through a seed-mediated growth strategy. In particular, the MNPs with a size of 16 nm show high transverse relaxivity of $420 \text{ mM}^{-1} \text{ s}^{-1}$, which is about 7-fold higher than that of MIONs.

4.2. Elemental Iron-Based MNPs

Monometallic MNPs, such as cobalt, iron, and nickel, have been extensively studied due to their prominent magnetic properties. ^{132,137,191} Monometallic MNPs exhibit superior magnetization than their corresponding oxides, making them an ideal choice for bioapplications including highly sensitive detection of biomolecules and molecular MRI. 134–139 The elemental ironbased MNPs are especially attractive, owing to their high saturation magnetization value (218 emu g⁻¹, in case of bulk) as well as biocompatibility originating from the nontoxic nature of iron. 192 Therefore, the controlled synthesis of elemental ironbased MNPs has been an important goal in magnetic nanomaterial science. The nonhydrolytic thermal decomposition is the most common method for preparing elemental iron MNPs. 139,193,194 However, there still remain challenges to obtaining pure monometallic iron MNPs because iron nanoparticles are extremely reactive and readily oxidized, resulting in undesired changes in the magnetic properties. Therefore, elemental iron-based MNPs require passivation by an oxidatively inert protection layer, such as carbon, 195 metal oxide, 44,128,196,19 noble metal, 198,199 polymers, 200 and silica. 201

The most representative strategy for producing such stable MNPs is nonhydrolytic thermal decomposition synthesis of elemental iron MNPs followed by a controlled oxidation process to form a protective iron oxide layer. 44,128,196,197 According to a method provided by Cabot et al., an iron pentacarbonyl precursor is thermally decomposed in air-free octadecene solvent containing oleylamine as a surfactant. 196 The as-synthesized iron nanoparticles are then heated in the presence of oxygen, resulting in a core-shell structured Fe@Fe3O4 MNPs. The size of the nanoparticles can vary from 5 to 18 nm by adjusting reaction parameters, such as the surfactant level, temperature, and time. The thickness of a surface iron oxide layer can also be precisely tuned by controlling the reaction temperature because the shell growth is dependent on iron diffusivities which are exponentially affected by the temperature. Under air exposure at room temperature, an oxide shell that is only a few nanometers thick is formed on the surface MNPs. When the reaction temperature increases up to 350 °C, the thickness of the shell reaches up to 10 nm, while simultaneously leaving a vacancy behind the Fe core. This vacancy formation can be explained by the Kirkendall effect. As the reaction proceeds, iron atoms are continuously diffused outward from the core, resulting in a growth of oxide shell on the surface of nanoparticle and inducing a void at the core. Therefore, to generate stable core-shell structured MNPs without a void, it is crucial to optimize the reaction conditions with an appropriate temperature and air exposure time.

Regardless of the thickness, the iron oxide shell in the assynthesized nanoparticles has poor crystallinity. ^{196,197} This is problematic because the amorphous iron oxide shell cannot effectively protect the metallic Fe core from deep oxidation. For example, as-synthesized MNPs with a 2.5 nm Fe₃O₄ shell and 4 nm Fe core are naturally oxidized at room temperature within 4 h of their exposure to air, leading to a thicker shell of 3.5 nm and a smaller core of 3 nm. ¹⁹⁷ This oxidation process reduces the M_p value of MNPs from 123.5 to 99.4 emu g⁻¹ ([Fe]). To make Fe@ Fe₃O₄ nanoparticles more stable, Peng et al. coated a crystalline Fe₃O₄ shell via a controlled oxidation process, which is mediated

by an oxidizing agent, $(CH_3)_3NO.^{197}$ This controlled oxidation results in an Fe₃O₄ shell with an inverse spinel crystal structure. In this technique, the thickness of the shell is modulated by adjusting the amount of $(CH_3)_3NO$. The M_p value of resulting MNPs is stably maintained upon air exposure.

Based on the synthetic methods mentioned above, 16 nm elemental iron-based MNPs, known as "cannonballs", were developed by Lee et al. 44 The cannonballs (CBs) have an 11 nm elemental Fe core coated with a 2.5 nm thick Fe₃O₄ shell. The CBs show a superior magnetization of 139 emu g^{-1} , which is 1.6fold higher than that of 16 nm Fe₃O₄ nanoparticles. To further enhance the magnetic properties, Yoon and co-workers utilized a synthetic approach that enables tuning of the shell composition. 128 Instead of oxidizing the surface of the Fe core, Fe MNPs are annealed in the presence of an iron oleate complex. In this method, transition metals (Mn²⁺ or Co²⁺) can easily be doped into a ferrite shell by co-injecting a stoichiometric amount of manganese oleate or cobalt oleate with iron oleate. This facile control of the shell composition allows for tailoring the magnetic properties of MNPs. For example, the high magnetic moment of MnFe₂O₄ allows Fe@MnFe₂O₄ MNPs to exhibit the highest M_p value of 145 emu g^{-1} of MNPs with other shell compositions. Consequently, the Fe@MnFe2O4 MNPs are successfully used in magnetic resonance-based sensing applications. 128

In addition to those iron nanoparticles covered with oxides, there are few other types of elemental iron-based MNPs such as iron silicide (Fe₃Si) and iron carbides (Fe₃C). In their bulk state, Fe_3Si and Fe_3C possess relatively high saturation magnetization values of 84 and 130 emu $g^{-1.202,203}$ These materials are known to be more resistant to oxidation than iron nanoparticles. They can therefore maintain their original magnetic properties for long-term biomedical applications. Fe₃Si and Fe₃C can be prepared via various synthetic means including a gas-phase method (e.g., chemical vapor deposition), 204 laser pyrolysis, ^{205,206} and other high-temperature methods (e.g., calcination). 207 Recently, nonhydrolytic thermal decomposition routes have been reported for Fe₃Si and Fe₃C MNPs. Dahal et al. prepared Fe₃Si MNPs by refluxing Fe(CO)₅ and silicone tetrachloride (SiCl₄) in a mixture of solvent and surfactants.²⁰² The size of Fe₃Si MNPs is controlled from 4.2 to 7.5 nm by increasing the concentration of precursors at fixed molar ratios for iron to silicon. The 7.5 nm Fe₃Si MNPs show an M_p value of 60 emu g^{-1} , which is similar to that of ferrite MNPs. Shultz et al. synthesized 2.7 nm Fe_3C MNPs by injecting $Fe(CO)_5$ into a refluxing trioctylphosphine oxide. ²⁰³ The Fe_3C MNPs are further coated with a thin layer of iron oxide and gold for more enhanced resistance to oxidation. The resulting Fe₃C@FeO_x@Au MNPs yield a high $M_{\rm p}$ value of 110 emu g⁻¹, which is comparable to that of 12 nm Mn-doped ferrite MNP. ¹⁴⁷

4.3. Iron-Based Bimetallic Alloy MNPs

Bimetallic alloy nanoparticles are another important class of MNPs. 143,144,146,208,209 Unlike ferrite-based MNPs, all magnetic spins in the bimetallic alloy MNPs align parallel to the external magnetic field. Therefore, in general, the magnetic moments of bimetallic alloy MNPs are higher than that of ferrite MNPs. For example, the magnetic moment of FeCo nanoparticles is 2.4 $\mu_{\rm B}$ per magnetic atom, which is about 2-fold larger than that of Fe $_3{\rm O}_4$ nanoparticles. 190,210 This superior magnetic property makes bimetallic alloy MNPs possible candidates for biomedical applications.

The bimetallic MNPs are classically fabricated by a physical deposition process, including vacuum-deposition technique and

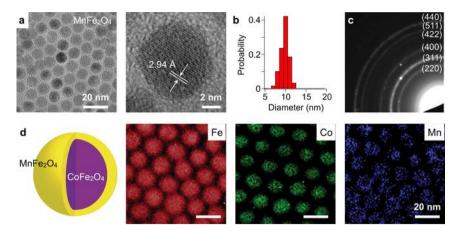


Figure 13. MNP analysis by TEM. (a) TEM imaging allows for fast assessment of particle shape (magnetic core), down to the atomic length scale. A crystal lattice plane of a ferrite MNP is shown. (b) Size distribution of particles in (a) were obtained. (c) In the diffraction mode, TEM can be used to display the reciprocal lattice pattern. Shown here is the electron diffraction pattern of MnFe₂O₄ MNPs. Concentric ring patterns corresponding to the spinel structure are identified. (d) By scanning the electron beam and performing spectroscopic measurements, the composition of particles can be mapped. The element of $CoFe_2O_4$ (core)/MnFe₂O₄ (shell) MNPs were imaged using the electron energy loss spectroscopy (EELS) method. Reproduced with permission from ref 44. Copyright 2009 National Academy of Sciences. Reproduced with permission from ref 217. Copyright 2011 Nature Publishing Group.

gas-phase evaporation. 144,211,212 However, MNPs produced by these physical methods often suffer from several limitations, such as particle aggregation, wide size distribution, and poor colloidal stability.²⁰⁸ In contrast, solution phase chemical synthesis offers an effective means of synthesizing monodisperse bimetallic MNPs. The most established chemical synthesis route is reduction decomposition of metal precursors. 143,145,208 In this method, iron pentacarbonyl is thermally decomposed to Fe and carbon monoxides and metal acetylacetonate (M(acac)₂, M = Pt or Co) is reduced by 1,2-alkanediol to pure metal. These two metal atoms are combined, forming bimetallic clusters (Fe-M), which act as nuclei. As more Fe-M species are deposited around the nuclei, the growth continues, leading to the formation of bimetallic alloy MNPs. Surfactants, such as oleic acid and oleylamine, are commonly introduced for particle stabilization. The composition of MNPs is controlled by the ratio between Fe(CO)₅ and M(acac)₂. ²¹³ Due to the difference in the rate of decomposition and reduction, the stoichiometric level of metal sources will lead to an unequal atomic percentage of Fe and M. To have bimetallic MNPs with near-equal levels of Fe and M, the compositional relation between the Fe(CO)₅/M(acac)₂ ratio and x in $\text{Fe}_x M_{(100-x)}$ should be experimentally investigated. For better control of composition, Na₂Fe(CO)₄, which acts as not only an Fe source but also a reducing agent, can be used instead of Fe(CO)₅. ²¹⁴ The Fe²⁻ from Na₂Fe(CO)₄ is oxidized to Fe, and M^{2+} is reduced to M by two electrons transferred from Fe²⁻. In this sense, bimetallic alloy nanoparticles with 1:1 stoichiometry can be obtained.

The size of bimetallic alloy MNPs is tuned by modulating the molar ratio between metal sources and surfactants, level of reducing agents, and reaction temperatures. Momose et al. achieved fine-tuning of the FePt MNP size through simply changing the amount of surfactants. As the amount of surfactants increases, the nanoparticle size proportionally increases from 2 to 5 nm, which is due to a decrease in the nucleation rate caused by surfactants. Chen et al. excluded reducing agent from the reaction mixture to modulate the size of the nanoparticles. Because the reduction of M(acac)₂ is essential to form nuclei, the exclusion of reducing agent slows down the nucleation rate, allowing more metals to deposit

around the nuclei, leading to a larger particle. The authors demonstrated that the reaction temperature also critically affects the nucleation rate and the size of MNPs. The higher reaction temperature induces the faster nucleation and smaller nanoparticles. For example, the size of MNPs synthesized at 240 $^{\circ}\text{C}$ is 6 nm, while the nanoparticles produced at 225 $^{\circ}\text{C}$ are 9 nm.

5. PHYSICAL CHARACTERIZATION

The physical properties of MNPs can be measured using conventional material characterization tools. When measurements are performed on large number of MNPs, the acquired data should be interpreted as a size-weighted ensemble average.

5.1. Particle Size

The most widely used methods to measure MNP size include transmission electron microscopy (TEM) and dynamic light scattering (DLS). These two modalities are complementary: TEM images the MNP cores in a dried powder form, whereas DLS measures the hydrodynamic diameter of particles in a suspension.

TEM is a versatile method that can provide morphological, compositional, and crystalline information on MNPs. The technique images electrical interactions between MNP crystals and a beam of electrons. The imaging resolution can be down to atomic scale (a few angstroms), due to the small wavelength of the electron beam (Figure 13a). TEM can visualize many individual MNP cores, and thereby facilitates the assessment of particle size distribution (Figure 13b). In the electron diffraction mode, TEM can project reciprocal crystal lattice into concentric ring patterns (Figure 13c), which is useful to quickly identify crystal structures. When combined with spectroscopic instruments (e.g., energy-dispersive X-ray (EDX) spectrometer, electron energy loss (EEL) spectrometer), TEM can generate atomic-scale elemental maps for compositional analysis (Figure 13d).

DLS measures the scattered light from MNPs upon their illumination with a monochromatic light source. The intensity of the scattered light fluctuates over time, as particles undergo Brownian motion. The fluctuation rate can be converted into the diffusivity of particles, and eventually into the hydrodynamic

Chemical Reviews Review Review

diameter (d_h) through the Stokes–Einstein relationship. Consequently, DLS estimates the effective particle size in fluid, which encompasses the magnetic core and its surface molecules. The data, however, should be carefully inspected. The original size distribution measured by DLS is intensity-weighted $(\sim d_h^{\ 6})$, and therefore can be dominated by the presence of MNP aggregates or oversized particles. To spot such distortion, the volume and the number distributions, mathematically derived from the intensity distribution, should be compared as well for consistency.

5.2. Crystal Structure

Similar to the electron diffraction in TEM, the crystal structure of MNPs can be analyzed through X-ray diffraction (XRD). The method measures X-ray waves reflected from solid crystals. When the X-ray incident on a crystal satisfies the Bragg's condition, the reflected waves from the lattice planes undergo constructive interferences, producing strong intensity peaks. By using powdered MNPs and scanning the incidence angle of the X-ray, diffraction peaks from all possible lattice orientations can be obtained. The measured diffractogram is then compared with standard patterns, to identify the crystal structure. The average crystal size $(d_{\rm XRD})$ can be further estimated from the Scherrer formula, $d_{\rm XRD} \approx \lambda(\beta\cos\theta)$, where λ is the X-ray wavelength, β is the peak width at half the maximum intensity, and θ is the Bragg angle. ²¹⁸ Figure 14 shows an XRD diffractogram of Fe₃O₄ MNPs

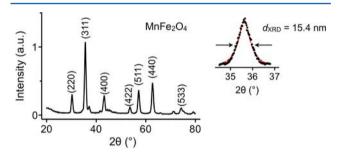


Figure 14. Structural analysis by X-ray diffraction (XRD). By scanning the incident angle (θ) of an X-ray beam and using powdered MNPs, the diffraction peaks of different lattice planes are measured. A diffraction pattern from powdered MnFe₂O₄ MNPs is shown, which conforms to that of a typical spinel structure of ferrite. The crystal size is also estimated by fitting the major peaks (311) to Scherrer's formula. Reproduced with permission from ref 44. Copyright 2009 National Academy of Sciences.

(16 nm in diameter under TEM), with each peak assigned to a distinct lattice plane of a spinel group. The estimated crystal size (d_{XRD}) from the (311) peak was 15.4 nm (Figure 14, inset), close to that by TEM (16 nm). This indicates that the prepared MNPs are mostly composed of single domain crystals.

5.3. Composition

Particle composition can be measured in several ways. To quickly obtain stoichiometric ratios of different elements within the particle, electron spectroscopies (e.g., EDX, EEL) can be applied during electron microscopy. For the quantification of absolute amounts, however, inductively coupled plasma atomic emission spectroscopy (ICP-AES) is often used. In this method, MNPs are chemically dissolved into constituent atoms, and the atomic electrons are thermally excited by Ar plasma. When the excited electrons return to ground state, they emit light at specific wavelengths that are characteristic of a given atom. ICP-AES has

exquisite sensitivity, down to parts-per-million level, and can identify multiple elements in a single measurement.

5.4. Magnetic Properties

For comprehensive magnetic characterization of MNPs, both the temperature (T) and the field (H) dependent magnetizations are measured. Superconducting quantum interference device (SQUID) or vibrating sample magnetometers are typically used.

5.4.1. Temperature-Dependent Magnetization. To measure temperature-dependent magnetization M(T), samples are first cooled down from high ($\approx 300 \text{ K}$) to low temperature (< 4 K) in the absence of external magnetic fields. The process, called zero-field cooling (ZFC), locks the magnetic moments of MNPs, which are randomized by thermal fluctuation at high temperature. Samples are then heated back to high temperature in the presence of a small measuring field ($\sim 100 \text{ G}$), and the magnetization is measured at different temperature.

A salient feature of M(T) is the existence of a characteristic temperature at which M has the maximum value (Figure 15a).

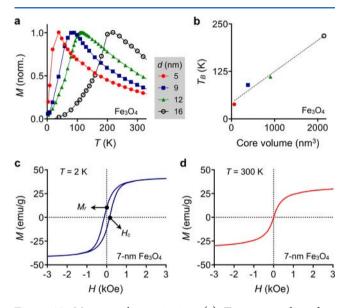


Figure 15. Magnetic characterization. (a) Temperature-dependent magnetization curves M(T) of differently sized Fe₃O₄ MNPs are shown. The temperature at which M has its maximum is defined as the blocking temperature (T_B) . When $T < T_B$, the magnetization increases with T, because thermal energy helps magnetic domains to rotate and align with the external magnetic fields. When $T > T_{\rm B}$, thermal energy is large enough to cause random fluctuations of magnetic domains, which leads to a decrease of M. (b) $T_{\rm B}$ from (a) is plotted against the core volume. $T_{\rm B}$ for a given material is generally proportional to the particle volume, because the anisotropy energy barrier scales with the particle volume. (c) Field-dependent magnetization M(H). Below the blocking temperature, MNPs display hysteresis in response to the applied magnetic field (H). The nonzero magnetization at H = 0 is called remanence (M_r) , and the field strength to reduce M = 0 is defined as coercivity (H_c) . (d) MNPs in a superparamagnetic state displays negligible M_r and H_c . The M value monotonically increases with H as in paramagnetic material. Reproduced with permission from ref 119. Copyright 2004 Nature Publishing Group.

This temperature, defined as the blocking temperature $(T_{\rm B})$, indicates the onset of the superparamagnetic state. When $T < T_{\rm B}$, the M values monotonically increase with temperature, because thermal energy helps the magnetic moments of individual particles to align with the external magnetic fields. Beyond $T_{\rm B}$, thermal energy becomes large enough to randomly

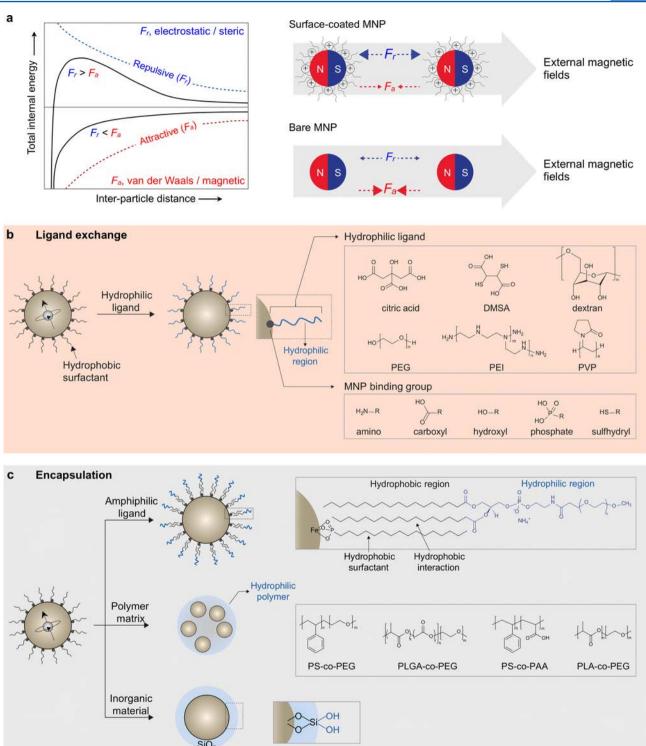


Figure 16. Surface modification methods for MNPs. (a) Total interaction energy between two MNPs as a function of the interparticle distance. The stability of MNPs results from the equilibrium between attractive (F_a , van der Waals and magnetic dipolar) and repulsive (F_r , electrostatic and steric) forces. Surface-coated MNPs are stabilized with electrostatic and steric repulsion provided by coating materials, while bare MNPs are aggregated. (b) Schematic illustration of ligand exchange. Hydrophobic surfactants of MNPs are replaced with hydrophilic ligands, which consist of a MNP binding group and hydrophilic region. Gray-lined boxes show several examples of hydrophilic ligands and MNP binding functional groups. DMSA, dimercaptosuccinic acid; PEG, poly(ethylene glycol); PEI, polyethylenimine; PVP, polyvinylpyrrolidone. (c) Schematic illustration of MNP encapsulation strategies. Hydrophobic MNPs are made hydrophilic by encapsulation with an amphiphilic ligand, embedding in polymer matrix, or coating with an inorganic material. Amphiphilic ligands possess hydrophobic and hydrophilic regions. The hydrophobic chains are intercalated into the layer of hydrophobic surfactants through hydrophobic interaction, while the hydrophilic regions interact with aqueous solution (gray-lined box, top). Several polymers are utilized as a hydrophilic matrix for MNP embedding. PS-co-PEG, polystyrene-co-PEG; PLGA-co-PEG, poly(lactic-co-glycolic acid)-co-PEG; PS-co-PAA, polystyrene-co-poly(acrylic acid); PLA-co-PEG, poly(lactic acid)-co-PEG (gray-lined box, middle). Hydrophilic silanol groups (Si-OH) on the SiO₂ surface make silica-coated MNPs water soluble (gray-lined box, bottom).

flip the magnetic moments, leading to a decrease of M. For a given MNP type, the blocking temperature is proportional to the particle volume (V), since MNPs become superparamagnetic when the thermal and the anisotropy energies are comparable to each other $(k_{\rm B}T_{\rm B}\approx KV)$. As an example, Figure 15a shows the M(T) curves of Fe₃O₄ MNPs with different core sizes. ¹¹⁹ All particles are superparamagnetic at room temperature $(T_{\rm B}<300~{\rm K})$, and $T_{\rm B}$ increases linearly with the particle volume (Figure 15b).

5.4.2. Field-Dependent Magnetization. In this measurement, samples are subjected to sweeping external magnetic fields (H), and their induced magnetization M(H) is monitored. The resulting M(H) curve provides much important information: 116,220,221 (i) the saturation magnetization (M_0) , the maximum magnetization value; (ii) the remanence (M_r) , the residual M at H=0; and (iii) the coercivity (H_c) , the external field required to reduce M=0. When particles assume permeant magnetic moments, M_r and H_c are nonzero, and the resulting M(H) displays a hysteresis loop. MNPs below the blocking temperature show such behavior, consistent with the ferromagnetic state of particles (Figure 15c). For superparamagnetic particles, however, M(H) collapses into a single curve (Figure 15d) as both M_r and H_c vanish. MNPs thus assume magnetic moments only in the presence of external fields.

6. SURFACE COATING STRATEGIES OF MAGNETIC NANOPARTICLES

Most biomedical applications require long-term stability of MNPs without aggregation or precipitation (i) in physiological media (high salt concentrations and/or proteins), (ii) at different pHs, and (iii) at room/body temperature. Because the interactions of MNPs with the surrounding media are governed by the chemical properties of the nanoparticle surface, it is necessary to develop efficient surface coating methods. The stability of nanoparticles depends on the equilibrium between interparticle attractive and repulsive forces (Figure 16a). 222-224 MNPs tend to aggregate due to the attractive interaction originating from van der Waals force and a magnetic dipolar force under an external magnetic field. Therefore, endowing MNPs with repulsive forces that exceed attractive forces is crucial in stabilizing MNPs. MNPs can exhibit repulsive forces of electrostatic and steric repulsion by having their surface modified with coating materials. 133,158,159,225 The surface coatings also (i) provide chemical functionalities for conjugation of affinity ligands and (ii) serve to reduce nonspecific serum protein adsorption in the form of a nanoparticle corona (opsonization). 226,227

In addition, the surface coating allows for the generation of biocompatible MNPs. Several ferrite MNPs such as maghemite and magnetite are generally regarded as nontoxic and biologically tolerated because they can be incorporated into the natural metabolic pathways of the body. Indeed, there currently exist MNPs which are approved for clinical trials (i.e., ferumoxytol; dextran-coated magnetite nanoparticle). However, when those MNPs are not coated, they can induce various toxic effects including reactive oxygen species generation and radical formation via the Fenton reaction. Pe-based MNPs containing transition metals (e.g., Co, Ni, Mn, etc.) can induce toxicity as a result of biodegradation followed by leaching of transition metals. Rapid oxidation of elemental iron MNPs also cause toxicity by resulting in oxidative stress. In this sense, MNPs should be protected from rapid degradation and/or oxidation in

physiological environments by employing surface coating strategies to reduce the risk of toxicity.

Depending on the synthetic routes, the as-synthesized MNPs are initially stabilized by either hydrophilic or hydrophobic surface ligands. For example, the ferrite MNPs fabricated by the coprecipitation method in the presence of water-soluble ligands (e.g., dextran, starch, albumin, alginate, or chitosan) are readily dispersible in aqueous solution due to the in situ hydrophilic surface coatings. ^{160,161,232–234} On the contrary, the non-hydrolytically synthesized MNPs are usually surrounded by a layer of hydrophobic surfactants and are only soluble in nonpolar organic solvents. Therefore, additional hydrophilic surface coatings are required.

This section focuses on surface coating strategies for stabilizing, protecting, and functionalizing nonhydrolytically produced MNPs. The coating methods depend on the type of MNPs, nature of coating materials, and intended applications. The MNP surface modification is generally achieved via ligand exchange or encapsulation. A diverse group of materials, such as small molecule organic ligands, polymeric ligands, amphiphilic micellar ligands, dense polymer matrix, and inorganic materials, are utilized in such coating processes.

6.1. Ligand Exchange

Metallic atoms on the MNP surface are electron deficient as they are coordinatively unsaturated; thus, they have an affinity for electron rich functional groups, such as amino, carboxyl, hydroxyl, phosphate, and sulfhydryl. In this sense, hydrophobic surfactants on the MNP surface can be replaced with hydrophilic ligands by reacting MNPs with excess hydrophilic molecules (Figure 16b). Such hydrophilic ligands consist of (i) an electron rich functional group that binds to the MNPs and (ii) a secondary functional group or hydrophilic region, which is exposed to the aqueous solution. The ligand exchange has several advantages, including the simple reaction procedure, thin coating layer, and small overall MNP size. There has been extensive research on the development of ligand systems that can effectively bind to MNPs.

6.1.1. Small Molecule Ligand. Among a variety of small molecules, dopamine and its derivatives are unique because of their robust binding to ferrite-based MNPs. The catechol unit of dopamine can be effectively coordinated with iron atoms on the nanoparticle surface by forming a stable five-membered ring.²³⁵ The first case study of MNP ligand exchange using dopamine is reported by Xu et al.²³⁵ They transferred the surface of Co@ Fe₂O₃ MNPs from hydrophobic to hydrophilic by using dopamine, which is premodified with nitrilotriacetic acid. Wei et al. synthesized a dopamine sulfonate ligand to improve the stability. 236 The combination of the amine and sulfonate groups gives dopamine sulfonate a zwitterionic character, which enhances the pH stability and prevents nonspecific interaction with proteins. Recently, Liu and colleagues converted hydrophobic Fe₃O₄ to an aqueous phase using a dopamine derivative (3,4-dihydroxyhydrocinnamic acid) without any complicated organic synthesis. The resultant hydrophilic MNPs show high colloidal stability over a wide pH range (pH 3-12).²³⁷

Another example of small molecule ligands is carboxylates, with one example being citric acid. Citric acid binds to the surface metal atoms by coordinating one or two carboxylic acid groups. As a result, at least one carboxylic acid group is exposed to the aqueous solvent, making the nanoparticle surface negatively charged and water-soluble. 238 2,3-Dimercaptosuccinic acid (DMSA), which contains two carboxyl groups and two sulfhydryl

groups, is another representative small molecule ligand. 147,239,240 The carboxylic acid groups at one end coordinatively bind to the nanoparticle surface, while the thiol groups at the other end stabilize nanoparticles by disulfide cross-linkage between other DMSA molecules. Jun et al. reported DMSA-coated Fe₃O₄ MNPs with high colloidal stability and their in vivo MRI applications. 239 Yoon et al. also utilized DMSA to stabilize Fe@ MnFe₂O₄ MNPs. 128 The DMSA-coated MNPs are further conjugated with affinity ligands, such as antibody and biotin, and utilized in μ NMR sensing applications.

6.1.2. Polymeric Ligand. Organic polymers are widely used as stabilizing ligands due to their distinctive characteristics, including multidentate binding capability and steric repulsion effects. Compared to small molecules, organic polymers attach to nanoparticles via multiple functional groups resulting in a stronger steric repulsive force.

Polyethylene glycol (PEG) is one of the most common polymeric ligands in MNP surface coating. PEG is an FDAapproved, biocompatible synthetic polymer that can be prepared with a wide range of sizes and functional groups.²⁴¹ PEGylated MNPs not only show high colloidal stability, but also are protein resistant. With these characteristics, PEGylated MNPs are not easily recognized by the immune system, and therefore, are often regarded as "stealth" nanoparticles. 242,243 PEGylated MNPs are especially effective for selective detection of biological targets, which is highly desirable for biomedical applications, such as magnetic-based biosensing or in vivo targeted imaging. For the PEGylation of MNPs, one or both ends of PEG are usually modified with functional groups that have affinity to the nanoparticle surface. Xie et al. reported surface modification of Fe₃O₄ MNPs using dopamine (DOPA) terminated PEG.²⁴⁴ Hydrophobic surfactants, such as oleate and oleylamine, are replaced with DOPA-PEG molecules via a ligand exchange reaction. To obtain better colloidal stability, Amstad and coworkers introduced a nitro group to DOPA-PEG molecules. 245 Although the exact mechanism has not yet to be determined, nitro-dopamines bind more tightly to MNPs with a significantly lower desorption rate compared to other dopamine derivatives. PEGs functionalized with a multidentate functional group have an enhanced ability to bind to nanoparticles. For example, polymeric phosphine oxide modified PEG can effectively bind to maghemite nanoparticles via a number of coordinative oxygen atoms. 246,247 Kohler et al. utilized a silane-terminated PEG ligand for PEGylation.²⁴⁸ The use of a silane binding group increases the PEG packing density by hydrogen bonding between the carbonyl and amine groups present within the ligand. Na et al. devised an oligoPEG-DOPA, which consists of a short poly(acrylic acid) backbone laterally appended with several catechol binding groups and PEGs.²⁴⁹ The resulting nanoparticles are stably dispersed in phosphate buffered saline (PBS) solution with a pH at 7.4.

Another widely utilized polymer is dextran. Dextran possesses excellent biocompatibility and has been used in other biomedical applications. Dextran and its derivatives (e.g., carboxy dextran and carboxymethyl dextran) can be naturally degraded into biocompatible glucose by endogenous dextranse enzyme. Most clinical type MNPs have used dextrans as a surface coating (Combidex, dextran; Feraheme, carboxymethyl dextran; Feridex, dextran; and Resovist, carboxydextran). As described in the previous section, dextran is usually coated in situ during the coprecipitation synthesis process. However, some studies describe postsynthesis dextran coating methods. For example,

Creixell and co-workers coated carboxymethyl dextran on the surface of peptized iron oxide nanoparticles. ²⁵²

In addition to PEG and dextran, numerous other polymeric systems are available for ligand exchange. Here we briefly introduce some of the widely used polymers, including poly(vinylpyrrolidone) (PVP), poly(vinyl alcohol) (PVA), and poly(ethylenimine) (PEI). PVP is an FDA-approved, watersoluble polymer that has been used as a plasma volume expander.²⁵³ Dong and colleagues coated Fe₃O₄ MNPs with PVP after removing previously bound surfactants with nitrosonium tetrafluoroborate (NOBF₄), which facilitates the removal through protonating the metal binding functional groups. ²⁵⁴ The PVP-coated MNPs in an aqueous media are stably dispersed without aggregation or precipitation for several months. Another FDA-approved synthetic polymer, PVA, has been widely used in medical applications (e.g., surgical sutures) due to its biodegradability and high water solubility. One typical example of PVA-coated MNP is AminoSpark, which is a commercial probe for in vitro or in vivo imaging.³⁵ To increase PVP coating stability, Liong et al. reported the use of carboxymethyl modified PVA (CMPVA). 255 Hydrophobic ligands on MnFe₂O₄ MNPs are first replaced with tetramethylammonium hydroxide (TMAOH) and then further coated with CMPVA. The resulting CMPVA-coated MNPs are highly stable in aqueous condition. PEI is a multidentate, water-soluble cationic polymer containing abundant primary amine and secondary amine groups that show strong affinity to surface metal atoms.²⁵⁶ PEI has been widely used as a transfection agent because PEI can electrostatically bind to the negatively charged phosphate backbone of DNA.²⁵ Therefore, MNPs coated with PEI can be effectively utilized for gene delivery.²⁵⁸ Duan et al. functionalized magnetite nanoparticles using PEI and PEG-modified PEI (PEI-co-PEG). Both surface-coated MNPs are well-dispersed in aqueous solution for more than 3 months.²⁵⁹

6.2. Encapsulation

Encapsulating MNPs in a biocompatible, hydrophilic shell is another method of phase transfer of nonhydrolytically produced MNPs. There are several nanoparticle encapsulation methods that can be classified according to the shell materials and encapsulation processes (Figure 16c). Amphiphilic ligands, water-soluble polymer matrix, and hydrophilic inorganic material (i.e., silica) are commonly used as shell materials.

6.2.1. Amphiphilic Micellar Ligand. The encapsulation of nanoparticles with amphiphilic ligands can be achieved by simply mixing the nanoparticles with amphiphilic ligands in an adequate solvent. This results in highly stable, micellar-coated nanoparticles. In this process, the hydrophobic region of amphiphilic ligand is intercalated with hydrophobic surfactants on nanoparticles by hydrophobic interactions, while the remaining hydrophilic region solubilizes the nanoparticles in the aqueous solvent. A number of amphiphilic molecules have been used for the phase transfer of MNPs. One typical example is PEGphospholipid copolymer. Lee et al. prepared MNPs with a high colloidal stability and good biocompatibility by encapsulating magnetite nanoparticles with PEG-phospholipid. 260 Seo and colleagues encapsulated FeCo MNPs in PEG-phospholipid micelles and demonstrated their colloidal stability which is sufficient for in vivo application. 144 In addition to PEGphospholipid, many other copolymers, such as PEG-2tetradecylether, ²⁶¹ polylactide–PEG, ²⁶² poly(maleic anhydride-alt-1-octadecene)–PEG, ²⁶³ polystyrene–poly(acrylic acid) (PS–PAA), ²⁶⁴ and tetradecylphosphonate ²⁶¹ can be used as

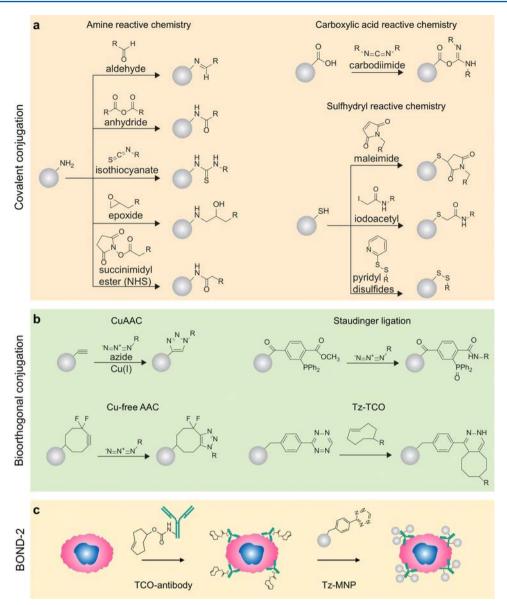


Figure 17. MNP surface conjugation chemistries. (a) Schematic illustration of covalent conjugation strategies, including amine, carboxylic acid, and sulfhydryl reactive chemistries. (b) Representative bioorthogonal covalent conjugation chemistries. CuAAC, Cu(I)-mediated [3 + 2] azide—alkyne cycloaddition; Tz, tetrazine; TCO, trans-cyclooctene. (c) The schematics of the bioorthogonal nanoparticle detection (BOND) technique, which utilizes Tz–TCO cycloaddition as the conjugation mechanism. Antibodies are modified with TCO and used as scaffolds to label more Tz modified MNPs onto target cells.

amphiphilic ligands. However, MNPs encapsulated in copolymers have a relatively large hydrodynamic size compared to those MNPs prepared by the ligand exchange method. This is due to large micelle coating thickness originating from the high molecular weight of copolymers. Considering that hydrodynamic size is highly related to the physical properties (e.g., Brownian relaxation) of MNPs, it is crucial to develop a method for controlling the thickness of micelle coating while maintaining the colloidal stability of MNPs. 265,266 Oligomeric or dendritic molecules can be a good candidate for providing a thin, micellar shell. In a study by Wang et al., micellar-coated MNPs with a thin coating are prepared using α -cyclodextrin, which is a naturally occurring, cyclic oligosaccharide containing hydrophobic cavities and hydrophilic rims. 267

6.2.2. Polymeric Matrix. The incorporation of MNPs in a hydrophilic, dense polymeric matrix is an additional way of generating water-soluble MNPs. Various copolymers, such as

polystyrene-co-PEG (PS-co-PEG), ²⁶⁸ poly(lactic-co-glycolic acid)-co-PEG (PLGA-co-PEG), ^{269,270} polystyrene-co-poly-(acrylic acid) (PS-co-PAA), ^{271,272} and poly(lactic acid)-co-PEG (PLA-co-PEG), ²⁷³ have been used as matrixes. Because single polymer matrix particles can contain a large number of MNPs, the nanoparticle—polymer hybrids can have a significantly high magnetic moment. ^{274–276} Typically, such hybrids can be fabricated by polymerization of monomers in the presence of MNPs. Xu and colleagues prepared PS/silica matrix particles containing hydrophobic Fe₃O₄ MNPs via oil-in-water emulsion polymerization. ²⁷⁷ The MNPs-PS/silica hybrid has an average size of 134 nm with a polydispersity of 7.5%. Kaewsaneha et al. embedded magnetite MNPs in a water-soluble PS-co-PAA matrix through polymerization of styrene and acrylic acid monomers in the presence of MNPs and azobis(isobutyronitrile) (AIBN) initiator. ²⁷⁸ The resulting product with a hydrodynamic size of 250 nm shows high colloidal stability. The application of such

MNP—polymer hybrids in POC diagnostics has been demonstrated by Neely and co-workers. They developed a highly sensitive T_2 magnetic resonance sensor system using a carboxylated polymer matrix (800 nm) embedded with numerous iron oxide MNPs. They successfully detected bloodstream infections of *Candida spp.* with a sensitivity ~100-fold higher than that of conventional techniques.

6.2.3. Hydrophilic Inorganic Material. Silica has been extensively studied as an efficient coating material due to its advantages of hydrophilicity, high density of surface functional groups, and easily controllable shell thickness. ^{280–283} The surface of silica is negatively charged as a result of deprotonation of terminal silanol groups. Therefore, electrostatic repulsive forces stabilize MNPs encapsulated in silica. Silica can also protect MNPs from undesirable chemical transformations, such as oxidation of elemental metallic nanoparticles. ²⁰¹

A common approach for encapsulating MNPs in silica is solgel reaction (Stöber process), where silica is synthesized via the hydrolysis and condensation of silicon orthoester (Si(OR)₄) (e.g., tetraethyl orthosilicate (TEOS) and tetramethyl orthosilicate (TMOS)). 281–284 In this process, silicon orthoesters are first hydrolyzed, yielding silicic acids (Si(OH)₄); then, they undergo polycondensation into a three-dimensional network of Si-O-Si. The reaction between uncondensed silanol and hydroxyl groups on the MNP surface forms a Si-O-M bond, which facilitates silica coating on the MNP surface. This process can be catalyzed by either acid or base, and the shell thickness is controlled by varying the concentration of silicon precursors.²⁸⁵ The surface silanol groups can further be modified with amine and sulfhydryl functional groups by employing respective aminoethoxysilane and mercaptoethoxysilane. Carboxylic acid groups can also be obtained by a reaction with aminoethoxysilane followed by succinic anhydride.

However, nonhydrolytically synthesized MNPs lack surface hydroxyl groups, which are essential to the formation of the Si–O–M bond. To overcome this limitation, Yi et al. utilized a base-catalyzed sol–gel reaction in an inverse micelle. The use of base not only catalyzes the sol–gel process, it also peels off hydrophobic surfactants and provides MNPs with hydroxyl groups. Based on a modification of Yi's method, Cheon's group synthesized metal-doped ferrite@SiO₂ MNPs with uniform and precisely controlled SiO₂ thickness. The so-called pomegranate-shaped MNP@SiO₂ is prepared through clustering the MnFe₂O₄ MNPs with PVP followed by silica coating using the Stöber method. The resulting MNPs show high colloidal stability in aqueous media and exhibit high r_2 of 695 mM⁻¹ s⁻¹.

7. CONJUGATION CHEMISTRIES FOR MAGNETIC NANOPARTICLES

MNPs can easily be functionalized with targeting molecules, such as antibodies, proteins, peptides, nucleic acids, and small molecules, and can take advantage of the enhanced binding affinity conferred by multivalency. Currently, various efficient conjugation strategies, which can be categorized into covalent conjugation and noncovalent conjugation, are utilized. The choice of conjugation strategy is determined by the nature of the MNP surface ligands and their available functional groups, the characteristics of targeting molecules, and the desired POC application. For example, understanding the functional groups available on an antibody is crucial to choosing the best method for modification. In particular, primary amines (lysines) are prominently found within the antigen-binding site of the

antibody.²⁹⁰ Therefore, labeling antibody through the primary amine may cause a significant decrease in the antigen-binding activity of the antibody. This drawback can be overcome by utilizing the hydroxyl group of the antibody.²⁹¹ The following paragraphs will highlight several conjugation strategies that are commonly used for MNP surface functionalization. These will include the bioorthogonal method, which has become a favored approach due to its rapid conjugation, site specific attachment capabilities, and high efficiency.²⁹²

7.1. Covalent Conjugation

The use of covalent linkages has been the primary method of choice for introducing targeting molecules to MNPs. Covalent bonds can be formed between functional groups such as amine $(-NH_2)$, carboxylic acid (-COOH), and sulfhydryl (-SH), at the MNP surface and targeting molecules. Bioorthogonal click chemistry that facilitates cross-linking between alkynes and azides $(-N_3)$ is another widely utilized covalent conjugation method. Alternatively, a coordination bond, also called a dative covalent bond, between metals and metal binding amino acids can be utilized. A number of straightforward protocols are available for linking those functional groups.

7.1.1. Conventional Covalent Linkage Chemistry. The most common and versatile techniques for covalent conjugation involve the use of chemical groups that readily react with functional groups on MNPs (Figure 17a). There are numerous synthetic reactive groups that form covalent bonds with functional groups.²⁹³ Chemicals, including aldehydes, anhydrides, epoxides, isothiocyanates, and NHS ester (N-hydroxysuccinimide), are popular amine-specific reactive groups that are usually incorporated in MNP functionalization. In the case of carboxylic acid, few chemicals are known to conjugate to them. Carbodiimide compounds (i.e., 1-ethyl-3-[3-(dimethylamino)propyl]carbodiimide hydrochloride (EDC)) are useful for labeling carboxylic acids. They can activate carboxylic acids for direct conjugation to primary amines via amide bonds. The sulfhydryl reactive groups include maleimides, haloacetyls, and pyridyl disulfides. These chemicals form stable thioether linkages or disulfide bonds upon reaction with sulfhydryl groups.

However, because targeting molecules usually lack reactive groups, they are modified prior to conjugation. In this sense, the most common strategy is to use bifunctional cross-linkers, which possess two reactive groups at both ends.²⁹³ They can be categorized into homobifunctional or heterobifunctional molecules depending on the reactive groups. For example, bis-(sulfosuccinimidyl)suberate, which has two NHS esters at each end of a carbon spacer arm, is a homobifunctional cross-linker that allows for amine-to-amine cross-linking. Sulfosuccinimidyl-4-(N-maleimidomethyl)cyclohexane-1-carboxylate (sulfo-SMCC), containing a maleimide group and NHS ester, is a heterobifunctional cross-linker for amine-to-sulfhydryl crosslinking. For carboxylic acid-to-amine coupling, zero-length crosslinker EDC can be utilized. EDC functions by converting carboxyls into amine-reactive isourea intermediates that bind to the primary amine. Unlike other heterobifunctional cross-linkers, EDC only serves as a catalyst for covalent bond formation.

The use of cross-linker molecules not only facilitates covalent bond formation, it also provides better conjugation efficiency. Steric hindrance around the MNPs can interfere with the cross-linking reactions, making it more difficult to label targeting molecules. Highly flexible bifunctional cross-linkers with long carbon chains allow for bioconjugation without steric hindrance, increasing the number and activity of targeting molecules

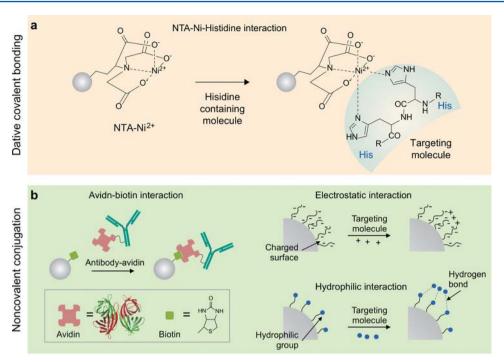


Figure 18. Alternative MNP surface conjugation chemistries. (a) Example of representative dative covalent bonding. (b) Schematic illustration of noncovalent conjugation commonly used for bioconjugation.

attached on MNPs. ^{295–297} One typical drawback of cross-linkers is MNP clusterization, which is induced by interparticle cross-linking. ^{223,298} To prevent such undesirable cross-linking, several reaction steps, including functional group protection, stepwise modification, and/or a number of purification processes, are required. Nevertheless, those additional steps often result in a low product yield.

7.1.2. Bioorthogonal Chemistry. An emerging concept in conjugation chemistry is bioorthogonality, which is defined by a chemical reaction that occurs inside living systems without interfering with native biochemical processes. Peactions are considered bioorthogonal when the two reactive groups are highly selective for each other and inert for the other functional groups present in biological systems. The reaction should proceed in mild conditions, such as water at or near neutral pH, and temperature between 25 and 37 °C, and it does not involve cytotoxic reagents or byproducts. Bioorthogonal conjugation has become one of the preferred methods of attaching targeting molecules to MNPs.

As a subclass of bioorthogonal chemistry, click chemistry is the most common approach for meeting the aforementioned requirements (Figure 17b).³⁰¹ One of the classic click reactions is the Huisgen 1,3-dipolar cycloaddition of azides and alkynes to form 1,2,3-triazoles. ^{302–304} When Cu(I) is used as a catalyst, this process can be accelerated $\sim 10^8$ -fold. Therefore, the reaction is commonly referred to as a Cu(I)-mediated [3 + 2] azide—alkyne cycloaddition (CuAAC). Compared to other conjugation strategies, CuAAC has distinctive advantages. Azide and alkyne have very high specificity for each other and they are unreactive to other functional groups, allowing for target-specific conjugation. Additionally, the resulting covalent bond is highly stable and not susceptible to harsh biological environments. However, the use of Cu(I) species as a catalyst requires an organic solvent or anaerobic conditions, which are not desirable in bioconjugation reactions.³⁰⁴ One approach for tackling this issue is the utilization of water-soluble Cu(II) species (e.g., CuSO₄) and

ascorbic acids that reduce Cu(II) to Cu(I). 305,306 This allows for CuAAC to proceed under mild aerobic aqueous conditions. The other approach is Cu-free click chemistry, which takes advantage of strained alkynes (e.g., difluorinated cyclooctyne). 307,308 The cyclooctyne is self-activated by its ring strain and electron-withdrawing fluorine, enabling the reaction to take place with kinetics that are comparable to CuAAC. The elimination of cytotoxic copper catalyst makes Cu-free click chemistry biocompatible and suitable for application within various MNP bioconjugation processes. Nevertheless, the reaction is still limited by the poor aqueous solubility of substrates and tedious syntheses. 308

Another example of a click reaction is Staudinger ligation. 309 This reaction utilizes an azide and ester containing aryl phosphine to induce an iminophosphorane (aza-ylide) intermediate. The aza-ylide undergoes spontaneous intramolecular cyclization, resulting in a stable amide bond. This reaction is biocompatible because it can proceed in a mild aqueous environment and does not require any catalysts or organic solvents. One limitation of this chemistry is the oxidation of phosphine in ambient conditions, which can cause a decreased reactivity and low production yield. Excess amounts of reagents are required to overcome this issue. 310

The other click reaction is the Diels—Alder reaction, which is [4 + 2] cycloaddition between a dienophile and diene. ³¹¹ This reaction works in aqueous buffers, at or near room temperature, and in a highly selective and efficient manner without the formation of byproducts. Recently, a reaction between a 1,2,4,5-tetrazine (Tz) and a *trans*-cyclooctene (TCO), which is a derivative of the Diels—Alder reaction, was introduced as an effective chemistry for MNP bioconjugation. ^{312–314} This Tz—TCO chemistry, pioneered by the Weissleder's group, benefits from the high aqueous stability of Tz molecules, high reactivity of strained TCO, sufficiently rapid kinetics, and no need for a catalyst. Termed "bioorthogonal nanoparticle detection" (BOND), this technique provides a novel targeting platform in

which Tz and TCO act as the coupling agents between MNPs and targeting antibodies (Figure 17c). Haun et al. demonstrated the utility of this reaction for cell-specific amplification of MNP binding which can be utilized to detect various biomolecules such as protein biomarkers. ^{292,315,316} To facilitate this process, aminefunctionalized MNPs are first modified with an NHS ester derivative of Tz to create Tz-MNPs. Targeting antibodies are modified with NHS containing TCO. In a two-step labeling strategy (BOND-2), the TCO-modified antibodies are first used for target (e.g., cancer cell) binding followed by covalent reaction with Tz-MNP. 292,317 The robust conjugation reaction of BOND-2 allows for higher MNP binding to targets compared to other conjugation techniques, resulting in a significantly improved detection sensitivity in the NMR-based sensor system. Moreover, this platform is capable of performing rapid, multiplexed analysis of human tumors and is broadly applicable for biomedical use.44,315,317

7.1.3. Amino Acid–Metal Dative Bonding. A dative covalent bond (coordination bond) is a covalent bond in which both electrons come from the same atom. Several amino acids can form dative covalent bonds with specific metals. For example, cysteine coordinatively binds to copper and gold through its sulfydryl side chains. This characteristic coordination bonding between amino acid and metal can serve as a novel bioconjugation method. The most widely used combination is polyhistidine (His_n) and divalent nickel (Ni²⁺) chelated nitrilotriacetic acid (NTA) (Figure 18a). The high affinity of His, and Ni-NTA interaction is characterized by a small dissociation constant of 10^{-13} M. To facilitate His_n -Ni-NTA mediated bioconjugation, NTA is first labeled on the surface of MNPs using conventional covalent conjugation chemistry, which is followed by Ni²⁺ chelation. ^{235,321,322} Targeting molecules that contain a His, motif are then conjugated with MNPs. Because a variety of biomolecules can be chemically modified to display a His, tag, this conjugation strategy has applicability beyond proteins or peptides.

In combination with MNPs, the His_n–Ni-NTA interaction can be an efficient and selective method for magnetic separation and purification of His_n-tagged proteins or cells. Xu and co-workers synthesized Ni-NTA-modified MNPs of FePt and Co@Fe₂O₃ and demonstrated their ability to separate His-tagged proteins. According to a study by Kim et al., a high density of Ni-NTA present on the MNP surface enhances the protein purification capacity. Kim and co-workers reported the use of Fe₂O₃@NiO MNPs for NTA free capture of His_n-tagged proteins. In particular, the MNPs themselves have affinity to His tags, owing to the presence of Ni²⁺ ions on the surface. Therefore, no additional Ni-NTA conjugation process is required.

7.2. Noncovalent Conjugation

Noncovalent conjugations differ from covalent conjugation in that they do not share electrons, but they take advantage of a variety of interactions, such as hydrogen bonding, van der Waals interaction, π -interaction, and hydrophobic interaction. ³²⁶ In general, noncovalent bonds are much weaker than covalent bonds. The bond-dissociation energy of noncovalent bonds is only 1–5 kcal/mol, while that of a covalent bond is an order of magnitude larger. ³²⁶ However, cooperative, multiple noncovalent interactions can produce stable, specific linkages between different molecules.

Several noncovalent interactions, including affinity, electrostatic, and hydrophilic interactions, are available for conjugation

of targeting molecules to MNPs (Figure 18b). 225,327 Among them, the avidin-biotin affinity interaction is one of the widely exploited strategies due to its exceptional bond strength (dissociation constant, $K_d = 10^{-15}$ M), which is comparable to that of a covalent bond.³²⁸ The bond formation is very rapid, and once formed, the bond is stable under extreme pH, temperature, organic solvent, and other denaturing agent conditions. 293,328,32 The high affinity is originated from an extensive network of hydrogen bonds, and there is high shape complementarity between the avidin binding pocket and biotin. 321 Avidin can interact with up to four biotin molecules, owing to its homotetrameric subunit structure, and each subunit is capable of binding to one biotin. Avidin—biotin conjugation is usually conducted via a two-step reaction. ^{240,292,328,330–332} First, targeting molecules and MNPs are functionalized with avidin and biotin (or vice versa). Because biotin is relatively small (244.3 Da), it can be labeled on targeting molecules without significantly altering their functionalities.³³³ Typically, biotin is cross-linked with amine or sulfhydryl functional groups using reactive biotin reagents, such as NHS-biotin and maleimidebiotin. Avidin can be labeled to the surface coatings of MNPs via various covalent conjugation chemistries. Then, avidin-coated MNPs are reacted with biotinylated molecules, leading to target molecule-conjugated MNPs. Although the avidin-biotin interaction is robust, it often suffers from the nonspecific binding of avidin, which originates from avidin's high carbohydrate content and isoelectric point $(pI, \sim 10)$. This issue can be solved by chemical deglycosylation of avidin. 335 As an alternative, streptavidin, which lacks carbohydrates and has a lower pI of 5–6, can be used.³³⁶

A number of studies utilizing avidin-biotin interactions have been reported. Most of them take advantage of the interaction to conjugate targeting molecules to MNPs. 240,292,330-332 Recently, the interaction was applied as a model system to demonstrate proof-of-concept of new MNP-based biosensing plat-forms. 23,128,337-340 The avidin-biotin interaction can be a good model in such biosensing platforms due to its high affinity, albeit adding considerable bulk. Yoon et al. utilized avidin-biotin interactions to demonstrate a magnetic resonance based biosensor. 128 In this system, biotinylated Fe@MnFe₂O₄ MNPs are clustered by avidin, resulting in an avidin dose-dependent change of the T_2 . Ilyas and colleagues biotinylated Fe₃O₄ MNPs to detect streptavidin-functionalized proteins. 339 The strong affinity between biotin and streptavidin allows for sensitive detection of streptavidin-bearing horseradish peroxidase. Ranzoni and co-workers conjugated biotinylated antibodies to streptavidin-coated MNPs for prostate specific antigen (PSA) detection.³⁴⁰ In the presence of PSA, antibody–MNPs are clustered and those clusters are detected by optical scattering at applied magnetic rotation frequencies.

8. CLINICAL APPLICATIONS

Magnetic POC technologies continue to evolve with everincreasing sensitivities, proffered by advances in MNP design, amplification strategies, and sensitive detectors. Collectively, the different technologies have now been used to detect and phenotype whole cells, exosomes, bacteria, viruses, proteins, drugs, and nucleic acids in unprocessed biological samples. The main clinical applications to date have been for cancer and infectious disease detection. Some of these devices and assays are entering the marketplace (see Table 1). One example is T2Biosystems, a company using NMR to develop applications aimed at lowering mortality rates, improving patient

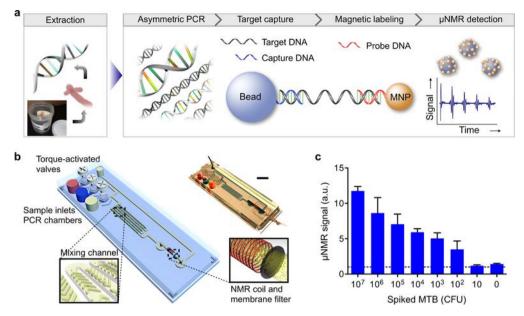


Figure 19. Magnetic barcode assay for bacterial detection. (a) Assay procedure. From unprocessed specimen, bacterial 16sRNA or DNA is extracted though an off-chip stressing. Extracted DNA samples are then loaded into a fluidic device. The target DNA sequences are amplified by asymmetric RT-PCR and captured by polymer beads modified with capture DNA. MNPs are then used to specifically coat the beads via complementary sequences, and the samples are subjected to NMR measurements. (b) A fluidic cartridge was developed to streamline the assay. The device integrates PCR chambers, mixing channels, and a microcoil for NMR measurements. (c) *Mycobacterium tuberculosis* targets in sputum samples were detected. The sensitivity was 10^2-10^3 CFU/mL. CFU, colony forming unit. Reproduced with permission from ref 52. Copyright 2013 Nature Publishing Group.

outcomes, and reducing the cost of healthcare. Their T2Dx Instrument and T2Candida Panel have already received marketing authorization from the U.S. Food and Drug Administration. Another platform, Magnotech, by developed by Philips, ¹⁰⁸ has been applied to detect cardiac troponin I (cTnI) for diagnosis of acute myocardial infarction. For the ex vivo POC applications, the stringent requirement for MNP biodegradation and biocompatibility could be relaxed; more critical particle requirements are high magnetic moments, colloidal stability, and ease of bioconjugation. As such, many commercially available or custom-designed MNPs have been used in combination with these detection systems.

8.1. Infection

Several different approaches to bacterial detection have been explored, including antibody or protein-based diagnostics, 344 magnetic Gram-staining, 49 antibiotic-based diagnostics, 48 and fast magnetogenetic profiling technologies. 50,52 The latter approach is particularly robust and enables rapid bacterial analyses of 16S rRNA in minimally processed samples 50 as well as bacterial DNA. 52,176,345 Figure 19 summarizes the principle of the magnetogenetic profiling technique. 52 Furthermore, fungal detection studies have shown that magnetogenetic detection is a rapid, automation-amenable opportunity for clinicians to detect and identify multiple human pathogens within hours of sample collection. 279 In essence, the magnetic detection technology, particularly the μ NMR, is quite mature and consequently is being commercialized for molecular testings of other pathogens. 279,346,347

8.2. Cancer

There is a need to more effectively detect and phenotype cancers. Such molecular analyses will rely on measuring multiple (dozens to hundreds of) proteins and nucleic acids (mRNA, miRNA, DNA) originating from cancer cells. Developments in this direction will be invaluable for earlier cancer detection, mapping

of heterogeneity, analysis of drug response, and resistance or recurrence. For example, the μ NMR technology has been used clinically to detect cancer cells and to perform rapid profiling during fine needle aspirations in 70 patients. These studies were expanded to apply the same technology to the detection of circulating tumor cells in blood of 25 patients and to lung cancer phenotyping in 47 patients. The technology has also been used successfully for exosome profiling in glioblastoma. It is likely that related technologies, also relying on nanoparticles, will continue to emerge to further improve the detection sensitivities.

8.3. Coagulation

Rapidly assessing hemostatic parameters is an important task in hospital (surgical and interventional practices) as well as in the battlefield and trauma settings. For example, approximately 25% of trauma patients have impaired hemostasis, which frequently goes undetected during the initial hospitalization. According to a study in the Journal of the American College of Surgeons, for trauma patients with symptoms of impaired hemostasis, mortality was reduced from 45 to 19% with more rapid delivery of therapy. Existing approaches, however, require multiple platform, generally consume 1-25 mL of sample, and take hours to provide results. An NMR system has been used to provide comprehensive blood clotting measurements in less than 20 min. Commercialized by T2Biosystems as T2HemoStat, the system measures clotting time, fibrinolysis, platelet activity, clot contraction, and clot lysis. The test is based on the unique fact that, in normal clots, paramagnetic red blood cells form closely packed polyhedral structures (polyhedrocytes) with platelets and fibrin, which leads to concomitant changes in transverse relaxation time.³⁴⁹ The platform allows for comprehensive assessment of hemostatic parameters on a single instrument and provides results within 15 min using 0.04 mL of blood with minimal sample handling.

8.4. Other Applications

The above clinical applications represent a few examples of what is possible. We expect that many more applications will be developed, now that highly efficient magnetic nanoparticles, sensors, and imaging systems have become mainstream. These applications include measurements of circulating protein biomarker, 62,350 exosomes, 43 viruses, 179 drugs, 108 and metabolites among others.

9. CONCLUSION AND PERSPECTIVES

Magnetic POC technologies have seen a spectacular rise over the past few years for good reasons. Compared to other approaches, they enable analyses in "dirty" samples, i.e, without major purification. This is possible because human tissue samples are usually devoid of magnetism. Because measurements can be directly done in virtually any body fluids and samples, it eliminates potential sample loss and speeds up the analysis. Combined with genetic detection technologies, 52,176,345 the analytical possibilities are endless.

We believe that there are a number of future developments which could make magnetic detection technologies even more widespread: (i) for early disease detection where lives can be saved and treatments are affordable, (ii) for the detection of diseases other than cancer and infection, (iii) for use in consumer goods, agriculture, and food/water safety, (iv) in applications where magnetic separation and analysis are integrated in a single chip, and (v) for multifunctional sensors combining magnetism with other modalities. It is these specific applications that will drive the need for new nanoparticle characteristics, affinity ligands, and magnetic sensing devices.

AUTHOR INFORMATION

Corresponding Author

*Tel.: 617-726-8226. E-mail: rweissleder@mgh.harvard.edu.

Notes

The authors declare the following competing financial interest: R.W. is a founder and consultant of T2Biosystems. The other authors declare no competing financial interest.

Biographies



Hakho Lee is associate professor at Harvard Medical School, and director of the Biomedical Engineering Program at the Center for Systems Biology, Massachusetts General Hospital (MGH). He received his Ph.D. in physics from Harvard University, and completed his postdoctoral training at MGH. Dr. Lee has extensive experience in nanomaterials, biophysics, microfluidics, and electrical engineering. His research is multidisciplinary and focuses on developing novel biomedical

sensors such as the world's smallest portable NMR device, integrated circuit (IC) chips for cancer cell detection, novel surface-plasmon-resonance chips for exosome profiling, and microfluidic devices for single cell analyses. Dr. Lee is a 2015 Final list of Blavatnik National Awards for Young Scientists.



Tae-Hyun Shin received his B.S. degree in Chemistry from Yonsei University in 2010. He is currently a graduate student at Yonsei University. His research interest is in designing and constructing functionalized inorganic nanoparticles for molecular imaging.



Jinwoo Cheon is the Horace G. Underwood Professor at Yonsei University and director of the National Creative Research Initiative Center for Evolutionary Nanoparticles. He graduated from Yonsei University with a B.S. and received his Ph.D. from the University of Illinois at Urbana—Champaign. After his postdoctoral training at the University of California, Berkeley, and at UCLA, he joined KAIST. In 2002, he moved to Yonsei University. He is a recipient of many awards, including the Ho-Am Prize, POSCO TJ Park Prize, Inchon Prize, and Song-gok Science Award. Currently, he is a senior editor of *Accounts of Chemical Research* and a fellow of the American Chemical Society and the Royal Society of Chemistry.



Ralph Weissleder is the Thrall Professor of Radiology and Professor of Systems Biology at Harvard Medical School (HMS), director of the Center for Systems Biology at Massachusetts General Hospital (MGH), senior faculty in the HMS Department of Systems Biology, and attending clinician (Interventional Radiology) at MGH. He graduated from Heidelberg University in 1985, obtained his postdoctoral and residency training at MGH (1986-1991), and has been on faculty at HMS since 1991. He has published >750 publications in peer-reviewed journals, authored several textbooks, and been named one of the "The World's Most Influential Scientific Minds" by Thomson Reuters in 2014. His work has been honored with numerous awards including the J. Taylor International Prize in Medicine, the Millenium Pharmaceuticals Innovator Award, the AUR Memorial Award, the ARRS President's Award, The Society for Molecular Imaging Lifetime Achievement Award, and the Academy of Molecular Imaging 2006 Distinguished Basic Scientist Award, among others. In 2009 he was elected member of the U.S. National Institute of Medicine.

ACKNOWLEDGMENTS

The authors thank Dr. Huilin Shao (MGH) for reviewing the manuscript. This work was supported in part by NIH Grants R01EB004626, R01EB010011, HHSN268201000044C, R01HL113156, US4-CA119349, and K12CA087723-09; DoD OCRP Award W81XWH-14-1-0279; the National Creative Research Initiative (2010-0018286 J.C.), and the Korea Healthcare Technology R&D Project, Ministry for Health & Welfare Affairs (HI08C2149 J.C.).

REFERENCES

- (1) Gubala, V.; Harris, L. F.; Ricco, A. J.; Tan, M. X.; Williams, D. E. Point of Care Diagnostics: Status and Future. *Anal. Chem.* **2012**, *84*, 487–515.
- (2) Ryan, F.; O'Shea, S.; Byrne, S. The 'Carry-Over' Effects of Patient Self-Testing: Positive Effects on Usual Care Management by an Anticoagulation Management Service. *Thromb. Res.* **2010**, *126*, e345–e348
- (3) von Lode, P. Point-of-Care Immunotesting: Approaching the Analytical Performance of Central Laboratory Methods. *Clin. Biochem.* **2005**, 38, 591–606.
- (4) Varmus, H.; Kumar, H. S. Addressing the Growing International Challenge of Cancer: A Multinational Perspective. *Sci. Transl. Med.* **2013**, *5*, 175cm2.
- (5) Wang, J. Electrochemical Glucose Biosensors. Chem. Rev. 2008, 108, 814–825.
- (6) Beneteau-Burnat, B.; Bocque, M. C.; Lorin, A.; Martin, C.; Vaubourdolle, M. Evaluation of the Blood Gas Analyzer GEM PREMIER 3000. *Clin. Chem. Lab. Med.* **2004**, 42, 96–101.
- (7) Christenson, R. H.; Azzazy, H. M. Cardiac Point of Care Testing: A Focused Review of Current National Academy of Clinical Biochemistry

Guidelines and Measurement Platforms. Clin. Biochem. 2009, 42, 150–157.

- (8) McDonnell, B.; Hearty, S.; Leonard, P.; O'Kennedy, R. Cardiac Biomarkers and the Case for Point-of-Care Testing. *Clin. Biochem.* **2009**, 42, 549–561.
- (9) Lewandrowski, K.; Flood, J.; Finn, C.; Tannous, B.; Farris, A. B.; Benzer, T. I.; Lee-Lewandrowski, E. Implementation of Point-of-Care Rapid Urine Testing for Drugs of Abuse in the Emergency Department of an Academic Medical Center: Impact on Test Utilization and ED Length of Stay. *Am. J. Clin. Pathol.* **2008**, *129*, 796–801.
- (10) Cervinski, M. A.; Gronowski, A. M. Reproductive-Endocrine Point-of-Care Testing: Current Status and Limitations. *Clin. Chem. Lab. Med.* **2010**, *48*, 935–942.
- (11) Kok, L.; Elias, S. G.; Witteman, B. J.; Goedhard, J. G.; Muris, J. W.; Moons, K. G.; de Wit, N. J. Diagnostic Accuracy of Point-of-Care Fecal Calprotectin and Immunochemical Occult Blood Tests for Diagnosis of Organic Bowel Disease in Primary Care: The Cost-Effectiveness of a Decision Rule for Abdominal Complaints in Primary Care (CEDAR) Study. Clin. Chem. 2012, 58, 989–998.
- (12) Curtis, C. M.; Kost, G. J.; Louie, R. F.; Sonu, R. J.; Ammirati, E. B.; Sumner, S. Point-of-Care Hematology and Coagulation Testing in Primary, Rural Emergency, and Disaster Care Scenarios. *Point Care* **2012**, *11*, 140–145.
- (13) Taylor, J. R.; Lopez, L. M. Cholesterol: Point-of-Care Testing. *Ann. Pharmacother.* **2004**, *38*, 1252–1257.
- (14) Dheda, K.; Ruhwald, M.; Theron, G.; Peter, J.; Yam, W. C. Point-of-Care Diagnosis of Tuberculosis: Past, Present and Future. *Respirology* **2013**, *18*, 217–232.
- (15) Park, S.; Zhang, Y.; Lin, S.; Wang, T. H.; Yang, S. Advances in Microfluidic PCR for Point-of-Care Infectious Disease Diagnostics. *Biotechnol. Adv.* **2011**, *29*, 830–839.
- (16) Castro, C. M.; Ghazani, A. A.; Chung, J.; Shao, H.; Issadore, D.; Yoon, T. J.; Weissleder, R.; Lee, H. Miniaturized Nuclear Magnetic Resonance Platform for Detection and Profiling of Circulating Tumor Cells. *Lab Chip* **2014**, *14*, 14–23.
- (17) Curtis, C. M.; Louie, R. F.; Vy, J. H.; Ferguson, W. J.; Lam, M.; Truong, A. T.; Rust, M. J.; Kost, G. J. Innovations in Point-of-Care Testing for Enhanced United States Disaster Caches. *Am. J. Disaster Med.* **2013**, *8*, 181–204.
- (18) Cheng, M. M.; Cuda, G.; Bunimovich, Y. L.; Gaspari, M.; Heath, J. R.; Hill, H. D.; Mirkin, C. A.; Nijdam, A. J.; Terracciano, R.; Thundat, T.; Ferrari, M. Nanotechnologies for Biomolecular Detection and Medical Diagnostics. *Curr. Opin. Chem. Biol.* **2006**, *10*, 11–19.
- (19) Giljohann, D. A.; Mirkin, C. A. Drivers of Biodiagnostic Development. *Nature* **2009**, *462*, 461–464.
- (20) Sun, T.; Holmes, D.; Gawad, S.; Green, N. G.; Morgan, H. High Speed Multi-Frequency Impedance Analysis of Single Particles in a Microfluidic Cytometer Using Maximum Length Sequences. *Lab Chip* **2007**, *7*, 1034–1040.
- (21) Ellerbee, A. K.; Phillips, S. T.; Siegel, A. C.; Mirica, K. A.; Martinez, A. W.; Striehl, P.; Jain, N.; Prentiss, M.; Whitesides, G. M. Quantifying Colorimetric Assays in Paper-Based Microfluidic Devices by Measuring the Transmission of Light through Paper. *Anal. Chem.* **2009**, *81*, 8447–8452.
- (22) Myers, F. B.; Lee, L. P. Innovations in Optical Microfluidic Technologies for Point-of-Care Diagnostics. *Lab Chip* **2008**, *8*, 2015–2031.
- (23) Lee, H.; Sun, E.; Ham, D.; Weissleder, R. Chip-NMR Biosensor for Detection and Molecular Analysis of Cells. *Nat. Med.* **2008**, *14*, 869–874.
- (24) Issadore, D.; Chung, J.; Shao, H.; Liong, M.; Ghazani, A. A.; Castro, C. M.; Weissleder, R.; Lee, H. Ultrasensitive Clinical Enumeration of Rare Cells *Ex Vivo* Using a Micro-Hall Detector. *Sci. Transl. Med.* **2012**, *4*, 141ra92.
- (25) Gaster, R. S.; Xu, L.; Han, S. J.; Wilson, R. J.; Hall, D. A.; Osterfeld, S. J.; Yu, H.; Wang, S. X. Quantification of Protein Interactions and Solution Transport Using High-Density GMR Sensor Arrays. *Nat. Nanotechnol.* **2011**, *6*, 314–320.

(26) Gijs, M. A.; Lacharme, F.; Lehmann, U. Microfluidic Applications of Magnetic Particles for Biological Analysis and Catalysis. *Chem. Rev.* **2010**, *110*, 1518–1563.

- (27) Plouffe, B. D.; Murthy, S. K.; Lewis, L. H. Fundamentals and Application of Magnetic Particles in Cell Isolation and Enrichment: A Review. *Rep. Prog. Phys.* **2014**, *78*, 016601.
- (28) Chalmers, J. J.; Zborowski, M.; Sun, L.; Moore, L. Flow through, Immunomagnetic Cell Separation. *Biotechnol. Prog.* **1998**, *14*, 141–148. (29) Zborowski, M.; Chalmers, J. J. *Magnetic Cell Separation*; Elsevier: Amsterdam, 2008; p xviii, 454 pp, [14] pp of plates.
- (30) Miltenyi, S.; Muller, W.; Weichel, W.; Radbruch, A. High Gradient Magnetic Cell Separation with MACS. *Cytometry* **1990**, *11*, 231–238
- (31) Harisinghani, M. G.; Barentsz, J.; Hahn, P. F.; Deserno, W. M.; Tabatabaei, S.; van de Kaa, C. H.; de la Rosette, J.; Weissleder, R. Noninvasive Detection of Clinically Occult Lymph-Node Metastases in Prostate Cancer. N. Engl. J. Med. 2003, 348, 2491–2499.
- (32) Weissleder, R.; Reimer, P.; Lee, A. S.; Wittenberg, J.; Brady, T. J. MR Receptor Imaging: Ultrasmall Iron Oxide Particles Targeted to Asialoglycoprotein Receptors. *Am. J. Roentgenol.* **1990**, *155*, 1161–1167.
- (33) Weissleder, R.; Elizondo, G.; Wittenberg, J.; Lee, A. S.; Josephson, L.; Brady, T. J. Ultrasmall Superparamagnetic Iron Oxide: An Intravenous Contrast Agent for Assessing Lymph Nodes with MR Imaging. *Radiology* **1990**, *175*, 494–498.
- (34) Harisinghani, M.; Ross, R. W.; Guimaraes, A. R.; Weissleder, R. Utility of a New Bolus-Injectable Nanoparticle for Clinical Cancer Staging. *Neoplasia* **2007**, *9*, 1160–1165.
- (35) Shaw, S. Y.; Westly, E. C.; Pittet, M. J.; Subramanian, A.; Schreiber, S. L.; Weissleder, R. Perturbational Profiling of Nanomaterial Biologic Activity. *Proc. Natl. Acad. Sci. U.S.A.* **2008**, *105*, 7387–7392.
- (36) Krishnan, K. M. Biomedical Nanomagnetics: A Spin through Possibilities in Imaging, Diagnostics, and Therapy. *IEEE Trans. Magn.* **2010**, *46*, 2523–2558.
- (37) Pankhurst, Q. A.; Connolly, J.; Jones, S. K.; Dobson, J. Applications of Magnetic Nanoparticles in Biomedicine. *J. Phys. D: Appl. Phys.* **2003**, *36*, R167–R181.
- (38) Issadore, D.; Park, Y. I.; Shao, H.; Min, C.; Lee, K.; Liong, M.; Weissleder, R.; Lee, H. Magnetic Sensing Technology for Molecular Analyses. *Lab Chip* **2014**, *14*, 2385–2397.
- (39) Gillis, P.; Koenig, S. H. Transverse Relaxation of Solvent Protons Induced by Magnetized Spheres: Application to Ferritin, Erythrocytes, and Magnetite. *Magn. Reson. Med.* 1987, 5, 323–345.
- (40) Danieli, E.; Perlo, J.; Blumich, B.; Casanova, F. Small Magnets for Portable NMR Spectrometers. *Angew. Chem., Int. Ed.* **2010**, *49*, 4133–4135.
- (41) Liu, Y.; Sun, N.; Lee, H.; Weissleder, R.; Ham, D. CMOS Mini Nuclear Magnetic Resonance System and Its Application for Biomolecular Sensing. *IEEE International Solid-State Circuits Conference*, 2008. ISSCC 2008. Digest of Technical Papers; IEEE: New York, 2008; p 140.
- (42) Massin, C.; Vincent, F.; Homsy, A.; Ehrmann, K.; Boero, G.; Besse, P. A.; Daridon, A.; Verpoorte, E.; de Rooij, N. F.; Popovic, R. S. Planar Microcoil-Based Microfluidic NMR Probes. *J. Magn. Reson.* **2003**, *164*, 242–255.
- (43) Shao, H.; Chung, J.; Balaj, L.; Charest, A.; Bigner, D. D.; Carter, B. S.; Hochberg, F. H.; Breakefield, X. O.; Weissleder, R.; Lee, H. Protein Typing of Circulating Microvesicles Allows Real-Time Monitoring of Glioblastoma Therapy. *Nat. Med.* **2012**, *18*, 1835–1840.
- (44) Lee, H.; Yoon, T. J.; Figueiredo, J. L.; Swirski, F. K.; Weissleder, R. Rapid Detection and Profiling of Cancer Cells in Fine-Needle Aspirates. *Proc. Natl. Acad. Sci. U.S.A.* **2009**, *106*, 12459–12464.
- (45) Issadore, D.; Min, C.; Liong, M.; Chung, J.; Weissleder, R.; Lee, H. Miniature Magnetic Resonance System for Point-of-Care Diagnostics. *Lab Chip* **2011**, *11*, 2282–2287.
- (46) Ghazani, A. A.; Castro, C. M.; Gorbatov, R.; Lee, H.; Weissleder, R. Sensitive and Direct Detection of Circulating Tumor Cells by Multimarker μ -Nuclear Magnetic Resonance. *Neoplasia* **2012**, *14*, 388–395.

- (47) Ghazani, A. A.; McDermott, S.; Pectasides, M.; Sebas, M.; Mino-Kenudson, M.; Lee, H.; Weissleder, R.; Castro, C. M. Comparison of Select Cancer Biomarkers in Human Circulating and Bulk Tumor Cells Using Magnetic Nanoparticles and a Miniaturized Micro-NMR System. *Nanomedicine* **2013**, *9*, 1009–1017.
- (48) Chung, H. J.; Reiner, T.; Budin, G.; Min, C.; Liong, M.; Issadore, D.; Lee, H.; Weissleder, R. Ubiquitous Detection of Gram-Positive Bacteria with Bioorthogonal Magnetofluorescent Nanoparticles. *ACS Nano* **2011**, *5*, 8834–8841.
- (49) Budin, G.; Chung, H. J.; Lee, H.; Weissleder, R. A Magnetic Gram Stain for Bacterial Detection. *Angew. Chem., Int. Ed.* **2012**, *51*, 7752–7755
- (50) Chung, H. J.; Castro, C. M.; Im, H.; Lee, H.; Weissleder, R. A Magneto-DNA Nanoparticle System for Rapid Detection and Phenotyping of Bacteria. *Nat. Nanotechnol.* **2013**, *8*, 369–375.
- (51) Liong, M.; Fernandez-Suarez, M.; Issadore, D.; Min, C.; Tassa, C.; Reiner, T.; Fortune, S. M.; Toner, M.; Lee, H.; Weissleder, R. Specific Pathogen Detection Using Bioorthogonal Chemistry and Diagnostic Magnetic Resonance. *Bioconjugate Chem.* **2011**, *22*, 2390–2394.
- (52) Liong, M.; Hoang, A. N.; Chung, J.; Gural, N.; Ford, C. B.; Min, C.; Shah, R. R.; Ahmad, R.; Fernandez-Suarez, M.; Fortune, S. M.; Toner, M.; Lee, H.; Weissleder, R. Magnetic Barcode Assay for Genetic Detection of Pathogens. *Nat. Commun.* **2013**, *4*, 1752.
- (53) Rho, J.; Chung, J.; Im, H.; Liong, M.; Shao, H.; Castro, C. M.; Weissleder, R.; Lee, H. Magnetic Nanosensor for Detection and Profiling of Erythrocyte-Derived Microvesicles. *ACS Nano* **2013**, *7*, 11227–11233.
- (54) Connolly, J.; St Pierre, T. G. Proposed Biosensors Based on Time-Dependent Properties of Magnetic Fluids. *J. Magn. Magn. Mater.* **2001**, 225, 156–160.
- (55) Stromberg, M.; Zardan Gomez de la Torre, T.; Goransson, J.; Gunnarsson, K.; Nilsson, M.; Svedlindh, P.; Stromme, M. Multiplex Detection of DNA Sequences Using the Volume-Amplified Magnetic Nanobead Detection Assay. *Anal. Chem.* **2009**, *81*, 3398–3406.
- (56) Park, K.; Harrah, T.; Goldberg, E. B.; Guertin, R. P.; Sonkusale, S. Multiplexed Sensing Based on Brownian Relaxation of Magnetic Nanoparticles Using a Compact AC Susceptometer. *Nanotechnology* **2011**, 22, 085501.
- (57) Astalan, A. P.; Ahrentorp, F.; Johansson, C.; Larsson, K.; Krozer, A. Biomolecular Reactions Studied Using Changes in Brownian Rotation Dynamics of Magnetic Particles. *Biosens. Bioelectron.* **2004**, 19, 945–951.
- (58) Grossman, H. L.; Myers, W. R.; Vreeland, V. J.; Bruehl, R.; Alper, M. D.; Bertozzi, C. R.; Clarke, J. Detection of Bacteria in Suspension by Using a Superconducting Quantum Interference Device. *Proc. Natl. Acad. Sci. U.S.A.* **2004**, *101*, 129–134.
- (59) Hall, D. A.; Gaster, R. S.; Makinwa, K.; Wang, S. X.; Murmann, B. A 256 Pixel Magnetoresistive Biosensor Microarray in 0.18 μ m CMOS. *IEEE J. Solid-State Circuits* **2013**, 48, 1290–1301.
- (60) Baselt, D. R.; Lee, G. U.; Natesan, M.; Metzger, S. W.; Sheehan, P. E.; Colton, R. J. A Biosensor Based on Magnetoresistance Technology. *Biosens. Bioelectron.* **1998**, *13*, 731–739.
- (61) Osterfeld, S. J.; Yu, H.; Gaster, R. S.; Caramuta, S.; Xu, L.; Han, S. J.; Hall, D. A.; Wilson, R. J.; Sun, S.; White, R. L.; Davis, R. W.; Pourmand, N.; Wang, S. X. Multiplex Protein Assays Based on Real-Time Magnetic Nanotag Sensing. *Proc. Natl. Acad. Sci. U.S.A.* 2008, 105, 20637–20640.
- (62) Gaster, R. S.; Hall, D. A.; Nielsen, C. H.; Osterfeld, S. J.; Yu, H.; Mach, K. E.; Wilson, R. J.; Murmann, B.; Liao, J. C.; Gambhir, S. S.; Wang, S. X. Matrix-Insensitive Protein Assays Push the Limits of Biosensors in Medicine. *Nat. Med.* **2009**, *15*, 1327–1332.
- (63) Besse, P.-A.; Boero, G.; Demierre, M.; Pott, V.; Popovic, R. Detection of a Single Magnetic Microbead Using a Miniaturized Silicon Hall Sensor. *Appl. Phys. Lett.* **2002**, *80*, 4199.
- (64) Mihajlović, G.; Xiong, P.; von Molnár, S.; Ohtani, K.; Ohno, H.; Field, M.; Sullivan, G. J. Detection of Single Magnetic Bead for Biological Applications Using an InAs Quantum-Well Micro-Hall Sensor. *Appl. Phys. Lett.* **2005**, *87*, 112502.

(65) Togawa, K.; Sanbonsugi, H.; Lapicki, A.; Abe, M.; Handa, H.; Sandhu, A. High-Sensitivity InSb Thin-Film Micro-Hall Sensor Arrays for Simultaneous Multiple Detection of Magnetic Beads for Biomedical Applications. *IEEE Trans. Magn.* **2005**, *41*, 3661–3663.

- (66) Aytur, T.; Foley, J.; Anwar, M.; Boser, B.; Harris, E.; Beatty, P. R. A Novel Magnetic Bead Bioassay Platform Using a Microchip-Based Sensor for Infectious Disease Diagnosis. *J. Immunol. Methods* **2006**, *314*, 21–29.
- (67) Gambini, S.; Skucha, K.; Liu, P. P.; Kim, J.; Krigel, R. A 10 kPixel CMOS Hall Sensor Array with Baseline Suppression and Parallel Readout for Immunoassays. *IEEE J. Solid-State Circuits* **2013**, 48, 302—317
- (68) Liu, P. P.; Skucha, K.; Duan, Y.; Megens, M.; Kim, J.; Izyumin, I. I.; Gambini, S.; Boser, B. Magnetic Relaxation Detector for Microbead Labels. *IEEE J. Solid-State Circuits* **2012**, 47, 1056–1064.
- (69) Issadore, D.; Chung, H. J.; Chung, J.; Budin, G.; Weissleder, R.; Lee, H. μHall Chip for Sensitive Detection of Bacteria. *Adv. Healthcare Mater.* **2013**, 2, 1224–1228.
- (70) Balasubramanian, G.; Chan, I. Y.; Kolesov, R.; Al-Hmoud, M.; Tisler, J.; Shin, C.; Kim, C.; Wojcik, A.; Hemmer, P. R.; Krueger, A.; Hanke, T.; Leitenstorfer, A.; Bratschitsch, R.; Jelezko, F.; Wrachtrup, J. Nanoscale Imaging Magnetometry with Diamond Spins Under Ambient Conditions. *Nature* **2008**, *455*, 648–651.
- (71) Maze, J. R.; Stanwix, P. L.; Hodges, J. S.; Hong, S.; Taylor, J. M.; Cappellaro, P.; Jiang, L.; Dutt, M. V.; Togan, E.; Zibrov, A. S.; Yacoby, A.; Walsworth, R. L.; Lukin, M. D. Nanoscale Magnetic Sensing with an Individual Electronic Spin in Diamond. *Nature* **2008**, *455*, 644–647.
- (72) Taylor, J. M.; Cappellaro, P.; Childress, L.; Jiang, L.; Budker, D.; Hemmer, P. R.; Yacoby, A.; Walsworth, R.; Lukin, M. D. High-Sensitivity Diamond Magnetometer with Nanoscale Resolution. *Nat. Phys.* **2008**, *4*, 810–816.
- (73) Waldherr, G.; Beck, J.; Neumann, P.; Said, R. S.; Nitsche, M.; Markham, M. L.; Twitchen, D. J.; Twamley, J.; Jelezko, F.; Wrachtrup, J. High-Dynamic-Range Magnetometry with a Single Nuclear Spin in Diamond. *Nat. Nanotechnol.* **2012**, *7*, 105–108.
- (74) Budker, D.; Jackson, K., Derek, F. *Optical Magnetometry*; Cambridge University Press: Cambridge, U.K., 2013; p xvii, 412 pp.
- (75) Le Sage, D.; Arai, K.; Glenn, D. R.; DeVience, S. J.; Pham, L. M.; Rahn-Lee, L.; Lukin, M. D.; Yacoby, A.; Komeili, A.; Walsworth, R. L. Optical Magnetic Imaging of Living Cells. *Nature* **2013**, 496, 486–489.
- (76) Mamin, H. J.; Kim, M.; Sherwood, M. H.; Rettner, C. T.; Ohno, K.; Awschalom, D. D.; Rugar, D. Nanoscale Nuclear Magnetic Resonance with a Nitrogen-Vacancy Spin Sensor. *Science* **2013**, 339, 557–560.
- (77) Staudacher, T.; Shi, F.; Pezzagna, S.; Meijer, J.; Du, J.; Meriles, C. A.; Reinhard, F.; Wrachtrup, J. Nuclear Magnetic Resonance Spectroscopy on a (5-Nanometer)³ Sample Volume. *Science* **2013**, 339, 561–563.
- (78) Lara, O.; Tong, X.; Zborowski, M.; Chalmers, J. J. Enrichment of Rare Cancer Cells through Depletion of Normal Cells Using Density and Flow-through, Immunomagnetic Cell Separation. *Exp. Hematol.* **2004**, 32, 891–904.
- (79) Choi, J.-W.; Ahn, C. H.; Bhansali, S.; Henderson, H. T. A New Magnetic Bead-Based, Filterless Bio-Separator with Planar Electromagnet Surfaces for Integrated Bio-Detection Systems. *Sens. Actuators, B* **2000**, *68*, 34–39.
- (80) Dupont, E. P.; Labonne, E.; Vandevyver, C.; Lehmann, U.; Charbon, E.; Gijs, M. A. Monolithic Silicon Chip for Immunofluorescence Detection on Single Magnetic Beads. *Anal. Chem.* **2010**, 82, 49–52.
- (81) Lee, H.; Purdon, A. M.; Westervelt, R. M. Manipulation of Biological Cells Using a Microelectromagnet Matrix. *Appl. Phys. Lett.* **2004**, 85, 1063.
- (82) Pamme, N. Magnetism and Microfluidics. *Lab Chip* **2006**, *6*, 24–38.
- (83) Gijs, M. A. M. Magnetic Bead Handling On-Chip: New Opportunities for Analytical Applications. *Microfluid. Nanofluid.* **2004**, *1*, 22–40.

- (84) Xia, N.; Hunt, T. P.; Mayers, B. T.; Alsberg, E.; Whitesides, G. M.; Westervelt, R. M.; Ingber, D. E. Combined Microfluidic-Micromagnetic Separation of Living Cells in Continuous Flow. *Biomed. Microdevices* **2006**, *8*, 299–308.
- (85) Smistrup, K.; Lund-Olesen, T.; Hansen, M. F.; Tang, P. T. Microfluidic Magnetic Separator Using an Array of Soft Magnetic Elements. *J. Appl. Phys.* **2006**, *99*, 08P102.
- (86) Inglis, D. W.; Riehn, R.; Austin, R. H.; Sturm, J. C. Continuous Microfluidic Immunomagnetic Cell Separation. *Appl. Phys. Lett.* **2004**, *85*, 5093.
- (87) Csordas, A.; Gerdon, A. E.; Adams, J. D.; Qian, J.; Oh, S. S.; Xiao, Y.; Soh, H. T. Detection of Proteins in Serum by Micromagnetic Aptamer PCR (MAP) Technology. *Angew. Chem., Int. Ed.* **2010**, 49, 355–358.
- (88) Adams, J. D.; Kim, U.; Soh, H. T. Multitarget Magnetic Activated Cell Sorter. *Proc. Natl. Acad. Sci. U.S.A.* **2008**, *105*, 18165–18170.
- (89) Berger, M.; Castelino, J.; Huang, R.; Shah, M.; Austin, R. H. Design of a Microfabricated Magnetic Cell Separator. *Electrophoresis* **2001**, *22*, 3883–3892.
- (90) Tibbe, A. G.; de Grooth, B. G.; Greve, J.; Liberti, P. A.; Dolan, G. J.; Terstappen, L. W. Optical Tracking and Detection of Immunomagnetically Selected and Aligned Cells. *Nat. Biotechnol.* **1999**, *17*, 1210–1213.
- (91) Choi, J. W.; Liakopoulos, T. M.; Ahn, C. H. An On-Chip Magnetic Bead Separator Using Spiral Electromagnets with Semi-Encapsulated Permalloy. *Biosens. Bioelectron.* **2001**, *16*, 409–416.
- (92) Lee, C. S.; Lee, H.; Westervelt, R. M. Microelectromagnets for the Control of Magnetic Nanoparticles. *Appl. Phys. Lett.* **2001**, *79*, 3308.
- (93) Cardoso, F.; Jankovic, J.; Grossman, R. G.; Hamilton, W. J. Outcome After Stereotactic Thalamotomy for Dystonia and Hemiballismus. *Neurosurgery* **1995**, *36*, 501–7.
- (94) Gossett, D. R.; Weaver, W. M.; Mach, A. J.; Hur, S. C.; Tse, H. T.; Lee, W.; Amini, H.; Di Carlo, D. Label-Free Cell Separation and Sorting in Microfluidic Systems. *Anal. Bioanal. Chem.* **2010**, *397*, 3249–3267.
- (95) Tibbe, A. G.; de Grooth, B. G.; Greve, J.; Liberti, P. A.; Dolan, G. J.; Terstappen, L. W. Cell Analysis System Based on Immunomagnetic Cell Selection and Alignment Followed by Immunofluorescent Analysis Using Compact Disk Technologies. *Cytometry* **2001**, *43*, 31–37.
- (96) Chung, J.; Issadore, D.; Ullal, A.; Lee, K.; Weissleder, R.; Lee, H. Rare Cell Isolation and Profiling on a Hybrid Magnetic/Size-Sorting Chip. *Biomicrofluidics* **2013**, *7*, 54107.
- (97) Issadore, D.; Shao, H.; Chung, J.; Newton, A.; Pittet, M.; Weissleder, R.; Lee, H. Self-Assembled Magnetic Filter for Highly Efficient Immunomagnetic Separation. *Lab Chip* **2011**, *11*, 147–151.
- (98) Rozenfel'd, E. V. Calculation of the Field of a Lattice of Point Magnetic Dipoles. *Phys. Solid State* **2000**, 42, 1680–1687.
- (99) Pamme, N.; Wilhelm, C. Continuous Sorting of Magnetic Cells via On-Chip Free-Flow Magnetophoresis. *Lab Chip* **2006**, *6*, 974–980. (100) Kang, J. H.; Super, M.; Yung, C. W.; Cooper, R. M.; Domansky, K.; Graveline, A. R.; Mammoto, T.; Berthet, J. B.; Tobin, H.; Cartwright, M. J.; Watters, A. L.; Rottman, M.; Waterhouse, A.; Mammoto, A.; Gamini, N.; Rodas, M. J.; Kole, A.; Jiang, A.; Valentin, T. M.; Diaz, A.; Takahashi, K.; Ingber, D. E. An Extracorporeal Blood-Cleansing Device
- (101) Ramadan, Q.; Samper, V.; Poenar, D. P.; Yu, C. An Integrated Microfluidic Platform for Magnetic Microbeads Separation and Confinement. *Biosens. Bioelectron.* **2006**, *21*, 1693–1702.

for Sepsis Therapy. Nat. Med. 2014, 20, 1211-1216.

- (102) Lee, H.; Liu, Y.; Ham, D.; Westervelt, R. M. Integrated Cell Manipulation System-CMOS/Microfluidic Hybrid. *Lab Chip* **2007**, *7*, 331–337.
- (103) Lehmann, U.; Vandevyver, C.; Parashar, V. K.; Gijs, M. A. Droplet-Based DNA Purification in a Magnetic Lab-On-a-Chip. *Angew. Chem., Int. Ed.* **2006**, 45, 3062–3067.
- (104) Pipper, J.; Inoue, M.; Ng, L. F.; Neuzil, P.; Zhang, Y.; Novak, L. Catching Bird Flu in a Droplet. *Nat. Med.* **2007**, *13*, 1259–1263.
- (105) Koh, I.; Hong, R.; Weissleder, R.; Josephson, L. Sensitive NMR Sensors Detect Antibodies to Influenza. *Angew. Chem., Int. Ed.* **2008**, *47*, 4119–4121.

(106) Yang, J.; Wei, F.; Schafer, C.; Wong, D. T. Detection of Tumor Cell-Specific mRNA and Protein in Exosome-Like Microvesicles from Blood and Saliva. *PLoS One* **2014**, *9*, e110641.

- (107) van Reenen, A.; de Jong, A. M.; den Toonder, J. M.; Prins, M. W. Integrated Lab-On-Chip Biosensing Systems Based on Magnetic Particle Actuation—A Comprehensive Review. *Lab Chip* **2014**, *14*, 1966–1986.
- (108) Bruls, D. M.; Evers, T. H.; Kahlman, J. A.; van Lankvelt, P. J.; Ovsyanko, M.; Pelssers, E. G.; Schleipen, J. J.; de Theije, F. K.; Verschuren, C. A.; van der Wijk, T.; van Zon, J. B.; Dittmer, W. U.; Immink, A. H.; Nieuwenhuis, J. H.; Prins, M. W. Rapid Integrated Biosensor for Multiplexed Immunoassays Based on Actuated Magnetic Nanoparticles. *Lab Chip* **2009**, *9*, 3504–3510.
- (109) Ashcroft, N. W.; Mermin, N. D. Solid State Physics; Holt, Rinehart and Winston: New York, 1976.
- (110) Morales, M. P.; Veintemillas-Verdaguer, S.; Montero, M. I.; Serna, C. J.; Roig, A.; Casas, L.; Martínez, B.; Sandiumenge, F. Surface and Internal Spin Canting in γ -Fe₂O₃ Nanoparticles. *Chem. Mater.* **1999**, 11, 3058–3064.
- (111) Kim, B. H.; Lee, N.; Kim, H.; An, K.; Park, Y. I.; Choi, Y.; Shin, K.; Lee, Y.; Kwon, S. G.; Na, H. B.; Park, J. G.; Ahn, T. Y.; Kim, Y. W.; Moon, W. K.; Choi, S. H.; Hyeon, T. Large-Scale Synthesis of Uniform and Extremely Small-Sized Iron Oxide Nanoparticles for High-Resolution T₁ Magnetic Resonance Imaging Contrast Agents. *J. Am. Chem. Soc.* 2011, 133, 12624–12631.
- (112) Jun, Y. W.; Seo, J. W.; Cheon, J. Nanoscaling Laws of Magnetic Nanoparticles and Their Applicabilities in Biomedical Sciences. *Acc. Chem. Res.* **2008**, *41*, 179–189.
- (113) Kim, D.; Lee, N.; Park, M.; Kim, B. H.; An, K.; Hyeon, T. Synthesis of Uniform Ferrimagnetic Magnetite Nanocubes. *J. Am. Chem. Soc.* **2009**, *131*, 454–455.
- (114) Noh, S. H.; Na, W.; Jang, J. T.; Lee, J. H.; Lee, E. J.; Moon, S. H.; Lim, Y.; Shin, J. S.; Cheon, J. Nanoscale Magnetism Control via Surface and Exchange Anisotropy for Optimized Ferrimagnetic Hysteresis. *Nano Lett.* **2012**, *12*, 3716–3721.
- (115) Bean, C. P.; Livingston, J. D. Superparamagnetism. *J. Appl. Phys.* **1959**, *30*, S120.
- (116) Kittel, C. Physical Theory of Ferromagnetic Domains. *Rev. Mod. Phys.* **1949**, *21*, 541–583.
- (117) Brown, W. Thermal Fluctuations of a Single-Domain Particle. *Phys. Rev.* **1963**, 130, 1677–1686.
- (118) Standley, K. J. Oxide Magnetic Materials; Clarendon Press: Oxford, U.K., 1972.
- (119) Park, J.; An, K.; Hwang, Y.; Park, J. G.; Noh, H. J.; Kim, J. Y.; Park, J. H.; Hwang, N. M.; Hyeon, T. Ultra-Large-Scale Syntheses of Monodisperse Nanocrystals. *Nat. Mater.* **2004**, *3*, 891–895.
- (120) Chung, S. H.; Hoffmann, A.; Bader, S. D.; Liu, C.; Kay, B.; Makowski, L.; Chen, L. Biological Sensors Based on Brownian Relaxation of Magnetic Nanoparticles. *Appl. Phys. Lett.* **2004**, *85*, 2971.
- (121) Walker, M.; Mayo, P. I.; O'Grady, K.; Charles, S. W.; Chantrell, R. W. The Magnetic Properties of Single-Domain Particles with Cubic Anisotropy. I. Hysteresis Loops. *J. Phys.: Condens. Matter* **1993**, *5*, 2779–2792.
- (122) Rosensweig, R. E. Heating Magnetic Fluid with Alternating Magnetic Field. J. Magn. Magn. Mater. 2002, 252, 370–374.
- (123) Koenig, S. H.; Kellar, K. E. Theory of $1/T_1$ and $1/T_2$ NMRD Profiles of Solutions of Magnetic Nanoparticles. *Magn. Reson. Med.* **1995**, 34, 227–233.
- (124) Gossuin, Y.; Gillis, P.; Hocq, A.; Vuong, Q. L.; Roch, A. Magnetic Resonance Relaxation Properties of Superparamagnetic Particles. *Wiley Interdiscip. Rev.: Nanomed. Nanobiotechnol.* **2009**, *1*, 299–310.
- (125) Gueron, M. Nuclear Relaxation in Macromolecules by Paramagnetic Ions: A Novel Mechanism. *J. Magn. Reson.* **1975**, *19*, 58–66.
- (126) Brooks, R. A. T_2 -Shortening by Strongly Magnetized Spheres: A Chemical Exchange Model. *Magn. Reson. Med.* **2002**, *47*, 388–391.
- (127) Yablonskiy, D. A.; Haacke, E. M. Theory of NMR Signal Behavior in Magnetically Inhomogeneous Tissues: The Static Dephasing Regime. *Magn. Reson. Med.* **1994**, 32, 749–763.

(128) Yoon, T. J.; Lee, H.; Shao, H.; Hilderbrand, S. A.; Weissleder, R. Multicore Assemblies Potentiate Magnetic Properties of Biomagnetic Nanoparticles. *Adv. Mater.* **2011**, *23*, 4793–4797.

- (129) Leslie-Pelecky, D. L.; Rieke, R. D. Magnetic Properties of Nanostructured Materials. *Chem. Mater.* **1996**, *8*, 1770–1783.
- (130) McCurrie, R. A. The Structure and Properties of Ferromagnetic Materials; Academic Press: Waltham, MA, 1994.
- (131) Jun, Y. W.; Choi, J. S.; Cheon, J. Heterostructured Magnetic Nanoparticles: Their Versatility and High Performance Capabilities. *Chem. Commun.* **2007**, 1203–1214.
- (132) Hyeon, T. Chemical Synthesis of Magnetic Nanoparticles. *Chem. Commun.* **2003**, 927–934.
- (133) Gupta, A. K.; Gupta, M. Synthesis and Surface Engineering of Iron Oxide Nanoparticles for Biomedical Applications. *Biomaterials* **2005**, *26*, 3995–4021.
- (134) Sun, S.; Murray, C. B. Synthesis of Monodisperse Cobalt Nanocrystals and Their Assembly into Magnetic Superlattices. *J. Appl. Phys.* **1999**, *85*, 4325.
- (135) Puntes, V. F.; Krishnan, K. M.; Alivisatos, A. P. Colloidal Nanocrystal Shape and Size Control: The Case of Cobalt. *Science* **2001**, 291, 2115–2117.
- (136) Osuna, J.; de Caro, D.; Amiens, C.; Chaudret, B.; Snoeck, E.; Respaud, M.; Broto, J.-M.; Fert, A. Synthesis, Characterization, and Magnetic Properties of Cobalt Nanoparticles from an Organometallic Precursor. *J. Phys. Chem.* **1996**, *100*, 14571–14574.
- (137) Huber, D. L. Synthesis, Properties, and Applications of Iron Nanoparticles. *Small* **2005**, *1*, 482–501.
- (138) Cordente, N.; Respaud, M.; Senocq, F.; Casanove, M.-J.; Amiens, C.; Chaudret, B. Synthesis and Magnetic Properties of Nickel Nanorods. *Nano Lett.* **2001**, *1*, 565–568.
- (139) Dumestre, F.; Chaudret, B.; Amiens, C.; Renaud, P.; Fejes, P. Superlattices of Iron Nanocubes Synthesized From Fe[N(SiMe₃)₂]₂. *Science* **2004**, 303, 821–823.
- (140) Ziolo, R. F.; Giannelis, E. P.; Weinstein, B. A.; O'horo, M. P.; Ganguly, B. N.; Mehrotra, V.; Russell, M. W.; Huffman, D. R. Matrix-Mediated Synthesis of Nanocrystalline γ -Fe₂O₃: A New Optically Transparent Magnetic Material. *Science* **1992**, 257, 219–223.
- (141) Rockenberger, J.; Scher, E. C.; Alivisatos, A. P. A New Nonhydrolytic Single-Precursor Approach to Surfactant-Capped Nanocrystals of Transition Metal Oxides. *J. Am. Chem. Soc.* **1999**, *121*, 11595–11596.
- (142) Castro, C.; Millan, A.; Palacio, F. Nickel Oxide Magnetic Nanocomposites in an Imine Polymer Matrix. *J. Mater. Chem.* **2000**, *10*, 1945–1947.
- (143) Shevchenko, E. V.; Talapin, D. V.; Rogach, A. L.; Kornowski, A.; Haase, M.; Weller, H. Colloidal Synthesis and Self-Assembly of CoPt Nanocrystals. *J. Am. Chem. Soc.* **2002**, *124*, 11480–11485.
- (144) Seo, W. S.; Lee, J. H.; Sun, X.; Suzuki, Y.; Mann, D.; Liu, Z.; Terashima, M.; Yang, P. C.; McConnell, M. V.; Nishimura, D. G.; Dai, H. FeCo/Graphitic-Shell Nanocrystals as Advanced Magnetic-Resonance-Imaging and Near-Infrared Agents. *Nat. Mater.* **2006**, *5*, 971–976.
- (145) Sun, S. Monodisperse FePt Nanoparticles and Ferromagnetic FePt Nanocrystal Superlattices. *Science* **2000**, 287, 1989–1992.
- (146) Zeng, H.; Rice, P. M.; Wang, S. X.; Sun, S. Shape-Controlled Synthesis and Shape-Induced Texture of MnFe₂O₄ Nanoparticles. *J. Am. Chem. Soc.* **2004**, *126*, 11458–11459.
- (147) Lee, J. H.; Huh, Y. M.; Jun, Y. W.; Seo, J. W.; Jang, J. T.; Song, H. T.; Kim, S.; Cho, E. J.; Yoon, H. G.; Suh, J. S.; Cheon, J. Artificially Engineered Magnetic Nanoparticles for Ultra-Sensitive Molecular Imaging. *Nat. Med.* **2007**, *13*, 95–99.
- (148) Jang, J. T.; Nah, H.; Lee, J. H.; Moon, S. H.; Kim, M. G.; Cheon, J. Critical Enhancements of MRI Contrast and Hyperthermic Effects by Dopant-Controlled Magnetic Nanoparticles. *Angew. Chem., Int. Ed.* **2009**, *48*, 1234–1238.
- (149) Jain, T. K.; Reddy, M. K.; Morales, M. A.; Leslie-Pelecky, D. L.; Labhasetwar, V. Biodistribution, Clearance, and Biocompatibility of Iron Oxide Magnetic Nanoparticles in Rats. *Mol. Pharmaceutics* **2008**, *5*, 316–327.

(150) Weissleder, R.; Stark, D. D.; Engelstad, B. L.; Bacon, B. R.; Compton, C. C.; White, D. L.; Jacobs, P.; Lewis, J. Superparamagnetic Iron Oxide: Pharmacokinetics and Toxicity. *Am. J. Roentgenol.* **1989**, 152, 167–173.

- (151) Reimer, P.; Rummeny, E. J.; Daldrup, H. E.; Balzer, T.; Tombach, B.; Berns, T.; Peters, P. E. Clinical Results with Resovist: A Phase 2 Clinical Trial. *Radiology* **1995**, *195*, 489–496.
- (152) Jung, C. W.; Jacobs, P. Physical and Chemical Properties of Superparamagnetic Iron Oxide MR Contrast Agents: Ferumoxides, Ferumoxtran, Ferumoxsil. *Magn. Reson. Imaging* **1995**, *13*, 661–674.
- (153) Bullivant, J. P.; Zhao, S.; Willenberg, B. J.; Kozissnik, B.; Batich, C. D.; Dobson, J. Materials Characterization of Feraheme/Ferumoxytol and Preliminary Evaluation of Its Potential for Magnetic Fluid Hyperthermia. *Int. J. Mol. Sci.* 2013, 14, 17501–17510.
- (154) Häfeli, U. Scientific and Clinical Applications of Magnetic Carriers; Springer: New York, 1997.
- (155) Weissleder, R.; Nahrendorf, M.; Pittet, M. J. Imaging Macrophages with Nanoparticles. *Nat. Mater.* **2014**, *13*, 125–138.
- (156) Carter, C. B.; Norton, G. Ceramic Materials: Science and Engineering; Springer: New York, 2013.
- (157) Varadan, V. K.; Chen, L. F.; Xie, J. Nanomedicine: Design and Applications of Magnetic Nanomaterials, Nanosensors and Nanosystems; Wiley: Hoboken, NJ, 2008.
- (158) Lu, A. H.; Salabas, E. L.; Schuth, F. Magnetic Nanoparticles: Synthesis, Protection, Functionalization, and Application. *Angew. Chem., Int. Ed.* **2007**, *46*, 1222–1244.
- (159) Laurent, S.; Forge, D.; Port, M.; Roch, A.; Robic, C.; Vander Elst, L.; Muller, R. N. Magnetic Iron Oxide Nanoparticles: Synthesis, Stabilization, Vectorization, Physicochemical Characterizations, and Biological Applications. *Chem. Rev.* **2008**, *108*, 2064–2110.
- (160) Josephson, L.; Tung, C. H.; Moore, A.; Weissleder, R. High-Efficiency Intracellular Magnetic Labeling with Novel Superparamagnetic-Tat Peptide Conjugates. *Bioconjugate Chem.* **1999**, *10*, 186–191.
- (161) Kim, D. K.; Mikhaylova, M.; Zhang, Y.; Muhammed, M. Protective Coating of Superparamagnetic Iron Oxide Nanoparticles. *Chem. Mater.* **2003**, *15*, 1617–1627.
- (162) Lutz, J. F.; Stiller, S.; Hoth, A.; Kaufner, L.; Pison, U.; Cartier, R. One-Pot Synthesis of PEGylated Ultrasmall Iron-Oxide Nanoparticles and Their *In Vivo* Evaluation as Magnetic Resonance Imaging Contrast Agents. *Biomacromolecules* **2006**, *7*, 3132–3138.
- (163) Li, Z.; Tan, B.; Allix, M.; Cooper, A. I.; Rosseinsky, M. J. Direct Coprecipitation Route to Monodisperse Dual-Functionalized Magnetic Iron Oxide Nanocrystals without Size Selection. *Small* **2008**, *4*, 231–239
- (164) Pardoe, H.; Chua-anusorn, W.; Pierre, T. G. S.; Dobson, J. Detection Limits for Ferrimagnetic Particle Concentrations Using Magnetic Resonance Imaging Based Proton Transverse Relaxation Rate Measurements. *Phys. Med. Biol.* **2003**, *48*, N89–N95.
- (165) Cornell, R. M.; Schwertmann, U. The Iron Oxides: Structure, Properties, Reactions, Occurrences and Uses; Wiley: Hoboken, NJ, 2006.
- (166) Tartaj, P.; Morales, M. P.; Veintemillas-Verdaguer, S.; Gonzalez-Carreño, T.; Serna, C. J. Chapter 5 synthesis, properties and biomedical applications of magnetic nanoparticles. *Handb. Magn. Mater.* **2006**, *16*, 403–482.
- (167) Massart, R.; Cabuil, V. Effect of Some Parameters on the Formation of Colloidal Magnetite in Alkaline-Medium-Yield and Particle-Size Control. *J. Chim. Phys. Phys.-Chim. Biol.* **1987**, *84*, 967.
- (168) Jolivet, J.-P.; Froidefond, C.; Pottier, A.; Chanéac, C.; Cassaignon, S.; Tronc, E.; Euzen, P. Size Tailoring of Oxide Nanoparticles by Precipitation in Aqueous Medium. A Semi-Quantitative Modelling. *J. Mater. Chem.* **2004**, *14*, 3281.
- (169) Babes, L.; Denizot, B.; Tanguy, G.; Le Jeune, J. J.; Jallet, P. Synthesis of Iron Oxide Nanoparticles Used as MRI Contrast Agents: A Parametric Study. *J. Colloid Interface Sci.* **1999**, 212, 474–482.
- (170) Gribanov, N. M.; Bibik, E. E.; Buzunov, O. V.; Naumov, V. N. Physico-Chemical Regularities of Obtaining Highly Dispersed Magnetite by the Method of Chemical Condensation. *J. Magn. Magn. Mater.* **1990**, 85, 7–10.

(171) Tronc, E.; Belleville, P.; Jolivet, J. P.; Livage, J. Transformation of Ferric Hydroxide into Spinel by Iron(II) Adsorption. *Langmuir* **1992**, *8*, 313–319.

- (172) Shen, T.; Weissleder, R.; Papisov, M.; Bogdanov, A.; Brady, T. J. Monocrystalline Iron Oxide Nanocompounds (MION): Physicochemical Properties. *Magn. Reson. Med.* **1993**, *29*, 599–604.
- (173) Constantinides, C. D.; Rogers, J.; Herzka, D. A.; Boada, F. E.; Bolar, D.; Kraitchman, D.; Gillen, J.; Bottomley, P. A. Superparamagnetic Iron Oxide MION as a Contrast Agent for Sodium MRI in Myocardial Infarction. *Magn. Reson. Med.* **2001**, *46*, 1164–1168.
- (174) Weissig, V.; Pettinger, T. K.; Murdock, N. Nanopharmaceuticals (Part 1): Products on the Market. *Int. J. Nanomed.* **2014**, *9*, 4357–4373. (175) Ferguson, R. M.; Khandhar, A. P.; Krishnan, K. M. Tracer Design for Magnetic Particle Imaging. *J. Appl. Phys.* **2012**, *111*, 07B318.
- (176) Perez, J. M.; Josephson, L.; O'Loughlin, T.; Hogemann, D.; Weissleder, R. Magnetic Relaxation Switches Capable of Sensing Molecular Interactions. *Nat. Biotechnol.* **2002**, *20*, 816–820.
- (177) Josephson, L.; Kircher, M. F.; Mahmood, U.; Tang, Y.; Weissleder, R. Near-Infrared Fluorescent Nanoparticles as Combined MR/Optical Imaging Probes. *Bioconjugate Chem.* **2002**, *13*, 554–560.
- (178) Perez, J. M.; O'Loughin, T.; Simeone, F. J.; Weissleder, R.; Josephson, L. DNA-Based Magnetic Nanoparticle Assembly Acts as a Magnetic Relaxation Nanoswitch Allowing Screening of DNA-Cleaving Agents. J. Am. Chem. Soc. 2002, 124, 2856–2857.
- (179) Perez, J. M.; Simeone, F. J.; Saeki, Y.; Josephson, L.; Weissleder, R. Viral-Induced Self-Assembly of Magnetic Nanoparticles Allows the Detection of Viral Particles in Biological Media. *J. Am. Chem. Soc.* **2003**, 125, 10192–10193.
- (180) Perez, J. M.; Simeone, F. J.; Tsourkas, A.; Josephson, L.; Weissleder, R. Peroxidase Substrate Nanosensors for MR Imaging. *Nano Lett.* **2004**, *4*, 119–122.
- (181) Perez, J. M.; Josephson, L.; Weissleder, R. Use of Magnetic Nanoparticles as Nanosensors to Probe for Molecular Interactions. *ChemBioChem* **2004**, *5*, 261–264.
- (182) Tassa, C.; Shaw, S. Y.; Weissleder, R. Dextran-Coated Iron Oxide Nanoparticles: A Versatile Platform for Targeted Molecular Imaging, Molecular Diagnostics, and Therapy. *Acc. Chem. Res.* **2011**, *44*, 842–852.
- (183) Colombo, M.; Carregal-Romero, S.; Casula, M. F.; Gutierrez, L.; Morales, M. P.; Bohm, I. B.; Heverhagen, J. T.; Prosperi, D.; Parak, W. J. Biological Applications of Magnetic Nanoparticles. *Chem. Soc. Rev.* **2012**, *41*, 4306–4334.
- (184) Hyeon, T.; Lee, S. S.; Park, J.; Chung, Y.; Na, H. B. Synthesis of Highly Crystalline and Monodisperse Maghemite Nanocrystallites without a Size-Selection Process. *J. Am. Chem. Soc.* **2001**, *123*, 12798–12801.
- (185) Sun, S.; Zeng, H.; Robinson, D. B.; Raoux, S.; Rice, P. M.; Wang, S. X.; Li, G. Monodisperse MFe_2O_4 (M=Fe, Co, Mn) Nanoparticles. *J. Am. Chem. Soc.* **2004**, *126*, 273–279.
- (186) Cheon, J.; Kang, N. J.; Lee, S. M.; Lee, J. H.; Yoon, J. H.; Oh, S. J. Shape Evolution of Single-Crystalline Iron Oxide Nanocrystals. *J. Am. Chem. Soc.* **2004**, *126*, 1950–1951.
- (187) Jun, Y. W.; Choi, J. S.; Cheon, J. Shape Control of Semiconductor and Metal Oxide Nanocrystals through Nonhydrolytic Colloidal Routes. *Angew. Chem., Int. Ed.* **2006**, *45*, 3414–3439.
- (188) Sun, S.; Zeng, H. Size-Controlled Synthesis of Magnetite Nanoparticles. J. Am. Chem. Soc. 2002, 124, 8204–8205.
- (189) Sugimoto, T. Monodispersed Particles; Elsevier Science: Amsterdam, 2001.
- (190) Jun, Y. W.; Lee, J. H.; Cheon, J. Chemical Design of Nanoparticle Probes for High-Performance Magnetic Resonance Imaging. *Angew. Chem., Int. Ed.* **2008**, *47*, 5122–5135.
- (191) Giersig, M.; Hilgendorff, M. Magnetic Nanoparticle Superstructures. Eur. J. Inorg. Chem. 2005, 2005, 3571–3583.
- (192) Lee, N.; Hyeon, T. Designed Synthesis of Uniformly Sized Iron Oxide Nanoparticles for Efficient Magnetic Resonance Imaging Contrast Agents. *Chem. Soc. Rev.* **2012**, *41*, 2575–2589.

(193) van Wonterghem, J.; Mørup, S.; Charles, S. W.; Wells, S.; Villadsen, J. Formation of a Metallic Glass by Thermal Decomposition of Fe(CO)₅. *Phys. Rev. Lett.* **1985**, *55*, 410–413.

- (194) Wilcoxon, J. P.; Provencio, P. P. Use of Surfactant Micelles to Control the Structural Phase of Nanosize Iron Clusters. *J. Phys. Chem. B* **1999**, *103*, 9809–9812.
- (195) Rudge, S. R.; Kurtz, T. L.; Vessely, C. R.; Catterall, L. G.; Williamson, D. L. Preparation, Characterization, and Performance of Magnetic Iron—Carbon Composite Microparticles for Chemotherapy. *Biomaterials* **2000**, *21*, 1411—1420.
- (196) Cabot, A.; Puntes, V. F.; Shevchenko, E.; Yin, Y.; Balcells, L.; Marcus, M. A.; Hughes, S. M.; Alivisatos, A. P. Vacancy Coalescence During Oxidation of Iron Nanoparticles. *J. Am. Chem. Soc.* **2007**, *129*, 10358–10360.
- (197) Peng, S.; Wang, C.; Xie, J.; Sun, S. Synthesis and Stabilization of Monodisperse Fe Nanoparticles. *J. Am. Chem. Soc.* **2006**, *128*, 10676–10677.
- (198) Ban, Z.; Barnakov, Y. A.; Li, F.; Golub, V. O.; O'Connor, C. J. The Synthesis of Core—Shell Iron@Gold Nanoparticles and Their Characterization. *J. Mater. Chem.* **2005**, *15*, 4660–4662.
- (199) Lu, Z.; Prouty, M. D.; Guo, Z.; Golub, V. O.; Kumar, C. S.; Lvov, Y. M. Magnetic Switch of Permeability for Polyelectrolyte Microcapsules Embedded with Co@Au Nanoparticles. *Langmuir* **2005**, *21*, 2042–2050.
- (200) Wilson, J. L. Synthesis and Magnetic Properties of Polymer Nanocomposites with Embedded Iron Nanoparticles. *J. Appl. Phys.* **2004**, 95, 1439.
- (201) Tang, N. J.; Chen, W.; Zhong, W.; Jiang, H. Y.; Huang, S. L.; Du, Y. W. Highly Stable Carbon-Coated Fe/SiO₂ Composites: Synthesis, Structure and Magnetic Properties. *Carbon* **2006**, *44*, 423–427.
- (202) Dahal, N.; Chikan, V. Phase-Controlled Synthesis of Iron Silicide (Fe₃Si and FeSi₂) Nanoparticles in Solution. *Chem. Mater.* **2010**, 22, 2892–2897.
- (203) Shultz, M. D.; Calvin, S.; Gonzalez-Jimenez, F.; Mujica, V.; Alleluia, B. C.; Carpenter, E. E. Gold-Coated Cementite Nanoparticles: An Oxidation-Resistant Alternative to α -Iron. *Chem. Mater.* **2009**, *21*, 5594–5600.
- (204) Jing, Y.; He, S.-H.; Wang, J.-P. Fe₃Si Nanoparticles for Alternating Magnetic Field Heating. *J. Nanopart. Res.* **2013**, *15*, 1–8.
- (205) Amendola, V.; Riello, P.; Meneghetti, M. Magnetic Nanoparticles of Iron Carbide, Iron Oxide, Iron@Iron Oxide, and Metal Iron Synthesized by Laser Ablation in Organic Solvents. *J. Phys. Chem. C* **2011**, *115*, 5140–5146.
- (206) Wrobel, R. J.; Helminiak, A.; Arabczyk, W.; Narkiewicz, U. Studies on the Kinetics of Carbon Deposit Formation on Nanocrystalline Iron Stabilized with Structural Promoters. *J. Phys. Chem. C* **2014**, *118*, 15434–15439.
- (207) Sharma, M.; Mantri, S.; Bahadur, D. Study of Carbon Encapsulated Iron Oxide/Iron Carbide Nanocomposite for Hyperthermia. *J. Magn. Magn. Mater.* **2012**, *324*, 3975–3980.
- (208) Sun, S. Recent Advances in Chemical Synthesis, Self-Assembly, and Applications of FePt Nanoparticles. *Adv. Mater.* **2006**, *18*, 393–403.
- (209) Park, J.-I.; Cheon, J. Synthesis of "Solid Solution" and "Core-Shell" Type Cobalt-Platinum Magnetic Nanoparticles via Transmetalation Reactions. *J. Am. Chem. Soc.* **2001**, *123*, 5743–5746.
- (210) Cullity, B. D.; Graham, C. D. Introduction to Magnetic Materials; Wiley: Hoboken, NJ, 2011.
- (211) Ristau, R. A.; Barmak, K.; Lewis, L. H.; Coffey, K. R.; Howard, J. K. On the Relationship of High Coercivity and L1₀ Ordered Phase in CoPt and FePt Thin Films. *J. Appl. Phys.* **1999**, *86*, 4527.
- (212) Stappert, S.; Rellinghaus, B.; Acet, M.; Wassermann, E. F. Gas-Phase Preparation of L1₀ Ordered FePt Nanoparticles. *J. Cryst. Growth* **2003**, 252, 440–450.
- (213) Sun, S.; Fullerton, E. E.; Weller, D.; Murray, C. B. Compositionally Controlled FePt Nanoparticle Materials. *IEEE Trans. Magn.* **2001**, *37*, 1239–1243.
- (214) Howard, L. E.; Nguyen, H. L.; Giblin, S. R.; Tanner, B. K.; Terry, I.; Hughes, A. K.; Evans, J. S. A Synthetic Route to Size-Controlled FCC

and FCT FePt Nanoparticles. J. Am. Chem. Soc. 2005, 127, 10140-10141.

- (215) Momose, S.; Kodama, H.; Uzumaki, T.; Tanaka, A. Fine Tuning of the Sizes of FePt Nanoparticles. *Jpn. J. Appl. Phys.* **2005**, *44*, 1147–1149
- (216) Chen, M.; Liu, J. P.; Sun, S. One-Step Synthesis of Fept Nanoparticles with Tunable Size. *J. Am. Chem. Soc.* **2004**, *126*, 8394–8395
- (217) Lee, J. H.; Jang, J. T.; Choi, J. S.; Moon, S. H.; Noh, S. H.; Kim, J. W.; Kim, J. G.; Kim, I. S.; Park, K. I.; Cheon, J. Exchange-Coupled Magnetic Nanoparticles for Efficient Heat Induction. *Nat. Nanotechnol.* **2011**, *6*, 418–422.
- (218) Patterson, A. The Scherrer Formula for X-Ray Particle Size Determination. *Phys. Rev.* **1939**, *56*, 978–982.
- (219) Hansen, M. F.; Mørup, S. Estimation of Blocking Temperatures From ZFC/FC Curves. J. Magn. Magn. Mater. 1999, 203, 214–216.
- (220) Joffe, I.; Heubregbr, R. Hysteresis Properties of Distributions of Cubic Single-Domain Ferromagnetic Particles. *Philos. Mag.* **1974**, *29*, 1051–1059.
- (221) Stoner, E. C.; Wohlfarth, E. P. A Mechanism of Magnetic Hysteresis in Heterogeneous Alloys. *Philos. Trans. R. Soc., A* **1948**, 240, 599–642.
- (222) Derjaguin, B.; Landau, L. D. Theory of the Stability of Strongly Charged Lyophobic Sols and of the Adhesion of Strongly Changed Particles in Solution of Electrolytes. *Acta Physicochim. URSS* **1941**, *14*, 633–662.
- (223) Verwey, E. J. W.; Overbeek, J. T. G. *Theory of the Stability of Lyophobic Colloids*; Dover Books on Chemistry; Dover Publications: Mineola, NY, 1999.
- (224) Vincent, B.; Edwards, J.; Emmett, S.; Jones, A. Depletion Flocculation in Dispersions of Sterically-Stabilised Particles ("Soft Spheres"). *Colloids Surf.* **1986**, *18*, 261–281.
- (225) Veiseh, O.; Gunn, J. W.; Zhang, M. Design and Fabrication of Magnetic Nanoparticles for Targeted Drug Delivery and Imaging. *Adv. Drug Delivery Rev.* **2010**, *62*, 284–304.
- (226) Salvati, A.; Pitek, A. S.; Monopoli, M. P.; Prapainop, K.; Bombelli, F. B.; Hristov, D. R.; Kelly, P. M.; Aberg, C.; Mahon, E.; Dawson, K. A. Transferrin-Functionalized Nanoparticles Lose Their Targeting Capabilities when a Biomolecule Corona Adsorbs on the Surface. *Nat. Nanotechnol.* **2013**, *8*, 137–143.
- (227) Nel, A. E.; Madler, L.; Velegol, D.; Xia, T.; Hoek, E. M.; Somasundaran, P.; Klaessig, F.; Castranova, V.; Thompson, M. Understanding Biophysicochemical Interactions at the Nano-Bio Interface. *Nat. Mater.* **2009**, *8*, 543–557.
- (228) Ling, D.; Hyeon, T. Chemical Design of Biocompatible Iron Oxide Nanoparticles for Medical Applications. *Small* **2013**, *9*, 1450–1466
- (229) Nel, A.; Xia, T.; Mädler, L.; Li, N. Toxic Potential of Materials at the Nanolevel. *Science* **2006**, *311*, 622–627.
- (230) Blackman, M. L.; Royzen, M.; Fox, J. M. Tetrazine Ligation: Fast Bioconjugation Based on Inverse-Electron-Demand Diels-Alder Reactivity. *J. Am. Chem. Soc.* **2008**, *130*, 13518–13519.
- (231) Mocan, T.; Clichici, S.; Agoşton-Coldea, L.; Mocan, L.; Şimon, Ş.; Ilie, I.; Biriş, A.; Mureşan, A. Implications of Oxidative Stress Mechanisms in Toxicity of Nanoparticles (Review). *Acta Physiol. Hung.* **2010**, *97*, 247–255.
- (232) Hadley, M. J.; Wright, A. J.; Rowson, N. A.; Grover, L. M. Acicular Nanoparticles Formed through Coprecipitation of Iron Salts in the Presence of Bovine Serum Albumin. *J. Mater. Chem.* **2011**, *21*, 13769.
- (233) Ma, H. L.; Qi, X. R.; Maitani, Y.; Nagai, T. Preparation and Characterization of Superparamagnetic Iron Oxide Nanoparticles Stabilized by Alginate. *Int. J. Pharm.* **2007**, 333, 177–186.
- (234) Javid, A.; Ahmadian, S.; Saboury, A. A.; Kalantar, S. M.; Rezaei-Zarchi, S. Chitosan-Coated Superparamagnetic Iron Oxide Nanoparticles for Doxorubicin Delivery: Synthesis and Anticancer Effect Against Human Ovarian Cancer Cells. *Chem. Biol. Drug Des.* **2013**, *82*, 296–306.
- (235) Xu, C.; Xu, K.; Gu, H.; Zheng, R.; Liu, H.; Zhang, X.; Guo, Z.; Xu, B. Dopamine as a Robust Anchor to Immobilize Functional

Molecules on the Iron Oxide Shell of Magnetic Nanoparticles. *J. Am. Chem. Soc.* **2004**, *126*, 9938–9939.

- (236) Wei, H.; Insin, N.; Lee, J.; Han, H. S.; Cordero, J. M.; Liu, W.; Bawendi, M. G. Compact Zwitterion-Coated Iron Oxide Nanoparticles for Biological Applications. *Nano Lett.* **2012**, *12*, 22–25.
- (237) Liu, Y.; Chen, T.; Wu, C.; Qiu, L.; Hu, R.; Li, J.; Cansiz, S.; Zhang, L.; Cui, C.; Zhu, G.; You, M.; Zhang, T.; Tan, W. Facile Surface Functionalization of Hydrophobic Magnetic Nanoparticles. *J. Am. Chem. Soc.* **2014**, *136*, 12552–12555.
- (238) Taupitz, M.; Wagner, S.; Schnorr, J.; Kravec, I.; Pilgrimm, H.; Bergmann-Fritsch, H.; Hamm, B. Phase I Clinical Evaluation of Citrate-Coated Monocrystalline Very Small Superparamagnetic Iron Oxide Particles as a New Contrast Medium for Magnetic Resonance Imaging. *Invest. Radiol.* 2004, 39, 394–405.
- (239) Jun, Y. W.; Huh, Y. M.; Choi, J. S.; Lee, J. H.; Song, H. T.; Kim, S.; Yoon, S.; Kim, K. S.; Shin, J. S.; Suh, J. S.; Cheon, J. Nanoscale Size Effect of Magnetic Nanocrystals and Their Utilization for Cancer Diagnosis via Magnetic Resonance Imaging. *J. Am. Chem. Soc.* 2005, 127, 5732–5733.
- (240) Huh, Y. M.; Jun, Y. W.; Song, H. T.; Kim, S.; Choi, J. S.; Lee, J. H.; Yoon, S.; Kim, K. S.; Shin, J. S.; Suh, J. S.; Cheon, J. In Vivo Magnetic Resonance Detection of Cancer by Using Multifunctional Magnetic Nanocrystals. *J. Am. Chem. Soc.* **2005**, *127*, 12387–12391.
- (241) Mahato, R. I. Biomaterials for Delivery and Targeting of Proteins and Nucleic Acids; CRC Press Inc.: Boca Raton, FL, 2004.
- (242) Otsuka, H.; Nagasaki, Y.; Kataoka, K. PEGylated Nanoparticles for Biological and Pharmaceutical Applications. *Adv. Drug Delivery Rev.* **2003**, *55*, 403–419.
- (243) Karakoti, A. S.; Das, S.; Thevuthasan, S.; Seal, S. PEGylated Inorganic Nanoparticles. *Angew. Chem., Int. Ed.* **2011**, *50*, 1980–1994.
- (244) Xie, J.; Xu, C.; Kohler, N.; Hou, Y.; Sun, S. Controlled PEGylation of Monodisperse Fe₃O₄ Nanoparticles for Reduced Non-Specific Uptake by Macrophage Cells. *Adv. Mater.* **2007**, *19*, 3163–3166
- (245) Amstad, E.; Gehring, A. U.; Fischer, H.; Nagaiyanallur, V. V.; Hähner, G.; Textor, M.; Reimhult, E. Influence of Electronegative Substituents on the Binding Affinity of Catechol-Derived Anchors to Fe₃O₄ Nanoparticles. *J. Phys. Chem. C* **2011**, *115*, 683–691.
- (246) Kim, S. W.; Kim, S.; Tracy, J. B.; Jasanoff, A.; Bawendi, M. G. Phosphine Oxide Polymer for Water-Soluble Nanoparticles. *J. Am. Chem. Soc.* **2005**, 127, 4556–4557.
- (247) Na, H. B.; Lee, I. S.; Seo, H.; Park, Y. I.; Lee, J. H.; Kim, S. W.; Hyeon, T. Versatile PEG-Derivatized Phosphine Oxide Ligands for Water-Dispersible Metal Oxide Nanocrystals. *Chem. Commun.* **2007**, 5167–5169.
- (248) Kohler, N.; Fryxell, G. E.; Zhang, M. A Bifunctional Poly(Ethylene Glycol) Silane Immobilized on Metallic Oxide-Based Nanoparticles for Conjugation with Cell Targeting Agents. *J. Am. Chem. Soc.* **2004**, *126*, 7206–7211.
- (249) Na, H. B.; Palui, G.; Rosenberg, J. T.; Ji, X.; Grant, S. C.; Mattoussi, H. Multidentate Catechol-Based Polyethylene Glycol Oligomers Provide Enhanced Stability and Biocompatibility to Iron Oxide Nanoparticles. *ACS Nano* **2012**, *6*, 389–399.
- (250) Juliano, R. L. Drug Delivery Systems: Characteristics and Biomedical Applications; Oxford University Press: Oxford, U.K., 1980.
- (251) Sery, T. W.; Hehre, E. J. Degradation of Dextrans by Enzymes of Intestinal Bacteria. *J. Bacteriol.* **1956**, *71*, 373–380.
- (252) Creixell, M.; Herrera, A. P.; Latorre-Esteves, M.; Ayala, V.; Torres-Lugo, M.; Rinaldi, C. The Effect of Grafting Method on the Colloidal Stability and In Vitro Cytotoxicity of Carboxymethyl Dextran Coated Magnetic Nanoparticles. *J. Mater. Chem.* **2010**, *20*, 8539.
- (253) Moffitt, E. A. Blood Substitutes. Can. Anaesth. Soc. J. 1975, 22, 12-19.
- (254) Dong, A.; Ye, X.; Chen, J.; Kang, Y.; Gordon, T.; Kikkawa, J. M.; Murray, C. B. A Generalized Ligand-Exchange Strategy Enabling Sequential Surface Functionalization of Colloidal Nanocrystals. *J. Am. Chem. Soc.* **2011**, *133*, 998–1006.

- (255) Liong, M.; Shao, H.; Haun, J. B.; Lee, H.; Weissleder, R. Carboxymethylated Polyvinyl Alcohol Stabilizes Doped Ferrofluids for Biological Applications. *Adv. Mater.* **2010**, *22*, 5168–5172.
- (256) Kircheis, R.; Wightman, L.; Wagner, E. Design and Gene Delivery Activity of Modified Polyethylenimines. *Adv. Drug Delivery Rev.* **2001**, *53*, 341–358.
- (257) Boussif, O.; Lezoualc'h, F.; Zanta, M. A.; Mergny, M. D.; Scherman, D.; Demeneix, B.; Behr, J. P. A Versatile Vector for Gene and Oligonucleotide Transfer into Cells in Culture and *In Vivo*: Polyethylenimine. *Proc. Natl. Acad. Sci. U.S.A.* **1995**, 92, 7297–7301.
- (258) Kievit, F. M.; Veiseh, O.; Bhattarai, N.; Fang, C.; Gunn, J. W.; Lee, D.; Ellenbogen, R. G.; Olson, J. M.; Zhang, M. PEI-PEG-Chitosan Copolymer Coated Iron Oxide Nanoparticles for Safe Gene Delivery: Synthesis, Complexation, and Transfection. *Adv. Funct. Mater.* **2009**, *19*, 2244–2251.
- (259) Duan, H.; Kuang, M.; Wang, X.; Wang, Y. A.; Mao, H.; Nie, S. Reexamining the Effects of Particle Size and Surface Chemistry on the Magnetic Properties of Iron Oxide Nanocrystals: New Insights into Spin Disorder and Proton Relaxivity. *J. Phys. Chem. C* **2008**, *112*, 8127–8131.
- (260) Lee, N.; Kim, H.; Choi, S. H.; Park, M.; Kim, D.; Kim, H. C.; Choi, Y.; Lin, S.; Kim, B. H.; Jung, H. S.; Kim, H.; Park, K. S.; Moon, W. K.; Hyeon, T. Magnetosome-Like Ferrimagnetic Iron Oxide Nanocubes for Highly Sensitive MRI of Single Cells and Transplanted Pancreatic Islets. *Proc. Natl. Acad. Sci. U.S.A.* **2011**, *108*, 2662–2667.
- (261) Robinson, D. B.; Persson, H. H.; Zeng, H.; Li, G.; Pourmand, N.; Sun, S.; Wang, S. X. DNA-Functionalized MFe_2O_4 (M = Fe, Co, or Mn) Nanoparticles and Their Hybridization to DNA-Functionalized Surfaces. *Langmuir* **2005**, *21*, 3096–3103.
- (262) Nasongkla, N.; Bey, E.; Ren, J.; Ai, H.; Khemtong, C.; Guthi, J. S.; Chin, S. F.; Sherry, A. D.; Boothman, D. A.; Gao, J. Multifunctional Polymeric Micelles as Cancer-Targeted, MRI-Ultrasensitive Drug Delivery Systems. *Nano Lett.* **2006**, *6*, 2427–2430.
- (263) Yu, W. W.; Chang, E.; Sayes, C. M.; Drezek, R.; Colvin, V. L. Aqueous Dispersion of Monodisperse Magnetic Iron Oxide Nanocrystals through Phase Transfer. *Nanotechnology* **2006**, *17*, 4483–4487.
- (264) Kim, B. S.; Qiu, J. M.; Wang, J. P.; Taton, T. A. Magnetomicelles: Composite Nanostructures from Magnetic Nanoparticles and Cross-Linked Amphiphilic Block Copolymers. *Nano Lett.* **2005**, *5*, 1987–1991.
- (265) Tanimoto, A.; Kuribayashi, S. Application of Superparamagnetic Iron Oxide to Imaging of Hepatocellular Carcinoma. *Eur. J. Radiol.* **2006**, *58*, 200–216.
- (266) Gupta, A. K.; Wells, S. Surface-Modified Superparamagnetic Nanoparticles for Drug Delivery: Preparation, Characterization, and Cytotoxicity Studies. *IEEE Trans. Nanobiosci.* **2004**, *3*, 66–73.
- (267) Wang, Y.; Wong, J. F.; Teng, X.; Lin, X. Z.; Yang, H. "Pulling" Nanoparticles into Water: Phase Transfer of Oleic Acid Stabilized Monodisperse Nanoparticles into Aqueous Solutions of α -Cyclodextrin. *Nano Lett.* **2003**, *3*, 1555–1559.
- (268) Muthiah, M.; Lee, S. J.; Moon, M.; Lee, H. J.; Bae, W. K.; Chung, I. J.; Jeong, Y. Y.; Park, I.-K. Surface Tunable Polymersomes Loaded with Magnetic Contrast Agent and Drug for Image Guided Cancer Therapy. *J. Nanosci. Nanotechnol.* **2013**, *13*, 1626–1630.
- (269) Cheng, J.; Teply, B. A.; Sherifi, I.; Sung, J.; Luther, G.; Gu, F. X.; Levy-Nissenbaum, E.; Radovic-Moreno, A. F.; Langer, R.; Farokhzad, O. C. Formulation of Functionalized PLGA-PEG Nanoparticles for In Vivo Targeted Drug Delivery. *Biomaterials* **2007**, *28*, 869–876.
- (270) Li, K.; Ding, D.; Huo, D.; Pu, K.-Y.; Thao, N. N. P.; Hu, Y.; Li, Z.; Liu, B. Conjugated Polymer Based Nanoparticles as Dual-Modal Probes for Targeted In Vivo Fluorescence and Magnetic Resonance Imaging. *Adv. Funct. Mater.* **2012**, *22*, 3107–3115.
- (271) Charoenmark, L.; Polpanich, D.; Thiramanas, R.; Tangboriboonrat, P. Preparation of Superparamagnetic Polystyrene-Based Nanoparticles Functionalized by Acrylic Acid. *Macromol. Res.* **2012**, *20*, 590–596.
- (272) Verena, H.; Myriam, L.; Clemens Kilian, W.; Hubert, S.; Katharina, L.; Volker, M. Synthesis and Biomedical Applications of Functionalized Fluorescent and Magnetic Dual Reporter Nanoparticles as Obtained in the Miniemulsion Process. *J. Phys.: Condens. Matter* **2006**, *18*, S2581.

(273) Ren, J.; Hong, H.; Ren, T.; Teng, X. Preparation and Characterization of Magnetic PLA-PEG Composite Nanoparticles for Drug Targeting. *React. Funct. Polym.* **2006**, *66*, 944–951.

- (274) Tan, H.; Xue, J. M.; Shuter, B.; Li, X.; Wang, J. Synthesis of PEOlated Fe₃O₄@SiO₂ Nanoparticles via Bioinspired Silification for Magnetic Resonance Imaging. *Adv. Funct. Mater.* **2010**, *20*, 722–731.
- (275) Taboada, E.; Solanas, R.; Rodríguez, E.; Weissleder, R.; Roig, A. Supercritical-Fluid-Assisted One-Pot Synthesis of Biocompatible Core- $(\gamma$ -Fe₂O₃)/Shell(SiO₂) Nanoparticles as High Relaxivity T₂-Contrast Agents for Magnetic Resonance Imaging. *Adv. Funct. Mater.* **2009**, *19*, 2319–2324.
- (276) Taboada, E.; Gich, M.; Roig, A. Nanospheres of Silica with an ε -Fe,O₃ Single Crystal Nucleus. ACS Nano **2009**, 3, 3377–3382.
- (277) Xu, X.; Friedman, G.; Humfeld, K. D.; Majetich, S. A.; Asher, S. A. Synthesis and Utilization of Monodisperse Superparamagnetic Colloidal Particles for Magnetically Controllable Photonic Crystals. *Chem. Mater.* **2002**, *14*, 1249–1256.
- (278) Kaewsaneha, C.; Tangboriboonrat, P.; Polpanich, D.; Eissa, M.; Elaissari, A. Anisotropic Janus Magnetic Polymeric Nanoparticles Prepared via Miniemulsion Polymerization. *J. Polym. Sci., Part A: Polym. Chem.* **2013**, *51*, 4779–4785.
- (279) Neely, L. A.; Audeh, M.; Phung, N. A.; Min, M.; Suchocki, A.; Plourde, D.; Blanco, M.; Demas, V.; Skewis, L. R.; Anagnostou, T.; Coleman, J. J.; Wellman, P.; Mylonakis, E.; Lowery, T. J. T₂ Magnetic Resonance Enables Nanoparticle-Mediated Rapid Detection of Candidemia in Whole Blood. *Sci. Transl. Med.* **2013**, *5*, 182ra54.
- (280) Ulman, A. Formation and Structure of Self-Assembled Monolayers. Chem. Rev. 1996, 96, 1533-1554.
- (281) Lu, Y.; Yin, Y.; Mayers, B. T.; Xia, Y. Modifying the Surface Properties of Superparamagnetic Iron Oxide Nanoparticles through a Sol-Gel Approach. *Nano Lett.* **2002**, *2*, 183–186.
- (282) Tago, T.; Hatsuta, T.; Miyajima, K.; Kishida, M.; Tashiro, S.; Wakabayashi, K. Novel Synthesis of Silica-Coated Ferrite Nanoparticles Prepared Using Water-in-Oil Microemulsion. *J. Am. Ceram. Soc.* **2002**, *85*, 2188–2194.
- (283) Graf, C.; Vossen, D. L. J.; Imhof, A.; van Blaaderen, A. General Method to Coat Colloidal Particles with Silica. *Langmuir* **2003**, *19*, 6693–6700.
- (284) Stöber, W.; Fink, A.; Bohn, E. Controlled Growth of Monodisperse Silica Spheres in the Micron Size Range. *J. Colloid Interface Sci.* **1968**, *26*, 62–69.
- (285) Hench, L. L.; West, J. K. The Sol-Gel Process. Chem. Rev. 1990, 33-72.
- (286) Yi, D. K.; Lee, S. S.; Papaefthymiou, G. C.; Ying, J. Y. Nanoparticle Architectures Templated by SiO₂/Fe₂O₃ Nanocomposites. *Chem. Mater.* **2006**, *18*, 614–619.
- (287) Choi, J. S.; Lee, J. H.; Shin, T. H.; Song, H. T.; Kim, E. Y.; Cheon, J. Self-Confirming "AND" Logic Nanoparticles for Fault-Free MRI. *J. Am. Chem. Soc.* **2010**, 132, 11015–11017.
- (288) Yoo, D.; Jeong, H.; Preihs, C.; Choi, J. S.; Shin, T. H.; Sessler, J. L.; Cheon, J. Double-Effector Nanoparticles: A Synergistic Approach to Apoptotic Hyperthermia. *Angew. Chem., Int. Ed.* **2012**, *51*, 12482–12485.
- (289) Shin, T. H.; Choi, J. S.; Yun, S.; Kim, I. S.; Song, H. T.; Kim, Y.; Park, K. I.; Cheon, J. T_1 and T_2 Dual-Mode MRI Contrast Agent for Enhancing Accuracy by Engineered Nanomaterials. *ACS Nano* **2014**, *8*, 3393–3401.
- (290) Misra, A. Challenges in Delivery of Therapeutic Genomics and Proteomics; Elsevier Science: Amsterdam, 2010.
- (291) Trubetskoy, V. S.; Torchilin, V. P.; Kennel, S. J.; Huang, L. Use of N-Terminal Modified Poly(L-Lysine)-Antibody Conjugate as a Carrier for Targeted Gene Delivery in Mouse Lung Endothelial Cells. *Bioconjugate Chem.* 1992, 3, 323–327.
- (292) Haun, J. B.; Devaraj, N. K.; Hilderbrand, S. A.; Lee, H.; Weissleder, R. Bioorthogonal Chemistry Amplifies Nanoparticle Binding and Enhances the Sensitivity of Cell Detection. *Nat. Nanotechnol.* **2010**, *5*, 660–665.
- (293) Hermanson, G. T. Bioconjugate Techniques; Elsevier Science: Amsterdam, 2013.

(294) Högemann, D.; Josephson, L.; Weissleder, R.; Basilion, J. P. Improvement of MRI Probes to Allow Efficient Detection of Gene Expression. *Bioconjugate Chem.* **2000**, *11*, 941–946.

- (295) Scarberry, K. E.; Dickerson, E. B.; McDonald, J. F.; Zhang, Z. J. Magnetic Nanoparticle-Peptide Conjugates for *In Vitro* and *In Vivo* Targeting and Extraction of Cancer Cells. *J. Am. Chem. Soc.* **2008**, *130*, 10258–10262.
- (296) Liu, C. H.; Sahoo, S. L.; Tsao, M. H. Acridine Orange Coated Magnetic Nanoparticles for Nucleus Labeling and DNA Adsorption. *Colloids Surf.*, B **2014**, 115, 150–156.
- (297) Long, J.; Jiao, A.; Wei, B.; Wu, Z.; Zhang, Y.; Xu, X.; Jin, Z. A Novel Method for Pullulanase Immobilized onto Magnetic Chitosan/Fe₃O₄ Composite Nanoparticles by *In Situ* Preparation and Evaluation of the Enzyme Stability. *J. Mol. Catal. B: Enzym.* **2014**, *109*, 53–61.
- (298) Sletten, E. M.; Bertozzi, C. R. Bioorthogonal Chemistry: Fishing for Selectivity in a Sea of Functionality. *Angew. Chem., Int. Ed.* **2009**, *48*, 6974–6998.
- (299) Sletten, E. M.; Bertozzi, C. R. From Mechanism to Mouse: A Tale of Two Bioorthogonal Reactions. *Acc. Chem. Res.* **2011**, *44*, 666–676.
- (300) McKay, C. S.; Finn, M. G. Click Chemistry in Complex Mixtures: Bioorthogonal Bioconjugation. *Chem. Biol.* **2014**, *21*, 1075–1101.
- (301) Kolb, H. C.; Finn, M. G.; Sharpless, K. B. Click Chemistry: Diverse Chemical Function from a Few Good Reactions. *Angew. Chem., Int. Ed.* **2001**, *40*, 2004–2021.
- (302) Rostovtsev, V. V.; Green, L. G.; Fokin, V. V.; Sharpless, K. B. A Stepwise Huisgen Cycloaddition Process: Copper(I)-Catalyzed Regioselective "Ligation" of Azides and Terminal Alkynes. *Angew. Chem., Int. Ed.* **2002**, *41*, 2596–2599.
- (303) Moses, J. E.; Moorhouse, A. D. The Growing Applications of Click Chemistry. *Chem. Soc. Rev.* **2007**, *36*, 1249–1262.
- (304) Tornøe, C. W.; Christensen, C.; Meldal, M. Peptidotriazoles on Solid Phase: [1,2,3]-Triazoles by Regiospecific Copper(I)-Catalyzed 1,3-Dipolar Cycloadditions of Terminal Alkynes to Azides. *J. Org. Chem.* **2002**, *67*, 3057–3064.
- (305) Chan, T. R.; Hilgraf, R.; Sharpless, K. B.; Fokin, V. V. Polytriazoles as Copper(I)-Stabilizing Ligands in Catalysis. *Org. Lett.* **2004**, *6*, 2853–2855.
- (306) Rodionov, V. O.; Presolski, S. I.; Gardinier, S.; Lim, Y. H.; Finn, M. G. Benzimidazole and Related Ligands for Cu-Catalyzed Azide-Alkyne Cycloaddition. *J. Am. Chem. Soc.* **2007**, *129*, 12696–12704.
- (307) Baskin, J. M.; Prescher, J. A.; Laughlin, S. T.; Agard, N. J.; Chang, P. V.; Miller, I. A.; Lo, A.; Codelli, J. A.; Bertozzi, C. R. Copper-Free Click Chemistry for Dynamic In Vivo Imaging. *Proc. Natl. Acad. Sci. U.S.A.* **2007**, *104*, 16793–16797.
- (308) Jewett, J. C.; Bertozzi, C. R. Cu-Free Click Cycloaddition Reactions in Chemical Biology. *Chem. Soc. Rev.* **2010**, *39*, 1272.
- (309) Saxon, E. Cell Surface Engineering by a Modified Staudinger Reaction. *Science* **2000**, 287, 2007–2010.
- (310) Zhang, H.; Ma, Y.; Sun, X. L. Chemically-Selective Surface Glyco-Functionalization of Liposomes through Staudinger Ligation. *Chem. Commun.* **2009**, 3032–3034.
- (311) de Araujo, A. D.; Palomo, J. M.; Cramer, J.; Kohn, M.; Schroder, H.; Wacker, R.; Niemeyer, C.; Alexandrov, K.; Waldmann, H. Diels-Alder Ligation and Surface Immobilization of Proteins. *Angew. Chem., Int. Ed.* **2005**, *45*, 296–301.
- (312) Devaraj, N. K.; Upadhyay, R.; Haun, J. B.; Hilderbrand, S. A.; Weissleder, R. Fast and Sensitive Pretargeted Labeling of Cancer Cells through a Tetrazine/Trans-Cyclooctene Cycloaddition. *Angew. Chem., Int. Ed.* **2009**, *48*, 7013–7016.
- (313) Devaraj, N. K.; Hilderbrand, S.; Upadhyay, R.; Mazitschek, R.; Weissleder, R. Bioorthogonal Turn-On Probes for Imaging Small Molecules Inside Living Cells. *Angew. Chem., Int. Ed.* **2010**, *49*, 2869–2872
- (314) Karver, M. R.; Weissleder, R.; Hilderbrand, S. A. Synthesis and Evaluation of a Series of 1,2,4,5-Tetrazines for Bioorthogonal Conjugation. *Bioconjugate Chem.* **2011**, 22, 2263–2270.

(315) Haun, J. B.; Castro, C. M.; Wang, R.; Peterson, V. M.; Marinelli, B. S.; Lee, H.; Weissleder, R. Micro-NMR for Rapid Molecular Analysis of Human Tumor Samples. *Sci. Transl. Med.* **2011**, *3*, 71ra16.

- (316) Haun, J. B.; Devaraj, N. K.; Marinelli, B. S.; Lee, H.; Weissleder, R. Probing Intracellular Biomarkers and Mediators of Cell Activation Using Nanosensors and Bioorthogonal Chemistry. *ACS Nano* **2011**, *5*, 3204–3213.
- (317) Liong, M.; Tassa, C.; Shaw, S. Y.; Lee, H.; Weissleder, R. Multiplexed Magnetic Labeling Amplification Using Oligonucleotide Hybridization. *Adv. Mater.* **2011**, 23, H254–H257.
- (318) Vallee, A.; Humblot, V.; Pradier, C. M. Peptide Interactions with Metal and Oxide Surfaces. *Acc. Chem. Res.* **2010**, *43*, 1297–1306.
- (319) Hochuli, E.; Bannwarth, W.; Döbeli, H.; Gentz, R.; Stüber, D. Genetic Approach to Facilitate Purification of Recombinant Proteins with a Novel Metal Chelate Adsorbent. *Nat. Biotechnol.* **1988**, *6*, 1321–1325.
- (320) Ueda, E. K. M.; Gout, P. W.; Morganti, L. Current and Prospective Applications of Metal Ion—Protein Binding. *J. Chromatogr.*, A 2003, 988, 1–23.
- (321) Xu, C.; Xu, K.; Gu, H.; Zhong, X.; Guo, Z.; Zheng, R.; Zhang, X.; Xu, B. Nitrilotriacetic Acid-Modified Magnetic Nanoparticles as a General Agent to Bind Histidine-Tagged Proteins. *J. Am. Chem. Soc.* **2004**, *126*, 3392–3393.
- (322) Kim, J. S.; Valencia, C. A.; Liu, R.; Lin, W. Highly-Efficient Purification of Native Polyhistidine-Tagged Proteins by Multivalent NTA-Modified Magnetic Nanoparticles. *Bioconjugate Chem.* **2007**, *18*, 333–341.
- (323) Durland, R. H.; Eastman, E. M. Manufacturing and Quality Control of Plasmid-Based Gene Expression Systems. *Adv. Drug Delivery Rev.* **1998**, *30*, 33–48.
- (324) Kim, J.; Piao, Y.; Lee, N.; Park, Y. I.; Lee, I. H.; Lee, J. H.; Paik, S. R.; Hyeon, T. Magnetic Nanocomposite Spheres Decorated with NiO Nanoparticles for a Magnetically Recyclable Protein Separation System. *Adv. Mater.* **2010**, *22*, 57–60.
- (325) Lee, I. S.; Lee, N.; Park, J.; Kim, B. H.; Yi, Y. W.; Kim, T.; Kim, T. K.; Lee, I. H.; Paik, S. R.; Hyeon, T. Ni/NiO Core/Shell Nanoparticles for Selective Binding and Magnetic Separation of Histidine-Tagged Proteins. J. Am. Chem. Soc. 2006, 128, 10658–10659.
- (326) Lodish, H.; Berk, A.; Kaiser, C. A.; Krieger, M.; Bretscher, A.; Ploegh, H.; Amon, A.; Scott, M. P. *Molecular Cell Biology*; W. H. Freeman: New York, 2012.
- (327) Sapsford, K. E.; Algar, W. R.; Berti, L.; Gemmill, K. B.; Casey, B. J.; Oh, E.; Stewart, M. H.; Medintz, I. L. Functionalizing Nanoparticles with Biological Molecules: Developing Chemistries that Facilitate Nanotechnology. *Chem. Rev.* **2013**, *113*, 1904–2074.
- (328) Livnah, O.; Bayer, E. A.; Wilchek, M.; Sussman, J. L. Three-Dimensional Structures of Avidin and the Avidin-Biotin Complex. *Proc. Natl. Acad. Sci. U.S.A.* **1993**, *90*, 5076–5080.
- (329) Green, N. M. Thermodynamics of the Binding of Biotin and Some Analogues by Avidin. *Biochem. J.* **1966**, *101*, 774–780.
- (330) Tiefenauer, L. X.; Kuehne, G.; Andres, R. Y. Antibody-Magnetite Nanoparticles: *In Vitro* Characterization of a Potential Tumor-Specific Contrast Agent for Magnetic Resonance Imaging. *Bioconjugate Chem.* **1993**, *4*, 347–352.
- (331) Guven, B.; Basaran-Akgul, N.; Temur, E.; Tamer, U.; Boyaci, I. H. SERS-Based Sandwich Immunoassay Using Antibody Coated Magnetic Nanoparticles for Escherichia Coli Enumeration. *Analyst* **2011**, *136*, 740–748.
- (332) Artemov, D. Molecular Magnetic Resonance Imaging with Targeted Contrast Agents. *J. Cell. Biochem.* **2003**, 90, 518–524.
- (333) Miller, B. T.; Collins, T. J.; Rogers, M. E.; Kurosky, A. Peptide Biotinylation with Amine-Reactive Esters: Differential Side Chain Reactivity. *Peptides* **1997**, *18*, 1585–1595.
- (334) Wilchek, M.; Bayer, E. A.; Livnah, O. Essentials of Biorecognition: The (Strept)avidin-Biotin System as a Model for Protein-Protein and Protein-Ligand Interaction. *Immunol. Lett.* **2006**, 103, 27–32.
- (335) Yao, Z.; Zhang, M.; Sakahara, H.; Nakamoto, Y.; Higashi, T.; Zhao, S.; Sato, N.; Arano, Y.; Konishi, J. The Relationship of

Glycosylation and Isoelectric Point with Tumor Accumulation of Avidin. J. Nucl. Med. 1999, 40, 479–483.

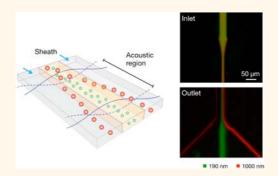
- (336) Chaiet, L.; Wolf, F. J. The Properties of Streptavidin, a Biotin-Binding Protein Produced by Streptomycetes. *Arch. Biochem. Biophys.* **1964**, *106*, 1–5.
- (337) Nash, M. A.; Yager, P.; Hoffman, A. S.; Stayton, P. S. Mixed Stimuli-Responsive Magnetic and Gold Nanoparticle System for Rapid Purification, Enrichment, and Detection of Biomarkers. *Bioconjugate Chem.* **2010**, *21*, 2197–2204.
- (338) Min, C.; Shao, H.; Liong, M.; Yoon, T. J.; Weissleder, R.; Lee, H. Mechanism of Magnetic Relaxation Switching Sensing. *ACS Nano* **2012**, *6*, 6821–6828.
- (339) Ilyas, S.; Ilyas, M.; van der Hoorn, R. A.; Mathur, S. Selective Conjugation of Proteins by Mining Active Proteomes through Click-Functionalized Magnetic Nanoparticles. *ACS Nano* **2013**, *7*, 9655–9663
- (340) Ranzoni, A.; Sabatte, G.; van Ijzendoorn, L. J.; Prins, M. W. One-Step Homogeneous Magnetic Nanoparticle Immunoassay for Biomarker Detection Directly in Blood Plasma. *ACS Nano* **2012**, *6*, 3134—3141.
- (341) Haun, J. B.; Yoon, T. J.; Lee, H.; Weissleder, R. Magnetic Nanoparticle Biosensors. *Wiley Interdiscip. Rev. Nanomed. Nanobiotechnol.* **2010**, 2, 291–304.
- (342) Shao, H.; Yoon, T. J.; Liong, M.; Weissleder, R.; Lee, H. Magnetic Nanoparticles for Biomedical NMR-Based Diagnostics. *Beilstein J. Nanotechnol.* **2010**, *1*, 142–154.
- (343) Shao, H.; Min, C.; Issadore, D.; Liong, M.; Yoon, T. J.; Weissleder, R.; Lee, H. Magnetic Nanoparticles and MicroNMR for Diagnostic Applications. *Theranostics* **2012**, *2*, 55–65.
- (344) Lee, H.; Yoon, T. J.; Weissleder, R. Ultrasensitive Detection of Bacteria Using Core-Shell Nanoparticles and an NMR-Filter System. *Angew. Chem., Int. Ed.* **2009**, *48*, 5657–5660.
- (345) Perez, J. M.; O'Loughin, T.; Simeone, F. J.; Weissleder, R.; Josephson, L. DNA-Based Magnetic Nanoparticle Assembly Acts as a Magnetic Relaxation Nanoswitch Allowing Screening of DNA-Cleaving Agents. J. Am. Chem. Soc. 2002, 124, 2856–2857.
- (346) Beyda, N. D.; Alam, M. J.; Garey, K. W. Comparison of the T2dx Instrument with T2Candida Assay and Automated Blood Culture in the Detection of Candida Species Using Seeded Blood Samples. *Diagn. Microbiol. Infect. Dis.* **2013**, *77*, 324–326.
- (347) Ling, Y.; Vassiliou, C. C.; Cima, M. J. Magnetic Relaxation-Based Platform for Multiplexed Assays. *Analyst* **2010**, *135*, 2360–2364.
- (348) Im, H.; Shao, H.; Park, Y. I.; Peterson, V. M.; Castro, C. M.; Weissleder, R.; Lee, H. Label-Free Detection and Molecular Profiling of Exosomes with a Nano-Plasmonic Sensor. *Nat. Biotechnol.* **2014**, *32*, 490–495.
- (349) Skewis, L. R.; Lebedeva, T.; Papkov, V.; Thayer, E. C.; Massefski, W.; Cuker, A.; Nagaswami, C.; Litvinov, R. I.; Kowalska, M. A.; Rauova, L.; Poncz, M.; Weisel, J. W.; Lowery, T. J.; Cines, D. B. T₂ Magnetic Resonance: A Diagnostic Platform for Studying Integrated Hemostasis in Whole Blood. *Clin. Chem.* **2014**, *60*, 1174–1182.
- (350) Dittmer, W. U.; Evers, T. H.; Hardeman, W. M.; Huijnen, W.; Kamps, R.; de Kievit, P.; Neijzen, J. H.; Nieuwenhuis, J. H.; Sijbers, M. J.; Dekkers, D. W.; Hefti, M. H.; Martens, M. F. Rapid, High Sensitivity, Point-of-Care Test for Cardiac Troponin Based on Optomagnetic Biosensor. *Clin. Chim. Acta* **2010**, *411*, 868–873.
- (351) Sun, E. Y.; Weissleder, R.; Josephson, L. Continuous Analyte Sensing with Magnetic Nanoswitches. *Small* **2006**, *2*, 1144–1147.

Acoustic Purification of Extracellular Microvesicles

Kyungheon Lee,† Huilin Shao,† Ralph Weissleder,†,‡ and Hakho Lee*,†

[†]Center for Systems Biology, Massachusetts General Hospital, 185 Cambridge Street, CPZN 5206, Boston, Massachusetts 02114, United States and [‡]Department of Systems Biology, Harvard Medical School, Boston, Massachusetts 02115, United States

ABSTRACT Microvesicles (MVs) are an increasingly important source for biomarker discovery and clinical diagnostics. The small size of MVs and their presence in complex biological environment, however, pose technical challenges in sample preparation, particularly when sample volumes are small. We herein present an acoustic nanofilter system that size-specifically separates MVs in a continuous and contact-free manner. The separation uses ultrasound standing waves to exert differential acoustic force on MVs according to their size and density. By optimizing the design of the ultrasound transducers and underlying electronics, we were able to achieve a high separation yield and resolution. The "filter size-cutoff" can be controlled electronically in situ, which



enables versatile MV-size selection. We applied the acoustic nanofilter to isolate nanoscale (<200 nm) vesicles from cell culture media as well as MVs in stored red blood cell products. With the capacity for rapid and contact-free MV isolation, the developed system could become a versatile preparatory tool for MV analyses.

KEYWORDS: nanotechnology · microvesicles · nanoparticle separation · microfluidics · acoustic wave

rith the growing recognition that microvesicles (MVs) can be harnessed for diagnostic purposes, 1,2 concomitantly increasing is the importance of separation technology to enrich these vesicles from biofluids. MVs are membranebound phospholipid vesicles ($\leq 1 \mu m$ in diameter) and are actively secreted by mammalian cells into the circulation. The vesicles carry molecular constituents of their originating cells,³⁻⁷ and are often viewed as partial surrogates of parental cells. Although MVs are abundant in the circulation (>10¹² vesicles in 1 mL of blood), isolating intact MVs is still a challenging task because of their small size and presence in complex media. Conventional batch processes (e.g., multiple filtration, ultracentrifugation) often require larger sample volumes, and entail time-consuming, extensive procedures,8 which can lead to sample loss, and potential structural or molecular changes.

Acoustics-based microfluidics is a simple and yet robust strategy for on-chip particle manipulation.^{9–15} The method generally uses ultrasound waves to exert radiation forces on particles; under the acoustic pressure, particles experience differential

forces according to their mechanical properties (size, density, compressibility). The operation is label-free and can be performed without any physical contact between the field sources and fluidics. These advantages render the technology biocompatible and ideally suited for integration with microfluidics. Many different types of acousto-microfluidic systems have been developed to manipulate micrometer-scale (>1 μ m) objects (e.g., mammalian cells, ^{16,17} droplets, ¹⁸ microspheres ¹⁹ and platelets ²⁰). Acoustic separation of submicrometer MVs, however, has yet to be demonstrated. A major difficulty in such implementation is the requirement for high radiation force, arising from the small size and low compressibility of MVs.

We herein report on an acoustic nanofilter system developed to separate MVs from other contents of biological samples. We hypothesized that acoustic forces could be used to fractionate MVs according to their size, thereby enabling size-selective MV isolation on chip. The device was optimized, specifically in the design of ultrasound transducers and its electronics, to exert maximal acoustic force on MVs. We further

Received for review November 17, 2014 and accepted February 11, 2015.

Published online 10.1021/nn506538f

© XXXX American Chemical Society

^{*} Address correspondence to hlee@mgh.harvard.edu.

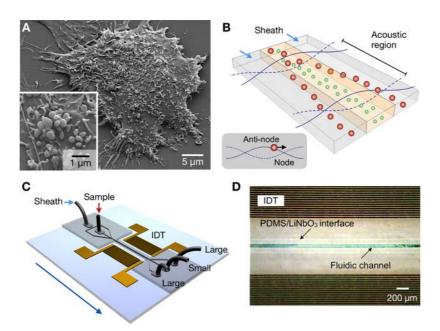


Figure 1. Acoustic nanofilter for label-separation of microvesicles (MVs). (A) Scanning electron microscopy image of MVs released by human brain tumor cells (GBM20/3). The size of MVs are typically <1 μ m. (B) Filter operation. MVs in the acoustic region are under the acoustic radiation pressure and transported to nodes of acoustic pressure region (inset). Larger MVs move faster as the acoustic force is proportional to the MV volume. Sheath flows, positioned at the node region, remove large MVs, whereas the center flow retains small MVs. (C) Device schematic. A pair of interdigitated transducer (IDT) electrodes are used to generate a standing surface acoustic wave across the flow direction. Large MVs are collected at the two side outlets, and small MV at the center outlet. (D) Micrographs of a prototype device. The IDT electrodes were patterned on a piezoelectric (LiNO₃) substrate. The fluidic channel was permanently bonded to the substrate.

constructed an analytical model to fine-tune the size cutoff as well as to estimate the separation yields. The developed system was applied to sort different types of extracellular MVs. We isolated exosomes (diameter <200 nm) from cell culture medium and erythrocyte-derived vesicles from stored blood units. The operation was fast and simple: MVs were collected inside a single microfluidic device in a label-free, continuous and size-tunable manner. The developed system could be a versatile preparatory tool for MV analyses to further extend the utility of acoustofluidics.

RESULTS

Acoustic Nanofilter. The acoustic nanofilter was designed to separate extracellular MVs ($\leq 1~\mu m$; Figure 1A) through in-flow size-fractionation. Figure 1B shows the operation principle. Particles in an acoustic field experience radiation forces and migrate toward the pressure nodes (Figure 1B, inset). The radiation force is proportional to the particle volume, ¹² whereas the viscous drag to the particle size. Larger particle thus move faster to the pressure nodes, and can be transferred into sheath streams to exit. The cutoff size (d_c) can be determined *in situ* through the control of acoustic power and flow speed. Because the filtering is performed in a continuous-flow manner, the risk of channel clogging is minimized.

The device schematic is illustrated in Figure 1C. A pair of interdigitated transducer (IDT) electrodes are

patterned, and used as an ultrasound source. The flow channel has two inlets for sample and sheath fluid, respectively, and is designed to focus the sample flow in the middle of the channel. The IDT electrodes generate a symmetric standing surface acoustic wave (SSAW) field across the channel direction, deflecting large particles toward the side outlets; small particles are collected at the center outlet.

We implemented a prototype device (Figure 1D) using LiNbO₃ piezoelectric wafer as a substrate. The IDT electrodes were patterned via standard lithography (see Materials and Methods for details). The fluidic structure, separately fabricated, was bonded to the SSAW chip (see Supporting Information (SI) Figure S1 for details on the device structure). We chose the acoustic wavelength $\lambda = 100 \ \mu m$ to accommodate a wide channel width (60 μ m) as well as to produce sufficient acoustic forces (>0.1 pN on 1- μ m MVs). The resulting signal frequency for SSAW generation was 38.5 MHz. We further matched the impedance between IDT electrodes and the signal source to maximize the energy transfer. The frequency response of the IDT electrodes was measured, and the equivalent circuit was generated (SI Figure S2). We then used the L-matching network topology to transform the device impedance to that of a signal generator (50 Ω).

Analytical Model. We set up an analytical model for the implemented acoustic nanofilter. The acoustic force (F_a) on a spherical particle (diameter, d) can be expressed as¹⁵

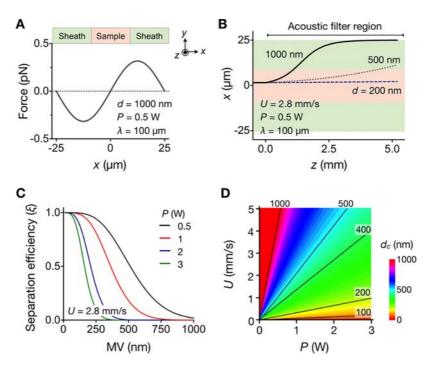


Figure 2. Analytical modeling of the implemented device. (A) Acoustic force (F_a) on MVs (diameter, d=1000 nm) was calculated across the flow direction. Note that F_a has its maximum magnitude inside the sheath flow region. (B) Trajectories of MVs with different diameters were simulated along the flow stream (z-direction). The time for MVs to reach the sheath flow is $\sim d^{-2}$, which can be exploited for size-selective MV sorting. (C) The separation efficiency (ξ) was obtained by estimating the fraction of MVs collected in the center outlet. Higher RF input power (P) leads to enrichment smaller MVs. (D) The filter size cutoff (d_c) was obtained by imposing $\xi < 0.1$. The cutoff values can be set by controlling the input RF power (P) and the flow speed (U). For a given (P, U) setting, MVs with $d < d_c$ will be collected in the center channel. Representative d_c contour lines are shown. This map was used to set the device parameters in the subsequent experiments.

$$F_a = \frac{\pi^2 p^2 d^3}{12\lambda} \cdot \beta_m \cdot \phi \cdot \sin\left(\frac{4\pi}{\lambda} y\right)$$

where p is the acoustic pressure, β_m is the compressibility of the medium, and x is the particle position across the fluidic channel (Figure 2A). The acoustic pressure is further determined from the device characteristics, $p=(PZ/A)^{1/2}$, where Z is the acoustic impedance of the substrate, A is the IDT area, and P is the power of the input signal. The mechanical properties of MVs are represented by the acoustic contrast factor $\phi=(5\rho_p-2\rho_m)/(2\rho_p+\rho_m)-(\beta_p/\beta_m)$, where ρ_p and β_p are the density and the compressibility of the particle, respectively, and ρ_m is the density of the media. Since $\phi>0$, MVs in aqueous buffer move to the pressure nodes where F_a has its extremum values. The wavelength λ is thus controlled to position the nodes in the sheath flow region (Figure 2A).

The motion of MVs in a viscous flow can be obtained by solving ${\bf F_a}+{\bf F_d}=0$ where ${\bf F_a}$ is the acoustic force and the ${\bf F_d}$ is the viscous drag (see Supporting Information for details). Figure 2B shows the simulated trajectory of MVs ($\rho_p=1130~{\rm kg/m^3}$, $\beta_p=3.5\times 10^{-10}~{\rm Pa^{-1}})^{21}$ with different sizes (d=200, 500, and 1000 nm) in an aqueous medium ($\rho_m=1000~{\rm kg/m^3}$, $\beta_m=5.1\times 10^{-10}~{\rm Pa^{-1}}$). Because the acoustic force is proportional to the particle volume and the drag force to the particle diameter, larger MVs move faster to the pressure nodes. Indeed, the transit time (t_0) of MVs

moving from the channel center to the sheath flow is $\sim 1/d^2$, which enables size-selective MV separation.

We further analyzed the separation efficiency (ξ) . As an initial input, we assumed a monodisperse MV population (diameter, d) entering the sample channel. We then calculated the MV fraction collected at the center outlet after the acoustic filtration (SI Figure S3). Figure 2C shows ξ with varying MV size. For a given flow rate (U) and the channel length (L), higher input power (P) leads to steeper rejection of large MVs. By determining the minimum d value for $\xi < 0.1$, we then estimated the size cutoff (d_c) of the device (Figure 2D and Supporting Information). Note that the cutoff can be readily adjusted in the optimal size ranges (100—1000 nm) for MV fractionation, by controlling the operation parameters (P and U).

System Evaluation. We validated the device performance using polystyrene beads. Samples were prepared by mixing two differently sized, fluorescent polystyrene beads (green, d=190 nm; red, d=1000 nm) in phosphate buffered saline (PBS) solution. Prior to sample injection, the fluidic channel was surface-treated (0.1% F127 in PBS) to prevent nonspecific binding of particles. We set the operation parameters (P=0.5 W, U=2.8 mm/s) to achieve $d_c=470$ nm; the acoustic contrast factor ϕ was 0.76, based on the density ($\rho_p=1050$ kg/m³) and the compressibility ($\beta_p=1.5\times10^{-10}$ Pa $^{-1}$) of polystyrene beads.

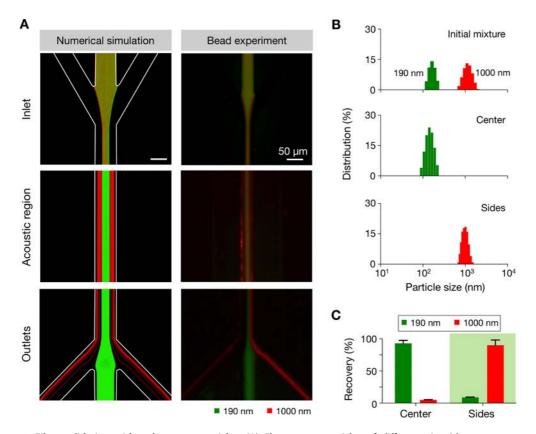


Figure 3. Filter validation with polystyrene particles. (A) Fluorescent particles of different size (d=190 nm, green; d=1000 nm, red) were mixed and processed by the acoustic nanofilter. Trajectories from the numerical simulation (left) and the experimental result (right) showed good agreement, with small and large particles respectively exiting to the center and the side outlets. (B) Particle size distribution measured by dynamic light scattering confirmed the size-selective enrichment of particles. (C) The recovery rate was estimated by comparing the fluorescence intensities of samples before and after the filtration. The observed recovery rate was >90% for both particles.

Fluorescence microscopy (Figure 3A, right) showed size-dependent separation of beads along the fluidic stream. Larger particles (red) migrated to the sheath streams and exited through the side outlets, whereas smaller particles (green) were collected at the center outlet (see SI Movie S1 for time-lapse images). The observed results agreed with those from hydrodynamic simulation (Figure 3A, left). The size distribution of particles, as measured by dynamic light scattering, further confirmed the device operation. We observed two distinct size groups in the initial mixture; these groups were correctly sorted in separate outlets after the acoustic nanofiltration (Figure 3B). The separation efficiency was determined from the fluorescence intensity of the collected particles and showed >90% for both small and large particles (Figure 3C). We further monitored the separation efficiency at different bead concentrations. Samples were prepared by spiking varying amounts of small beads (190 nm) into the suspension of large beads (1000 nm). The acoustic nanofilter maintained a consistent separation efficiency (>90%) with the dynamic range spanning 2 decades (SI Figure S4).

Exosome Purification. We next applied the acoustic nanofilter to enrich exosomes from other types of extracellular MVs. The size of exosomes is considered 1,22 < 200 nm. We thus tuned the device setting (P = 1.5 W,

U=1.5 mm/s) to set the size cutoff $d_c=300$ nm for exosome isolation, using the acoustic contrast factor $\phi=0.38$ for lipid vesicles ($\rho_p=1130$ kg/m³, $\beta_p=3.5\times 10^{-10}$ Pa $^{-1}$). For quantitative analyses, exosomes and larger MVs were prepared from cell culture media via filtration and ultracentrifugation (see Materials and Methods), and were independently labeled with green and red fluorescence, respectively. Known amounts of exosomes and larger MVs were then mixed and processed by the acoustic nanofilter.

Figure 4A shows the size distribution of samples measured by nanoparticle-tracking analysis (NTA) system. The initial mixture displayed two vesicle populations with their median diameter positioned at 149 and 410 nm, respectively. Following the acoustic filtration, the small and large particle populations were separated into the center and side outlets, respectively (see SI Figure S5 for electron micrographs). The recovery rates, estimated from fluorescence intensity measurements, were >80% for exosomes and >90% for larger MVs (Figure 4B). Western blotting (Figure 4C) and immunofluorescent microscopy (SI Figure S5b) further showed the enrichment of exosomes. Samples at the center outlet displayed high expression of exosomal markers, both extravesicular (CD63) and intravesicular (Flotillin-1, HSP70, HSP90), whereas the expression of

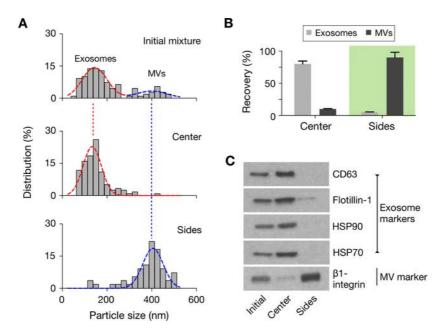


Figure 4. Exosome separation. (A) The acoustic nanofilter was used to separate exosomes (d < 200 nm) from other types of extracellular MVs. The size cutoff (d_c) was set to 300 nm by controlling P = 1.5 W and U = 1.5 mm/s (see Figure 2D). The size distribution of samples after the acoustic filtration was measured via nanoparticle tracking analysis (NTA), which showed the respective enrichment of small and large vesicles in the center and the side outlets. (B) The recovery rate was measured using a mixture of prestained exosomes and bigger MVs. (C) Western blotting further confirmed the enrichment of exosomes. Vesicles collected at the center outlet displayed high expression of exosome protein markers (CD63, Flotillin-1, HSP90, HSP70). MVs at the side outlets had high expression of β 1-integrin, a marker for larger membrane MVs.

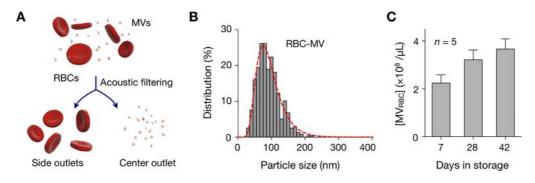


Figure 5. Monitoring of MVs in packed red blood cell (pRBC) units. (A) As a part of their aging process, red blood cells (RBCs) shed MVs. In stored pRBC units, MV numbers thus increase over time. The acoustic nanofilter was used to enrich RBC-derived MVs directly from pRBC samples. The size cutoff (d_c) was set to 450 nm. (B) The size distribution of collected MVs was analyzed by NTA. A single MV population with the mean d=90.9 nm was observed. (c) The concentration of RBC-derived MVs [MV_{RBC}] was serially monitored in pRBC units (n=5). The acoustic nanofilter was used to collect MVs from 10 μ L of pRBC samples. The average [MV_{RBC}] value increased with the storage time.

other vesicular marker (Integrin β 1) was low. The profile was reverse with MVs collected at the side outlets. The results also pointed to the vesicle integrity, demonstrating negligible acoustic damage from bubble cavitation.

MV Separation from Red Blood Cells. We further applied the acoustic filter to purify MVs in packed red blood cell (pRBC) units. As a part of their aging process, RBCs shed MVs (Figure 5A), effectively removing toxic, denatured hemoglobin and membrane proteins. In stored blood units, the number of these RBC-derived MVs increases over time.^{23–25} MV separation and counting thus can be applied in monitoring the quality of blood products. To separate MVs from RBCs, we set the size cutoff

 d_c = 450 nm (P = 1.5 W, U = 2.5 mm/s). pRBC samples were directly processed by the acoustic filter. RBC-MVs were enriched at the center outlet, whereas RBCs were streamed to the side outlets. The size of the collected RBC-MVs was <200 nm (Figure 5B), in agreement with previous reports. The performance of the acoustic filtration was as effective as that of a standard method (see Materials and Methods); the enriched MVs assumed a similar size distribution, and the separation yields were comparable (SI Figure S6). We also monitored the temporal changes of RBC-MV counts. Stored pRBCs units (n = 5) were sampled (10 μ L per sample per time point) and processed at different time points. RBC-MVs were collected by the acoustic nanofilter.

RBC-MV numbers, measured by NTA, indeed significantly increased over time (p < 0.03, ANOVA), thereby confirming their potential as a metric of blood aging.

CONCLUSION

We have developed an acoustic-based microfluidic system for label-free and continuous filtration of MVs. We identified two key parameters which are important in assuring efficient manipulation: (i) high ultrasound frequency and (ii) efficient energy transfer to the sound transducer. We met these requirements by optimizing the transducer geometry (IDT electrodes) and by utilizing the impedance matching network. The resulting system achieved >90% separation yields, and allowed for *in situ* control of size cutoff. Analytical and numerical analyses validated experimental observations, and guided the setting of device parameters for specific MV targets.

The developed system could be a potential preparatory tool for MV analyses. Compared to conventional isolation methods (e.g., ultracentrifugation, membrane

filtration), acoustic filtering is fast, gentle on vesicles, and compatible with limited sample volumes. It also provides an easy approach to change the size-cutoff. In this study, we performed a binary separation (exosomes *vs* larger vesicles; microvesicles *vs* red blood cells). By cascading the separation regions with different size-cutoffs, it would be possible to differentiate multiple types of vesicles according to their size profile (*e.g.*, exosomes, oncosomes, apoptotic bodies). ^{21,26–28}

Several aspects of the system could be further developed to expand its functionality. First, different transducer designs, such as slanted-fingers²⁹ and tilted-angle electrodes,³⁰ could be investigated to better control the acoustic force and improve the sample throughput. Second, integrating analytical components (*e.g.*, sensors, polymerase chain reaction) into the same platform would be another promising approach to realize a portable lab-on-chip for MV analyses. Such advances will facilitate both clinical applications and biological studies of MVs, as well as extend the utility of acoustic microfluidics toward the nanoscale regime.

MATERIALS AND METHODS

Device Fabrication. The acoustic nanofilter consisted of two parts: a standing-surface-acoustic-wave (SSAW) chip and a microfluidic channel. The SSAW chip was fabricated on a piezoelectric substrate. A LiNbO3 wafer with XY 128° cut was purchased (University Wafer). Interdigitated transducer (IDT) electrodes were patterned via conventional optical lithography, and metal layers (Ti, 50 Å; Au, 800 Å) were deposited. The patterned wafer was then cut into a desired size (21 mm imes21 mm) with a dicing saw. The microfluidic structure was fabricated in polydimethylsiloxane (PDMS; Dow Corning) via soft-lithography technique. The channel mold was formed on a Si wafer, using an epoxy-based photoresists (SU-8 2050, Microchem). The cross-section of the channel was 60 μ m \times 80 μ m (width \times height). Both the SSAW chip and the microfluidic block were treated with oxygen plasma, aligned and irreversibly bonded. We used ethanol as a temporary lubricant during the alignment. To strengthen the bonding, the assembly was cured on a hot plate (80 °C) for overnight.

System Setup. As a RF source, a signal generator (Agilent, N5158a) and power amplifiers (Mini circuits, TB-45) were used. The device operation was monitored by an inverted fluorescence microscope (Ti-E, Nikon). Images were recorded by a scientific-CMOS camera (Zyla 5.5, Andor) and analyzed by Image-J software.

Separation Assay with Polystyrene Particles. Fluorescent polystyrene particles with diameters of 190 nm (Dragon Green, Bangs laboratory) and 1000 nm (Flashred, Bangs laboratory) were used. Varying concentration of both particles were mixed in phosphate buffered saline (PBS) solution. Aliquots (50 μL) of the particle mixture were then processed by the acoustic nanofilter. The size distribution of particles at the sample inlet and outlets were measured by dynamic light scattering (Zetasizer Nano ZS, Malvern Instruments). To estimate the separation yields, the fluorescence intensities of the original and the separated samples were measured at the emission wavelength of 513 and 680 nm (Varian Cary Eclipse, Agilent).

Exosome Separation. Microvesicles (MVs) were isolated from cell culture. Human ovarian carcinoma cells (OvCA429, ATCC) were cultured in RPMI-1640 medium (Cellgro) supplemented with fetal bovine serum (FBS, Cellgro, 10%), penicillin and streptomycin (Cellgro, 1%), and L-glutamine (1%). Cells were cultured at 37 °C in a humidified atmosphere containing 5% CO₂.

Cells at passages 1-15 were cultured in vesicle-depleted medium (with 5% depleted FBS) for 48 h. At their 70% confluence, conditioned culture medium was collected from $\sim 10^7$ cells and differentially centrifuged to isolated larger MVs as previously described.⁷ In brief, the medium was filtered through a membrane filter (0.8 μ m pore, Millipore) and centrifuged (10000g, 90 min). The pellet was retrieved as a large MV fraction.³¹ Remaining supernatant was filtered through a 0.22-µm membrane filter (Millipore) and concentrated by differential centrifugation (100000q, 90 min) to isolate exosomes. Vesicle size was independently confirmed by the nanoparticle tracking analysis (NTA; LM10, NanoSight). Exosomes and larger MVs were labeled respectively with green and red fluorescent cell membrane dyes (PKH67 and PKH26, Sigma-Aldrich) before being mixed for sorting. The mixture (50 μ L) was processed by the acoustic nanofilter. The sorted populations were analyzed for their size distribution and fluorescence intensity as described above.

Western Blotting. Isolated MVs were lysed in radio-immuno-precipitation assay buffer and supplemented with protease inhibitors (RIPA buffer, Thermo Scientific). MV samples were collected from the outlets of the microfluidic device and stored at $-20\,^{\circ}\mathrm{C}$ before analysis. Protein concentration was quantified using the bicinchoninic acid assay (BCA assay kit, Thermo Scientific). Protein lysates were loaded and resolved by sodium dodecyl sulfate polyacrylamide gel electrophoresis (SDS-PAGE) and transferred to PVDF membrane (Life Technologies). The PVDF membrane was then incubated overnight with antibodies against CD63 (Santa Cruz), Flotillin-1 (BD Biosciences), HSP90 (Cell Signaling), HSP70 (Cell Signaling) and β 1-integrin (Cell Signaling). Following incubation with secondary antibody (Cell Signaling), enhanced chemiluminescence was used for detection.

MV Isolation from Stored Red Blood Cell (RBC) Units. Packed RBC (pRBC) units were obtained from the Massachusetts General Hospital (MGH) Blood Bank (Boston, MA). The units were preserved in Adsol solution, and stored at 4 °C. For serial MV monitoring, a 10-µL sample was drawn from each pRBC unit using a sterile coupler and 25G needle, after 7, 28, and 42 days of storage. All samples were used directly for sorting with the acoustic nanofilter. The standard MV samples were prepared *via* differential centrifugation steps (400g 20 min, 10000g, 3 min) followed by membrane filtration (0.22 µm pore). The size distribution and concentration of MVs were measured by NTA.

Conflict of Interest: The authors declare no competing financial interest.

Acknowledgment. The authors thank X. O. Breakefield (Massachusetts General Hospital) for access to and assistance with the NTA. The acoustic device was fabricated using the facilities at the Center for Nanoscale Systems (CNS) at Harvard University (National Science Foundation award ECS-0335765). This work was supported in parts by NIH Grants R01 HL113156 (H.L.), P01 CA069246 (R.W.), U54 CA151884 (R.W.), and DoD OCRP Award W81XWH-14-1-0279 (H.L.). This research was also partially supported by Basic Science Research Program through the National Research Foundation of Korea (NRF) funded by the Ministry of Education 2012R1A6A3A03040166 (K.L.)

Supporting Information Available: Design of the microfluidic system; impedance matching; MV distribution in the system; scanning electron micrographs of MV samples; separation efficiency measurement of exosome and MVs from pRBCs; supporting notes for analytical equations and movie. This material is available free of charge via the Internet at http://pubs.acs.org.

REFERENCES AND NOTES

- Thery, C.; Ostrowski, M.; Segura, E. Membrane Vesicles as Conveyors of Immune Responses. *Nat. Rev. Immunol.* 2009, 9, 581–593.
- Simpson, R. J.; Lim, J. W.; Moritz, R. L.; Mathivanan, S. Exosomes: Proteomic Insights and Diagnostic Potential. Expert Rev. Proteomics 2009, 6, 267–283.
- Graner, M. W.; Alzate, O.; Dechkovskaia, A. M.; Keene, J. D.; Sampson, J. H.; Mitchell, D. A.; Bigner, D. D. Proteomic and Immunologic Analyses of Brain Tumor Exosomes. FASEB J. 2009, 23, 1541–1557.
- Skog, J.; et al. Glioblastoma Microvesicles Transport RNA and Proteins That Promote Tumour Growth and Provide Diagnostic Biomarkers. Nat. Cell Biol. 2008, 10, 1470–1476.
- Balaj, L.; Lessard, R.; Dai, L.; Cho, Y. J.; Pomeroy, S. L.; Breakefield, X. O.; Skog, J. Tumour Microvesicles Contain Retrotransposon Elements and Amplified Oncogene Sequences. Nat. Commun. 2011, 2, 180.
- Valadi, H.; Ekstrom, K.; Bossios, A.; Sjostrand, M.; Lee, J. J.; Lotvall, J. O. Exosome-Mediated Transfer of Mrnas and Micrornas is a Novel Mechanism of Genetic Exchange Between Cells. Nat. Cell Biol. 2007, 9, 654–659.
- Shao, H.; Chung, J.; Balaj, L.; Charest, A.; Bigner, D. D.; Carter, B. S.; Hochberg, F. H.; Breakefield, X. O.; Weissleder, R.; Lee, H. Protein Typing of Circulating Microvesicles Allows Real-Time Monitoring of Glioblastoma Therapy. *Nat. Med.* 2012, 18, 1835–1840.
- Thery, C.; Amigorena, S.; Raposo, G.; Clayton, A. Isolation and Characterization of Exosomes from Cell Culture Supernatants and Biological Fluids. *Current Protocols in Cell Biology*; Wiley: New York, 2006; Chapter 3, No. Unit 3.22.
- Bruus, H.; Dual, J.; Hawkes, J.; Hill, M.; Laurell, T.; Nilsson, J.; Radel, S.; Sadhal, S.; Wiklund, M. Forthcoming Lab on a Chip Tutorial Series on Acoustofluidics: Acoustofluidics-Exploiting Ultrasonic Standing Wave Forces and Acoustic Streaming in Microfluidic Systems for Cell and Particle Manipulation. Lab Chip 2011, 11, 3579–3580.
- Yeo, L. Y.; Friend, J. R. Surface Acoustic Wave Microfluidics. Annu. Rev. Fluid Mech. 2014, 46, 379–406.
- Shi, J.; Ahmed, D.; Mao, X.; Lin, S. C.; Lawit, A.; Huang, T. J. Acoustic Tweezers: Patterning Cells and Microparticles Using Standing Surface Acoustic Waves (SSAW). *Lab Chip* 2009, 9, 2890–2895.
- Bruus, H. Acoustofluidics 7: The Acoustic Radiation Force on Small Particles. Lab Chip 2012, 12, 1014–1021.
- Lenshof, A.; Magnusson, C.; Laurell, T. Acoustofluidics 8: Applications of Acoustophoresis in Continuous Flow Microsystems. *Lab Chip* 2012, 12, 1210–1223.
- Lenshof, A.; Laurell, T. Continuous Separation of Cells and Particles in Microfluidic Systems. Chem. Soc. Rev. 2010, 39, 1203–1217.

- Shi, J.; Huang, H.; Stratton, Z.; Huang, Y.; Huang, T. J. Continuous Particle Separation in a Microfluidic Channel via Standing Surface Acoustic Waves (Ssaw). Lab Chip 2009, 9, 3354–3359.
- Ding, X.; et al. Standing Surface Acoustic Wave (Ssaw) Based Multichannel Cell Sorting. Lab Chip 2012, 12, 4228– 4231.
- Franke, T.; Braunmuller, S.; Schmid, L.; Wixforth, A.; Weitz,
 D. A. Surface Acoustic Wave Actuated Cell Sorting (SAWACS). Lab Chip 2010, 10, 789–794.
- Franke, T.; Abate, A. R.; Weitz, D. A.; Wixforth, A. Surface Acoustic Wave (SAW) Directed Droplet Flow in Microfluidics for PDMS Devices. *Lab Chip* 2009, 9, 2625–2627.
- Destgeer, G.; Lee, K. H.; Jung, J. H.; Alazzam, A.; Sung, H. J. Continuous Separation of Particles in a PDMS Microfluidic Channel via Travelling Surface Acoustic Waves (TSAW). Lab Chip 2013, 13, 4210–4216.
- Nam, J.; Lim, H.; Kim, D.; Shin, S. Separation of Platelets From Whole Blood Using Standing Surface Acoustic Waves in a Microchannel. Lab Chip 2011, 11, 3361–3364.
- Vader, P.; Breakefield, X. O.; Wood, M. J. Extracellular Vesicles: Emerging Targets for Cancer Therapy. *Trends Mol. Med.* 2014, 20, 385–393.
- Thery, C.; Zitvogel, L.; Amigorena, S. Exosomes: Composition, Biogenesis and Function. *Nat. Rev. Immunol.* 2002, 2, 569–579.
- Tissot, J. D.; Rubin, O.; Canellini, G. Analysis and Clinical Relevance of Microparticles from Red Blood Cells. Curr. Opin. Hematol. 2010, 17, 571–577.
- Rubin, O.; Crettaz, D.; Canellini, G.; Tissot, J. D.; Lion, N. Microparticles in Stored Red Blood Cells: An Approach Using Flow Cytometry and Proteomic Tools. Vox Sang 2008. 95, 288–297.
- Rho, J.; Chung, J.; Im, H.; Liong, M.; Shao, H.; Castro, C. M.; Weissleder, R.; Lee, H. Magnetic Nanosensor for Detection and Profiling of Erythrocyte-Derived Microvesicles. ACS Nano 2013. 7, 11227–11233.
- EL Andaloussi, S.; Mager, I.; Breakefield, X. O.; Wood, M. J. Extracellular Vesicles: Biology and Emerging Therapeutic Opportunities. Nat. Rev. Drug Discovery 2013, 12, 347–357.
- 27. Di Vizio, D.; et al. Large Oncosomes in Human Prostate Cancer Tissues and in the Circulation of Mice with Metastatic Disease. Am. J. Pathol. 2012, 181, 1573–1584.
- Morello, M.; et al. Large Oncosomes Mediate Intercellular Transfer of Functional Microrna. Cell Cycle 2013, 12, 3526– 3536.
- Bourquin, Y.; Syed, A.; Reboud, J.; Ranford-Cartwright, L. C.; Barrett, M. P.; Cooper, J. M. Rare-Cell Enrichment By a Rapid, Label-Free, Ultrasonic Isopycnic Technique for Medical Diagnostics. *Angew. Chem., Int. Ed. Engl.* 2014, 53. 5587–5590.
- Ding, X.; et al. Cell Separation Using Tilted-Angle Standing Surface Acoustic Waves. Proc. Natl. Acad. Sci. U. S. A. 2014, 12992–12997.
- Witwer, K. W.; et al. Standardization of Sample Collection, Isolation and Analysis Methods in Extracellular Vesicle Research. J. Extracell. Vesicles 2013, 2, 20360.



Digital diffraction analysis enables low-cost molecular diagnostics on a smartphone

Hyungsoon Im^{a,b,1}, Cesar M. Castro^{a,c,1}, Huilin Shao^a, Monty Liong^{a,2}, Jun Song^{a,d}, Divya Pathania^{a,b}, Lioubov Fexon^a, Changwook Min^a, Maria Avila-Wallace^e, Omar Zurkiya^{a,b}, Junsung Rho^a, Brady Magaoay^a, Rosemary H. Tambouret^f, Misha Pivovarov^{a,b}, Ralph Weissleder^{a,b,g,3}, and Hakho Lee^{a,b,3}

^aCenter for Systems Biology, Massachusetts General Hospital, Boston, MA 02114; ^bDepartment of Radiology, Massachusetts General Hospital, Boston, MA 02114; Massachusetts General Hospital Cancer Center, Harvard Medical School, Boston, MA 02114; School of Engineering and Applied Sciences, Harvard University, Cambridge, MA 02138; ^eDepartment of Obstetrics and Gynecology, Massachusetts General Hospital, Boston, MA 02114; ^fDepartment of Pathology, Massachusetts General Hospital, Boston, MA 02114; and ⁹Department of Systems Biology, Harvard Medical School, Boston, MA 02115

Edited by Stephen R. Quake, Stanford University, Stanford, CA, and approved March 18, 2015 (received for review January 29, 2015)

The widespread distribution of smartphones, with their integrated sensors and communication capabilities, makes them an ideal platform for point-of-care (POC) diagnosis, especially in resourcelimited settings. Molecular diagnostics, however, have been difficult to implement in smartphones. We herein report a diffractionbased approach that enables molecular and cellular diagnostics. The D3 (digital diffraction diagnosis) system uses microbeads to generate unique diffraction patterns which can be acquired by smartphones and processed by a remote server. We applied the D3 platform to screen for precancerous or cancerous cells in cervical specimens and to detect human papillomavirus (HPV) DNA. The D3 assay generated readouts within 45 min and showed excellent agreement with gold-standard pathology or HPV testing, respectively. This approach could have favorable global health applications where medical access is limited or when pathology bottlenecks challenge prompt diagnostic readouts.

cancer diagnostics | smartphone | molecular sensing | point-of-care diagnostics | cervical cancer

he rapid dissemination of electronic communication devices such as smartphones, tablets, and wearable electronics, all with integrated sensors, creates new possibilities for inexpensive point-of-care (POC) diagnostics and care delivery. One example is detecting cancer in low- and middle-income countries where limited resources and geographical constraints often lead to missed opportunities for intervention, resulting in mortalities even with treatable cancers (1). Current efforts to control cancer thus focus on implementing population-based early screening programs; a key element for success is a cost-effective, robust diagnostic platform that can be readily deployed into POC settings (2). Whereas conventional microscopy of human samples (smears, aspirates, biopsies, blood) is the most widely used to diagnose cancer, its POC adaptation is limited by inherent drawbacks such as bulky optics, requirements for trained microscopists, and operatordependent variability.

Recent advances in digital sensors and computational approaches have introduced new microscopy techniques. Digital holography, in particular, has emerged as one alternative to conventional bright-field microscopy. Following the initial description of lens-free holography by Kreuzer's group (3), various diffractionbased imaging systems have been developed (4–8). The majority of recent work, however, is based on identifying targets by their inherent morphology (e.g., blood cells, bacteria, Caenorhabditis elegans) (4, 9–14). We reasoned that it would be possible to impart molecular specificity to improve disease detection and phenotyping akin to other molecular profiling strategies (15, 16).

Here we describe a digital diffraction diagnostics (D3)—a computational analysis of distinct diffraction patterns generated by microbeads that bind to biological target of interest. The strategy can detect a broad range of targets (SI Appendix, Table S1): soluble proteins, nucleic acids, or cellular proteins. To provide effective

POC operation at remote sites, we adopted a client-server model: the data acquired by a smartphone were digitally processed by a remote parallel-computing server. We tested the approach by exploring cancer cell profiling with immunomicrobeads. Diffraction patterns generated by microbeads were detected with a smartphone camera in a bright-field setting, and digital processing reconstructed the images of bead-bound cells to retrieve molecular information. The assay protocol enabled molecular analyses on $>10^4$ individual cells in a single still image, with the entire assav complete in 45 min. As an initial proof-of-principle in human clinical samples, we used D3 to screen for cervical cancer, the third most prevalent cancer in women worldwide, with 80% of cases occurring in resource-limited countries (16). Cellular analyses using the D3 assay reliably identified patients at high clinical risk for malignancy. To show its versatility, we further extended the D3 assay to other disease targets, including human papillomavirus (HPV) DNA and lymphoma cell detection in fine-needle aspirates.

Results

D3 Platform. The D3 assay for cell detection is illustrated in Fig. 1.4. Specimens are obtained from minimally invasive procedures (e.g., smears, brushings, fine-needle aspiration, blood draw), and

Significance

Smartphones and wearable electronics have advanced tremendously over the last several years but fall short of allowing their use for molecular diagnostics. We herein report a generic approach to enable molecular diagnostics on smartphones. The method utilizes molecular-specific microbeads to generate unique diffraction patterns of "blurry beads" which can be recorded and deconvoluted by digital processing. We applied the system to resolve individual precancerous and cancerous cells as well as to detect cancer-associated DNA targets. Because the system is compact, easy to operate, and readily integrated with the standard, portable smartphone, this approach could enable medical diagnostics in geographically and/or socioeconomically limited settings with pathology bottlenecks.

Author contributions: R.W. and H.L. oversaw all research studies; H.I., C.M.C., R.W., and H.L. designed individual projects; C.M.C., M.A.-W., O.Z., and R.W. designed clinical studies and obtained samples; H.I., H.S., J.S., D.P., C.M., O.Z., J.R., and B.M. performed research; C.M.C., H.S., M.L., D.P., and J.R. contributed new reagents/analytic tools; H.I., C.M.C., H.S., M.L., J.S., D.P., L.F., C.M., M.A.-W., O.Z., J.R., B.M., R.H.T., M.P., R.W., and H.L. analyzed data; and H.I., C.M.C., R.W., and H.L. wrote the paper

The authors declare no conflict of interest.

This article is a PNAS Direct Submission.

¹H.I. and C.M.C. contributed equally to this work.

²Present address: Cardno ChemRisk, San Francisco, CA 94105.

³To whom correspondence may be addressed. Email: rweissleder@mgh.harvard.edu or hlee@mgh.harvard.edu.

This article contains supporting information online at www.pnas.org/lookup/suppl/doi:10. 1073/pnas.1501815112/-/DCSupplemental

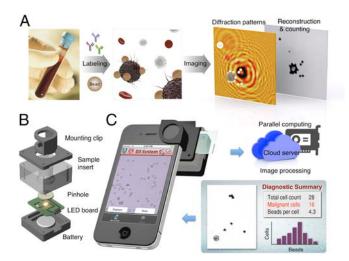


Fig. 1. D3 platform. (A) Assay schematic for cellular detection. Target cells in patient samples (e.g., blood or biopsy) are immunolabeled with microbeads, and their diffraction patterns are recorded. The diffraction images are then digitally reconstructed into object images wherein bead-labeled target cells are identified. For the detection of other types of targets, see SI Appendix, Table S1. (B) The snap-on module for a smartphone consists of an LED powered by a coin battery, a pinhole for uniform illumination with partial coherence, and a sample mount. (C) The D3-mounted smartphone's embedded phone camera is used to record the diffraction images of the specimen. The recorded images are transferred to a server via the cloud service for real-time image reconstruction and analyses, which can be returned to the smartphone in less than 2 min.

cells are labeled with molecular-specific microbeads. Labeled samples are placed directly on the imaging device. Interference patterns between scattered light from the specimen and the reference light are recorded (17, 18). Digital signal processing then recovers and analyzes object images. Because individual cells are spatially resolved and only target-cell-associated beads are counted, there is no need for washing steps, leading to simplified assays. Selective microbead binding is critical to distinguishing target cells from other host cells and quantitatively profiling protein markers in individual cells.

To perform the D3 assay in POC settings, we implemented a portable sensing terminal that uses the embedded optics and communication functions of a smartphone (Fig. 1B). We constructed a snap-on module, containing both a light source and sample insert, to mount over the phone camera (SI Appendix, Fig. S1). The acquired diffraction patterns were transferred to a dedicated server for postprocessing (SI Appendix, Fig. S2). Following this step, the analytical readouts (e.g., target cell counts, bead counts per cell) and reconstructed images were sent back to the smartphone for display. This scheme frees the sensing terminals from heavy computation load, thereby making their implementation simple and cost-effective. All data were communicated through a secure cloud service, and we programmed a user-friendly interface to streamline the process (SI Appendix, Movie S1). The system had a wide field-of-view (FOV), whereas microscopic resolution could be achieved through numerical reconstruction. The FOV and the spatial resolution for iPhone 4S were 14 mm² and 2 μm, respectively. Alternatively, a miniaturized imager connected to a local computer can be used (e.g., MT9P031, Aptina Imaging Inc.; SI Appendix, Fig. S3), which had an FOV and spatial resolution of 24 mm² and 2 µm, respectively.

D3 Processing. To accurately detect bead-bound target cells, we formulated a processing algorithm for image reconstruction and postanalysis (Fig. 2A). The reconstruction was based on the Rayleigh–Sommerfeld diffraction principle but was extended to digitally retrieve both transmittance and phase shift of objects

through an iterative optimization (19–21). In each iteration, the routine applied physical constraints (i.e., light transmittance and object supports) to a reconstructed object image and updated the corresponding diffraction patterns with retrieved phase information (see *Materials and Methods* for details). The method provided high phase contrast between cells and microbeads (Fig. 2B). Each type could be easily distinguished, even when the size was similar (*SI Appendix*, Fig. S4).

Following reconstruction, images were processed by the detection routine. The algorithm generated transmittance and phase-correlation maps by scanning a microbead reference image over the reconstructed images (*SI Appendix*, Fig. S5). Cells and microbeads could be differentiated from the transmittance and phase correlations, respectively. Subsequently, cells labeled with microbeads were automatically identified, and their individual bead counts were recorded.

To accelerate imaging analyses, we used a server equipped with a graphics processing unit (GPU). The code executed massively parallel image processing threads (>5,000) using its multicore processors, which permitted near-instantaneous image reconstruction and postanalyses (SI Appendix, Table S2). For instance, using a 448-core GPU (Tesla C-2070), a 16-bit 1024×1024 diffraction pattern could be analyzed within 90 ms, ~3,000-fold faster than relying on a conventional central processing unit (4 cores 2.4 GHz; Fig. 2C).

We adopted an encrypted cloud storage for data transfer. The scheme provides a buffer for asynchronous communication between smartphones and the server, and is readily scalable to global networks. To minimize data transfer time, especially from

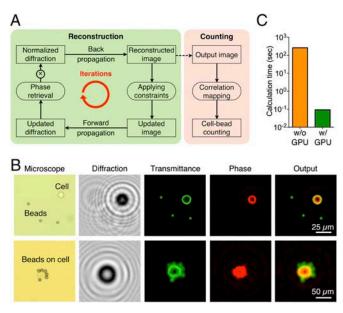


Fig. 2. Real-time reconstruction and counting process. (*A*) Diagram of reconstruction and counting algorithm. A diffraction image, normalized by a reference image obtained in the absence of specimens, is reconstructed through an iterative process. Following the image reconstruction, cells and beads are detected using a counting algorithm, which scanned a reference image of a microbead over the reconstructed image. (*B*) Examples of the image reconstruction. Raw diffraction patterns of cancer cells and 7-μm microbeads show undecipherable patterns. The reconstruction algorithm recovers both transmittance and phase information. Cells and microbeads can be differentiated from their high phase contrast. The bead-bound cells are automatically identified, and the bead numbers are counted. The transmittance (green) and phase contrast (red) images are pseudocolored to better visualize optical properties of cells and beads. (*C*) Computational time for image reconstruction and cell/bead counting (1-MB pixel image) with and without GPU-implemented systems.

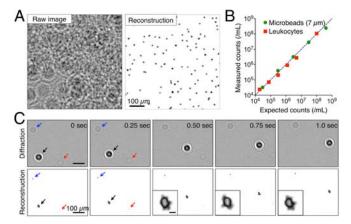


Fig. 3. High-throughput cell and bead identification. (*A*) Diffraction and reconstructed images of 7-μm microbeads at a concentration of 5×10^7 beads per mL. More than 10^5 objects can be detected at microscopic resolution from a single image (also see *SI Appendix*, Fig. S7). (*B*) Comparison between the D3-counted microbeads and leukocytes and their expected counts. Note the linearity ($R^2 > 0.97$) even at very high bead or cell concentrations (4×10^8 beads per mL and 1×10^8 cells per mL). (*C*) Temporal image reconstruction of cells in flow. Diffraction images were recorded at 4 frames per s and reconstructed in real time by the D3 server. A bead-labeled cancer cell (black arrow), a nontargeted cell (red), and a free-floating microbead (blue) are automatically identified. (*Inset*) High-resolution details of the bead-labeled cell undergoing rotational motion in the flow stream.

smartphones to a cloud storage, we converted original uncompressed color images (24 MB) into lossless gray-scale images (2.9 MB, Portable Network Graphics/PNG format). When microbeads with the diameter of >5 µm were used, the file could be further compressed (0.4 MB, Joint Photographic Experts Group/JPEG format) without affecting bead counts (*SI Appendix*, Fig. S6). These final images can be transferred to the cloud storage within 3 min, even through legacy 2G cellular network (transfer speed, 20 kbps).

High-Throughput D3 Assay for Cell Detection. With its large FOV (14 mm² for iPhone 4S and 24 mm² for the image sensor) and rapid image processing, the D3 platform enabled high-throughput cellular analyses. In a single image acquisition, more than 100,000 individual objects can be detected at microscopic resolution (Fig. 3A and SI Appendix, Fig. S7). The dynamic range of detection spanned over 4 orders of magnitude (Fig. 3B), with the object concentration reaching up to $\sim 10^8$ microbeads or cells per milliliter of sample (SI Appendix, Figs. S7–S9). The capacity for high-density imaging, combined with the recognition of beadbound cells, made it possible to detect target cells in the presence of abundant host cells (e.g., leukocytes) and unbound microbeads. Importantly, this eliminated the need for external washing and purification steps. The assay throughput could be further increased by flowing target cells through a microfluidic channel and imaging in real-time (FOV, $2.5 \times 2.5 \text{ mm}^2$; 10 frames per s) (Fig. 3C and SI Appendix, Fig. S10 and Movie S2). This is akin to a flow cytometer with imaging capabilities for quantitative analysis (22), but in a miniaturized system.

Quantitative Profiling. We next applied the D3 assay to cell profiling (Fig. 4*A*). Human cancer cell lines were immunolabeled with microbeads to generate specific diffraction signatures. Whereas it is possible to use antibody-coated microbeads directly on cells, we found that a two-step approach increased bead binding (23). We thus opted for highly efficient bioorthogonal [e.g., between transcyclooctene and tetrazine (24)] or streptavidin/biotin approaches. For example, using the latter, cells were first targeted by biotinylated antibodies and subsequently incubated with

streptavidin-coated microbeads. We further tested commercially available microbeads in different sizes (diameter 3–22 μ m). A bead diameter between 5 and 7 μ m was found to optimize accurate bead counting while minimizing cell clustering (*SI Appendix*, Fig. S11).

To validate D3-based cellular profiling, we measured the expression of three protein markers, human epidermal growth factor receptor 2 (HER2)/neu, epithelial cell adhesion molecule (EpCAM), and epidermal growth factor receptor (EGFR), on human cells (SkBr3, human breast carcinoma). Samples were immunolabeled with 7-µm microbeads and analyzed using the D3 system (Fig. 4A and SI Appendix, Fig. S12). The average bead count per cell was highest for HER2/neu targeting (8.0 beads per cell), followed by EpCAM (3.9 beads per cell) and EGFR (0.5 beads per cell); these results were consistent with immunofluorescence microscopy. Unlike microscopy, however, the D3 assay enabled simultaneous analyses of far greater numbers of cells (>10,000 cells) because of its wide FOV. The cellular bead counts generated with automated D3 analyses were statistically identical with those from manual microscopy enumeration (P = 0.43; paired t test; Fig. 4B and SI Appendix, Fig. S13). Further comparison with flow cytometry validated D3 assay's analytically capacity (Fig. 4C). The number of beads per cell correlated linearly with levels of marker expression ($R^2 = 0.99$). Similar D3 profiling on a different cell line (A431, human epidermoid carcinoma) also matched well with immunofluorescence microscopy and flow cytometry results (SI Appendix, Fig. S14).

Whereas the above examples used parallel profiling of separate images, it is also possible to perform multiplexing within the same sample using microbeads of different optical signatures. For instance, we tested three bead sizes and three different materials (e.g., polystyrene, silica, silica coated with silver) that can be effectively distinguished through nominal size and transmittance, respectively. Combining these sets could provide nine-channel multiplexing (*SI Appendix*, Fig. S15).

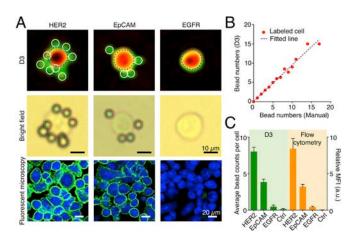


Fig. 4. Detecting cancer cell markers with immunobead labeling. (A) Cancer cells (SkBr3, human breast carcinoma) were immunobead-labeled for HER2, EpCAM, and EGFR. ($Top\ Row$) Representative reconstructed images in pseudocolor (green, transmittance; red, phase). (Middle Row) Corresponding bright-field micrographs. ($Bottom\ Row$) Cells labeled with fluorescent antibodies for comparison. HER2, human epidermal growth factor receptor 2; EpCAM, epithelial cell adhesion molecule; EGFR, epidermal growth factor receptor. (B) The bead numbers on labeled cells, determined automatically by D3, were in good agreement ($R^2=0.97$) with those counted manually from microscope images. (C) The average bead count per cell correlated with the expression level of a target marker as determined by flow cytometry ($R^2=0.99$). MFI, mean fluorescence intensity. a.u., arbitrary unit.

Im et al. PNAS Early Edition | 3 of 6

Clinical Applications of D3. We evaluated the clinical utility of D3 by first focusing on cervical cancer surveillance. Cervical cancer maintains high incidence rates in resource-poor countries (16) where the availability of objective early screening systems is limited. We reasoned that the portable D3 system could be used as a first-line diagnostic tool without subjective readouts to promptly triage suspicious or high-risk cases. The strategy could potentially offset pathology bottlenecks and reduce repeated patient visits to central clinics, which are often complicated by geographical and/or socioeconomic constraints (25, 26).

We obtained cervical specimens through brushing, loop electrosurgical excision procedure (LEEP), or biopsies during colposcopic evaluation. Twenty-five patients with previously abnormal Pap smear results were recruited. Cellular samples were labeled with a mixture of tagged antibodies against EpCAM, CD44, or tumor-associated calcium signal transducer2 (TACD2/Trop2). These cancer markers were chosen for their elevated expression in cervical cancer as described in literature (27-29). We counted the total number of bead-bound cells as well as the number of microbeads per cell. Blinded to D3 results, patient specimens were separately examined through conventional pathology, and classified into three risk classes: "high risk," "low risk," or "benign" (Fig. 5A) The D3 analyses showed that bead counts among targeted cells increased along the clinical risk (Fig. 5B). The mean bead counts (n_{bead}) per targeted cell were significantly different among the clinical risk classifications (P < 0.05, Tukey multiple comparison test), indicating that n_{bead} could serve as a single diagnostic measure (Fig. 5C). The class boundaries, determined

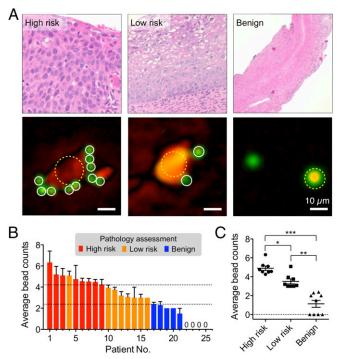


Fig. 5. Cervical cancer diagnosis with the D3 platform. (A) Histology (Top) and representative reconstructed image of cells (Bottom) from high-risk (cervical intraepithelial neoplasia/CIN 2, 3), low-risk (CIN 1), and benign patient samples. Samples were targeted with a mixture of EpCAM. CD44, and Trop2 antibodies, followed by microbead labeling. More beads were bound to cells in higher risk patient samples. The transmittance (green) and the phase (red) were pseudocolored for clarification. (B and C) The profiling result of patient samples (n = 25). The average numbers of beads per labeled cell were significantly different among high-risk, low-risk, and benign groups. The dotted lines indicate the class boundaries. *P = 0.035; **P < 0.001; ****P* < 0.001.

from multiclass logistic regression, were $n_{bead} > 4.2$ between high risk and low risk; and $n_{bead} > 2.4$ between low risk and benign. We further dichotomized the patients into two groups, high risk versus low risk/benign, to reflect the conventional clinical process for intervention and/or follow-up. In our limited data set, the detection sensitivity was 100% and the specificity 92% (high risk vs. low risk/benign).

We also adopted the same D3 platform for the HPV-DNA detection (SI Appendix, Fig. S16A), given its high relevance in cervical cancer diagnostics. We applied the bead-dimer assay format: a pair of oligonucleotides, whose sequences were complementary to that of target DNA, were conjugated to silica and polystyrene microbeads, respectively. The target DNA was captured on polystyrene (PS) beads and sequentially labeled with silica beads. The hybridization yielded PS-silica bead dimers with unique diffraction signature (SI Appendix, Fig. S16B). The number of PS-silica hybrids was then counted to quantify the amount of target DNA. The D3 assay was highly sensitive; HPV 16 and 18 DNA targets could be detected down to atto-mole range without PCR amplification (SI Appendix, Fig. S16 C and D). Compared with fluorescent detection, the bead-based D3 assay benefited from simpler optics (i.e., no filter sets) and stronger light signal (bright field).

Extending the clinical utility of D3 to other malignancies, we conducted a pilot study to detect lymphoma cells in fine-needle aspirates (FNA) of lymph nodes in patients with lymphadenopathy. POC lymphoma diagnostics would be of particular interest in sub-Saharan Africa plagued by a high prevalence of AIDSrelated cancers and lymphoma (the "second wave of AIDS") (25, 30, 31). Freshly harvested FNA samples were incubated with immunobeads specific to CD20, one lymphoma marker (SI Appendix, Fig. S17). Subsequent D3 analysis allowed the correct diagnosis of four patients with pathology confirmed lymphoma and also excluded the diagnosis in another four patients with confirmed benign lymphadenopathy.

Discussion

Global cancer rates continue to increase, and the World Health Organization predicts new cases to rise to 19.3 million by 2025 as the world's population grows, ages, and gains access to antiretroviral drugs (1, 32-35). Rapid cancer screening, however, remains an unmet clinical need. The D3 strategy reported here could address some of the diagnostic challenges in resourcelimited areas. It capitalizes on the already widespread distribution of smartphones and allows fast (minutes-hours for a final answer), very low cost (compared with sectioning, microscopes, and flow cytometers), and simple diagnostics. Molecular diagnoses are achieved by integrating immunolabeling assays, cloud computing, and digital processing. The resulting system enables quantitative and operator-independent cellular analysis and reports not only cancer cell counts but also the expression levels of molecular markers. In a pilot study of cervical cancer screening, we used three molecular markers to define risk categories based on invasiveness. The D3 assay was fast (40 min for immunolabeling, most of which is "hands-off" time and 3 min for data processing; SI Appendix, Table S3) and cost-effective (\$1.80 per assay; SI Appendix, Table S4). We expect that the assay costs will ultimately be much cheaper once scaled up and further optimized.

We anticipate further improvements in some analytical capabilities of D3. First, a next-generation system would incorporate multiplexed cellular detection based on different optical properties of microbeads. We have shown that microbeads can be differentiated based on their size and absorbance (SI Appendix, Fig. S15). Applying these signatures would enable multiplexed molecular profiling of the same cells to improve detection accuracy. In parallel, superresolution approaches could be used to improve the spatial resolution (6, 14, 36–38), and thereby further boost D3's multiplexing capacity. Compressive sensing is particularly appealing (39, 40), as it can numerically reconstitute high-frequency information (i.e., small features in images) with no modification in the current D3 setup. By incorporating compressive sensing, we expect to reconstruct images with submicrometer resolution ($\sim 0.6 \mu m$), which would allow analyses of all types of mammalian cells. Second, DNA detection should be further developed for POC operation. This would require implementing disposable cartridges (41, 42) and portable systems (43, 44) for DNA extraction and amplification. Finally, the platform should be tested for robust field operation. We plan to establish a lyophilization protocol for transport and storage of reagents (e.g., antibodies, microbeads) (45). The validation tests will be extended using larger cohorts, variably skilled operators, and diverse environment settings to obtain better statistical power (reproducibility, accuracy, diagnostic performance). In this light, the work presented here has catalyzed two larger clinical trials focused, respectively, on cervical cancer (including HPV testing) and lymphoma detection (FNAs of enlarged lymph nodes). We envision that these advances will position D3 as a versatile screening tool for various cancer types (e.g., cervix, breast, lymphoma) and infectious diseases (e.g., Ebola, HIV, tuberculosis) with applications in field work, mobile clinics, and home care settings.

Materials and Methods

D3 Imaging Terminal. Electrical components [e.g., light-emitting diode (LED), battery socket, switch] were purchased (Digi-Key) and mounted on a custom-designed printed circuit board. The main body of the snap-on module was machined out of black acrylic plastic, and housed the light source (590 nm), a 100-µm pinhole, and a minilens. The focal length (4 mm) of the lens was similar to that of the embedded lens (4.2 mm) in the phone camera (*SI Appendix*, Fig. 51). By pairing these two lenses, we achieved a unit magnification to maximize the FOV, and used the phone camera without any modification. The size of the snap-on was 4 × 4 × 5.5 cm³.

D3 App. The D3 app was programmed with user-friendly interfaces for operation in iOS 6 or higher version. The app has three main screens: (i) image capturing and processing, (ii) reconstruction parameters settings, and (iii) data communication with a cloud service. The images captured by a phone camera module were saved as uncompressed data (PNG) or compressed image (JPEG), and uploaded along with other imaging information (e.g., wavelength, diagnosis location, time, patient data) into a dedicated folder in a cloud storage (Dropbox). The uploaded images were processed by a D3 image GPU server (see below), and the results were saved into a subfolder. The D3 app subsequently downloaded reconstructed images and analysis results. All data were encrypted according to the 256-bit Advanced Encryption Standard. The application program interface library from the vendor (Dropbox) was used to implement the data transfer routine.

D3 Imaging Server. The D3 server (HP xw4600 workstation, Hewlett Packard) had the following system specifications (SI Appendix, Table S2): CPU, Core2 Duo E8500 3.16 GHz (Intel); memory, 8-GB DDR2 (double data rate2); GPU, Tesla C-2070 (Nvidia); operating system, Ubuntu 12.04 64-bit. The GPU had 448 CUDA (Compute Unified Device Architecture) cores and 6 GB memory. The signal processing program was written in C++ language and used vendor-provided modules (CUDA extensions, CUDA driver 5.0, CUFFT library). The image analysis workflow is shown in SI Appendix, Fig. S2. The imaging server cyclically polled a dedicated folder in a cloud storage (Dropbox). When new images and image information were uploaded, the imaging server executed image reconstruction and postimaging analyses (cell and bead counting). The reconstructed images and counting statistics were then saved into a subfolder. When synchronized in the cloud storage, the image and data files could be accessed by users.

Image Reconstruction. The size of an uncompressed image file on the iPhone 4S was \sim 24 MB (2,448 \times 3,264 pixels, 24-bit RGB). This raw image file was converted to gray-scale PNG (\sim 2.9 MB) or JPEG (\sim 0.4 MB) files (SI Appendix, Fig. S6), and normalized by a reference image recorded without samples. The normalization removed intrinsic defects and accurately calculated object transmittance (21). The normalized diffraction images were up-sampled four times through linear interpolation and used as input data for reconstruction. The reconstruction was based on phase retrieval algorithms, which can recover phase information from intensity-based diffraction patterns through iterative

processes (4, 18, 19). The algorithm has four steps: (i) back-propagate an input image, (ii) apply constraints, (iii) forward-propagate updated image, and (iv) update retrieved phase information. First, the normalized diffraction image was numerically back-propagated by an optical distance between the object and the imager. We calculated the optimal optical distance by finding a focal depth with the sharpest object boundary (46). Calculating field propagation was based on the Rayleigh-Sommerfeld diffraction integral in a convolution approach, where the propagated field was calculated by the inverse Fourier transform of the multiplication between the Fourier transform of field and the transfer function (20). During the first iteration, object supports were defined using a segmentation method, where object boundaries were found by thresholding intensity variances (46). For the back-propagated image, pixels outside the object supports were regarded as background, and their transmittance values (i.e., the modulus of field) were set to unity. If a pixel inside the object support had a transmittance value larger than unity due to artificial twinimage superimposition, its transmittance value was also forced to unity. After applying the constraints, the updated image was propagated to the image plane, where the forward-propagated field had nonzero phase information. The phase information was added to the measured diffraction image as a new input. The process was usually repeated $10\sim30$ times until the reconstructed image with retrieved phase information converged.

Counting Algorithm. For detecting beads and cells, a microbead reference image was scanned over the reconstructed images to generate modulus and phase correlation maps as shown in SI Appendix, Fig. S5. The reference microbead image was obtained by averaging microbead images in a pure bead solution. The correlation coefficients for modulus and phase were calculated from pixel-to-pixel comparison between reference and reconstructed images. Cells were first detected when a local maximum phase correlation coefficient was larger than the threshold value of phase correlation coefficient, which was obtained from images of pure cell population. For each cell detected, microbeads within the object support were detected from the local maxima of the modulus correlation coefficients. Microbeads within a distance of 10 pixels (or 22 μm) from a center of cells were considered bound to cells. This search radius was experimentally determined for 7-µm beads. The detection algorithm was validated by comparing bead counts with manual counting using a conventional microscopy. The microscope was equipped with a 10x objective (N.A. = 0.17) and a cooled CCD camera (7.4 \times 7.4- μm^2 pixel size; Spot RT3, Diagnostic Instruments Inc.), and produced images with 1.4 pixel/µm resolution.

Clinical Samples. The clinical study was approved by the Partners Healthcare Institutional Review Board (Massachusetts General Hospital/Brigham and Women's Hospital). Informed consent was obtained from adult women who were referred to the Colposcopy Clinic for previously abnormal Pap smears. Samples were obtained by brushing, cervical biopsy, or LEEP. One clinical provider (M.A.-W.) performed all cervical procedures and provided excess or otherwise discarded ectocervical or endocervical specimens. Biopsies entailed visualizing the exocervix and bathing with 5% acetic acid using clinically standard procedures. Suspicious aceto-white epithelial changes were identified with a colposcope (Foto Optik; Leisegang Medical Inc.) followed by punch biopsies. Before the use of acetic acid, brushing samples were collected with surgical brushes (Surgipath C-E Brush, Leica Microsystems; Cytobrush Plus GT Gentle Touch, BD Surepath). Samples were suspended in sterile PBS (1 mL), and incubated (30 min, 20 °C) with a mixture of antibodies against EpCAM (clone MAB9601, R&D Systems), CD44 (clone IM7, Biolegend), and Trop2 (Clone 162-46.2, Abcam). The antibody concentration was 5 µg/mL for each. Targeted samples were then incubated with streptavidin-coated polystyrene microbeads (0.5 mg, $7\text{-}\mu\text{m}$ diameter, Spherotech) for 10 min at room temperature and analyzed using the D3 platform. Here, the sample volume examined was 10 μ L; the number of microbeads per cell was automatically counted using D3 software. All experiments were conducted blind to pathology results and clinical interpretation of risk. Please see SI Appendix for cell preparation, fluorescence measurements, HPV-DNA detection, and clinical lymph node samples.

ACKNOWLEDGMENTS. The authors thank M. Birrer, D. Dizon, and M. Del Carmen for many helpful suggestions; Melina Pectasides for assistance with clinical sample collection; and K. Joyes for reviewing the manuscript. This work was supported in part by US NIH Grants R01-HL113156 (to H.L.), R01-EB010011 (to R.W.), R01-EB00462605A1 (to R.W.), T32CA79443 (to R.W.), K12CA087723-11A1 (to C.M.C.), Massachusetts General Hospital Physician Scientist Development Award (to C.M.C.), National Heart, Lung, and Blood Institute Contract HHSN268201000044C (to R.W.), and Department of Defense Ovarian Cancer Research Program Award W81XWH-14-1-0279 (to H.L.)

Im et al. PNAS Early Edition | **5 of 6**

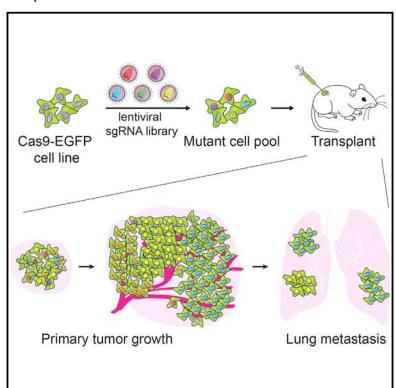
- 1. Varmus H, Trimble EL (2011) Integrating cancer control into global health. Sci Transl Med 3(101):01cm28.
- 2. Chin CD, Linder V, Sia SK (2012) Commercialization of microfluidic point-of-care diagnostic devices. Lab Chip 12(12):2118-2134.
- 3. Xu W, Jericho MH, Meinertzhagen IA, Kreuzer HJ (2001) Digital in-line holography for biological applications. Proc Natl Acad Sci USA 98(20):11301-11305.
- 4. Garcia-Sucerquia J, et al. (2006) Digital in-line holographic microscopy. Appl Opt 45(5):836-850.
- 5. Gurkan UA, et al. (2011) Miniaturized lensless imaging systems for cell and microorganism visualization in point-of-care testing. Biotechnol J 6(2):138-149.
- 6. Zheng G, Lee SA, Antebi Y, Elowitz MB, Yang C (2011) The ePetri dish, an on-chip cell imaging platform based on subpixel perspective sweeping microscopy (SPSM). Proc Natl Acad Sci USA 108(41):16889-16894.
- 7. Kim SB, et al. (2011) A cell-based biosensor for real-time detection of cardiotoxicity using lensfree imaging. Lab Chip 11(10):1801-1807.
- 8. Greenbaum A, et al. (2012) Imaging without lenses: Achievements and remaining challenges of wide-field on-chip microscopy. Nat Methods 9(9):889–895.
- 9. Seo S, et al. (2010) High-throughput lens-free blood analysis on a chip. Anal Chem 82(11):4621-4627.
- 10. Mudanyali O, Bishara W, Ozcan A (2011) Lensfree super-resolution holographic microscopy using wetting films on a chip. Opt Express 19(18):17378-17389.
- 11. Lee SA, et al. (2011) Color capable sub-pixel resolving optofluidic microscope and its application to blood cell imaging for malaria diagnosis. PLoS ONE 6(10):e26127.
- 12. Greenbaum A, Akbari N, Feizi A, Luo W, Ozcan A (2013) Field-portable pixel superresolution colour microscope. PLoS ONE 8(9):e76475.
- 13. Su T-W, Choi I, Feng J, Huang K, McLeod E, Ozcan A (2013) Sperm trajectories form chiral ribbons. Sci Rep 3:1664.
- 14. Zheng G, Horstmeyer R, Yang C (2013) Wide-field, high-resolution Fourier ptychographic microscopy. Nat Photonics 7(9):739–745.
- Ojesina AI, et al. (2014) Landscape of genomic alterations in cervical carcinomas. Nature 506(7488):371-375
- 16. Schiffman M, Solomon D (2013) Clinical practice. Cervical-cancer screening with human papillomavirus and cytologic cotesting. N Engl J Med 369(24):2324–2331.
- 17. Fung J, et al. (2011) Measuring translational, rotational, and vibrational dynamics in colloids with digital holographic microscopy. Opt Express 19(9):8051-8065.
- 18. Mudanyali O, et al. (2010) Compact, light-weight and cost-effective microscope based on lensless incoherent holography for telemedicine applications. Lab Chip 10(11):
- 19. Fienup JR (1982) Phase retrieval algorithms: A comparison. Appl Opt 21(15):2758-2769.
- 20. Kreis TM (2002) Frequency analysis of digital holography with reconstruction by convolution. Opt Eng 41(8):1829-1839.
- Latychevskaia T, Fink H-W (2007) Solution to the twin image problem in holography. Phys Rev Lett 98(23):233901.
- 22. Basiji DA, Ortyn WE, Liang L, Venkatachalam V, Morrissey P (2007) Cellular image analysis and imaging by flow cytometry. Clin Lab Med 27(3):653-670, viii
- Agasti SS, et al. (2012) Supramolecular host-guest interaction for labeling and detection of cellular biomarkers. Angew Chem Int Ed Engl 51(2):450-454.
- 24. Haun JB, Devaraj NK, Hilderbrand SA, Lee H, Weissleder R (2010) Bioorthogonal chemistry amplifies nanoparticle binding and enhances the sensitivity of cell detection. Nat Nanotechnol 5(9):660-665.
- 25. Chabner BA, Efstathiou J, Dryden-Peterson S (2013) Cancer in Botswana: The second wave of AIDS in Sub-Saharan Africa. Oncologist 18(7):777-778.

- 26. Ramogola-Masire D, et al. (2012) Cervical cancer prevention in HIV-infected women using the "see and treat" approach in Botswana. J Acquir Immune Defic Syndr 59(3): 308-313.
- 27. Dall P, et al. (1994) Surface protein expression and messenger RNA-splicing analysis of CD44 in uterine cervical cancer and normal cervical epithelium. Cancer Res 54(13):
- 28. Varughese J, et al. (2011) Cervical carcinomas overexpress human trophoblast cellsurface marker (Trop-2) and are highly sensitive to immunotherapy with hRS7, a humanized monoclonal anti-Trop-2 antibody. Am J Obstet Gynecol 205(6):e1-e7.
- 29. Went PTH, et al. (2004) Frequent EpCam protein expression in human carcinomas. Hum Pathol 35(1):122-128.
- 30. Varmus H, Kumar HS (2013) Addressing the growing international challenge of cancer: A multinational perspective. Sci Transl Med 5(175):cm2.
- 31. Livingston J (2013) Cancer in the shadow of the AIDS epidemic in southern Africa. Oncologist 18(7):783-786
- 32. Beaglehole R, et al.; Lancet NCD Action Group (2011) UN High-Level Meeting on Non-Communicable Diseases: Addressing four questions. Lancet 378(9789):449-455.
- 33. Daar AS, et al. (2007) Grand challenges in chronic non-communicable diseases. Nature 450(7169):494-496.
- 34. Narayan KMV, Ali MK, del Rio C, Koplan JP, Curran J (2011) Global noncommunicable diseases—lessons from the HIV-AIDS experience, N Engl J Med 365(10):876-878.
- 35. Trimble EL (2010) Global cooperation in gynecologic cancer. J Gynecol Oncol 21(1):
- 36. Gazit S, Szameit A, Eldar YC, Segev M (2009) Super-resolution and reconstruction of sparse sub-wavelength images. Opt Express 17(26):23920-23946.
- 37. Bishara W, et al. (2011) Holographic pixel super-resolution in portable lensless on-chip microscopy using a fiber-optic array. Lab Chip 11(7):1276-1279.
- 38. Mudanyali O, et al. (2013) Wide-field optical detection of nanoparticles using on-chip microscopy and self-assembled nanolenses. Nat Photonics 7(3):247-254
- 39. Brady DJ, Choi K, Marks DL, Horisaki R, Lim S (2009) Compressive holography. Opt Express 17(15):13040-13049.
- 40. Rivenson Y, Stern A, Javidi B (2013) Overview of compressive sensing techniques applied in holography [Invited]. Appl Opt 52(1):A423-A432.
- 41. Hoffmann J, Mark D, Lutz S, Zengerle R, von Stetten F (2010) Pre-storage of liquid reagents in glass ampoules for DNA extraction on a fully integrated lab-on-a-chip cartridge, Lab Chip 10(11):1480-1484.
- 42. Liu C, Mauk MG, Hart R, Qiu X, Bau HH (2011) A self-heating cartridge for molecular diagnostics. Lab Chip 11(16):2686-2692.
- 43. Huang S, et al. (2013) Low cost extraction and isothermal amplification of DNA for infectious diarrhea diagnosis. PLoS ONE 8(3):e60059.
- 44. Jiang L. Mancuso M. Lu Z. Akar G. Cesarman E. Erickson D (2014) Solar thermal polymerase chain reaction for smartphone-assisted molecular diagnostics. Sci Rep 4:
- 45. Bhambhani A, Blue JT (2010) Lyophilization strategies for development of a highconcentration monoclonal antibody formulation: Benefits and pitfalls. Am Pharm Rev
- 46. McElhinney CP, et al. (2007) Depth-independent segmentation of macroscopic threedimensional objects encoded in single perspectives of digital holograms. Opt Lett 32(10):1229-1231.



Genome-wide CRISPR Screen in a Mouse Model of **Tumor Growth and Metastasis**

Graphical Abstract



Authors

Sidi Chen, Neville E. Sanjana, ..., Feng Zhang, Phillip A. Sharp

Correspondence

zhang@broadinstitute.org (F.Z.), sharppa@mit.edu (P.A.S.)

In Brief

Using an in vivo genome-wide CRISPR/ Cas9 screen, loss-of-function mutations that drive tumor growth and metastasis to the lung have been identified, demonstrating Cas9-based screening as a robust method to systematically assay gene phenotypes in cancer evolution.

Highlights

- Genome-wide in vivo CRISPR-Cas9 screen in mice reveals genes regulating lung metastasis
- Screen identifies loss-of-function mutations in known tumor suppressors and novel genes
- Candidate metastasis genes are validated using a pooled competition assay
- Effect of mutations on primary tumor growth positively correlates with metastasis





Genome-wide CRISPR Screen in a Mouse Model of Tumor Growth and Metastasis

Sidi Chen, 1,2,3,10 Neville E. Sanjana, 3,4,5,6,7,10 Kaijie Zheng, 3,4 Ophir Shalem, 3,4 Kyungheon Lee, 8 Xi Shi, 3,4 David A. Scott, 3,4 Jun Song, 8 Jen Q. Pan, 3,4 Ralph Weissleder, 8,9 Hakho Lee, 8 Feng Zhang, 3,4,5,6,7,* and Phillip A. Sharp^{1,2,*}

Massachusetts Institute of Technology, Cambridge, MA 02139, USA

SUMMARY

Genetic screens are powerful tools for identifying genes responsible for diverse phenotypes. Here we describe a genome-wide CRISPR/Cas9-mediated loss-of-function screen in tumor growth and metastasis. We mutagenized a non-metastatic mouse cancer cell line using a genome-scale library with 67,405 single-guide RNAs (sgRNAs). The mutant cell pool rapidly generates metastases when transplanted into immunocompromised mice. Enriched sgRNAs in lung metastases and late-stage primary tumors were found to target a small set of genes, suggesting that specific loss-of-function mutations drive tumor growth and metastasis. Individual sgRNAs and a small pool of 624 sgRNAs targeting the top-scoring genes from the primary screen dramatically accelerate metastasis. In all of these experiments, the effect of mutations on primary tumor growth positively correlates with the development of metastases. Our study demonstrates Cas9-based screening as a robust method to systematically assay gene phenotypes in cancer evolution in vivo.

INTRODUCTION

Cancer genomes have complex landscapes of mutations and diverse types of genetic aberrations (Lawrence et al., 2013; Weinberg, 2007). A major challenge in understanding the cancer genome is to disentangle alterations that are driving the processes of tumor evolution from passenger mutations (Garraway and Lander, 2013). Primary tumor growth and metastasis are distinct yet linked processes in the progression of solid tumors (Nguyen et al., 2009; Valastyan and Weinberg, 2011; Vanharanta and Massagué, 2013). It has been observed in the clinic that the

probability of detecting metastases in a patient correlates positively with the size of a primary tumor (Heimann and Hellman, 1998). Several possible explanations have been suggested: metastatic properties may only be acquired in late-stage tumors, larger tumors may seed proportionally more cells into circulation that eventually migrate to other sites, or cells with a strong ability to proliferate may also have enhanced ability to metastasize (Weinberg, 2007). In early studies using random insertional mutagenesis, it was observed that metastatic cell subpopulations overgrow to complete dominance in the primary tumor, suggesting progressive selection at both sites (Korczak et al., 1988; Waghorne et al., 1988).

Genetic screens are powerful tools for assaying phenotypes and identifying causal genes in various hallmarks of cancer progression (Hanahan and Weinberg, 2011). RNAi and overexpression of open reading frames (ORFs) have been utilized for screening cancer genes in several models of oncogenesis in mice (Schramek et al., 2014; Shao et al., 2014; Zender et al., 2008). Recently, the Cas9 nuclease (Barrangou et al., 2007; Bolotin et al., 2005; Chylinski et al., 2013, 2014; Deltcheva et al., 2011; Garneau et al., 2010; Gasiunas et al., 2012; Jinek et al., 2012; Sapranauskas et al., 2011) from the microbial type II CRISPR (clustered regularly interspaced short palindromic repeats) system has been harnessed to facilitate loss-of-function mutations in eukaryotic cells (Cong et al., 2013; Mali et al., 2013). When the Cas9 nuclease is targeted to specific locations in the genome, DNA cleavage results in double-stranded breaks (DSBs), which are repaired via non-homologous endjoining (NHEJ) (Rouet et al., 1994). NHEJ repair results in insertion or deletion (indel) mutations that can cause loss of function if the DSB occurs in a coding exon. The Cas9 nuclease can be guided to its DNA target by a single-guide RNA (sgRNA) (Jinek et al., 2012), a synthetic fusion between the CRISPR RNA (crRNA) and trans-activating crRNA (tracrRNA) (Deltcheva et al., 2011). In cells, Cas9-mediated gene disruption requires the full-length tracrRNA (Cong et al., 2013; Mali et al., 2013), in which secondary structures at the 3' end of tracrRNA are



¹David H. Koch Institute for Integrative Cancer Research, Cambridge, MA 02139, USA

²Department of Biology, Massachusetts Institute of Technology, Cambridge, MA 02139, USA

³Broad Institute of MIT and Harvard, Cambridge, MA 02142, USA

⁴Stanley Center for Psychiatric Research, Cambridge, MA 02142, USA

⁵McGovern Institute for Brain Research

⁶Department of Brain and Cognitive Sciences

⁷Department of Biological Engineering

⁸Center for Systems Biology, Massachusetts General Hospital, Boston, MA 02114, USA

⁹Department of Systems Biology, Harvard Medical School, Boston, MA 02115, USA

¹⁰Co-first author

^{*}Correspondence: zhang@broadinstitute.org (F.Z.), sharppa@mit.edu (P.A.S.) http://dx.doi.org/10.1016/j.cell.2015.02.038

critical for Cas9-mediated genome modification (Cong et al., 2013; Hsu et al., 2013).

Screens utilizing Cas9 have identified genes that are essential for cell survival and genes involved in drug resistance in various cell lines (Shalem et al., 2014; Wang et al., 2014; Koike-Yusa et al., 2014; Zhou et al., 2014). In vivo pooled screens are challenging due to many factors, such as the complexity of the library, limitations of virus delivery and/or cell transplantation, uniformity of viral transduction at a low MOI, and the complex dynamics and interactions of cells in animals. In this study, we report a genome-wide Cas9 knockout screen in a mouse model of tumor evolution. This screen provides a systematic phenotypic measurement of loss-of-function mutations in primary tumor growth and metastasis.

RESULTS

CRISPR/Cas9 Library-Mediated Mutagenesis Promotes Metastasis

We derived and cloned a cell line (Chen et al., 2014) from a mouse non-small-cell lung cancer (NSCLC) (Kumar et al., 2009). This cell line possesses an oncogenic *Kras* in conjunction with homozygous *p53* and heterozygous *Dicer1* loss of function (*Kras*^{G12D/+};*p53*^{-/-};*Dicer1*^{+/-}, denoted KPD) and is capable of inducing tumors when transplanted into immunocompromised mice (Chen et al., 2014; Kumar et al., 2009). We transduced this cell line with a lentivirus carrying a Cas9 transgene fused to a GFP and generated clonal cell lines (Cas9-GFP KPD) (Experimental Procedures) (Figures S1A and S1B). A clonal Cas9-GFP KPD cell line (clone 5) was selected to provide genetic and cellular homogeneity for subsequent screens.

We utilized a pooled genome-wide mouse sgRNA library (termed mouse genome-scale CRISPR knockout library A, or mGeCKOa) containing 67,405 sgRNAs targeting 20,611 protein-coding genes and 1,175 microRNA precursors in the mouse genome (Sanjana et al., 2014). The library also contains 1,000 control sgRNAs (termed non-targeting sgRNAs) designed to have minimal homology to sequences in the mouse genome (Sanjana et al., 2014; Shalem et al., 2014). We transduced the Cas9-GFP KPD cell line with the mGeCKOa library in three independent infection replicate experiments; for each replicate, the library representation (cells per lentiviral CRISPR construct) was greater than 400× (Figure 1A) (Experimental Procedures).

After in vitro culture for 1 week, we subcutaneously transplanted 3×10^7 cells into the flanks of immunocompromised Nu/Nu mice (Figure 1A). We transplanted the cells from each infection replicate into four mice, using one mouse for early tumor sequencing and three mice for sequencing of late-stage primary tumor and metastases (Figure 1A). Both mGeCKOatransduced and untransduced Cas9-GFP KPD cells formed tumors at the injection site (Figure 1B). Like most subcutaneously transplanted tumors, these tumors were poorly differentiated. The primary tumors induced by mGeCKOa-transduced cells grew slightly faster than tumors from the untransduced cells at an early stage (Figure 1C) (2 weeks post-transplantation) (paired two-tailed t test, p = 0.18 for data at 4 weeks, p = 0.6 for data at 6 weeks) (Figure 1C).

At 6 weeks post-transplantation, we imaged the mice using micro-computed tomography (μCT) and found tumors in the lungs of the mice transplanted with mGeCKOa-transduced Cas9-GFP KPD cells (mGeCKOa mice), but not in the mice transplanted with untransduced Cas9-GFP KPD cells (control mice) (Figure 1D, Figure S1C). Mice were sacrificed and examined for metastases in various organs. Under a fluorescent stereoscope at 6× magnification, metastases were visually detected in the lung in 89% (8/9) of the mGeCKOa mice (Figure S1D). The mGeCKOa mice on average had 80% of their lung lobes positive for metastases (Figure 1E). In contrast, none (0/3) of the control mice developed detectable metastases in the lung (Figure 1E). At this time, metastases were not detected in the liver, kidney, or spleen in either group (Figure 1F). These data indicated that mGeCKOa library transduction enhanced the ability of the Cas9-GFP KPD cells to form metastases in the lung.

Dynamic Evolution of sgRNA Library Representation during Tumor Growth and Metastasis

To investigate the sgRNA representation through different stages of tumor evolution and to identify genes where loss of function confers a proliferative or metastatic phenotype, we used deep sequencing to readout the sgRNA representation (see Data S1 in Dataset S1). At 6 weeks post transplantation, we sequenced the late-stage primary tumor and three random lobes from the lung of each of the nine mGeCKOa mice (Figure 1A) (Experimental Procedures). In parallel, we also sequenced the mGeCKOa input plasmid library, the pre-transplantation mGeCKOa-transduced Cas9-GFP KPD cells (cultured in vitro for 7 days after transduction), and early-stage primary tumors (2 weeks post transplantation, one mouse from each infection replicate). In the cell samples, the sgRNA representations showed high concordance between technical replicates (correlation, $\rho = 0.95$ on average, n = 3) and biological infection replicates (correlation, ρ = 0.84 on average, n = 3) (Figures 2A, S2A, S2B, and S2E). The sgRNA representation of cell samples correlates highly with the plasmid representation (correlation, $\rho = 0.93$ on average, n = 3) (Figures 2A, S2C, and S2E). Furthermore, different sgRNAs that target the same gene are correlated in terms of rank change (correlation, ρ = 0.49 on average, n = 3) (Figure S2D). Using gene set enrichment analysis (GSEA), we found that the sgRNAs with significantly decreased abundance in cells compared to plasmid are enriched for genes involved in fundamental cellular processes, such as ribosomal proteins, translation factors, RNA splicing factors, and RNA processing factors, indicating selection against the loss of these genes after 1 week in culture (Figure S2F).

To investigate the sgRNA library dynamics in different sample types (plasmid, pre-transplantation cells, early primary tumor, late primary tumor, and lung metastases), we compared the overall distributions of sgRNAs from all samples sequenced. Cell samples clustered tightly with each other and the plasmid, forming a cell-plasmid clade (Figures 2A and S2E). Early primary tumor samples also clustered with each other and then with the cell-plasmid clade, whereas late tumors and lung metastases clustered together in a distinct group (Figures 2A and S2E). The overlap of detected sgRNAs between different pre-transplantation infection replicates is over 95% (Figure S3A). The detected sgRNAs in the three infection replicates of early tumor

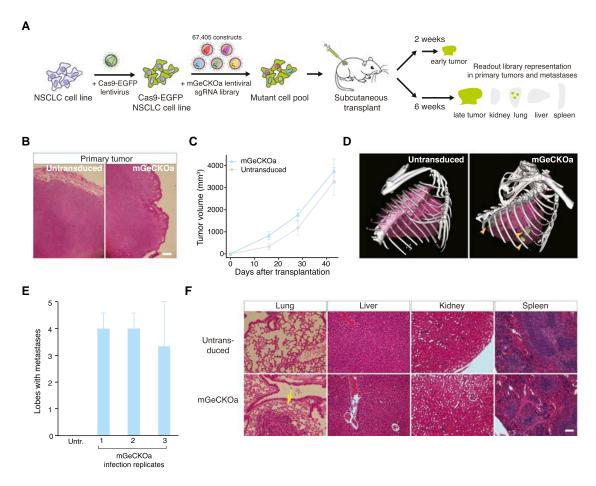


Figure 1. Tumor Growth and Metastasis in Transplanted Cas9-GFP KPD Cells with mGeCKOa Library

- (A) Schematic representation of the loss-of-function metastasis screen using the mouse genome-scale CRISPR/Cas9 knockout library (mGeCKOa).
- (B) Representative H&E stains of primary tumor from *Nu/Nu* mice subcutaneously transplanted with a Cas9-GFP *Kras*^{G12D/+};*p*53^{-/-};*Dicer1*^{+/-} (KPD) NSCLC cell line that was either untransduced or transduced with the mGeCKOa lentiviral library. Scale bar, 200 μm.
- (C) Primary tumor growth curve of Nu/Nu mice transplanted with untransduced cells (n = 3 mice) or mGeCKOa-transduced Cas9-GFP KPD cells (n = 9 mice). Error bars indicate SEM.
- (D) MicroCT 3D reconstruction of the lungs of representative mice transplanted with control (untransduced) and mGeCKOa-transduced (mGeCKOa) cell pools. Lung metastases were identified and traced in each 2D section (green).
- (E) Percent of lobes with metastases visible after dissection under a fluorescence stereoscope in *Nu/Nu* mice transplanted with untransduced Cas9-GFP KPD cells (n = 3 mice) or mGeCKOa-transduced Cas9-GFP KPD cells with three independent infection replicate experiments (1, 2, and 3; n = 3 mice per replicate). Error bars indicate SEM.
- (F) Representative H&E stains from various organs of *Nu/Nu* mice subcutaneously transplanted with untransduced and mGeCKOa-transduced Cas9-GFP KPD cells. Yellow arrow indicates a lung metastasis. Scale bar, 40 μm. See also Figure S1.

samples overlap 63%–76% with each other (Figure S3B). Early primary tumors retained less than half (32%–49%) of the sgRNAs found in the transplanted cell populations (Figures 2B, 2C, S3C, and S3D). Compared to the cell populations, sgRNAs whose targets are genes involved in fundamental cellular processes are further depleted in early tumors (Table S1).

Interestingly, only a small fraction of sgRNAs (less than 4% of all sgRNAs, or less than 8% of sgRNAs in the early primary tumor of the corresponding replicate) were detected in the late-stage primary tumor samples (Figures 2B, 2C, S3C, and S3D). The sgRNA diversity (i.e., number of different sgRNAs detected) further decreased in samples from lung metastases (Figures

2B, 2C, S3C, and S3D). The lung samples retained \leq 0.4% of all sgRNAs in the mGeCKOa library, or \leq 1.1% of sgRNAs found in the early primary tumor of the corresponding replicate, with a subset of highly enriched sgRNAs (Figures 2B, 2C, S3C, and S3D). The global patterns of sgRNA distributions in different sample types are distinct, as is evident in the strong shifts in the respective cumulative distribution functions (Kolmogorov-Smirnov [KS] test, p < 10 $^{-15}$ for all pairwise comparisons) (Figure 2D).

Enriched sgRNAs in Primary Tumors

Late primary tumors retain few sgRNAs (on average 813 ± 264 sgRNAs, n = 9 mice), with even fewer at high frequencies

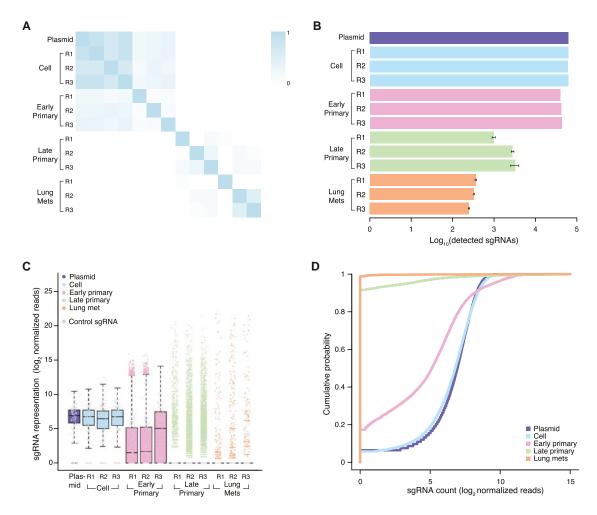


Figure 2. Representation of mGeCKOa Library at Different Stages of Tumor Growth and Metastasis

(A) Pearson correlation coefficient of the normalized sgRNA read counts from the mGeCKOa plasmid library, transduced cells before transplantation (day 7 after spinfection), early primary tumors (~2 weeks after transplantation), late primary tumors (~6 weeks after transplantation), and lung metastases (~6 weeks after transplantation). For each biological sample type, three independent infection replicates (R1, R2, and R3) are shown. n = 1 mouse per infection replicate for early primary tumors; n = 3 mice per infection replicate for late primary tumors and lung samples.

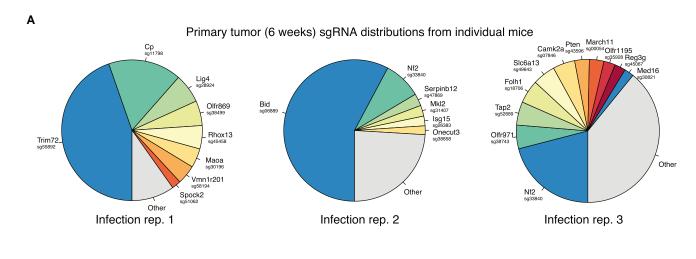
(B) Number of unique sgRNAs in the plasmid, cells before transplantation, early and late primary tumors, and lung metastases as in (A). Error bars for late primary tumors and lung metastases denote SEM for n = 3 mice per infection replicate.

(C) Boxplot of the sgRNA normalized read counts for the mGeCKOa plasmid pool, cells before transplantation, early and late primary tumors, and lung metastases as in (A). Outliers are shown as colored dots for each respective sample. Gray dots overlaid on each boxplot indicate read counts for the 1,000 control (non-targeting) sgRNAs in the mGeCKOa library. Distributions for late primary tumors and lung metastases are averaged across individual mice from the same infection replication.

(D) Cumulative probability distribution of library sgRNAs in the plasmid, cells before transplantation, early and late primary tumors, and lung metastases as in (A). Distributions for each sample type are averaged across individual mice and infection replications. See also Figures S2 and S3.

(4 \pm 1 sgRNAs with >5% of total reads) in each mouse (Figures 2B, 2C, S2C, S2D, 3A, and S4H). We used three methods to identify enriched sgRNAs in late primary tumors: (1) sgRNAs above a certain threshold, (2) top-ranked sgRNAs in the tumor of each mouse, and (3) using false discovery rate (FDR), i.e., sgRNAs enriched compared to the distribution of the 1,000 non-targeting sgRNAs. All three methods generated similar results (Figure S4A). Taking the results from (3) as an example, a total of 935 sgRNAs (targeting 909 genes) are enriched over the non-targeting controls (FDR cutoff = 0.2%) in the late primary tumor of one or more mice (Figures 3B and 3C). These sgRNAs are targeting genes highly enriched in apoptosis pathways (Table S2), with many of them being pro-apoptotic, such as BH3 interacting-domain death agonist (Bid), phosphatase and tensin homolog (Pten), cyclin-dependent kinase inhibitor 2a (Cdkn2a), and O-6-methylguanine-DNA methyltransferase (Mgmt), suggesting strong selection for mutations that inactivate apoptosis in primary tumor cells.

We identified 24 candidate genes that were targeted by two or more independent sgRNAs enriched in late primary tumors



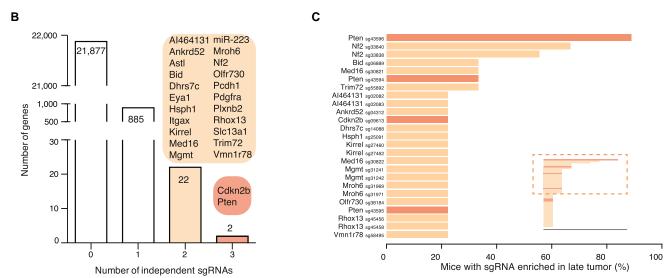


Figure 3. Enriched sgRNAs from the mGeCKOa Screen in Primary Tumors

(A) Pie charts of the most abundant sgRNAs in the primary tumors (at \sim 6 weeks post-transplantation) of three representative mice (one from each replicate mGeCKOa infection). The area for each sgRNA corresponds to the fraction of total reads from the primary tumor for the sgRNA. All sgRNAs with \geq 2% of total reads are plotted individually.

(B) Number of genes with 0, 1, 2, or 3 significantly enriched (FDR < 0.2% for at least one mouse) mGeCKOa sgRNAs targeting that gene. For genes/miRs with 2 or more enriched sgRNAs, genes/miRs are categorized by how many sgRNAs targeting that gene/miR are enriched as indicated in the colored bubbles adjacent to each bar.

(C) Inset: waterfall plot of sgRNAs where multiple sgRNAs targeting the same gene are significantly enriched in primary tumors. Each sgRNA is ranked by the percent of mice in which it is enriched. Only sgRNAs enriched in two or more mice are shown in the main panel. Main panel: enlargement and gene labels for sgRNAs at the top of the list from the inset (boxed region).

See also Figures S3, S4, and S5.

(Figures 3B and 3C). These genes were found to be mutated in patients in many previously reported cancer sequencing studies curated by cBioPortal (Cerami et al., 2012; Gao et al., 2013) (Figure S5A). For example, in somatic mutations identified by The Cancer Genome Atlas (TCGA) for NSCLC, including adenocarcinoma (LUAD) (Cancer Genome Atlas Research Network, 2014) and lung squamous cell carcinoma (LUSC) (Cancer Genome Atlas Research Network, 2012), 36% (107/407) of patients have one or more of these 24 genes mutated (Figures S5B and S5C). Several candidates were well-known tumor suppressors,

such as *Pten*, cyclin-dependent kinase inhibitor 2b (*Cdkn2b*), neurofibromin 2 (*Nf2/Merlin*), alpha-type platelet-derived growth factor receptor (*Pdgfra*), and integrin alpha X (*Itgax*).

Enriched sgRNAs in Metastases

We also sequenced the sgRNA distributions from three lung lobes for each mouse transplanted with mGeCKOa-transduced Cas9-GFP KPD cells. In each lobe, the sgRNA representation is dominated by one or a few sgRNAs (Figures 4A, S3D, and S4I). In each mouse, the lung sgRNA representation (average of

normalized sgRNA representations from three lobes) is also dominated by a small number of sgRNAs (on average, 3.4 ± 0.4 sgRNAs with >5% of total reads) (Figure 4B), suggesting that metastases were seeded by a small set of cells, which grew to dominance over this timescale. Non-targeting sgRNAs were occasionally detected in the metastases but were never observed at high frequency (<0.1% of total reads in any lobe; Figures 2C, 4A and 4B, and S4I). These observations are consistent with our finding that untransduced tumors are not metastatic (Figure 1E), suggesting that specific sgRNA-mediated mutations led to metastasis.

The sgRNA representations in the lung metastases are similar to those in the late-stage primary tumors in several ways. First, the detected sgRNAs in lung samples overlap significantly with those in late tumor samples (chi-square test, $p < 10^{-15}$) (Figure S3E). Second, the number of sgRNAs detected in lung samples correlates, albeit weakly, with the number of sgRNAs detected in late primary tumor samples (ρ = 0.42, F test, p = 0.097) (Figure S3F). Third, the abundance (number of reads) of sgRNAs in the lung correlates positively with that in the late primary tumors of the same mouse (correlation, $\rho = 0.18$ on average, F test, p < 0.01, n = 9) (Figure S3G). Fourth, in most mice (8/9), the lung metastasis enriched sgRNAs also occupy a large fraction of reads in the late primary tumor of the same mouse (Figure 4C, left panel), significantly larger than a random sampling of the same number of sgRNAs from the mGeCKOa library (Figure 4C, right panel). These data indicate that mutants with preferential ability to proliferate in late primary tumors are more likely to dominate the metastases.

The three methods (threshold, rank, or FDR) of finding enriched sgRNAs in the lung metastases yield similar results (Figure S4B). Using the non-targeting sgRNA distribution to set a FDR-based cutoff for enrichment, the enriched sgRNAs in different lobes of the same mouse overlap with each other by $62\% \pm 5\%$ (chi-square test, p < 10^{-15}) (Figure S4C), while different mice show greater variability while still overlapping significantly (29% \pm 3%, chi-square test, p < 10⁻¹⁵) (Figure S4D). The overlap between sgRNAs in different biological/infection replicate experiments when pooling enriched sgRNAs from all mice in the same replicate is 54% (chi-square test, p < 10^{-15}) (Figure S4E), suggesting that pooling sgRNAs from mice in the same experiment facilitates the identification of shared hits. These data suggest that the three independent experiments reproducibly captured a common set of hits and provide a picture for in vivo experimental variation between different lobes, different animals, and different infection replicates.

We found 147 sgRNAs enriched in more than one lobe, and 105 sgRNAs enriched in the lung of more than one mouse (Figures 4D and 4E). These include sgRNAs targeting Nf2, Pten, tripartite motif-containing protein 72 (Trim72), fibrinogen alpha chain (Fga), Bid, cyclin-dependent kinase inhibitor 2a (Cdkn2a), zinc finger FYVE domain-containing 28 (Zfyve28), reproductive homeobox 13 (Rhox13), and BRISC and BRCA1 A complex member 1 (Babam1), as well as microRNA genes miR-152 and miR-345. Intriguingly, a few sgRNAs targeting the Pol II subunits and olfactory receptor are also enriched in the lung, possibly due to off-target effects or unknown roles of these genes. For most sgRNAs detected in lung metastases, the relative abundance in metastases is lower than that in the late primary tumor of the

same mouse, with a metastasis-primary ratio (MPR) less than 1 (Figure S4F), likely due to more skewed distributions of sgRNAs in the metastases compared to those in the late primary tumors. A small subset of sgRNAs, however, are more abundant in metastases than in primary tumors (MPR > 1) in multiple mice, e.g., sgRNAs targeting Nf2, Trim72, prostaglandin E synthase 2 (Ptges2), or ubiquitin-conjugating enzyme E2G 2 (Ube2g2) (Figure 4F).

For four genes, Nf2, Pten, Trim72, and Zfyve28, two independent sgRNAs targeting different regions of the same gene were enriched in lung metastases (Figure 4G). One of the Zfyve28-targeting sgRNAs, however, is enriched in only one mouse, whereas Nf2, Pten, and Trim72 all have two sgRNAs enriched in multiple mice (Figure 4H). These three genes, several representative genes with one frequently enriched sgRNA (Cdkn2a, Fga, and Cryba4), and the two top-scoring microRNAs (miR-152 and miR-345) were chosen to assay individually for primary tumor growth and metastases formation.

Validation In Vivo Using Individual sgRNAs

For these eight genes (Nf2, Pten, Trim72, Cdkn2a, Fga, Cryba4, miR-152, and miR-345), we cloned multiple sgRNAs targeting each of them into the lentiGuide-Puro vector and transduced them into the Cas9-GFP KPD cell line (Figure 5A) (Experimental Procedures). As expected, these sgRNAs generated a broad distribution of NHEJ-mediated indels at the target site when examined 3 days post-transduction, with a bias toward deletions (Figure 5B). For protein-coding genes, the majority (>80%) of indels are out of frame, which potentially disrupts the protein functions. For miR-152 and miR-345, the sqRNAs generated mostly deletions (>90% of indels are deletions, average indel size -7 bp) (Figure 5B), overlapping with the loop or mature microRNA sequences in the hairpins, which are structures required for maturation of microRNAs. For proteins where specific antibodies are available (Nf2 and Pten), we found that the majority of the protein products were significantly reduced 1 week after lentiviral sgRNA infection (Figure S6A).

When these single-sgRNA-transduced cells were transplanted into the flanks of immunocompromised mice, they all formed tumors in situ. With two mice injected per sgRNA and three sgRNAs per gene, all genes tested showed increased lung metastasis formation compared to controls (untransduced and non-targeting sgRNAs), with the most significant ones being *Nf2*, *Pten*, and *Cdkn2a* (Fisher's exact test, one-tailed, $p < 10^{-3}$) (Figures 5C and 5D). Fga and Trim72 also have effects on metastasis acceleration (Fga p = 0.001, Trim72 p = 0.046). Cryba4 is not statistically different from controls (p = 0.1). sgRNAs targeting miR-345 or miR-152 significantly increased the rate of metastasis (miR-345 p = 0.01, miR-152 p = 0.046). These data suggest that loss-of-function mutations in any of Nf2, Pten, Cdkn2a, Trim72, Fga, miR345, or miR-152 are sufficient to accelerate the rate of metastasis formation in this genetic background.

Most genes targeted by single sgRNAs also contributed to accelerated primary tumor growth compared to controls (Figure 5E). Nf2 and Pten loss of function dramatically speed up tumor growth (KS test, p < 0.001) (Figure 5E); Cdkn2a-, Trim72-, and Fga-targeting sgRNAs slightly accelerate primary tumor growth (KS test, p = 0.003-0.01); Cryba4 has a marginal effect

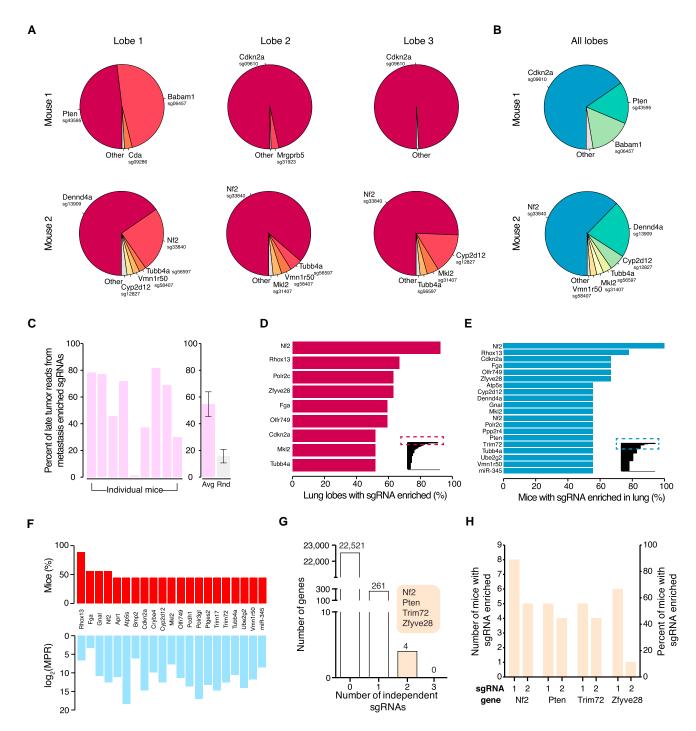


Figure 4. Enriched sgRNAs from the mGeCKOa Screen in Lung Metastases

(A) Pie charts of the most abundant sgRNAs in three individual lobes of the lungs of two representative mice transplanted with mGeCKOa-transduced cells. The area for each sgRNA corresponds to the fraction of total reads from the lobe for the sgRNA. All sgRNAs with $\geq 2\%$ of total reads are plotted individually. (B) Pie charts of the most abundant sgRNAs in the lung (averaged across three individual lobes) for the two mice shown in (A). All sgRNAs with $\geq 2\%$ of average reads are plotted individually.

(C) Left: percentage of late tumor reads for the significantly enriched (FDR < 0.2%) mGeCKOa sgRNAs found in the lung metastases (averaged across three dissected lobes). Right: in purple, the percentage of late tumor reads for the significantly enriched (FDR < 0.2%) mGeCKOa sgRNAs found in the lung metastases (average across all mice, n = 9 mice). In gray, the percentage of late tumor reads for random, size-matched samplings of sgRNAs present in the late tumor (n = 100 samplings). Error bars indicate SD.

(legend continued on next page)

(KS test, p = 0.08); and neither miR-152- nor miR-345-targeting sgRNAs promote primary tumor growth (KS test, p > 0.1). Overall, for the targets we examined using individual sgRNAs, the number of lobes with lung metastases strongly correlates with the terminal volume of the late primary tumor (or average primary tumor growth rate) (correlation, $\rho = 0.83$, F test, p < 0.01) (Figure 5F), indicating at a single-gene level that mutant cells with a stronger ability to promote primary tumor growth generate metastases faster.

To analyze blood samples for the presence of circulating tumor cells (CTCs), we designed a microfluidic device based on the physical size of the Cas9-GFP KPD cells (Figures S6B and S6C). We performed CTC capture with terminal blood samples from mice injected with Cas9-GFP KPD cells transduced with sgRNAs targeting Nf2, Pten, Trim72, Cdkn2a, and miR-152 and from mice injected with Cas9-GFP KPD control cells (untransduced or non-targeting sgRNA) (Figures S6C and S6D). Mice transplanted with cells transduced with sgRNAs targeting Nf2, Pten, Trim72, or Cdkn2a had a higher concentration of CTCs as compared to controls (Figures S6D-S6G), consistent with the higher rate of lung metastasis formation.

Competitive Dynamics of Top Hits Assessed Using an sgRNA Minipool

To better understand the relative metastatic potential of multiple genes from our genome-wide screen, we designed a targeted pooled screen with a smaller library. This small library (termed validation minipool) contains 524 sgRNAs targeting 53 genes that had highly enriched sgRNAs in lung metastases in the genome-wide screen (ten sgRNAs per gene for most genes) plus 100 non-targeting sgRNAs. We also created a size-matched library containing 624 non-targeting sgRNAs (termed control minipool) (Figure 6A). Lentiviruses from these two pools were used to transduce the Cas9-GFP KPD cells, which were cultured in vitro for 1 week and then transplanted into Nu/Nu mice (Figure 6A). Both validation minipool- and control minipool-transduced cells induced primary tumor growth at a similar rate (Figure 6B). However, mice transplanted with validation minipool cells had a dramatically elevated rate of lung metastasis formation (Figure 6C).

We sequenced the validation minipool plasmid library and the transduced cells pre-transplantation, as well as the late-stage primary tumors and whole lungs of the mice at 5 weeks posttransplantation (see Data S2 in Dataset S1). The sgRNA representations correlate strongly between technical replicates of the transduced cell pool, late primary tumors, and lung metastases (Figures S7A and S7D). The sgRNA representation in the cell sample strongly correlated with the plasmid (correlation, $\rho = 0.91$) (Figures S7B and S7D). Almost all (99.4%) sgRNAs were recovered in the plasmid and the cell population (Figure S7C). The late primary tumors retained less than half of the sgRNAs, and the metastases in the whole lung retained only a small fraction (2%-7%) of all sgRNAs (Figure S7C). Enriched sgRNAs from lung metastases clustered with each other and with late primary tumors (Figure S7D). Similar to the genome-wide library, in this validation minipool, the plasmid and cell samples had a unimodal distribution of sgRNAs, whereas the late primary tumors and lung metastases contained a bimodal distribution, with the majority of sgRNAs being absent and a small fraction spanning a large range of non-zero read counts (Figure 6D). Intriguingly, two mice retained relatively high sgRNA diversity in late primary tumors (Figure 6D), likely due to dormant or slowly proliferating cells that remained in low numbers during tumor growth. Similar to the genome-wide library, large shifts in the sgRNA distribution exist between different sample types (KS test, p $< 10^{-15}$ for pairwise comparisons between the cell, primary tumor, and lung metastases, p = 0.02 between plasmid and cell) (Figure 6E).

In the validation minipool, the sgRNAs detected in the late primary tumors or the lungs of five different mice significantly overlap with each other (Figures S7E and S7F). The late primary tumors and lung metastases are dominated by a few sgRNAs (Figures 7A and S7G-S7I), suggesting that these sgRNAs outcompete others during tumor growth and metastasis. With the validation library, the sgRNA representations are highly correlated between late primary tumors and lung metastases (correlation, $\rho = 0.55$ on average, F test, p < 0.01, n = 5) (Figure 7B). The late primary tumors and lung metastases have dozens of sgRNAs at moderate to high frequencies (Figures 7B and 7C). Several genes have multiple independent sgRNAs that are enriched in the lung over the primary tumor (MPR > 1), such as Nf2 (eight sgRNAs), Pten (four sgRNAs), Trim72 (three sgRNAs), Ube2g2 (three sgRNAs), Ptges2 (two sgRNAs), and ATP-dependent DNA ligase IV (Lig4) (two sgRNAs) (Figures 7C and 7D). Two Cdkn2a sgRNAs were present in both late primary tumors and lung metastases in two mice, but with MPR < 1. Fga-, Cryba4-, miR-152-, and miR-345-targeting sgRNAs were not found at high frequency in either late primary tumors or lung metastases, suggesting that they are outcompeted by other loss-of-function mutations (such as Nf2), which agrees with the relatively reduced metastasis formation of these genes in the

⁽D) Inset: all sgRNAs found in individual lung lobes, ordered by the percent of lobes in which a particular sgRNA was among the significantly enriched (FDR < 0.2%) sgRNAs for that lobe. Only sgRNAs enriched in two or more lobes are shown. Main panel: enlargement and gene labels for sgRNAs at the top of the list from the inset (boxed region).

⁽E) Inset: all sgRNAs found in individual mice (averaged across three dissected lobes), ordered by the percent of mice in which a particular sgRNA was among the significantly enriched (FDR < 0.2%) sgRNAs for that mouse. Only sgRNAs enriched in two or more mice are shown. Main panel: enlargement and gene labels for sqRNAs at the top of the list from the inset (boxed region).

⁽F) Bottom: metastasis primary ratio (MPR) for the sgRNAs in mGeCKOa with enrichment in metastases over late tumors (MPR > 1) observed in at least three mice. The sgRNAs are sorted by the number of mice in which the MPR for the sgRNA is greater than 1. Top: number of mice in which the MPR for this sgRNA is greater than 1. In both panels, individual sgRNAs are labeled by gene target.

⁽G) Number of genes with 0, 1, 2, or 3 significantly enriched (FDR < 0.2% for at least one mouse) mGeCKOa sgRNAs in the lung metastases. For genes with 2 enriched sqRNAs, gene names are indicated in the colored bubble adjacent to the bar.

⁽H) Number of mice and percentage of mice in which each sgRNA was enriched in the lung metastases for all genes with multiple enriched sgRNAs. See also Figures S4 and S5.

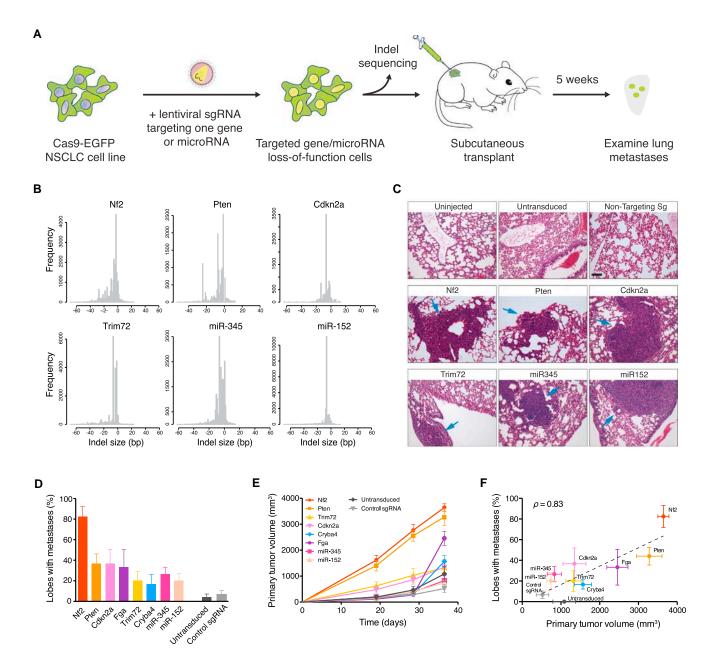
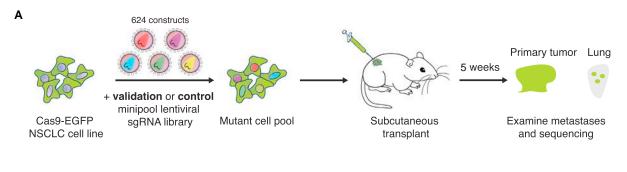


Figure 5. Validation of Target Genes and MicroRNAs from mGeCKOa Screen Using Individual sgRNAs

(A) Schematic representation of lentiviral transduction of Cas9-GFP KPD cells with single sgRNAs designed to target one gene or miR. After puromycin selection, the cell population was transplanted into *Nu/Nu* mice and also deep sequenced to examine the distribution of indels at the target site. After 5 weeks, the primary tumor and lungs were examined.

- (B) Histograms of indel sizes at the genomic locus targeted by a representative sgRNA for each gene/miR after 3 days of puromycin selection. Indels from sgRNAs targeting the same gene were pooled (6 sgRNAs for each protein-coding gene; 4 sgRNAs for each miR).
- (C) Representative H&E staining of lung lobes from uninjected mice (n = 3 mice), mice transplanted with cells transduced with Cas9 only (n = 5), and mice transplanted with cells containing Cas9 and a single sgRNA (n = 6). Single sgRNAs are either control/non-targeting sgRNAs (n = 6 mice for control sgRNAs, 3 distinct control sgRNAs with 2 mice each) or targeting sgRNAs (n = 6 mice for each gene/miR target, 3 sgRNAs per target with 2 mice each). Blue arrows indicate lung metastases. Scale bar, 10 μ m.
- (D) Percent of lung lobes with metastases after 6 weeks for the mice in (C). Error bars indicate SEM.
- (E) Primary tumor growth curve of Nu/Nu mice transplanted with NSCLC cells transduced with Cas9 only (n = 5) or single sgRNAs (n = 6 mice per gene/miR target, 3 sgRNAs per target with 2 mice each; n = 6 mice for control sgRNAs, 3 control sgRNAs with 2 mice each). Error bars indicate SEM.
- (F) Correlation between primary tumor volume and percent of lobes with metastases for each gene in (D) and (E). Error bars indicate SEM. See also Figure S6.



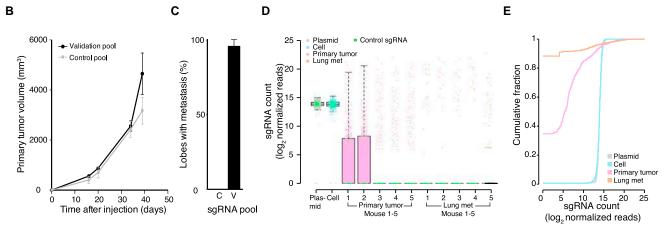


Figure 6. Tumor Evolution and Library Representation in Transplanted Cas9-GFP KPD Cells with Minipool Libraries

(A) Schematic representation of the loss-of-function metastasis minipool screen. Briefly, Cas9-GFP KPD cells were transduced with either validation minipool (524 gene-targeting + 100 non-targeting sgRNAs) or control minipool (624 non-targeting sgRNAs). After puromycin selection, the cell pools were transplanted into Nu/Nu mice. After 5 weeks, validation minipool sgRNAs were sequenced from primary tumor and lung samples.

(B) Primary tumor growth curve of Nu/Nu mice transplanted with Cas9 vector + validation minipool cells (n = 5 mice) or Cas9 + control minipool cells (n = 5 mice). Error bars indicate SEM.

- (C) Percent of lung lobes with metastases after 6 weeks for the mice in (B). C, control minipool; V, validation minipool. Error bars indicate SEM.
- (D) Boxplot of the sgRNA normalized read counts for the plasmid library, cells before transplantation, primary tumors, and lung metastases using the validation
- (E) Cumulative probability distribution of library sgRNAs in the validation plasmid pool, cells before transplantation, primary tumors, and lung metastases. Distributions of primary tumor and lung metastases are averaged across five mice. See also Figure S7.

individual sgRNA validation. These results further validate several of the top hits from the primary screen, using either sgRNA dominance (e.g., Nf2, Pten, Trim72) or MPR (e.g., Nf2, Trim72, Ube2g2, Ptges2). This validation minipool reveals the dynamics of multiple competing mutants chosen from the primary screen hits and indicates that mutants with strong progrowth effects tend to enhance metastasis (Figure 7E).

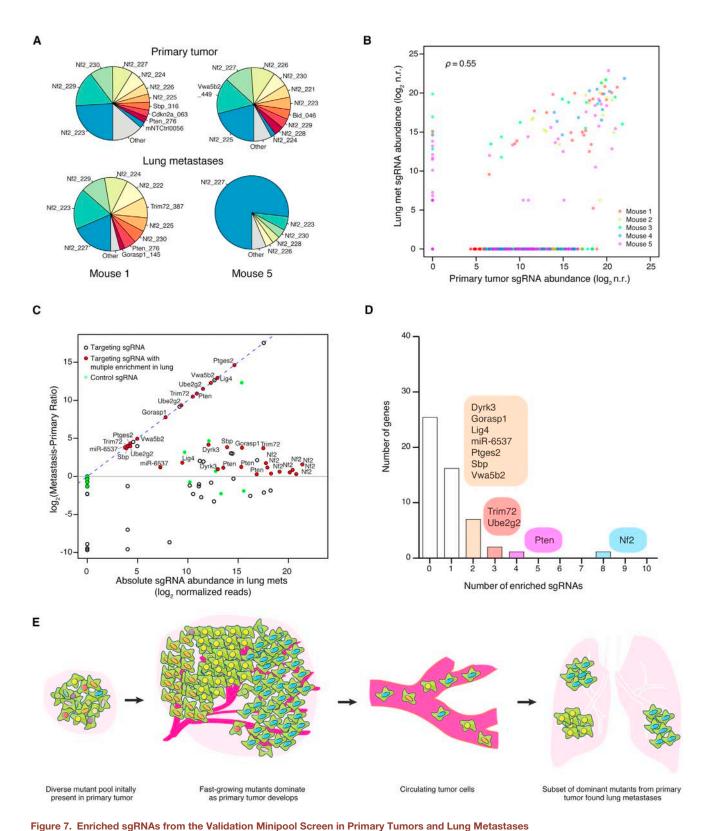
TCGA Gene Expression of Screen Hits in Human Lung Cancer

To assess the relevance of our mGeCKOa and validation minipool screen hits (genes targeted by sgRNAs enriched in lung metastases) to pathological metastasis in human cancer, we performed gene expression analysis of the human orthologs of these genes. We compared mRNA levels in metastatic compared to non-metastatic primary tumors in patient samples using TCGA mRNA sequencing data. We found that most (61%-75%) of these genes are downregulated in metastatic tumors in NSCLC patients (Figures S5D and S5E; Table S6). These data suggest that downregulation of these genes is selected for in metastatic tumors from patients.

DISCUSSION

Pooled Mutagenesis in a Metastasis Model

Distal metastases develop as primary tumors shed CTCs into the circulation, from which CTCs travel to the destination site, move out of the blood or lymphatic vessels, and initiate clonal growth (Valastyan and Weinberg, 2011; Vanharanta and Massagué, 2013; Weinberg, 2007). In this study, cancer cells transplanted into the flanks of mice form primary tumors in situ, and cells from this mass undergo the intravasation-circulation-extravasation-clonal growth cascade to form distal metastases (Francia et al., 2011). The initial lung cancer cell line has little capacity to form metastases; in contrast, after being mutagenized with the mGeCKOa genome-scale Cas9 knockout library, the cell



(A) Pie charts of the most abundant sgRNAs in the primary tumor and the whole lung of two representative mice transplanted with validation minipool-transduced Cas9-GFP KPD cells. The area for each sgRNA corresponds to the fraction of total reads from the tissue (primary tumor or lung metastases) for the sgRNA. All sgRNAs with ≥2% of total reads are plotted individually.

population forms highly metastatic tumors. Thus, these mutations, acting in simple or complex pleiotropic ways, accelerate metastasis. In this model, the effect of mutations on metastasis strongly correlates with their abundance in late-stage primary tumors.

sgRNA Dynamics during Tumor Evolution

The dynamics of the sgRNA population changed dramatically over the course of tumor development and metastasis, reflecting the selection and bottlenecks of cellular evolution in vitro and in vivo. After a week in culture, cells retained most of the sgRNAs present in the plasmid library, with decreases in sgRNAs targeting genes involved in fundamental cellular processes. The distribution of non-targeting control sgRNAs is almost identical to those targeting genes, suggesting that the selective pressure of in vitro culture alone does not radically alter sgRNA representation, similar to previous observations in human melanoma cells (Shalem et al., 2014).

In contrast, less than half of the sgRNAs survive in an earlystage primary tumor. This loss of representation occurs with both gene-targeting sgRNAs and non-targeting control sgRNAs. suggesting that random sampling influences sgRNA dynamics during the transplantation and tumor initiation processes, although we cannot exclude that some of the non-targeting sgRNAs might have detrimental or pro-growth effects. We also detected further dropout of genes involved in fundamental cellular processes in early tumor samples compared to cell samples. Thus, it is likely that the sgRNA dynamics are influenced by a combination of selection and random sampling during transplantation and tumor initiation.

As primary tumors grow, the mutant cells proliferate and compete as a pool. This creates strong selection for sgRNAs targeting anti-apoptotic genes and other tumor suppressors. The majority of the genetic diversity in early tumors is lost during the subsequent 4 weeks of primary tumor growth in mice. Accordingly, sequencing revealed a smaller set of dominant sgRNAs, usually on the order of hundreds to a few thousand per mouse. In addition, almost all of non-targeting sgRNAs are lost during primary tumor growth, which is consistent with selection for cells with special growth and survival properties. This observation is also consistent with earlier transplantation studies by Kerbel and colleagues using small pools of randomly mutagenized cells, which found that the majority of clonal variants detectable by Southern blot disappeared within 6 weeks of primary tumor growth, leaving one dominant clone (Korczak et al., 1988; Waghorne et al., 1988).

Each step toward metastasis has a bottleneck effect. In the lung metastases, we detected very few sgRNAs at high abundance. As with the primary tumor, we found only a few non-targeting sgRNAs at low frequencies in metastases. Their presence could be due to unknown off-target effects of these sgRNAs, random shedding of CTCs in the primary tumor, or clustering together with other strongly selected CTCs during metastasis (Aceto et al., 2014).

Relevance of Screen Hits to Human Cancer

Several of the genes enriched in late-stage primary tumors are associated with cancer, but their functions in tumor growth are poorly understood. For example, Mgmt, a gene with two enriched sgRNAs, is required for DNA repair and is thus crucial for genome stability (Tano et al., 1990). Mutation, silencing, or promoter methylation of MGMT is associated with primary glioblastomas (Jesien-Lewandowicz et al., 2009). Med16, another gene with two enriched sgRNAs, encodes a subunit of the mediator complex of transcription regulation, which has been recently implicated in cancer (Huang et al., 2012; Schiano et al., 2014).

We found that the genes that are significantly enriched in lung metastases largely overlap with those found in abundance in the late primary tumor. Several of these hits were validated in vivo using multiple individual sgRNAs, including Nf2, Pten, Cdkn2a, Trim72, Fga, miR-152, and miR-345. Nf2, Pten, and Cdkn2a are well-known tumor suppressor genes. Intriguingly, the NF2 locus is mutated at only 1% frequency in primary tumors of human NSCLC patients (LUAD and/or LUSC) (Cancer Genome Atlas Research Network, 2012, 2014). Nf2 mutant mice develop a range of highly metastatic tumors (McClatchey et al., 1998). It is possible that NF2 mutations influence metastases to a greater degree than primary tumor growth, but this awaits metastasis genomics from patient samples. Pten mutations are also associated with advanced stages of tumor progression in a mouse model of lung cancer (McFadden et al., 2014), and PTEN was found to be mutated at 8% in adenocarcinoma patients (LUAD). CDKN2A has been shown to be often inactivated in lung cancer (Kaczmarczyk et al., 2012; Yokota et al., 2003). Fga encodes fibrinogen, an extracellular matrix protein involved in blood clot formation. Fga mutations have been found in various cancer types in TCGA (Lawrence et al. 2013), as well as circulating tumor cells (Lohr et al., 2014). Trim72 is an E3 ubiquitin ligase, and its role in cancer metastasis is largely unknown. Studies have shown that miR-152 and miR-345 are associated with cancer and metastasis (Cheng et al., 2014; Tang et al., 2011). FGF2 and BAG3, which promote metastasis, were predicted targets of miR-152 and miR-345; thus, loss of these

See also Figure S7.

⁽B) Scatterplot of normalized sgRNA read counts in primary tumor and lung metastases for all sgRNAs in the validation minipool for each mouse (different color dots indicate sgRNAs from different mice). log₂ n.r., log₂ normalized reads.

⁽C) log₂ ratio of sgRNA abundance in the lung metastases over the primary tumor (MPR) plotted against the abundance in the lung metastases (n = 5 mice per sgRNA). Green dots are the 100 control sgRNAs. Dots with black outlines are non-control sgRNAs that target genes or miRs. Red dots indicate non-control sgRNAs for which more than one sgRNA targeting the same gene/miR is enriched in the lung metastases over the primary tumor (i.e., log₂(MPR) > 0) and are labeled with the gene/miR targeted. The lung-primary ratio is calculated for individual mice, and these quantities are averaged across mice.

⁽D) Number of genes with 0 to 10 significantly enriched validation minipool sgRNAs in lung metastases. For genes/miRs with 2 or more enriched sgRNAs, genes/ miRs are categorized by how many sgRNAs targeting that gene/miRs are enriched, as indicated in the colored bubbles adjacent to each bar.

⁽E) Schematic illustration of tumor growth and metastasis in the library-transduced NSCLC transplant model. The initially diverse set of loss-of-function mutations in the subcutaneously transplanted pool is selected over time for mutations that promote growth of the primary tumor. A subset of these mutants also dominate lung metastases.

microRNAs may lead to acceleration of metastases, likely due to de-repression of these genes (Cheng et al., 2014; Tang et al., 2011).

In our own analysis of TCGA samples from lung cancer patients, we observed downregulation of the human orthologs of the genes identified in the genome-wide and validation minipool screens at the mRNA level in metastatic tumors compared to non-metastatic tumors, suggesting that these genes may also be inactivated during pathological metastasis. Human orthologs of these genes are often found to be mutated in cancers. Moreover, these genes have been implicated in various pathways and biological processes in tumorigenesis and/or metastasis in human cancer (Tables S7A–S7C). However, most cancer sequencing studies involve samples from primary tumors of patients. In the clinic, metastases are rarely sampled. Future patient sequencing directly from metastases may further connect genes identified in the mouse model to those mutated or silenced in clinical metastases.

Future In Vivo Functional Genomic Screens

Our study provides a roadmap for in vivo Cas9 screens, and future studies can take advantage of this model to explore other oncogenotypes, delivery methods, or metastasis target organs. Genome-scale CRISPR screening is feasible using a transplant model with virtually any cell line or genetic background (e.g., mutations in *EGFR*, *KRAS*, *ALK*, etc.), including a large repertoire of human cell lines from diverse cancer types (Barretina et al., 2012). Other cell delivery methods, such as intravenous injection or orthotopic transplantation, may help identify genes regulating extravasation and clonalization. Examining samples from other stages or sites, such as CTCs or metastases to other organs, can provide a more refined picture of tumor evolution.

In addition to these parameters, several aspects of the screen perturbations themselves can also be modified. Targeted drug therapies or immunotherapies can be applied in conjunction with the in vivo screening strategy to identify genes involved in acquired resistance. Other screening technologies, such as Cas9-mediated activation (Gilbert et al., 2014; Konermann et al., 2015), can identify metastasis-regulating factors that act in a gain-of-function manner. Activation screens that identify oncogenes, as well as dropout screens that identify genetic dependencies, may facilitate identification of novel therapeutic targets. Targeted subpool strategies can be used to reduce the library size and facilitate further confirmation of primary screens. In a customized library, genes can be chosen based on genomic analysis, pathways, or clinical relevance for focused screening libraries. Additionally, application of pooled sgRNA libraries using individually barcoded cells will allow quantitative assessment of the robustness and significance of each candidate hit and will enable analysis of the competitive dynamics among different perturbations. With these promising future directions and the results of our study, Cas9-based in vivo screening establishes a new platform for functional genomics discovery.

EXPERIMENTAL PROCEDURES

Generation of Cas9-GFP Expression Vector

A lentiviral vector, lenti-Cas9-NLS-FLAG-2A-EGFP (lentiCas9-EGFP), was generated by subcloning Cas9 into a lentiviral vector.

Pooled Guide-Only Library Cloning and Viral Production

The Cas9-GFP KPD cell line was transduced at a MOI of \sim 0.4 with lentivirus produced from a genome-wide lentiviral mouse CRISPR knockout guide-only library (Sanjana et al., 2014) containing 67,405 sgRNAs (mGeCKOa, Addgene 1000000053) with at least 400-fold representation (cells per construct) in each infection replicate. A detailed viral production and infection protocol can be found in Extended Experimental Procedures.

Animal Work Statement

All animal work was performed under the guidelines of the MIT Division of Comparative Medicine, with protocols (0411-040-14, 0414-024-17, 0911-098-11, 0911-098-14, and 0914-091-17) approved by the MIT Committee for Animal Care, and were consistent with the Guide for the Care and Use of Laboratory Animals, National Research Council, 1996 (institutional animal welfare assurance no. A-3125-01).

Mice, Tumor Transplant, and Metastasis Analysis in the Primary Screen

Untransduced or mGeCKOa-transduced Cas9-GFP KPD cells were injected subcutaneously into the right side flank of Nu/Nu mice at 3 \times 10 7 cells per mouse. Transplanted primary tumor sizes were measured by caliper. At 6 weeks post-transplantation, mice were sacrificed and several organs (liver, lung, kidney, and spleen) were dissected for examination of metastases under a fluorescence stereoscope.

Mouse Tissue Collection

Primary tumors and other organs were dissected manually. For molecular biology, tissues were flash frozen with liquid nitrogen and ground in 24-well polyethylene vials with metal beads in a GenoGrinder machine (OPS Diagnostics). Homogenized tissues were used for DNA/RNA/protein extractions using standard molecular biology protocols. Tissues for histology were then fixed in 4% formaldehyde or 10% formalin overnight, embedded in paraffin, and sectioned at $6\,\mu m$ with a microtome as described previously (Chen et al., 2014). Slices were subjected to H&E staining as described previously (Chen et al., 2014).

Genomic DNA Extraction from Cells and Mouse Tissues

Genomic DNA from cells and tissues (primary tumors and lungs) was extracted using a homemade modified salt precipitation method similar to the Puregene (QIAGEN/Gentra) procedure. The sgRNA cassette was amplified and prepared for Illumina sequencing as described previously (Shalem et al., 2014). A detailed readout protocol can be found in Extended Experimental Procedures.

Individual Gene and MicroRNA Validation

Six sgRNAs per protein-coding gene and four sgRNAs per microRNA gene were chosen for validation using individual sgRNAs (Table S4). For protein-coding genes, we cloned both the three sgRNAs from the mGeCKOa library and three additional sgRNAs to target each gene. For microRNAs, we used all four sgRNAs from the mGeCKOa library.

Validation and Control Minipool Synthesis and In Vivo Transplantation

Validation and control minipools (Table S5) were synthesized using array oligonucleotide synthesis (CustomArray) and transduced at >1,000-fold representation in Cas9-GFP KPD cells. After 7 days in culture, Cas9-GFP KPD cells transduced with the validation minipool or control minipool were injected subcutaneously into the right side flank of Nu/Nu mice at 3 \times 10 7 cells per mouse with five replicate mice. After 5 weeks, mice were sacrificed, and primary tumors and lungs were dissected.

ACCESSION NUMBERS

Genomic sequencing data have been deposited in the NCBI Sequence Read Archive under accession number PRJNA273894. Plasmids and pooled libraries have been deposited in Addgene (LentiCas9-EGFP: 63592, Metastasis Validation Minipool library: 63594, Mouse Non-targeting Control Minipool: 63595).

SUPPLEMENTAL INFORMATION

Supplemental Information includes Extended Experimental Procedures, seven figures, seven tables, and a dataset and can be found with this article online at http://dx.doi.org/10.1016/j.cell.2015.02.038.

AUTHOR CONTRIBUTIONS

S.C, N.E.S., O.S., F.Z., and P.A.S. conceived and designed the study. S.C., N.E.S., and K.Z. performed all screening and validation experiments. S.C., N.E.S., O.S., and D.A.S. analyzed the data. K.L., J.S., R.W., and H.L. designed the CTC chip and performed CTC analysis. X.S. and J.Q.P. performed western blots. S.C., N.E.S., F.Z., and P.A.S. wrote the manuscript with the input from all authors. P.A.S. and F.Z. supervised the work.

ACKNOWLEDGMENTS

We thank R. Weinberg and R. Kerbel for critically reading the manuscript; the entire P.A.S. lab and F.Z. lab, L. Cong, T. Kelly, X. Ni, M. Nobel, J. Boehm, A. Tsherniak, S. Levine, M. Cornwall-Brady, S. Malstrom, M. Jennings, E. Vasile, C. Whittaker, K. Cormier, R. Bronson, and colleagues at the Koch Institute, Broad Institute, McGovern Institute, and Department of Biology for technical assistance and/or discussion; the Swanson Biotechnology Center for technical support (Genomics, Animal Imaging and Preclinical Testing, Bioinformatics and Computing, Microscopy, Flow Cytometry, Microscopy, and Histology, in particular). This work is supported by grants to P.A.S., including a United States Public Health Service grant R01-CA133404 from the NIH, an MIT-Harvard Center for Cancer Nanotechnology Excellence Grant U54 CA151884 from the National Cancer Institute, a generous gift from the Marie D. and Pierre Casimir-Lambert Fund, an SkTech/MIT Initiative Grant from the Skolkovo Foundation, and the Koch Institute Support (core) grant P30-CA14051 from the National Cancer Institute. F.Z. is supported by the NIH through NIMH grant 5DP1-MH100706) and NIDDK grant 5R01-DK097768; a Waterman Award from the National Science Foundation; the Keck, New York Stem Cell, Damon Runyon, Searle Scholars, Merkin, and Vallee foundations; and Bob Metcalfe. F.Z. is a New York Stem Cell Foundation Robertson Investigator. S.C. is a Damon Runyon Cancer Research Fellow (DRG-2117-12) and also supported by the Dale Frey Award for Breakthrough Scientists. N.E.S. is supported by a Simons Center for the Social Brain Postdoctoral Fellowship and NIH NHGRI award K99-HG008171. O.S. is a fellow of the Klarman Cell Observatory. R.W. is supported by NIH grant U54 CA151884. D.A.S. is supported by a NSF Graduate Research Fellowship. H.L. is supported by Department of Defense grant OCRP W81XWH-14-1-0279. CRISPR reagents (plasmids and libraries) are available to the academic community through Addgene. F.Z. is a co-founder of Editas Medicine and a scientific advisor for Editas Medicine and Horizon Discovery.

Received: December 30, 2014 Revised: February 3, 2015 Accepted: February 18, 2015 Published: March 5, 2015

REFERENCES

Aceto, N., Bardia, A., Miyamoto, D.T., Donaldson, M.C., Wittner, B.S., Spencer, J.A., Yu, M., Pely, A., Engstrom, A., Zhu, H., et al. (2014). Circulating tumor cell clusters are oligoclonal precursors of breast cancer metastasis. Cell 158. 1110-1122.

Barrangou, R., Fremaux, C., Deveau, H., Richards, M., Boyaval, P., Moineau, S., Romero, D.A., and Horvath, P. (2007). CRISPR provides acquired resistance against viruses in prokaryotes. Science 315, 1709-1712.

Barretina, J., Caponigro, G., Stransky, N., Venkatesan, K., Margolin, A.A., Kim, S., Wilson, C.J., Lehár, J., Kryukov, G.V., Sonkin, D., et al. (2012). The Cancer Cell Line Encyclopedia enables predictive modelling of anticancer drug sensitivity. Nature 483, 603-607.

Bolotin, A., Quinquis, B., Sorokin, A., and Ehrlich, S.D. (2005). Clustered regularly interspaced short palindrome repeats (CRISPRs) have spacers of extrachromosomal origin. Microbiology 151, 2551–2561.

Cancer Genome Atlas Research Network (2012). Comprehensive genomic characterization of squamous cell lung cancers. Nature 489, 519-525.

Cancer Genome Atlas Research Network (2014). Comprehensive molecular profiling of lung adenocarcinoma. Nature 511, 543-550.

Cerami, E., Gao, J., Dogrusoz, U., Gross, B.E., Sumer, S.O., Aksoy, B.A., Jacobsen, A., Byrne, C.J., Heuer, M.L., Larsson, E., et al. (2012). The cBiol. cancer genomics portal: an open platform for exploring multidimensional cancer genomics data. Cancer Discovery 2, 401-404.

Chen, S., Xue, Y., Wu, X., Le, C., Bhutkar, A., Bell, E.L., Zhang, F., Langer, R., and Sharp, P.A. (2014). Global microRNA depletion suppresses tumor angiogenesis. Genes Dev. 28, 1054-1067.

Cheng, Z., Ma, R., Tan, W., and Zhang, L. (2014). MiR-152 suppresses the proliferation and invasion of NSCLC cells by inhibiting FGF2. Exp. Mol. Med. 46,

Chylinski, K., Le Rhun, A., and Charpentier, E. (2013). The tracrRNA and Cas9 families of type II CRISPR-Cas immunity systems. RNA Biol. 10, 726-737.

Chylinski, K., Makarova, K.S., Charpentier, E., and Koonin, E.V. (2014). Classification and evolution of type II CRISPR-Cas systems. Nucleic Acids Res. 42, 6091-6105.

Cong, L., Ran, F.A., Cox, D., Lin, S., Barretto, R., Habib, N., Hsu, P.D., Wu, X., Jiang, W., Marraffini, L.A., and Zhang, F. (2013). Multiplex genome engineering using CRISPR/Cas systems. Science 339, 819-823.

Deltcheva, E., Chylinski, K., Sharma, C.M., Gonzales, K., Chao, Y., Pirzada, Z.A., Eckert, M.R., Vogel, J., and Charpentier, E. (2011). CRISPR RNA maturation by trans-encoded small RNA and host factor RNase III. Nature 471,

Francia, G., Cruz-Munoz, W., Man, S., Xu, P., and Kerbel, R.S. (2011). Mouse models of advanced spontaneous metastasis for experimental therapeutics. Nat. Rev. Cancer 11, 135-141.

Gao, J., Aksoy, B.A., Dogrusoz, U., Dresdner, G., Gross, B., Sumer, S.O., Sun, Y., Jacobsen, A., Sinha, R., Larsson, E., et al. (2013). Integrative analysis of complex cancer genomics and clinical profiles using the cBioPortal. Sci. Signal. 6, p11.

Garneau, J.E., Dupuis, M.E., Villion, M., Romero, D.A., Barrangou, R., Boyaval, P., Fremaux, C., Horvath, P., Magadán, A.H., and Moineau, S. (2010). The CRISPR/Cas bacterial immune system cleaves bacteriophage and plasmid DNA. Nature 468, 67-71.

Garraway, L.A., and Lander, E.S. (2013). Lessons from the cancer genome. Cell 153, 17-37.

Gasiunas, G., Barrangou, R., Horvath, P., and Siksnys, V. (2012). Cas9-crRNA ribonucleoprotein complex mediates specific DNA cleavage for adaptive immunity in bacteria. Proc. Natl. Acad. Sci. USA 109, E2579-E2586.

Gilbert, L.A., Horlbeck, M.A., Adamson, B., Villalta, J.E., Chen, Y., Whitehead, E.H., Guimaraes, C., Panning, B., Ploegh, H.L., Bassik, M.C., et al. (2014). Genome-scale CRISPR-mediated control of gene repression and activation. Cell 159, 647-661.

Hanahan, D., and Weinberg, R.A. (2011). Hallmarks of cancer: the next generation. Cell 144, 646-674.

Heimann, R., and Hellman, S. (1998). Aging, progression, and phenotype in breast cancer. J. Clin. Oncol. 16, 2686-2692.

Hsu, P.D., Scott, D.A., Weinstein, J.A., Ran, F.A., Konermann, S., Agarwala, V., Li, Y., Fine, E.J., Wu, X., Shalem, O., et al. (2013). DNA targeting specificity of RNA-guided Cas9 nucleases. Nat. Biotechnol. 31, 827-832.

Huang, S., Hölzel, M., Knijnenburg, T., Schlicker, A., Roepman, P., McDermott, U., Garnett, M., Grernrum, W., Sun, C., Prahallad, A., et al. (2012). MED12 controls the response to multiple cancer drugs through regulation of TGF-β receptor signaling. Cell 151, 937–950.

Jesien-Lewandowicz, E., Jesionek-Kupnicka, D., Zawlik, I., Szybka, M., Kulczycka-Wojdala, D., Rieske, P., Sieruta, M., Jaskolski, D., Och, W., Skowronski, W., et al. (2009). High incidence of MGMT promoter methylation in primary glioblastomas without correlation with TP53 gene mutations. Cancer Genet. Cytogenet, 188, 77-82.

Jinek, M., Chylinski, K., Fonfara, I., Hauer, M., Doudna, J.A., and Charpentier, E. (2012). A programmable dual-RNA-guided DNA endonuclease in adaptive bacterial immunity. Science 337, 816-821.

Kaczmarczyk, G., Lewandowski, R., Trautsolt, W., Ziółkowski, A., and Kozielski, J. (2012). Cytological examination of pleural cavity lavage accompanied by the study of gene promoter hypermethylation of p16 and O6methylguanine-DNA-methyltransferase genes in diagnostics of non-small cell lung cancer metastatic changes into pleura. Contemp Oncol (Pozn) 16, 322-327.

Koike-Yusa, H., Li, Y., Tan, E.P., Velasco-Herrera, Mdel.C., and Yusa, K. (2014). Genome-wide recessive genetic screening in mammalian cells with a lentiviral CRISPR-guide RNA library. Nat. Biotechnol. 32, 267-273.

Konermann, S., Brigham, M.D., Trevino, A.E., Joung, J., Abudayyeh, O.O., Barcena, C., Hsu, P.D., Habib, N., Gootenberg, J.S., Nishimasu, H., et al. (2015). Genome-scale transcriptional activation by an engineered CRISPR-Cas9 complex. Nature 517, 583-588.

Korczak, B., Robson, I.B., Lamarche, C., Bernstein, A., and Kerbel, R.S. (1988). Genetic tagging of tumor cells with retrovirus vectors: clonal analysis of tumor growth and metastasis in vivo. Mol. Cell. Biol. 8, 3143-3149.

Kumar, M.S., Pester, R.E., Chen, C.Y., Lane, K., Chin, C., Lu, J., Kirsch, D.G., Golub, T.R., and Jacks, T. (2009). Dicer1 functions as a haploinsufficient tumor suppressor. Genes Dev. 23, 2700-2704.

Lawrence, M.S., Stojanov, P., Polak, P., Kryukov, G.V., Cibulskis, K., Sivachenko, A., Carter, S.L., Stewart, C., Mermel, C.H., Roberts, S.A., et al. (2013). Mutational heterogeneity in cancer and the search for new cancerassociated genes. Nature 499, 214-218.

Lohr, J.G., Adalsteinsson, V.A., Cibulskis, K., Choudhury, A.D., Rosenberg, M., Cruz-Gordillo, P., Francis, J.M., Zhang, C.Z., Shalek, A.K., Satija, R., et al. (2014). Whole-exome sequencing of circulating tumor cells provides a window into metastatic prostate cancer. Nat. Biotechnol. 32, 479-484.

Mali, P., Yang, L., Esvelt, K.M., Aach, J., Guell, M., DiCarlo, J.E., Norville, J.E., and Church, G.M. (2013). RNA-guided human genome engineering via Cas9. Science 339, 823-826.

McClatchey, A.I., Saotome, I., Mercer, K., Crowley, D., Gusella, J.F., Bronson, R.T., and Jacks, T. (1998). Mice heterozygous for a mutation at the Nf2 tumor suppressor locus develop a range of highly metastatic tumors. Genes Dev. 12, 1121-1133.

McFadden, D.G., Papagiannakopoulos, T., Taylor-Weiner, A., Stewart, C., Carter, S.L., Cibulskis, K., Bhutkar, A., McKenna, A., Dooley, A., Vernon, A., et al. (2014). Genetic and clonal dissection of murine small cell lung carcinoma progression by genome sequencing. Cell 156, 1298–1311.

Nguyen, D.X., Bos, P.D., and Massagué, J. (2009). Metastasis: from dissemination to organ-specific colonization. Nat. Rev. Cancer 9, 274-284.

Rouet, P., Smih, F., and Jasin, M. (1994). Introduction of double-strand breaks into the genome of mouse cells by expression of a rare-cutting endonuclease. Mol. Cell. Biol. 14, 8096-8106.

Sanjana, N.E., Shalem, O., and Zhang, F. (2014). Improved vectors and genome-wide libraries for CRISPR screening. Nat. Methods 11, 783-784.

Sapranauskas, R., Gasiunas, G., Fremaux, C., Barrangou, R., Horvath, P., and Siksnys, V. (2011). The Streptococcus thermophilus CRISPR/Cas system provides immunity in Escherichia coli. Nucleic Acids Res. 39, 9275-9282.

Schiano, C., Casamassimi, A., Rienzo, M., de Nigris, F., Sommese, L., and Napoli, C. (2014). Involvement of Mediator complex in malignancy. Biochim. Biophys. Acta 1845, 66-83.

Schramek, D., Sendoel, A., Segal, J.P., Beronja, S., Heller, E., Oristian, D., Reva, B., and Fuchs, E. (2014). Direct in vivo RNAi screen unveils myosin Ila as a tumor suppressor of squamous cell carcinomas. Science 343, 309-313.

Shalem, O., Sanjana, N.E., Hartenian, E., Shi, X., Scott, D.A., Mikkelsen, T.S., Heckl, D., Ebert, B.L., Root, D.E., Doench, J.G., and Zhang, F. (2014). Genome-scale CRISPR-Cas9 knockout screening in human cells. Science 343, 84-87,

Shao, D.D., Xue, W., Krall, E.B., Bhutkar, A., Piccioni, F., Wang, X., Schinzel, A.C., Sood, S., Rosenbluh, J., Kim, J.W., et al. (2014). KRAS and YAP1 converge to regulate EMT and tumor survival. Cell 158, 171-184.

Tang, J.T., Wang, J.L., Du, W., Hong, J., Zhao, S.L., Wang, Y.C., Xiong, H., Chen, H.M., and Fang, J.Y. (2011). MicroRNA 345, a methylation-sensitive microRNA is involved in cell proliferation and invasion in human colorectal cancer. Carcinogenesis 32, 1207-1215.

Tano, K., Shiota, S., Collier, J., Foote, R.S., and Mitra, S. (1990). Isolation and structural characterization of a cDNA clone encoding the human DNA repair protein for O6-alkylguanine. Proc. Natl. Acad. Sci. USA 87, 686-690.

Valastyan, S., and Weinberg, R.A. (2011). Tumor metastasis: molecular insights and evolving paradigms. Cell 147, 275-292.

Vanharanta, S., and Massagué, J. (2013). Origins of metastatic traits. Cancer Cell 24, 410-421.

Waghorne, C., Thomas, M., Lagarde, A., Kerbel, R.S., and Breitman, M.L. (1988). Genetic evidence for progressive selection and overgrowth of primary tumors by metastatic cell subpopulations. Cancer Res. 48, 6109-6114.

Wang, T., Wei, J.J., Sabatini, D.M., and Lander, E.S. (2014). Genetic screens in human cells using the CRISPR-Cas9 system. Science 343, 80-84.

Weinberg, R.A. (2007). The Biology of Cancer (Garland Science).

Yokota, J., Nishioka, M., Tani, M., and Kohno, T. (2003). Genetic alterations responsible for metastatic phenotypes of lung cancer cells. Clin. Exp. Metastasis 20, 189-193

Zender, L., Xue, W., Zuber, J., Semighini, C.P., Krasnitz, A., Ma, B., Zender, P., Kubicka, S., Luk, J.M., Schirmacher, P., et al. (2008), An oncogenomics-based in vivo RNAi screen identifies tumor suppressors in liver cancer. Cell 135,

Zhou, Y., Zhu, S., Cai, C., Yuan, P., Li, C., Huang, Y., and Wei, W. (2014). Highthroughput screening of a CRISPR/Cas9 library for functional genomics in human cells. Nature 509, 487-491.

Expert Reviews

Nano-plasmonic exosome diagnostics

Expert Rev. Mol. Diagn. 15(6), 725-733 (2015)

Hyungsoon Im¹, Huilin Shao^{1,2}, Ralph Weissleder^{1,3}, Cesar M Castro*^{1,4} and Hakho Lee*¹

¹Center for Systems Biology, Massachusetts General Hospital, Harvard Medical School, Boston, MA 02114. USA ²Institute of Molecular and Cell Biology, Agency for Science, Technology and Research, Singapore 138673, Singapore ³Department of Systems Biology, Harvard Medical School, Boston, MA 02114, USA ⁴Massachusetts General Hospital Cancer Center, Harvard Medical School, Boston, MA 02114, USA *Authors for correspondence: Tel.: +1 617 726 8226 cmcastro@mgh.harvard.edu

hlee@mgh.harvard.edu

Exosomes have emerged as a promising biomarker. These vesicles abound in biofluids and harbor molecular constituents from their parent cells, thereby offering a minimally-invasive avenue for molecular analyses. Despite such clinical potential, routine exosomal analysis, particularly the protein assay, remains challenging, due to requirements for large sample volumes and extensive processing. We have been developing miniaturized systems to facilitate clinical exosome studies. These systems can be categorized into two components: microfluidics for sample preparation and analytical tools for protein analyses. In this report, we review a new assay platform, nano-plasmonic exosome, in which sensing is based on surface plasmon resonance to achieve label-free exosome detection. Looking forward, we also discuss some potential challenges and improvements in exosome studies.

Keywords: cancer • exosome • extracellular vesicles • molecular diagnosis • surface plasmon resonance

The growing emphasis on targeted and personalized therapy concomitantly increases the need to analyze and monitor key cancer proteins and pathway activation [1–3]. Although tissue biopsies remain the gold standard, their invasiveness and limited sampling often present practical challenges with patient management [4].

Exosomes have emerged as a new class of cancer biomarker for clinical diagnostics [5,6]. Exosomes are membrane-bound phospholipid vesicles (50-200 nm in diameter) that are actively secreted by cancer cells (Figure 1). These vesicles carry cellular constituents of their originating cells, including transmembrane and intracellular proteins [7], mRNA [8], DNA [9], miRNA [10], lipids and metabolites and can serve as cellular surrogates [11]. Combined with their large abundance and ubiquitous presence in bodily fluids (e.g., blood, ascites, urine) [5,12,13], exosomes offer significant advantages for cancer monitoring [14-16]. Namely, an exosomal assay can be robust and minimally invasive for repeated tests. As most tumor cells shed exosomes, the assay can also report relatively unbiased readouts of the whole tumor burden, less affected by the scarcity of the samples (e.g., circulating tumor cells to circulating DNAs) or intra-tumoral heterogeneity (e.g., fine-needle aspiration) [17]. Furthermore, the amount and molecular profile of cancer exosomes have been shown to correlate with tumor burden as well as treatment efficacy [17,18]. A number of recent

review articles have highlighted exosomes' role in diagnostics, cell-to-cell interactions and therapeutic opportunities [5,6,19-23]. Despite such clinical potential, routine exosome analysis is still a challenging task. Conventional methods (e.g., Western blotting, ELISA) require large sample volumes (>500 µl per biomarker) and extensive processing (e.g., 3 h with ultracentrifugation) [6,24]. Such assays become impractical when multiple markers need to be profiled or the sample volume is inherently limited (e.g., cerebrospinal fluid)

Various exosome detection platforms have been introduced to overcome these challenges (Figure 2 & Table 1) [17,18,25-30]. Integration with microfluidics allows for exosome analyses in small volumes; adoption into novel sensing methods (e.g., surface plasmon resonance, magnetic resonance) generated exosomal assays with shorter assay time, higher sensitivity and higher throughput. Commercialized nucleic acid sensing technologies (e.g., RainDrop) have been adapted for a variety of exosomal RNA components with high sensitivity. With their high sensitivity and throughput, these new technologies have shown great promise for both exosomal RNA and protein detection over conventional analytical methods.

We have been advancing miniaturized systems to facilitate exosome studies (FIGURE 3). These systems are comprised of two components: microfluidics to facilitate sample preparation and

informahealthcare.com 10.1586/14737159.2015.1041378 © 2015 Informa UK Ltd ISSN 1473-7159 **725**

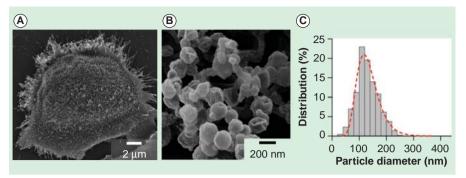


Figure 1. Exosomes shed from ovarian cancer cell. (A) Electron microscopy image of a primary human ovarian cancer cell (CaOV3) confirms the avid release of membrane vesicles by the cell. **(B)** High magnification image shows that the vesicles on the cell surface assumed typical saucer-shaped characteristics of exosomes. **(C)** The size distribution of the exosomes, as characterized by the nanoparticle tracking analysis, ranges from 20 to 250 nm.

Reproduced with permission from [18] © Nature Publishing Group (2014).

analytical tools for protein analyses. The microfluidic devices are designed to collect intact exosomes directly from biological samples, replacing ultracentrifugation or proprietary precipitation methods. The first developed device used a detachable membrane filter (1 µm pore) to sizeselectively enrich exosomes from large sample volumes [31]; the next developed system was based on acoustic actuation, which enabled controllable size-cutoff and continuous, inflow filtration [32]. For protein analyses, we initially adopted the µNMR technology to magnetically profile exosomal proteins [17]. In μNMR, target proteins were labeled with magnetic nanoparticles, and changes in transverse relaxation of the samples were measured. The signal

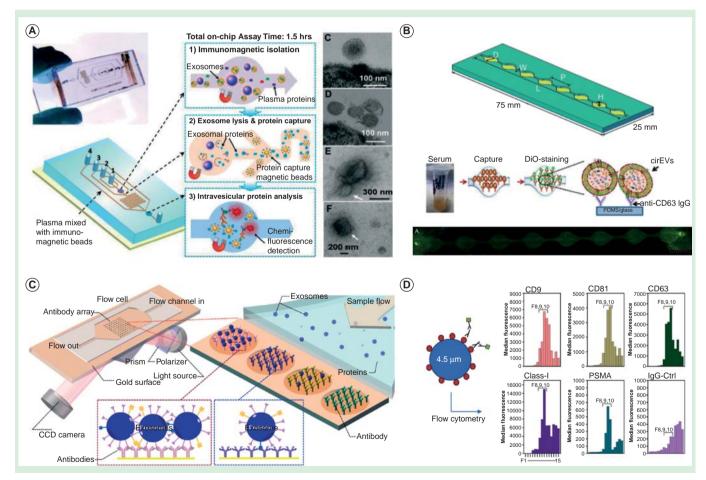


Figure 2. New exosome sensing platforms. (A) An integrated microfluidic chip for exosome isolation, chemical lysis and exosomal protein analysis. Reproduced with permission from [26] published by The Royal Society of Chemistry. **(B)** A microfluidic device (ExoChip) for on-chip exosome capture and analysis. Reproduced from [27] with permission of The Royal Society of Chemistry. **(C)** A surface plasmon resonance imaging (SPRi) system for label-free exosome detection. Reprinted with permission from [29] © American Chemical Society (2014). **(D)** Aptamer-based platform (SOMAscanTM) for proteomic analysis of cancer exosomes. Reproduced with permission from [28].

726Expert Rev. Mol. Diagn. 15(6), (2015)

Table 1. Comparison of exosomal sensing platforms.					
Method	Sensing principle	Target	Sensitivity	Throughput	Ref.
nPLEX	SPR	Protein	~10 ³ exosomes	High (>100 arrays)	[18]
μ NMR	Magnetic resonance	Protein	~10 ⁴ exosomes	Low (single channel)	[17]
ExoChip	Fluorescence	CD63+/Rab5 + EVs	0.5 pM	Low (three channels)	[27]
SOMAscan	Fluorescence	Protein	100 fM	Very high (1129)	[28]
Microfluidic chip	Fluorescence	Protein	0.3 pg/ml	Low (single channel)	[26]
SPRi	SPR	Protein	5×10^7 exosomes/cm ²		[29]
BEAMing & digital PCR	Fluorescence	RNA	0.01% (mutant detection)	High	[25]
miRNA microarray/NanoString	Fluorescence	miRNA		Very high (>1000)	[30]
nPLEX: Nano-plasmonic exosome; SPR: Surface plasmon resonance.					

detection is robust against biological background, and the assay was demonstrated to benefit from such a well-established platform [33–36]. The μNMR assay, however, was difficult to scale up for high-throughput detection. The task requires a large NMR-grade magnet to accommodate multiple NMR probes, and also entails labeling with magnetic nanoparticles. Recently, we developed a new assay system, termed nano-plasmonic exosome (nPLEX) [18] that could overcome these challenges. The nPLEX sensing is based on surface plasmon resonance (SPR) through periodic nanohole arrays, wherein target-specific exosome binding on the array causes significant SPR signal changes. The system is scalable with a large number of sensing units (>100) integrated into a single chip, and the assay is label-free (i.e., no need for secondary labeling with nanoparticles) [37,38].

This special report will review this nascent nPLEX technology, assessing its sensor design, assay protocols, and clinical applications. We will specifically focus on nPLEX's capacity for fast, high-throughput exosome analyses and also discuss directions to further improvements.

nPLEX Technology Sensing principle

The nPLEX system comprises of periodic nanohole arrays made in an opaque gold (Au) film (Figure 4A). Light illumination to the nanohole arrays can excite strong electromagnetic fields, called surface plasmons on the surface (Figure 4B), which lead to SP-mediated extraordinary optical transmission [39,40]. The transmission spectral peak positions are highly sensitive to the refractive index on the nanohole surface, and exosome binding to the nanohole surface (via affinity ligands) would red-shift the optical transmission peaks (Figure 4C). The amount of spectral shift correlates with the molecular mass density [41], which enables quantification of captured exosomes on the sensing surface. Because exosome binding itself induces a spectral shift, the nPLEX can detect exosomes in a label-free manner.

The nanohole-based plasmonic detection has unique advantages over conventional SPR systems (e.g., Kretschmann configuration [42]). First, a simple, collinear optical setup can be used for signal measurements [38,43], and the system can be readily

miniaturized [18,44]. Second, the system is scalable for high-throughput detection. The minimal array size for the extraordinary optical transmission could be as small as 5-by-5 periodic nanoholes (foot print < $10~\mu m^2$) [45], which allows for the integration of high density arrays (> 10^6 detection sites per cm²) [46–48]. Such high density is difficult to achieve with the Kretschmann configuration. The large tilt angle of incidence

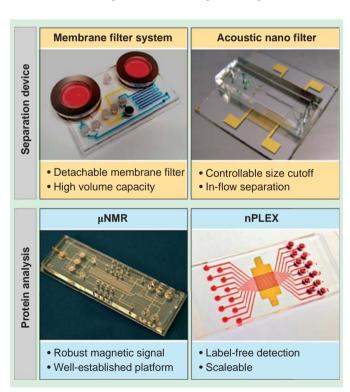


Figure 3. Miniaturized devices developed for exosome separation (top) and its protein profiling (bottom).

Images are adapted with permission from [17,18] © Nature Publishing Group (2014).

Adapted with permission from [31] © American Chemical Society

Adapted with permission from [32] © American Chemical Society (2015).

informahealthcare.com 727

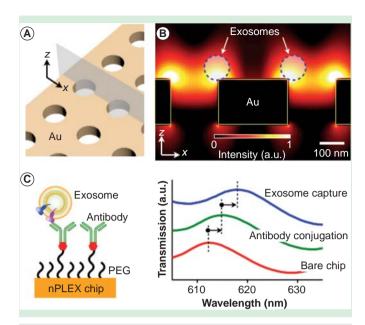


Figure 4. Nano-plasmonic exosome sensing principle. (A) A sensing site comprises a periodic nanohole array patterned in a gold film. (B) Finite-difference time-domain simulation shows the enhanced electromagnetic fields tightly confined near a periodic nanohole surface. The field distribution overlaps with the size of exosomes captured onto the sensing surface. (C) Antibodies were immobilized on the nPLEX chip, and exosomes were captured based on their expression of extravesicular markers (left). Antibody conjugation and exosome binding were monitored by measuring spectral shifts via the nPLEX sensor (right). a.u.: Arbitrary unit; nPLEX: Nano-plasmonic exosome. Reproduced with permission from [18] © Nature Publishing Group (2014).

could lead to optical aberration when a numerical aperture is used to increase spatial resolution or defocusing when imaging arrays in a large area.

System design

The geometry of the nanoholes was optimized through three-dimensional simulation to match the sensing range with the mean diameter of exosomes (~100 nm; Figure 5A). The nPLEX signal was measured by monitoring the transmission spectrum via a spectrometer setup. In this mode, individual arrays are sequentially scanned, and a spectral shift of resonance peak from exosome binding is detected. Although the spectrum-based measurements provide comprehensive information of the nanohole's optical characteristics, it could be time-consuming with large sensing arrays. For faster readout, we alternatively measured changes in transmission intensity at an excitation wavelength (Figure 5B). This intensity-based method could monitor multiple sensing arrays simultaneously, enabling high-throughput parallel measurements.

FIGURE 6A shows the first nPLEX prototype. The structure was patterned in a 200 nm-thick Au film on a glass substrate. We laid out a 12 × 3 array of sensing units with multichannel microfluidics placed on top (FIGURE 6B). Each channel spanned over three sensing units for triplicate measurements. The sample volume per channel was ~1 µl. For parallel measurements of nPLEX arrays, an intensity-based detection system integrated with miniaturized optics consisting of a laser diode and an image sensor was also developed (FIGURE 6C). This system can simultaneously monitor changes in the transmitted light intensities of 36 arrays for high-throughput parallel measurements.

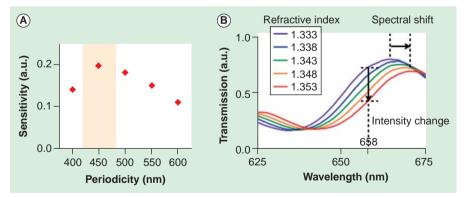


Figure 5. Device design optimization. (A) The sensitivity of the nPLEX sensor was defined as $\Delta\lambda/w$, where $\Delta\lambda$ and w are the shift and the width of SPR spectrum, respectively. The nanohole array with 450-nm hole-pitch showed the highest sensitivity for the detection of 100 nm exosomes. **(B)** Increase in the refractive index on the nPLEX surface induces a spectral shift $(\Delta\lambda)$ of resonance peak to a longer wavelength. The increase of refractive index also causes intensity changes (Δp) at a given wavelength (e.g., at 658 nm). Therefore, exosome binding can be detected by either tracking $\Delta\lambda$ by spectrometry or Δp by imaging.

a.u.: Arbitrary unit; nPLEX: Nano-plasmonic exosome.

Reproduced with permission from [18] © Nature Publishing Group (2014).

Analytical nPLEX assay for molecular profiling

To impart molecular specificity, the nanohole surface was coated with different antibodies in each channel. Following antibody conjugation, exosomes were introduced and spectral shifts were measured before and after exosome binding. An IgG control channel was incorporated to measure the contribution from nonspecific binding and its signal was subtracted from each target channel.

To determine the detection sensitivity, we functionalized the sensor surface with antibodies against CD63, a type III lysosomal membrane protein enriched in exosomes. Alternatively, other exosomespecific lysosomal membrane proteins (e.g., CD9, CD81) were also used [49]. Samples were prepared from CaOV3 (human ovarian carcinoma) cell lines, and their initial exosome concentrations were estimated by nanoparticle-tracking

analysis. A pair of nPLEX sensors, functionalized with CD63 and control IgG antibodies, respectively, were used to measure the relative spectral ($\Delta\lambda^{\text{CD63}}$) or intensity (Δp^{CD63}) changes against known exosome counts. The titration experiments established the limit of detection of ~ 3000 exosomes (670 aM) with the label-free nPLEX assay (Figure 7A). The observed sensitivity based on the limit of detection was 10^4 - and 10^2 -fold higher than Western blotting and chemiluminescence ELISA, respectively.

To quantitatively detect exosome proteins, we functionalized the nPLEX sensors with antibodies against target markers and measured associated signals $(\Delta \lambda^{\text{target}})$ or Δp^{target} from exosome capture. Next, we defined the expression level (ξ^{target}) of the target marker by scaling the marker-associated changes to those of CD63 (i.e., $\xi^{\text{target}} = \Delta \lambda^{\text{target}}/\Delta \lambda^{\text{CD63}} \approx \Delta p^{\text{target}}/\Delta p^{\text{CD63}}$). Such normalization accounted for differences in exo-

some counts among samples and thereby reported the average expression level of a target marker per exosome [17,18]. This method was applied to profile exosomes from different cell lines (CaOV3, OV90) for various extravesicular markers (FIGURE 7B). Expression levels were well-matched ($R^2 > 98\%$) between nPLEX and ELISA, verifying the accuracy of the developed nPLEX assay. In addition, the nPLEX assay could be adapted for downstream genetic analyses by releasing

captured exosomes from the device using surface regeneration protocols [17,18].

Clinical potential of exosomes

We first explored the correlation between exosomes and their parental cells. Multiplexed *in vitro* nPLEX screening showed good agreement of protein expression between exosomes and their parental cells across different ovarian cancer cell lines (FIGURE 8A). Such close matching of molecular profiles between exosome and cells was previously identified in glioblastoma multiforme cell lines using μNMR [17]. In addition, our nPLEX screening showed that EpCAM and CD24 were highly expressed in tested ovarian cancer cell lines.

Based on these results, the nPLEX system was applied to detect ovarian cancer exosomes in patient-derived ascites (Figure 8B). Thirty ascites samples were obtained: 20 patients were diagnosed with Stage 3 (n=10) and 4 (n=10) ovarian

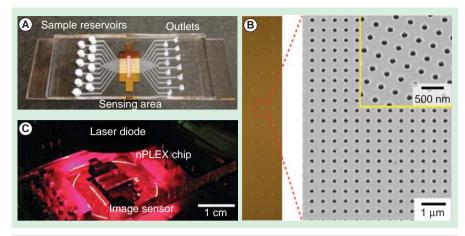


Figure 6. First nano-plasmonic exosome. prototype. (A) A photograph of the nanohole device integrated with microfluidics. A 12-channel fluidic cell was placed on top of a glass slide containing nanohole arrays. **(B)** A total of 36 measurement sites were arranged into a 12×3 array. Each measurement site had periodic nanoholes (right). The structure was patterned in a gold film (200 nm thick) deposited on a glass substrate. **(C)** A photograph of the miniaturized nPLEX imaging system. The nPLEX chip was located directly on an image sensor, which measured transmitted light intensities of the 36 sites simultaneously.

nPLEX: Nano-plasmonic exosome.

Reproduced with permission from [18] © Nature Publishing Group (2014).

cancer and 10 control ascites patients were diagnosed with liver cirrhosis [18]. The study demonstrated that unprocessed ascites contained large quantities (>10⁹ per ml) of exosomes; nPLEX was sensitive enough to detect exosomes directly isolated from ascites by simple syringe membrane filtration; and the levels of EpCAM and CD24 per exosome were significantly higher in ovarian cancer patient samples than in control groups. For 30 samples tested, the detection accuracy was 97% using

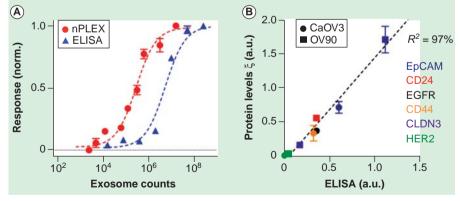


Figure 7. Exosome quantification and protein profiling with nano-plasmonic exosome. (A) Exosomes isolated from human ovarian cancer cell line were introduced onto a nPLEX sensor functionalized with CD63 antibody for exosomal capture. The nPLEX platform showed considerably higher sensitivity than ELISA. (B) Comparison between nPLEX and ELISA measurements. Exosomes isolated from human ovarian cancer cell lines were used. The expression level (ξ) was determined by normalizing the marker signal with that of CD63, which accounted for variation in exosomal counts across samples. All measurements were in triplicate and the data is displayed as mean \pm s.d. nPLEX: Nano-plasmonic exosome.

Reproduced with permission from [18] © Nature Publishing Group (2014).

informahealthcare.com 729

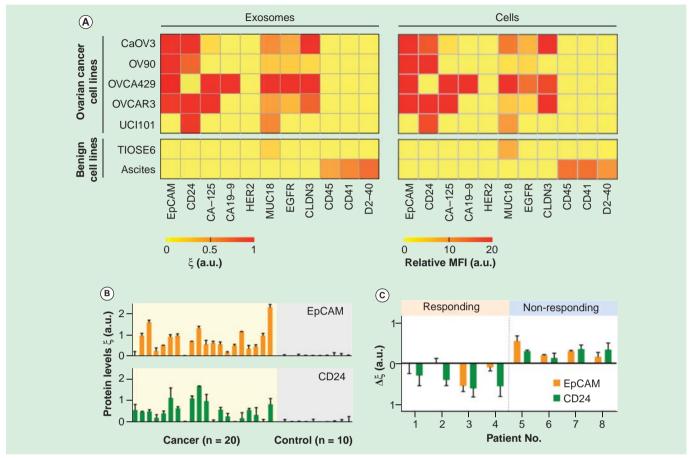


Figure 8. Molecular profiling of ovarian cancer exosomes. (A) *In-vitro* study. Ovarian cancer associated markers (EpCAM, CD24, CA-125, CA19-9, HER2, MUC18, EGFR, Claudin3), immune host cell markers (CD41, CD45) and a mesothelial marker (D2-40) were profiled on both parental ovarian cells (right, using flow cytometry) and their derived exosomes (left, using nPLEX sensor). Exosomal protein profiles showed an excellent match with those of originating cells. A two-marker combination comprising EpCAM and CD24 could effectively distinguish cancer exosomes from benign exosomes. (B) Ascites exosomes from ovarian cancer and non-cancer patients were evaluated by the nPLEX sensor. Cancer exosomes were captured on EpCAM and CD24-specific sensor sites, and the exosomal expression levels of these markers were measured. Ovarian cancer patients (n = 20) were associated with elevated EpCAM and CD24 expression, while non-cancer patients (n = 10) showed negligible signals. (C) Longitudinal nPLEX assays. Ascites samples were collected sequentially from ovarian cancer patients undergoing chemotherapy (n = 8). Measuring temporal changes in exosomal expressions of EpCAM and CD24 could distinguish treatment response.

MFI: Mean fluorescence intensity; nPLEX: Nano-plasmonic exosome.

Reproduced with permission from [18] © Nature Publishing Group (2014).

EpCAM and CD24 as diagnostic markers. The nPLEX screening was further used to evaluate the prognostic values of exosomes for treatment monitoring (Figure 8C). For ovarian cancer patients (n = 8) undergoing standard chemotherapy, the study demonstrated that the levels of exosomal EpCAM, CD24 or both decreased among responding patients, whereas levels of these markers increased in non-responding patients.

Expert commentary

Exosomes present new opportunities for cancer diagnoses and treatment monitoring. These vesicles abound in biological fluids and carry cell-specific cargos (lipids, proteins and genetic materials), which can be harnessed as a minimally invasive means to probe the molecular status of tumors. Significant technical developments are underway to channel exosome

analysis into clinical settings: fluidic-based tools have been devised to facilitate sample preparation, and analytical platforms have been adapted to detect exosomes in clinical samples. Such efforts have started to unveiling tumor-associated exosomal fingerprints, particularly in RNA profiles (both coding and noncoding).

Exosomal protein analysis, on the other hand, still remains challenging. With the lack of universal amplification strategy (e.g., PCR), protein analysis generally requires large quantities of exosomes and often involves extensive sample processing. The nPLEX technology was developed to address these issues. The nPLEX's high sensitivity allows for quantitative measurements on small sample amounts; the detection is label-free to minimize assay time and potential sample loss/degradation; and the system is scalable to a large array for high-throughput assays.

Extended insight into exosomal proteins could help capture dynamic snapshots of tumors, which are hard to detect with genetic assays. Aberrant changes in cancer cells, in response to microenvironmental stress, are reflected in protein levels and its post-translational modification, which have significant effects on disease progression and therapeutic response. As such, the improved exosomal proteomic analyses, proffered by nPLEX, could pave the way for the potential use of exosomes as companion diagnostics and pharmacodynamic readouts.

We identify two immediate directions to further improve the nPLEX technology. First, the assay format needs to be developed to measure both extra- and intravesicular proteins. The initial nPLEX studies were limited to detecting transmembrane or lipid-bound proteins, since the assay was based on capturing whole exosomes on the device surface. Devising a new assay for intravesicular proteins is critical to probe the activation status of proteins as well as to measure cytosolic protein targets. Second, the clinical utility of nPLEX requires further validation under the auspices of larger clinical trials. The large datasets thus generated would aid in identifying key exosomal finger-prints for cancer. These efforts would establish nPLEX as a transformative platform facilitating cancer research and clinical practice.

Five-year view

The trajectories undertaken by the exosome field's development of first-generation analytical tools parallel those of the more mature circulating tumor cell research. Exosomes are abundant and stable in circulation. These advantages impart significant practical value on exosomes as noninvasive and unbiased surrogates for tissue-based biomarkers. As seen in cellular analyses, we envision that more advanced technologies for exosome

enrichment and detection will be developed to ultimately enable high-throughput profiling of single exosomes. This will potentially lead to the identification of exosome subpopulations, highly specific to cancer, which could be prospectively explored in cancer clinical trials. Additional investigations will focus on whether testing of cancer exosomes could generate pharmacodynamic readouts. Coupled with the ready access of liquid biopsies, earlier 'go-no go' decisions could inform drug development. Improved understanding of the mechanisms driving exosomal signaling will accelerate the efforts to exploit exosomal targeting to deliver therapeutic payloads. This transition to theranostics could be a key step for the exosome field and usher in further attention from pharmaceutical stakeholders, among others. Such diverse opportunities create an exciting venue for exosome research - we anticipate an expanding pipeline of committed and accomplished junior and seasoned investigators across disciplines, along with increased funding opportunities for the next 5 years and beyond.

Acknowledgement

The authors thank XO Breakefield (Massachusetts General Hospital, Boston, MA, USA) for help with discussion.

Financial & competing interests disclosure

This work was supported in part by NIH grants R01 HL113156 to H Lee; NIH grants P01 CA069246, U54 CA151884 and T32-CA79443 to R.Weissleder; and DoD OCRP Award W81XWH-14-1-0279 to H Lee. H Shao acknowledges financial support from the B.S.-Ph.D. National Science Scholarship awarded by the Agency for Science, Technology and Research, Singapore. The authors have no other relevant affiliations or financial involvement with any organization or entity with a financial interest in or financial conflict with the subject matter or materials discussed in the manuscript apart from those disclosed.

Kev issues

- Exosomes are membrane-bound vesicles that contain molecular constituents of their cell of origin, including proteins, nucleic acids, lipids and metabolites.
- Exosomes can serve as a minimally invasive biomarker for cancer diagnosis and treatment monitoring.
- Miniatured devices are being developed to expedite exosome isolation and its downstream analyses. These devices could shorten the hands-on assay time and minimize required samples volumes.
- The surface plasmon resonance -based nano-plasmonic exosome (nPLEX) technology enables rapid, sensitive, label-free profiling of exosomal proteins.
- The nPLEX assay is quantitative, reporting the average expression level of target protein markers per exosomes.
- The detection platform is scalable for high-throughput, automated detection.
- By changing the affinity ligands, the nPLEX platform could be used to detect exosomes from virtually any cell type, and hence could serve as a universal platform for exosome analyses.
- Intra-exosomal biology remains an area of active interest given its potential to generate novel pharmacodynamic readouts or therapeutic approaches.

informahealthcare.com 731

References

Papers of special note have been highlighted as:
• of interest

- of considerable interest
- Bidard FC, Weigelt B, Reis-Filho JS. Going with the flow: from circulating tumor cells to DNA. Sci Transl Med 2013;5:207ps14
- Pantel K, Alix-Panabieres C. Real-time liquid biopsy in cancer patients: fact or fiction? Cancer Res 2013;73:6384-8
- Basik M, Aguilar-Mahecha A, Rousseau C, et al. Biopsies: next-generation biospecimens for tailoring therapy. Nat Rev Clin Oncol 2013;10:437-50
- Gerlinger M, Rowan AJ, Horswell S, et al. Intratumor heterogeneity and branched evolution revealed by multiregion sequencing. N Engl J Med 2012;366: 883-92
- Thery C, Ostrowski M, Segura E. Membrane vesicles as conveyors of immune responses. Nat Rev Immunol 2009;9:581-93
- Simpson RJ, Lim JW, Moritz RL, Mathivanan S. Exosomes: proteomic insights and diagnostic potential. Expert Rev Proteomics 2009;6:267-83
- Graner MW, Alzate O, Dechkovskaia AM, et al. Proteomic and immunologic analyses of brain tumor exosomes. FASEB J 2009;23:1541-57
- Skog J, Wurdinger T, van Rijn S, et al. Glioblastoma microvesicles transport RNA and proteins that promote tumour growth and provide diagnostic biomarkers. Nat Cell Biol 2008;10:1470-6
- First paper reporting the role of microvesicles in tumor growth and the potential use as diagnostic biomarkers for glioblastoma.
- Balaj L, Lessard R, Dai L, et al. Tumour microvesicles contain retrotransposon elements and amplified oncogene sequences. Nat Commun 2011;2:180
- Valadi H, Ekström K, Bossios A, et al. Exosome-mediated transfer of mRNAs and microRNAs is a novel mechanism of genetic exchange between cells. Nat Cell Biol 2007;9:654-9
- Kalra H, Simpson RJ, Ji H, et al. Vesiclepedia: a compendium for extracellular vesicles with continuous community annotation. PLoS Biol 2012;10:e1001450
- Raimondo F, Morosi L, Chinello C, et al. Advances in membranous vesicle and exosome proteomics improving biological understanding and biomarker discovery. Proteomics 2011;11:709-20

- Thery C, Zitvogel L, Amigorena S. Exosomes: composition, biogenesis and function. Nat Rev Immunol 2002;2:569-79
- Andre F, Schartz NEC, Movassagh M, et al. Malignant effusions and immunogenic tumour-derived exosomes. Lancet 2002;360: 295-305
- Peinado H, Alečković M, Lavotshkin S, et al. Melanoma exosomes educate bone marrow progenitor cells toward a pro-metastatic phenotype through MET. Nat Med 2012;18:883-91
- Grange C, Tapparo M, Collino F, et al. Microvesicles released from human renal cancer stem cells stimulate angiogenesis and formation of lung premetastatic niche. Cancer Res 2011;71:5346-56
- Shao H, Chung J, Balaj L, et al. Protein typing of circulating microvesicles allows real-time monitoring of glioblastoma therapy. Nat Med 2012;18:1835-40
- Original paper reporting exosome detection in glioblastoma multiforme patients using a miniaturized NMR system.
- Im H, Shao H, Park YI, et al. Label-free detection and molecular profiling of exosomes with a nano-plasmonic sensor. Nat Biotechnol 2014;32:490-5
- Original paper reporting the nPLEX technology; SPR systems were optimized for the exosome analysis.
- Colombo M, Raposo G, Thery C. Biogenesis, secretion, and intercellular interactions of exosomes and other extracellular vesicles. Annu Rev Cell Dev Biol 2014;30:255-89
- Kooijmans SA, Vader P, van Dommelen SM, et al. Exosome mimetics: a novel class of drug delivery systems. Int J Nanomedicine 2012;7: 1525-41
- Kourembanas S. Exosomes: vehicles of intercellular signaling, biomarkers, and vectors of cell therapy. Annu Rev Physiol 2015;77:13-27
- Thery C. Exosomes: secreted vesicles and intercellular communications. F1000 Biol Rep 2011;3:15
- Vlassov AV, Magdaleno S, Setterquist R, Conrad R. Exosomes: current knowledge of their composition, biological functions, and diagnostic and therapeutic potentials. Biochim Biophys Acta 2012;1820:940-8
- Taylor DD, Zacharias W, Gercel-Taylor C. Exosome isolation for proteomic analyses and RNA profiling. Methods Mol Biol 2011;728:235-46

- Chen WW, Balaj L, Liau LM, et al. BEAMing and Droplet Digital PCR Analysis of Mutant IDH1 mRNA in Glioma Patient Serum and Cerebrospinal Fluid Extracellular Vesicles. Mol Ther-Nucl Acids 2013:2
- He M, Crow J, Roth M, et al. Integrated immunoisolation and protein analysis of circulating exosomes using microfluidic technology. Lab Chip 2014;14:3773-80
- Kanwar SS, Dunlay CJ, Simeone DM, Nagrath S. Microfluidic device (ExoChip) for on-chip isolation, quantification and characterization of circulating exosomes. Lab Chip 2014;14:1891-900
- Webber J, Stone TC, Katilius E, et al. Proteomics analysis of cancer exosomes using a novel modified aptamer-based array (SOMAscanTM) Platform. Mol Cell Proteomics 2014;13:1050-64
- Zhu L, Wang K, Cui J, et al. Label-free quantitative detection of tumor-derived exosomes through surface plasmon resonance imaging. Anal Chem 2014;86: 8857-64
- Donker RB, Mouillet JF, Chu T, et al. The expression profile of C19MC microRNAs in primary human trophoblast cells and exosomes. Mol Hum Reprod 2012;18: 417-24
- Rho J, Chung J, Im H, et al. Magnetic Nanosensor for Detection and Profiling of Erythrocyte-Derived Microvesicles. ACS Nano 2013;7:11227-33
- Original paper describing a membrane-based microfluidic devices for vesicle isolation.
- Lee K, Shao H, Weissleder R, Lee H. Acoustic purification of extracellular microvesicles. ACS Nano 2015;9:2321-7
- Original paper reporting the acoustic-wave microfluidic system that performs in-flow separation of microvesicles.
- Lee H, Sun E, Ham D, Weissleder R. Chip-NMR biosensor for detection and molecular analysis of cells. Nat Med 2008;14:869-74
- •• First demonstration of miniaturized NMR system for molecular analysis.
- Haun JB, Castro CM, Wang R, et al. Micro-NMR for rapid molecular analysis of human tumor samples. Sci Transl Med 2011;3:71ra16
- Lee H, Yoon TJ, Figueiredo JL, et al. Rapid detection and profiling of cancer cells in fine-needle aspirates. Proc Natl Acad Sci USA 2009;106:12459-64

732 Expert Rev. Mol. Diagn. 15(6), (2015)

- Issadore D, Min C, Liong M, et al. Miniature magnetic resonance system for point-of-care diagnostics. Lab Chip 2011;11:2282-7
- Im H, Wittenberg NJ, Lesuffleur A, et al. Membrane protein biosensing with plasmonic nanopore arrays and pore-spanning lipid membranes. Chem Sci 2010;1:688-96
- Brolo AG. Plasmonics for future biosensors.
 Nat Photonics 2012;6:709-13
- Ebbesen TW, Lezec HJ, Ghaemi HF, et al. Extraordinary optical transmission through sub-wavelength hole arrays. Nature 1998;391:667-9
- Dahlin AB. Sensing applications based on plasmonic nanopores: The hole story.
 Analyst. 2015. [Epub ahead of print]
- A recent review paper discussing the development of nanopore-based plasmonic nanosensors and their applications.
- 41. Jung LS, Campbell CT, Chinowsky TM, et al. Quantitative interpretation of the

- response of surface plasmon resonance sensors to adsorbed films. Langmuir 1998;14:5636-48
- 42. Homola J. Present and future of surface plasmon resonance biosensors. Anal Bioanal Chem 2003;377:528-39
- Im H, Sutherland JN, Maynard JA, Oh SH. Nanohole-based surface plasmon resonance instruments with improved spectral resolution quantify a broad range of antibody-ligand binding kinetics. Anal Chem 2012;84:1941-7
- Cetin AE, Coskun AF, Galarreta BC, et al. Handheld high-throughput plasmonic biosensor using computational on-chip imaging. Light-Sci Appl 2014;3:e122
- Przybilla F, Degiron A, Genet C, et al. Efficiency and finite size effects in enhanced transmission through subwavelength apertures. Opt Express 2008;16:9571-9
- Im H, Lesuffleur A, Lindquist NC, Oh SH. Plasmonic nanoholes in a multichannel microarray format for parallel kinetic assays

- and differential sensing. Anal Chem 2009:81:2854-9
- Lindquist NC, Lesuffleur A, Im H, Oh SH. Sub-micron resolution surface plasmon resonance imaging enabled by nanohole arrays with surrounding Bragg mirrors for enhanced sensitivity and isolation. Lab Chip 2009;9:382-7
- Escobedo C, Chou YW, Rahman M, et al. Quantification of ovarian cancer markers with integrated microfluidic concentration gradient and imaging nanohole surface plasmon resonance. Analyst 2013;138: 1450-8
- Lotvall J, Hill AF, Hochberg F, et al. Minimal experimental requirements for definition of extracellular vesicles and their functions: a position statement from the International Society for Extracellular Vesicles. J Extracell Vesicles 2014;3:26913
- A recent report describing molecular characteristics of extracellular vesicles.

informahealthcare.com 733



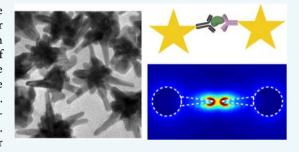
Nanostar Clustering Improves the Sensitivity of Plasmonic Assays

Yong Il Park, † Hyungsoon Im, † Ralph Weissleder, **,†,‡ and Hakho Lee*,†

[†]Center for Systems Biology, Massachusetts General Hospital, Harvard Medical School, Boston, Massachusetts 02114, United States [‡]Department of Systems Biology, Harvard Medical School, Boston, Massachusetts 02115, United States

Supporting Information

ABSTRACT: Star-shaped Au nanoparticles (Au nanostars, AuNS) have been developed to improve the plasmonic sensitivity, but their application has largely been limited to single-particle probes. We herein describe a AuNS clustering assay based on nanoscale self-assembly of multiple AuNS and which further increases detection sensitivity. We show that each cluster contains multiple nanogaps to concentrate electric fields, thereby amplifying the signal via plasmon coupling. Numerical simulation indicated that AuNS clusters assume up to 460fold higher field density than Au nanosphere clusters of similar mass. The results were validated in model assays of protein biomarker detection. The AuNS clustering assay showed higher sensitivity than Au



nanosphere. Minimizing the size of affinity ligand was found important to tightly confine electric fields and improve the sensitivity. The resulting assay is simple and fast and can be readily applied to point-of-care molecular detection schemes.

ocalized surface plasmon resonance (LSPR) is a promising biosensing strategy for molecular detection. 1-4 Based on surface plasmons that are tightly confined on metallic nanoparticles, LSPR is highly sensitive to changes in dielectric environment surrounding the particles. This unique property has been exploited to detect molecular targets upon their binding to a nanoparticle surface. 5-8

The most widely used LSPR materials are noble metal (Ag, Au) nanospheres; their synthetic methods are well established, and these particles show plasmon resonance in visible wavelengths. Recently, star-shaped nanoparticles (nanostars) have been explored as an alternative substate to improve the LSPR sensitivity. Nanostars have multiple branches with sharp tips that generate more localized electromagnetic fields than do spherical nanoparticles and thereby produce larger spectral changes upon molecular binding. Indeed, Au nanostars have shown >5-fold higher sensitivity than Au nanospheres in LSPR sensing. Most previous studies, however, used nanostars as single-particle LSPR probes. 10,13 Namely, the analytical signal was generated when individual nanostars were labeled with target molecules. We hypothesized that the plasmonic signal could be further amplified by inducing the formation of nanostar clusters. This configuration would create multiple nanogaps between nanostars, where electric fields are concentrated and plasmons are coupled.

We herein report on the development and the optimization of such a clustering assay. Using Au nanostars (AuNS) as a substrate, we designed an assay wherein target molecules assemble AuNS into nanoscale-clusters with nanogap junctions. Small AuNS (70 nm in size) with a thiolated ligand were found optimal for sensitive and stable plasmonic sensing. Numerical simulation (finite-difference time-domain/FDTD) showed that a cluster of AuNS can concentrate up to 460-fold higher energy

density than an Au nanosphere cluster. We then experimentally verified the results using different molecular interactions (i.e., biotin-avidin and antigen-antibody). The AuNS clustering assay produced much larger spectral shifts than AuNS-ligand alone. Notably, the signal improvement inversely depended on the interparticle distance, which highlighted the importance of minimizing the size of the capturing ligand. The developed assay benefits from fast binding kinetics (<30 min) and a simple signal readout (colorimetry) and could be a potential tool for point-of-care molecular detection.

To synthesize AuNS, we adopted a seed-mediated growth method (see Experimental Procedures in the Supporting Information). Spherical Au nanoparticles (AuNP) with a mean diameter of 13 nm were prepared as a seed (Figure 1a, left) and dispersed in an Au precursor (HAuCl₄) solution. Starshaped Au nanoparticles with multiple branches were formed when ascorbic acid and silver nitrate were injected into the seed solution (Figure 1a, right). The reaction was rapid (<1 min for completion) and produced AuNS with size variations of <30% (Figure S1). We further controlled the overall size of AuNS by changing the molar concentration ratio between Au3+ and AuNP seeds ($[Au^{3+}]/[AuNP]$). Higher $[Au^{3+}]/[AuNP]$ ratios led to the synthesis of larger AuNS (Figures 1b and S2). When the ratio was $>2 \times 10^7$, Au precursors spontaneously nucleated, resulting in a mixed phase of AuNP and AuNS (Figure S2). Larger AuNS exhibited a LSPR peak at longer wavelength (Figure 1c and d), because they support more extended longitudinal plasmon resonance along their branches.²¹ The peak width also broadened with the particle size (Figure S3),

Received: June 17, 2015 Revised: June 23, 2015

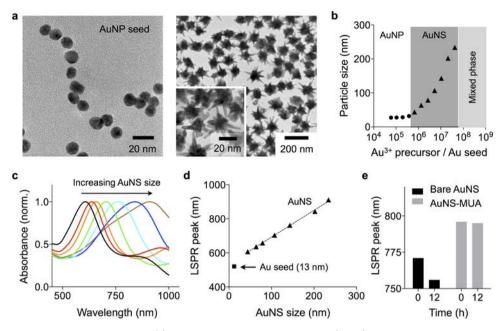


Figure 1. Synthesis and characterization of AuNS. (a) Transmission electron microscopy (TEM) images of AuNP and AuNS. Spherical particles (diameter 13 nm, left) were used as a seed to grow AuNS (right). (b) The size of AuNS was controlled by changing the ratio between AuNP seed and Au³⁺ precursor concentrations. (c, d) Absorbance spectra of AuNS. Increasing the particle size led to shifts of the LSPR peaks to longer wavelengths. (e) Bare AuNS showed a drift in LSPR peak over time. Passivating the AuNS with a thiol ligand (11-mercaptoundecanoic acid/MUA) stabilized the LSPR spectra.

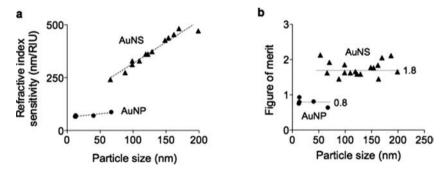


Figure 2. Detection sensitivities of AuNP and AuNS. (a) The refractive index sensitivity (RIS) of AuNS and AuNP of different sizes was measured. The RIS linearly increased with the overall size of the particles. (b) The figure of merit (FOM) was obtained by dividing the RIS with the corresponding full width at half-maximum of the LSPR peak. AuNS assumed higher FOM than AuNP. For a given particle type (i.e., AuNS or AuNP), the FOM values were found similar, independent of the particle size (P = 0.87, AuNS; P = 0.18, AuNP).

which was likely due to the increasing polydispersity (different branch length and number of branches per particle).

As-synthesized bare AuNS were found spectrally unstable; the sharp tips with high surface energy were susceptible to atomic reorganization, which resulted in the shift of the LSPR peaks to shorter wavelengths (Figure 1e). We reasoned that thiol-based ligands could stabilize AuNP by forming a covalent bond with surface Au atoms. Indeed, when AuNS were coated with thiol ligands (e.g., lipoic acid, 11-mercaptoundecanoic acid/MUA, thiolated-polyethylene glycol/PEG), the particles maintained their LSPR peak positions (>12 h in phosphate-buffered saline) (Figures 1e and S4).

We next characterized the LSPR properties of individual AuNS. The refractive index sensitivity (RIS) was determined by measuring spectral shifts of particles suspended in solutions of different refractive indices. Water and dimethyl sulfoxide were mixed at varying volume ratios to control the refractive index (see Experimental Procedures in the Supporting Information). The measured RIS of AuNS increased with the overall particle

size, ranging from 250 to 500 nm/RIU (refractive index unit, Figure 2a). With similar particle volume, AuNS showed higher RIS than AuNP, validating the advantage of forming sharp branches. For example, the sensitivity of 66 nm AuNS (241 nm/RIU) was 3-fold higher than that of 40 nm spherical AuNP (70 nm/RIU). We also compared the figure of merit (FOM) of particles, that was defined as RIS divided by the full width at half-maximum of the LSPR peak (Figure 2b). Particles with high FOM are preferred as they improve the LSPR detection sensitivity. Overall, AuNS had higher FOM (~1.8) than spherical AuNP (~0.8). For a given shape, however, the FOM remained similar (coefficient of variation <12%), because both the RIS and peak-width increased with the particle size. For clustering assays, we thus used small AuNS (~70 nm) for their superior colloidal stability, compared to larger particles.

For molecular sensing with AuNS, we adopted a clustering assay format: AuNS coated with affinity ligands self-assemble into nanoscale clusters in the presence of target molecules (Figure 3a). Such clustering could produce strong plasmonic

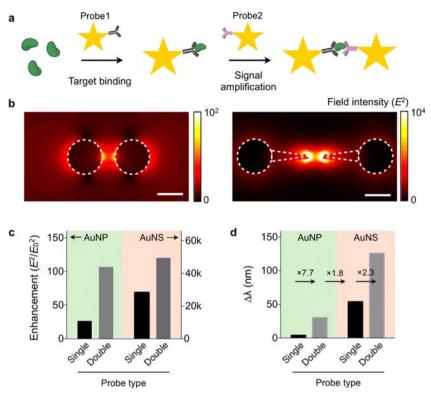


Figure 3. Electromagnetic simulation of the clustering assay. (a) Schematic of the AuNS clustering assay. The target molecule bridges the metal tips of AuNS probes to concentrate electrical fields. (b) Simulated electric field intensity (E^2) surrounding a particle pair. The field magnitude is 460 times higher in the AuNS dimer (right) than in the AuNP dimer (left). Scale bar, 50 nm. (c) The field intensity (E^2) relative to that of the incident light (E_0^2) was compared for different assay configurations. The clustering assay amplifies the signal from the single-probe assay. (d) The spectral shift $(\Delta \lambda)$ for each assay type was calculated from the E-field data. The overall sensitivity improved by >32 fold with the AuNS-clustering assay.

coupling among AuNS to increase the spectral shift. We first performed a three-dimensional finite-difference time-domain (FDTD) simulation (Figure S5). We calculated the electricfield (E-field) of AuNP and AuNS dimers, a simplified version of clusters. The map showed the field intensity (E^2) concentrated at the junction of two metal particles (Figure 3b). The AuNS dimer showed up to 460-fold higher enhancement than the AuNP dimer (Figure 3c), with E-field more efficiently concentrated between tips. The maximum enhancement was observed when two tips of AuNS aligned in a line. Even with misaligned tips, however, the AuNP dimer still showed higher field intensity than the AuNP dimer (Figure S5). The simulation also confirmed that signal amplification could be achieved though particle clustering. Forming a particle-dimer increased the field intensity by 1.7-fold for AuNS (4-fold for AuNP; Figure 3c). Such increases resulted in larger spectral shift $(\Delta \lambda)$. The $\Delta \lambda$ for the AuNS dimer, as estimated from the field information, was 2.3-fold larger than AuNS single particle

We applied the AuNS clustering assay to detect protein targets. As a model system, we used avidin—biotin interaction and first compared the detection sensitivity between AuNS and AuNP. Biotinylated particles with similar volumes (AuNP, 40 nm in diameter; AuNS, 70 nm in overall size) were prepared and concentration-matched (see Experimental Procedures in the Supporting Information for details). Varying concentrations of avidin were added to particle solutions, and resulting spectral shifts ($\Delta\lambda$) were measured. In the presence of avidin, the particles clustered and their spectral peaks red-shifted (Figure 4a). Dynamic light scattering measurements confirmed the avidin-specific clustering; the hydrodynamic diameter increased

with avidin concentration (Figure S6). Dark-field microscopy could also detect AuNS clustering. The aggregated particles appeared brighter than individual particles due to the increased scattering cross-section (Figure S7). The microscopy, however, has a limited assay speed and throughput and requires fine-tuning of particle concentrations to obtain optimal particle numbers in a field-of-view. In all concentrations tested, AuNS showed larger $\Delta \lambda$ than AuNP. For instance, with the addition of 16 nM of avidin, $\Delta \lambda = 19$ nm for AuNS, and $\Delta \lambda = 1.5$ nm for AuNP. Titration measurements further confirmed the superiority of AuNS over AuNP (Figure 4b), with AuNS displaying a 7-fold lower limit of detection (LOD = 3.4 nM) than AuNP (LOD = 23.4 nM).

We next examined the effect of the interparticle distance on the clustering assay sensing. Reducing the interparticle distance (d_{vv}) is crucial in improving the detection sensitivity, since the field enhancement between the tips decreases exponentially with d_{pp} (Figure S8). As a model detection target, we used the kidney injury molecule-1 (KIM1), a urinary protein marker for kidney injury.²⁷ To control the particle distance, we prepared two types of probes (see Experimental Procedures in the Supporting Information): AuNS conjugated with full polyclonal antibodies (Ab-AuNS) and AuNS with half antibody fragments (A $b_{1/2}$ -AuNS). As a control, we prepared AuNS conjugated with isotype-matched IgG antibodies. The KIM1 titration experiments showed dose-dependent spectral shifts (Figure 4c), with the half antibody configuration displaying larger spectral shifts than that with the full-antibody probes. When BSA was used as a control analyte, we observed negligible signal changes (Figure S9); this confirmed that the signal changes were due to antibody-antigen specific aggregation. The LOD for $Ab_{1/2}$ -

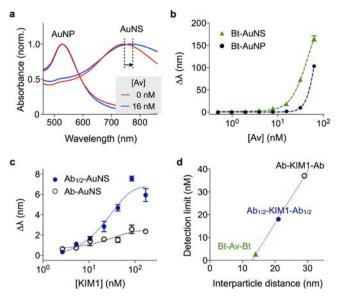


Figure 4. Protein detection with AuNS. (a) Biotinylated AuNP (Bt-AuNP) and AuNS (Bt-AuNS) with similar particle volumes were incubated with avidin, and the corresponding spectral changes were monitored. With the addition of 16 nM of avidin, Bt-AuNS displayed more pronounced spectral shifts ($\Delta \lambda = 19 \text{ nm}$) than Bt-AuNP ($\Delta \lambda = 19 \text{ nm}$) than Bt-AuNP ($\Delta \lambda = 19 \text{ nm}$) 1.5 nm). (b) Avidin-titration experiments confirmed the superior sensitivity of the AuNS system. The limit of detection (LOD) of Bt-AuNS was 7 times lower than that of Bt-AuNP. (c) The effect of the interparticle distance on the assay sensitivity was studied. Kidney injury molecule-1 (KIM1) was used as the detection target. To change the interparticle distance, AuNS was conjugated with either full antibody against KIM1 (Ab-AuNS) or half antibody fragments (Ab_{1/2}-AuNS). The shorter probe (Ab_{1/2}-AuNS) produced larger LSPR spectral shifts in KIM1 titration measurements. AuNS conjugated with isotype-matched goat IgG was used as control. (d) The detection limits of the three systems in (b) and (c) were compared. The detection sensitivity was found to be inversely proportional to the interparticle distance.

AuNS was 2-fold lower than that of Ab-AuNS. We further compared the detection sensitivity as a function of the interparticle distance (Figure 4d, Table S1). The LOD values were obtained from the titration experiments (Figure 4b and 4c), and d_{pp} was estimated from the lengths of the passivation layer, affinity ligands, and target molecules. The avidin—biotin system ($d_{pp} \approx 12$ nm) showed the lowest detection limit (the highest sensitivity), followed by the half antibody—antigen ($d_{pp} \approx 19$ nm) and the full-antibody—antigen ($d_{pp} \approx 33$ nm) systems. The improved sensitivity (2-fold) with a shorter interparticle distance is consistent with our numerical simulation data (Figure S8).

In summary, AuNS are promising nanoprobes for plasmonic biosensing. With multiple branched tips at their surface, AuNS can concentrate electromagnetic fields more efficiently compared to spherical particles and thereby generate larger plasmonic spectral shifts upon molecular binding. In this study, we found three key aspects to improve sensitive biosensing with AuNS, namely 1) a covalent surface coating to maintain particle morphology and its resonance spectra; 2) AuNS clustering to more strongly concentrate electromagnetic energy; and 3) minimizing the interparticle distance in AuNS clusters. The resulting AuNS assay was simple and fast, as the reaction occurs in bulk solution and the signals can be read out from visual color changes. Compared to the microscopic observation of individual AuNS, the method is also scalable for high

throughput detection. We envision that this assay could have potential applications in point-of-care molecular detection.

ASSOCIATED CONTENT

S Supporting Information

Experimental procedures, Figures S1–S9, and Table S1. The Supporting Information is available free of charge on the ACS Publications website at DOI: 10.1021/acs.bioconjchem.5b00343.

AUTHOR INFORMATION

Corresponding Authors

*Phone: 617-726-8226. E-mail: rweissleder@mgh.harvard.edu. Corresponding author address: Center for Systems Biology, Massachusetts General Hospital, 185 Cambridge St, CPZN 5206, Boston, MA 02114 (R.W.).

*E-mail: hlee@mgh.harvard.edu. Corresponding author address: Center for Systems Biology, Massachusetts General Hospital, 185 Cambridge St, CPZN 5206, Boston, MA 02114 (H.L.).

Notes

The authors declare no competing financial interest.

ACKNOWLEDGMENTS

We thank K. Lee for microscopy imaging and H. Shao and H. J. Chung for helpful discussions. This work was supported in part by NIH Grants R01HL113156, R01EB004626, R01EB010011, HHSN268201000044C, U54-CA119349, and T32-CA79443 and Department of Defense OCRP Program Award W81XWH-14-1-0279.

■ REFERENCES

- (1) Hutter, E., and Fendler, J. H. (2004) Exploitation of localized surface plasmon resonance. *Adv. Mater.* 16, 1685–1706.
- (2) Anker, J. N., Hall, W. P., Lyandres, O., Shah, N. C., Zhao, J., and Van Duyne, R. P. (2008) Biosensing with plasmonic nanosensors. *Nat. Mater.* 7, 442–453.
- (3) Jain, P. K., Huang, X., El-Sayed, I. H., and El-Sayed, M. A. (2008) Noble metals on the nanoscale: optical and photothermal properties and some applications in imaging, sensing, biology, and medicine. *Acc. Chem. Res.* 41, 1578–1586.
- (4) Sepulveda, B., Angelome, P. C., Lechuga, L. M., and Liz-Marzan, L. M. (2009) LSPR-based nanobiosensors. *Nano Today* 4, 244–251.
- (5) Haes, A. J., and Van Duyne, R. P. (2002) A nanoscale optical blosensor: Sensitivity and selectivity of an approach based on the localized surface plasmon resonance spectroscopy of triangular silver nanoparticles. *J. Am. Chem. Soc.* 124, 10596–10604.
- (6) Sherry, L. J., Jin, R., Mirkin, C. A., Schatz, G. C., and Van Duyne, R. P. (2006) Localized surface plasmon resonance spectroscopy of single silver triangular nanoprisms. *Nano Lett.* 6, 2060–2065.
- (7) Mayer, K. M., and Hafner, J. H. (2011) Localized surface plasmon resonance sensors. *Chem. Rev.* 111, 3828–3857.
- (8) Gao, B., Rozin, M. J., and Tao, A. R. (2013) Plasmonic nanocomposites: polymer-guided strategies for assembling metal nanoparticles. *Nanoscale 5*, 5677–5691.
- (9) Lu, X., Rycenga, M., Skrabalak, S. E., Wiley, B., and Xia, Y. (2009) Chemical synthesis of novel plasmonic nanoparticles. *Annu. Rev. Phys. Chem.* 60, 167–192.
- (10) Nehl, C. L., Liao, H., and Hafner, J. H. (2006) Optical properties of star-shaped gold nanoparticles. *Nano Lett.* 6, 683–688.
- (11) Hao, F., Nehl, C. L., Hafner, J. H., and Nordlander, P. (2007) Plasmon resonances of a gold nanostar. *Nano Lett.* 7, 729–732.
- (12) Senthil, K., Pandian, Pastoriza-Santos, I., Rodriguez-Gonzalez, B., Garcia, d. A., Javier, F., and Liz-Marzan, L. M. (2008) High-yield

synthesis and optical response of gold nanostars. Nanotechnology 19, 015606.

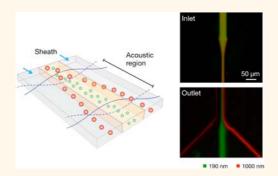
- (13) Dondapati, S. K., Sau, T. K., Hrelescu, C., Klar, T. A., Stefani, F. D., and Feldmann, J. (2010) Label-free biosensing based on single gold nanostars as plasmonic transducers. *ACS Nano* 4, 6318–6322.
- (14) Barbosa, S., Agrawal, A., Rodriguez-Lorenzo, L., Pastoriza-Santos, I., Alvarez-Puebla, R. A., Kornowski, A., Weller, H., and Liz-Marzan, L. M. (2010) Tuning size and sensing properties in colloidal gold nanostars. *Langmuir* 26, 14943—14950.
- (15) Guerrero-Martinez, A., Barbosa, S., Pastoriza-Santos, I., and Liz-Marzan, L. M. (2011) Nanostars shine bright for you Colloidal synthesis, properties and applications of branched metallic nanoparticles. *Curr. Opin. Colloid Interface Sci. 16*, 118–127.
- (16) Vo-Dinh, T., Fales, A. M., Griffin, G. D., Khoury, C. G., Liu, Y., Ngo, H., Norton, S. J., Register, J. K., Wang, H. N., and Yuan, H. (2013) Plasmonic nanoprobes: from chemical sensing to medical diagnostics and therapy. *Nanoscale* 5, 10127–10140.
- (17) Webb, J. A., Erwin, W. R., Zarick, H. F., Aufrecht, J., Manning, H. W., Lang, M. J., Pint, C. L., and Bardhan, R. (2014) Geometry-Dependent Plasmonic Tunability and Photothermal Characteristics of Multibranched Gold Nanoantennas. *J. Phys. Chem. C* 118, 3696–3707.
- (18) Solis, D. M., Taboada, J. M., Obelleiro, F., Liz-Marzan, L. M., and Garcia de Abajo, F. J. (2014) Toward ultimate nanoplasmonics modeling. *ACS Nano* 8, 7559–7570.
- (19) Lu, W., Singh, A. K., Khan, S. A., Senapati, D., Yu, H., and Ray, P. C. (2010) Gold nano-popcorn-based targeted diagnosis, nanotherapy treatment, and in situ monitoring of photothermal therapy response of prostate cancer cells using surface-enhanced Raman spectroscopy. J. Am. Chem. Soc. 132, 18103–18114.
- (20) Yuan, H., Liu, Y., Fales, A. M., Li, Y. L., Liu, J., and Vo-Dinh, T. (2013) Quantitative surface-enhanced resonant Raman scattering multiplexing of biocompatible gold nanostars for in vitro and ex vivo detection. *Anal. Chem.* 85, 208–212.
- (21) Khoury, C. G., and Vo-Dinh, T. (2008) Gold Nanostars For Surface-Enhanced Raman Scattering: Synthesis, Characterization and Optimization. *J. Phys. Chem. C* 2008, 18849—18859.
- (22) Im, H., and Oh, S. H. (2014) Oxidation sharpening, template stripping, and passivation of ultra-sharp metallic pyramids and wedges. *Small* 10, 680–684.
- (23) Malinsky, M. D., Kelly, K. L., Schatz, G. C., and Van Duyne, R. P. (2001) Chain length dependence and sensing capabilities of the localized surface plasmon resonance of silver nanoparticles chemically modified with alkanethiol self-assembled monolayers. *J. Am. Chem. Soc.* 123, 1471–1482.
- (24) Vega, M. M., Bonifacio, A., Lughi, V., Marsi, S., Carrato, S., and Sergo, V. (2014) Long-term stability of surfactant-free gold nanostars. *J. Nanopart. Res.* 16, 2729.
- (25) Joshi, G. K., McClory, P. J., Muhoberac, B. B., Kumbhar, A., Smith, K. A., and Sardar, R. (2012) Designing Efficient Localized Surface Plasmon Resonance-Based Sensing Platforms: Optimization of Sensor Response by Controlling the Edge Length of Gold Nanoprisms. *J. Phys. Chem. C* 116, 20990–21000.
- (26) Bu, T., Zako, T., Fujita, M., and Maeda, M. (2013) Detection of DNA induced gold nanoparticle aggregation with dark field imaging. *Chem. Commun.* 49, 7531–7533.
- (27) Waanders, F., van Timmeren, M. M., Stegeman, C. A., Bakker, S. J., and van Goor, H. (2010) Kidney injury molecule-1 in renal disease. *J. Pathol.* 220, 7–16.

Acoustic Purification of Extracellular Microvesicles

Kyungheon Lee,† Huilin Shao,† Ralph Weissleder,†,‡ and Hakho Lee*,†

[†]Center for Systems Biology, Massachusetts General Hospital, 185 Cambridge Street, CPZN 5206, Boston, Massachusetts 02114, United States and [‡]Department of Systems Biology, Harvard Medical School, Boston, Massachusetts 02115, United States

ABSTRACT Microvesicles (MVs) are an increasingly important source for biomarker discovery and clinical diagnostics. The small size of MVs and their presence in complex biological environment, however, pose technical challenges in sample preparation, particularly when sample volumes are small. We herein present an acoustic nanofilter system that size-specifically separates MVs in a continuous and contact-free manner. The separation uses ultrasound standing waves to exert differential acoustic force on MVs according to their size and density. By optimizing the design of the ultrasound transducers and underlying electronics, we were able to achieve a high separation yield and resolution. The "filter size-cutoff" can be controlled electronically in situ, which



enables versatile MV-size selection. We applied the acoustic nanofilter to isolate nanoscale (<200 nm) vesicles from cell culture media as well as MVs in stored red blood cell products. With the capacity for rapid and contact-free MV isolation, the developed system could become a versatile preparatory tool for MV analyses.

KEYWORDS: nanotechnology · microvesicles · nanoparticle separation · microfluidics · acoustic wave

rith the growing recognition that microvesicles (MVs) can be harnessed for diagnostic purposes, 1,2 concomitantly increasing is the importance of separation technology to enrich these vesicles from biofluids. MVs are membranebound phospholipid vesicles ($\leq 1 \mu m$ in diameter) and are actively secreted by mammalian cells into the circulation. The vesicles carry molecular constituents of their originating cells,³⁻⁷ and are often viewed as partial surrogates of parental cells. Although MVs are abundant in the circulation (>10¹² vesicles in 1 mL of blood), isolating intact MVs is still a challenging task because of their small size and presence in complex media. Conventional batch processes (e.g., multiple filtration, ultracentrifugation) often require larger sample volumes, and entail time-consuming, extensive procedures,8 which can lead to sample loss, and potential structural or molecular changes.

Acoustics-based microfluidics is a simple and yet robust strategy for on-chip particle manipulation.^{9–15} The method generally uses ultrasound waves to exert radiation forces on particles; under the acoustic pressure, particles experience differential

forces according to their mechanical properties (size, density, compressibility). The operation is label-free and can be performed without any physical contact between the field sources and fluidics. These advantages render the technology biocompatible and ideally suited for integration with microfluidics. Many different types of acousto-microfluidic systems have been developed to manipulate micrometer-scale (>1 μ m) objects (e.g., mammalian cells, ^{16,17} droplets, ¹⁸ microspheres ¹⁹ and platelets ²⁰). Acoustic separation of submicrometer MVs, however, has yet to be demonstrated. A major difficulty in such implementation is the requirement for high radiation force, arising from the small size and low compressibility of MVs.

We herein report on an acoustic nanofilter system developed to separate MVs from other contents of biological samples. We hypothesized that acoustic forces could be used to fractionate MVs according to their size, thereby enabling size-selective MV isolation on chip. The device was optimized, specifically in the design of ultrasound transducers and its electronics, to exert maximal acoustic force on MVs. We further

Received for review November 17, 2014 and accepted February 11, 2015.

Published online 10.1021/nn506538f

© XXXX American Chemical Society

^{*} Address correspondence to hlee@mgh.harvard.edu.

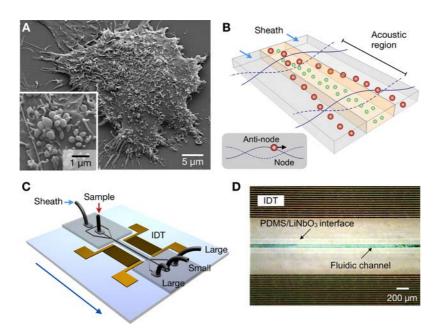


Figure 1. Acoustic nanofilter for label-separation of microvesicles (MVs). (A) Scanning electron microscopy image of MVs released by human brain tumor cells (GBM20/3). The size of MVs are typically <1 μ m. (B) Filter operation. MVs in the acoustic region are under the acoustic radiation pressure and transported to nodes of acoustic pressure region (inset). Larger MVs move faster as the acoustic force is proportional to the MV volume. Sheath flows, positioned at the node region, remove large MVs, whereas the center flow retains small MVs. (C) Device schematic. A pair of interdigitated transducer (IDT) electrodes are used to generate a standing surface acoustic wave across the flow direction. Large MVs are collected at the two side outlets, and small MV at the center outlet. (D) Micrographs of a prototype device. The IDT electrodes were patterned on a piezoelectric (LiNO₃) substrate. The fluidic channel was permanently bonded to the substrate.

constructed an analytical model to fine-tune the size cutoff as well as to estimate the separation yields. The developed system was applied to sort different types of extracellular MVs. We isolated exosomes (diameter <200 nm) from cell culture medium and erythrocyte-derived vesicles from stored blood units. The operation was fast and simple: MVs were collected inside a single microfluidic device in a label-free, continuous and size-tunable manner. The developed system could be a versatile preparatory tool for MV analyses to further extend the utility of acoustofluidics.

RESULTS

Acoustic Nanofilter. The acoustic nanofilter was designed to separate extracellular MVs ($\leq 1~\mu m$; Figure 1A) through in-flow size-fractionation. Figure 1B shows the operation principle. Particles in an acoustic field experience radiation forces and migrate toward the pressure nodes (Figure 1B, inset). The radiation force is proportional to the particle volume, ¹² whereas the viscous drag to the particle size. Larger particle thus move faster to the pressure nodes, and can be transferred into sheath streams to exit. The cutoff size (d_c) can be determined *in situ* through the control of acoustic power and flow speed. Because the filtering is performed in a continuous-flow manner, the risk of channel clogging is minimized.

The device schematic is illustrated in Figure 1C. A pair of interdigitated transducer (IDT) electrodes are

patterned, and used as an ultrasound source. The flow channel has two inlets for sample and sheath fluid, respectively, and is designed to focus the sample flow in the middle of the channel. The IDT electrodes generate a symmetric standing surface acoustic wave (SSAW) field across the channel direction, deflecting large particles toward the side outlets; small particles are collected at the center outlet.

We implemented a prototype device (Figure 1D) using LiNbO₃ piezoelectric wafer as a substrate. The IDT electrodes were patterned via standard lithography (see Materials and Methods for details). The fluidic structure, separately fabricated, was bonded to the SSAW chip (see Supporting Information (SI) Figure S1 for details on the device structure). We chose the acoustic wavelength $\lambda = 100 \ \mu m$ to accommodate a wide channel width (60 μ m) as well as to produce sufficient acoustic forces (>0.1 pN on 1- μ m MVs). The resulting signal frequency for SSAW generation was 38.5 MHz. We further matched the impedance between IDT electrodes and the signal source to maximize the energy transfer. The frequency response of the IDT electrodes was measured, and the equivalent circuit was generated (SI Figure S2). We then used the L-matching network topology to transform the device impedance to that of a signal generator (50 Ω).

Analytical Model. We set up an analytical model for the implemented acoustic nanofilter. The acoustic force (F_a) on a spherical particle (diameter, d) can be expressed as¹⁵

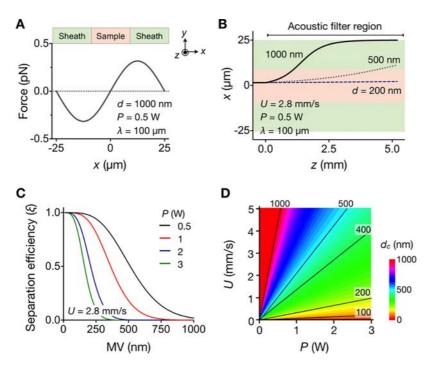


Figure 2. Analytical modeling of the implemented device. (A) Acoustic force (F_a) on MVs (diameter, d=1000 nm) was calculated across the flow direction. Note that F_a has its maximum magnitude inside the sheath flow region. (B) Trajectories of MVs with different diameters were simulated along the flow stream (z-direction). The time for MVs to reach the sheath flow is $\sim d^{-2}$, which can be exploited for size-selective MV sorting. (C) The separation efficiency (ξ) was obtained by estimating the fraction of MVs collected in the center outlet. Higher RF input power (P) leads to enrichment smaller MVs. (D) The filter size cutoff (d_c) was obtained by imposing $\xi < 0.1$. The cutoff values can be set by controlling the input RF power (P) and the flow speed (U). For a given (P, U) setting, MVs with $d < d_c$ will be collected in the center channel. Representative d_c contour lines are shown. This map was used to set the device parameters in the subsequent experiments.

$$F_a = \frac{\pi^2 p^2 d^3}{12\lambda} \cdot \beta_m \cdot \phi \cdot \sin\left(\frac{4\pi}{\lambda} y\right)$$

where p is the acoustic pressure, β_m is the compressibility of the medium, and x is the particle position across the fluidic channel (Figure 2A). The acoustic pressure is further determined from the device characteristics, $p=(PZ/A)^{1/2}$, where Z is the acoustic impedance of the substrate, A is the IDT area, and P is the power of the input signal. The mechanical properties of MVs are represented by the acoustic contrast factor $\phi=(5\rho_p-2\rho_m)/(2\rho_p+\rho_m)-(\beta_p/\beta_m)$, where ρ_p and β_p are the density and the compressibility of the particle, respectively, and ρ_m is the density of the media. Since $\phi>0$, MVs in aqueous buffer move to the pressure nodes where F_a has its extremum values. The wavelength λ is thus controlled to position the nodes in the sheath flow region (Figure 2A).

The motion of MVs in a viscous flow can be obtained by solving ${\bf F_a}+{\bf F_d}=0$ where ${\bf F_a}$ is the acoustic force and the ${\bf F_d}$ is the viscous drag (see Supporting Information for details). Figure 2B shows the simulated trajectory of MVs ($\rho_p=1130~{\rm kg/m^3}$, $\beta_p=3.5\times 10^{-10}~{\rm Pa^{-1}})^{21}$ with different sizes (d=200, 500, and 1000 nm) in an aqueous medium ($\rho_m=1000~{\rm kg/m^3}$, $\beta_m=5.1\times 10^{-10}~{\rm Pa^{-1}}$). Because the acoustic force is proportional to the particle volume and the drag force to the particle diameter, larger MVs move faster to the pressure nodes. Indeed, the transit time (t_0) of MVs

moving from the channel center to the sheath flow is $\sim 1/d^2$, which enables size-selective MV separation.

We further analyzed the separation efficiency (ξ) . As an initial input, we assumed a monodisperse MV population (diameter, d) entering the sample channel. We then calculated the MV fraction collected at the center outlet after the acoustic filtration (SI Figure S3). Figure 2C shows ξ with varying MV size. For a given flow rate (U) and the channel length (L), higher input power (P) leads to steeper rejection of large MVs. By determining the minimum d value for $\xi < 0.1$, we then estimated the size cutoff (d_c) of the device (Figure 2D and Supporting Information). Note that the cutoff can be readily adjusted in the optimal size ranges (100—1000 nm) for MV fractionation, by controlling the operation parameters (P and U).

System Evaluation. We validated the device performance using polystyrene beads. Samples were prepared by mixing two differently sized, fluorescent polystyrene beads (green, d=190 nm; red, d=1000 nm) in phosphate buffered saline (PBS) solution. Prior to sample injection, the fluidic channel was surface-treated (0.1% F127 in PBS) to prevent nonspecific binding of particles. We set the operation parameters (P=0.5 W, U=2.8 mm/s) to achieve $d_c=470$ nm; the acoustic contrast factor ϕ was 0.76, based on the density ($\rho_p=1050$ kg/m³) and the compressibility ($\beta_p=1.5\times10^{-10}$ Pa $^{-1}$) of polystyrene beads.

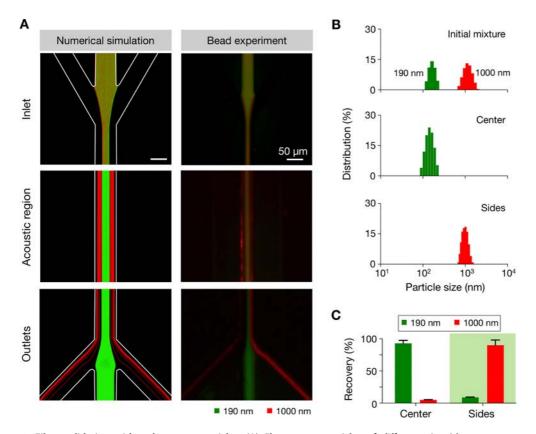


Figure 3. Filter validation with polystyrene particles. (A) Fluorescent particles of different size (d=190 nm, green; d=1000 nm, red) were mixed and processed by the acoustic nanofilter. Trajectories from the numerical simulation (left) and the experimental result (right) showed good agreement, with small and large particles respectively exiting to the center and the side outlets. (B) Particle size distribution measured by dynamic light scattering confirmed the size-selective enrichment of particles. (C) The recovery rate was estimated by comparing the fluorescence intensities of samples before and after the filtration. The observed recovery rate was >90% for both particles.

Fluorescence microscopy (Figure 3A, right) showed size-dependent separation of beads along the fluidic stream. Larger particles (red) migrated to the sheath streams and exited through the side outlets, whereas smaller particles (green) were collected at the center outlet (see SI Movie S1 for time-lapse images). The observed results agreed with those from hydrodynamic simulation (Figure 3A, left). The size distribution of particles, as measured by dynamic light scattering, further confirmed the device operation. We observed two distinct size groups in the initial mixture; these groups were correctly sorted in separate outlets after the acoustic nanofiltration (Figure 3B). The separation efficiency was determined from the fluorescence intensity of the collected particles and showed >90% for both small and large particles (Figure 3C). We further monitored the separation efficiency at different bead concentrations. Samples were prepared by spiking varying amounts of small beads (190 nm) into the suspension of large beads (1000 nm). The acoustic nanofilter maintained a consistent separation efficiency (>90%) with the dynamic range spanning 2 decades (SI Figure S4).

Exosome Purification. We next applied the acoustic nanofilter to enrich exosomes from other types of extracellular MVs. The size of exosomes is considered 1,22 < 200 nm. We thus tuned the device setting (P = 1.5 W,

U=1.5 mm/s) to set the size cutoff $d_c=300$ nm for exosome isolation, using the acoustic contrast factor $\phi=0.38$ for lipid vesicles ($\rho_p=1130$ kg/m³, $\beta_p=3.5\times 10^{-10}$ Pa $^{-1}$). For quantitative analyses, exosomes and larger MVs were prepared from cell culture media via filtration and ultracentrifugation (see Materials and Methods), and were independently labeled with green and red fluorescence, respectively. Known amounts of exosomes and larger MVs were then mixed and processed by the acoustic nanofilter.

Figure 4A shows the size distribution of samples measured by nanoparticle-tracking analysis (NTA) system. The initial mixture displayed two vesicle populations with their median diameter positioned at 149 and 410 nm, respectively. Following the acoustic filtration, the small and large particle populations were separated into the center and side outlets, respectively (see SI Figure S5 for electron micrographs). The recovery rates, estimated from fluorescence intensity measurements, were >80% for exosomes and >90% for larger MVs (Figure 4B). Western blotting (Figure 4C) and immunofluorescent microscopy (SI Figure S5b) further showed the enrichment of exosomes. Samples at the center outlet displayed high expression of exosomal markers, both extravesicular (CD63) and intravesicular (Flotillin-1, HSP70, HSP90), whereas the expression of

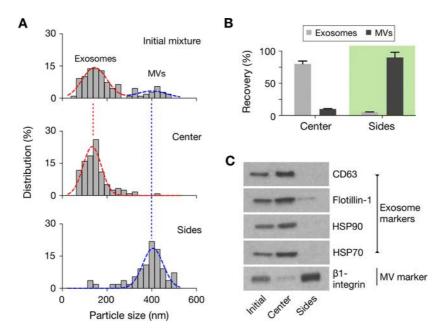


Figure 4. Exosome separation. (A) The acoustic nanofilter was used to separate exosomes (d < 200 nm) from other types of extracellular MVs. The size cutoff (d_c) was set to 300 nm by controlling P = 1.5 W and U = 1.5 mm/s (see Figure 2D). The size distribution of samples after the acoustic filtration was measured via nanoparticle tracking analysis (NTA), which showed the respective enrichment of small and large vesicles in the center and the side outlets. (B) The recovery rate was measured using a mixture of prestained exosomes and bigger MVs. (C) Western blotting further confirmed the enrichment of exosomes. Vesicles collected at the center outlet displayed high expression of exosome protein markers (CD63, Flotillin-1, HSP90, HSP70). MVs at the side outlets had high expression of β 1-integrin, a marker for larger membrane MVs.

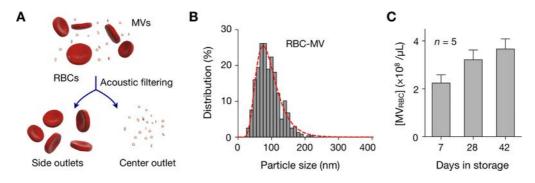


Figure 5. Monitoring of MVs in packed red blood cell (pRBC) units. (A) As a part of their aging process, red blood cells (RBCs) shed MVs. In stored pRBC units, MV numbers thus increase over time. The acoustic nanofilter was used to enrich RBC-derived MVs directly from pRBC samples. The size cutoff (d_c) was set to 450 nm. (B) The size distribution of collected MVs was analyzed by NTA. A single MV population with the mean d=90.9 nm was observed. (c) The concentration of RBC-derived MVs [MV_{RBC}] was serially monitored in pRBC units (n=5). The acoustic nanofilter was used to collect MVs from 10 μ L of pRBC samples. The average [MV_{RBC}] value increased with the storage time.

other vesicular marker (Integrin β 1) was low. The profile was reverse with MVs collected at the side outlets. The results also pointed to the vesicle integrity, demonstrating negligible acoustic damage from bubble cavitation.

MV Separation from Red Blood Cells. We further applied the acoustic filter to purify MVs in packed red blood cell (pRBC) units. As a part of their aging process, RBCs shed MVs (Figure 5A), effectively removing toxic, denatured hemoglobin and membrane proteins. In stored blood units, the number of these RBC-derived MVs increases over time.^{23–25} MV separation and counting thus can be applied in monitoring the quality of blood products. To separate MVs from RBCs, we set the size cutoff

 d_c = 450 nm (P = 1.5 W, U = 2.5 mm/s). pRBC samples were directly processed by the acoustic filter. RBC-MVs were enriched at the center outlet, whereas RBCs were streamed to the side outlets. The size of the collected RBC-MVs was <200 nm (Figure 5B), in agreement with previous reports. The performance of the acoustic filtration was as effective as that of a standard method (see Materials and Methods); the enriched MVs assumed a similar size distribution, and the separation yields were comparable (SI Figure S6). We also monitored the temporal changes of RBC-MV counts. Stored pRBCs units (n = 5) were sampled (10 μ L per sample per time point) and processed at different time points. RBC-MVs were collected by the acoustic nanofilter.

RBC-MV numbers, measured by NTA, indeed significantly increased over time (p < 0.03, ANOVA), thereby confirming their potential as a metric of blood aging.

CONCLUSION

We have developed an acoustic-based microfluidic system for label-free and continuous filtration of MVs. We identified two key parameters which are important in assuring efficient manipulation: (i) high ultrasound frequency and (ii) efficient energy transfer to the sound transducer. We met these requirements by optimizing the transducer geometry (IDT electrodes) and by utilizing the impedance matching network. The resulting system achieved >90% separation yields, and allowed for *in situ* control of size cutoff. Analytical and numerical analyses validated experimental observations, and guided the setting of device parameters for specific MV targets.

The developed system could be a potential preparatory tool for MV analyses. Compared to conventional isolation methods (e.g., ultracentrifugation, membrane

filtration), acoustic filtering is fast, gentle on vesicles, and compatible with limited sample volumes. It also provides an easy approach to change the size-cutoff. In this study, we performed a binary separation (exosomes *vs* larger vesicles; microvesicles *vs* red blood cells). By cascading the separation regions with different size-cutoffs, it would be possible to differentiate multiple types of vesicles according to their size profile (*e.g.*, exosomes, oncosomes, apoptotic bodies). ^{21,26–28}

Several aspects of the system could be further developed to expand its functionality. First, different transducer designs, such as slanted-fingers²⁹ and tilted-angle electrodes,³⁰ could be investigated to better control the acoustic force and improve the sample throughput. Second, integrating analytical components (*e.g.*, sensors, polymerase chain reaction) into the same platform would be another promising approach to realize a portable lab-on-chip for MV analyses. Such advances will facilitate both clinical applications and biological studies of MVs, as well as extend the utility of acoustic microfluidics toward the nanoscale regime.

MATERIALS AND METHODS

Device Fabrication. The acoustic nanofilter consisted of two parts: a standing-surface-acoustic-wave (SSAW) chip and a microfluidic channel. The SSAW chip was fabricated on a piezoelectric substrate. A LiNbO3 wafer with XY 128° cut was purchased (University Wafer). Interdigitated transducer (IDT) electrodes were patterned via conventional optical lithography, and metal layers (Ti, 50 Å; Au, 800 Å) were deposited. The patterned wafer was then cut into a desired size (21 mm imes21 mm) with a dicing saw. The microfluidic structure was fabricated in polydimethylsiloxane (PDMS; Dow Corning) via soft-lithography technique. The channel mold was formed on a Si wafer, using an epoxy-based photoresists (SU-8 2050, Microchem). The cross-section of the channel was 60 μ m \times 80 μ m (width \times height). Both the SSAW chip and the microfluidic block were treated with oxygen plasma, aligned and irreversibly bonded. We used ethanol as a temporary lubricant during the alignment. To strengthen the bonding, the assembly was cured on a hot plate (80 °C) for overnight.

System Setup. As a RF source, a signal generator (Agilent, N5158a) and power amplifiers (Mini circuits, TB-45) were used. The device operation was monitored by an inverted fluorescence microscope (Ti-E, Nikon). Images were recorded by a scientific-CMOS camera (Zyla 5.5, Andor) and analyzed by Image-J software.

Separation Assay with Polystyrene Particles. Fluorescent polystyrene particles with diameters of 190 nm (Dragon Green, Bangs laboratory) and 1000 nm (Flashred, Bangs laboratory) were used. Varying concentration of both particles were mixed in phosphate buffered saline (PBS) solution. Aliquots (50 μL) of the particle mixture were then processed by the acoustic nanofilter. The size distribution of particles at the sample inlet and outlets were measured by dynamic light scattering (Zetasizer Nano ZS, Malvern Instruments). To estimate the separation yields, the fluorescence intensities of the original and the separated samples were measured at the emission wavelength of 513 and 680 nm (Varian Cary Eclipse, Agilent).

Exosome Separation. Microvesicles (MVs) were isolated from cell culture. Human ovarian carcinoma cells (OvCA429, ATCC) were cultured in RPMI-1640 medium (Cellgro) supplemented with fetal bovine serum (FBS, Cellgro, 10%), penicillin and streptomycin (Cellgro, 1%), and L-glutamine (1%). Cells were cultured at 37 °C in a humidified atmosphere containing 5% CO₂.

Cells at passages 1-15 were cultured in vesicle-depleted medium (with 5% depleted FBS) for 48 h. At their 70% confluence, conditioned culture medium was collected from $\sim 10^7$ cells and differentially centrifuged to isolated larger MVs as previously described.⁷ In brief, the medium was filtered through a membrane filter (0.8 μ m pore, Millipore) and centrifuged (10000g, 90 min). The pellet was retrieved as a large MV fraction.³¹ Remaining supernatant was filtered through a 0.22-µm membrane filter (Millipore) and concentrated by differential centrifugation (100000q, 90 min) to isolate exosomes. Vesicle size was independently confirmed by the nanoparticle tracking analysis (NTA; LM10, NanoSight). Exosomes and larger MVs were labeled respectively with green and red fluorescent cell membrane dyes (PKH67 and PKH26, Sigma-Aldrich) before being mixed for sorting. The mixture (50 μ L) was processed by the acoustic nanofilter. The sorted populations were analyzed for their size distribution and fluorescence intensity as described above.

Western Blotting. Isolated MVs were lysed in radio-immuno-precipitation assay buffer and supplemented with protease inhibitors (RIPA buffer, Thermo Scientific). MV samples were collected from the outlets of the microfluidic device and stored at $-20\,^{\circ}\mathrm{C}$ before analysis. Protein concentration was quantified using the bicinchoninic acid assay (BCA assay kit, Thermo Scientific). Protein lysates were loaded and resolved by sodium dodecyl sulfate polyacrylamide gel electrophoresis (SDS-PAGE) and transferred to PVDF membrane (Life Technologies). The PVDF membrane was then incubated overnight with antibodies against CD63 (Santa Cruz), Flotillin-1 (BD Biosciences), HSP90 (Cell Signaling), HSP70 (Cell Signaling) and β 1-integrin (Cell Signaling). Following incubation with secondary antibody (Cell Signaling), enhanced chemiluminescence was used for detection.

MV Isolation from Stored Red Blood Cell (RBC) Units. Packed RBC (pRBC) units were obtained from the Massachusetts General Hospital (MGH) Blood Bank (Boston, MA). The units were preserved in Adsol solution, and stored at 4 °C. For serial MV monitoring, a 10-µL sample was drawn from each pRBC unit using a sterile coupler and 25G needle, after 7, 28, and 42 days of storage. All samples were used directly for sorting with the acoustic nanofilter. The standard MV samples were prepared *via* differential centrifugation steps (400g 20 min, 10000g, 3 min) followed by membrane filtration (0.22 µm pore). The size distribution and concentration of MVs were measured by NTA.

Conflict of Interest: The authors declare no competing financial interest.

Acknowledgment. The authors thank X. O. Breakefield (Massachusetts General Hospital) for access to and assistance with the NTA. The acoustic device was fabricated using the facilities at the Center for Nanoscale Systems (CNS) at Harvard University (National Science Foundation award ECS-0335765). This work was supported in parts by NIH Grants R01 HL113156 (H.L.), P01 CA069246 (R.W.), U54 CA151884 (R.W.), and DoD OCRP Award W81XWH-14-1-0279 (H.L.). This research was also partially supported by Basic Science Research Program through the National Research Foundation of Korea (NRF) funded by the Ministry of Education 2012R1A6A3A03040166 (K.L.)

Supporting Information Available: Design of the microfluidic system; impedance matching; MV distribution in the system; scanning electron micrographs of MV samples; separation efficiency measurement of exosome and MVs from pRBCs; supporting notes for analytical equations and movie. This material is available free of charge via the Internet at http://pubs.acs.org.

REFERENCES AND NOTES

- Thery, C.; Ostrowski, M.; Segura, E. Membrane Vesicles as Conveyors of Immune Responses. *Nat. Rev. Immunol.* 2009, 9, 581–593.
- Simpson, R. J.; Lim, J. W.; Moritz, R. L.; Mathivanan, S. Exosomes: Proteomic Insights and Diagnostic Potential. Expert Rev. Proteomics 2009, 6, 267–283.
- Graner, M. W.; Alzate, O.; Dechkovskaia, A. M.; Keene, J. D.; Sampson, J. H.; Mitchell, D. A.; Bigner, D. D. Proteomic and Immunologic Analyses of Brain Tumor Exosomes. FASEB J. 2009, 23, 1541–1557.
- Skog, J.; et al. Glioblastoma Microvesicles Transport RNA and Proteins That Promote Tumour Growth and Provide Diagnostic Biomarkers. Nat. Cell Biol. 2008, 10, 1470–1476.
- Balaj, L.; Lessard, R.; Dai, L.; Cho, Y. J.; Pomeroy, S. L.; Breakefield, X. O.; Skog, J. Tumour Microvesicles Contain Retrotransposon Elements and Amplified Oncogene Sequences. Nat. Commun. 2011, 2, 180.
- Valadi, H.; Ekstrom, K.; Bossios, A.; Sjostrand, M.; Lee, J. J.; Lotvall, J. O. Exosome-Mediated Transfer of Mrnas and Micrornas is a Novel Mechanism of Genetic Exchange Between Cells. Nat. Cell Biol. 2007, 9, 654–659.
- Shao, H.; Chung, J.; Balaj, L.; Charest, A.; Bigner, D. D.; Carter, B. S.; Hochberg, F. H.; Breakefield, X. O.; Weissleder, R.; Lee, H. Protein Typing of Circulating Microvesicles Allows Real-Time Monitoring of Glioblastoma Therapy. *Nat. Med.* 2012, 18, 1835–1840.
- Thery, C.; Amigorena, S.; Raposo, G.; Clayton, A. Isolation and Characterization of Exosomes from Cell Culture Supernatants and Biological Fluids. *Current Protocols in Cell Biology*; Wiley: New York, 2006; Chapter 3, No. Unit 3.22.
- Bruus, H.; Dual, J.; Hawkes, J.; Hill, M.; Laurell, T.; Nilsson, J.; Radel, S.; Sadhal, S.; Wiklund, M. Forthcoming Lab on a Chip Tutorial Series on Acoustofluidics: Acoustofluidics-Exploiting Ultrasonic Standing Wave Forces and Acoustic Streaming in Microfluidic Systems for Cell and Particle Manipulation. Lab Chip 2011, 11, 3579–3580.
- Yeo, L. Y.; Friend, J. R. Surface Acoustic Wave Microfluidics. Annu. Rev. Fluid Mech. 2014, 46, 379–406.
- Shi, J.; Ahmed, D.; Mao, X.; Lin, S. C.; Lawit, A.; Huang, T. J. Acoustic Tweezers: Patterning Cells and Microparticles Using Standing Surface Acoustic Waves (SSAW). *Lab Chip* 2009, 9, 2890–2895.
- Bruus, H. Acoustofluidics 7: The Acoustic Radiation Force on Small Particles. Lab Chip 2012, 12, 1014–1021.
- Lenshof, A.; Magnusson, C.; Laurell, T. Acoustofluidics 8: Applications of Acoustophoresis in Continuous Flow Microsystems. *Lab Chip* 2012, 12, 1210–1223.
- Lenshof, A.; Laurell, T. Continuous Separation of Cells and Particles in Microfluidic Systems. Chem. Soc. Rev. 2010, 39, 1203–1217.

- Shi, J.; Huang, H.; Stratton, Z.; Huang, Y.; Huang, T. J. Continuous Particle Separation in a Microfluidic Channel via Standing Surface Acoustic Waves (Ssaw). Lab Chip 2009, 9, 3354–3359.
- Ding, X.; et al. Standing Surface Acoustic Wave (Ssaw) Based Multichannel Cell Sorting. Lab Chip 2012, 12, 4228– 4231.
- Franke, T.; Braunmuller, S.; Schmid, L.; Wixforth, A.; Weitz,
 D. A. Surface Acoustic Wave Actuated Cell Sorting (SAWACS). Lab Chip 2010, 10, 789–794.
- Franke, T.; Abate, A. R.; Weitz, D. A.; Wixforth, A. Surface Acoustic Wave (SAW) Directed Droplet Flow in Microfluidics for PDMS Devices. *Lab Chip* 2009, 9, 2625–2627.
- Destgeer, G.; Lee, K. H.; Jung, J. H.; Alazzam, A.; Sung, H. J. Continuous Separation of Particles in a PDMS Microfluidic Channel via Travelling Surface Acoustic Waves (TSAW). Lab Chip 2013, 13, 4210–4216.
- Nam, J.; Lim, H.; Kim, D.; Shin, S. Separation of Platelets From Whole Blood Using Standing Surface Acoustic Waves in a Microchannel. Lab Chip 2011, 11, 3361–3364.
- Vader, P.; Breakefield, X. O.; Wood, M. J. Extracellular Vesicles: Emerging Targets for Cancer Therapy. *Trends Mol. Med.* 2014, 20, 385–393.
- Thery, C.; Zitvogel, L.; Amigorena, S. Exosomes: Composition, Biogenesis and Function. *Nat. Rev. Immunol.* 2002, 2, 569–579.
- Tissot, J. D.; Rubin, O.; Canellini, G. Analysis and Clinical Relevance of Microparticles from Red Blood Cells. Curr. Opin. Hematol. 2010, 17, 571–577.
- Rubin, O.; Crettaz, D.; Canellini, G.; Tissot, J. D.; Lion, N. Microparticles in Stored Red Blood Cells: An Approach Using Flow Cytometry and Proteomic Tools. Vox Sang 2008. 95, 288–297.
- Rho, J.; Chung, J.; Im, H.; Liong, M.; Shao, H.; Castro, C. M.; Weissleder, R.; Lee, H. Magnetic Nanosensor for Detection and Profiling of Erythrocyte-Derived Microvesicles. ACS Nano 2013. 7, 11227–11233.
- EL Andaloussi, S.; Mager, I.; Breakefield, X. O.; Wood, M. J. Extracellular Vesicles: Biology and Emerging Therapeutic Opportunities. Nat. Rev. Drug Discovery 2013, 12, 347–357.
- 27. Di Vizio, D.; et al. Large Oncosomes in Human Prostate Cancer Tissues and in the Circulation of Mice with Metastatic Disease. Am. J. Pathol. 2012, 181, 1573–1584.
- Morello, M.; et al. Large Oncosomes Mediate Intercellular Transfer of Functional Microrna. Cell Cycle 2013, 12, 3526– 3536.
- Bourquin, Y.; Syed, A.; Reboud, J.; Ranford-Cartwright, L. C.; Barrett, M. P.; Cooper, J. M. Rare-Cell Enrichment By a Rapid, Label-Free, Ultrasonic Isopycnic Technique for Medical Diagnostics. *Angew. Chem., Int. Ed. Engl.* 2014, 53. 5587–5590.
- Ding, X.; et al. Cell Separation Using Tilted-Angle Standing Surface Acoustic Waves. Proc. Natl. Acad. Sci. U. S. A. 2014, 12992–12997.
- Witwer, K. W.; et al. Standardization of Sample Collection, Isolation and Analysis Methods in Extracellular Vesicle Research. J. Extracell. Vesicles 2013, 2, 20360.



Digital diffraction analysis enables low-cost molecular diagnostics on a smartphone

Hyungsoon Im^{a,b,1}, Cesar M. Castro^{a,c,1}, Huilin Shao^a, Monty Liong^{a,2}, Jun Song^{a,d}, Divya Pathania^{a,b}, Lioubov Fexon^a, Changwook Min^a, Maria Avila-Wallace^e, Omar Zurkiya^{a,b}, Junsung Rho^a, Brady Magaoay^a, Rosemary H. Tambouret^f, Misha Pivovarov^{a,b}, Ralph Weissleder^{a,b,g,3}, and Hakho Lee^{a,b,3}

^aCenter for Systems Biology, Massachusetts General Hospital, Boston, MA 02114; ^bDepartment of Radiology, Massachusetts General Hospital, Boston, MA 02114; Massachusetts General Hospital Cancer Center, Harvard Medical School, Boston, MA 02114; School of Engineering and Applied Sciences, Harvard University, Cambridge, MA 02138; ^eDepartment of Obstetrics and Gynecology, Massachusetts General Hospital, Boston, MA 02114; ^fDepartment of Pathology, Massachusetts General Hospital, Boston, MA 02114; and ⁹Department of Systems Biology, Harvard Medical School, Boston, MA 02115

Edited by Stephen R. Quake, Stanford University, Stanford, CA, and approved March 18, 2015 (received for review January 29, 2015)

The widespread distribution of smartphones, with their integrated sensors and communication capabilities, makes them an ideal platform for point-of-care (POC) diagnosis, especially in resourcelimited settings. Molecular diagnostics, however, have been difficult to implement in smartphones. We herein report a diffractionbased approach that enables molecular and cellular diagnostics. The D3 (digital diffraction diagnosis) system uses microbeads to generate unique diffraction patterns which can be acquired by smartphones and processed by a remote server. We applied the D3 platform to screen for precancerous or cancerous cells in cervical specimens and to detect human papillomavirus (HPV) DNA. The D3 assay generated readouts within 45 min and showed excellent agreement with gold-standard pathology or HPV testing, respectively. This approach could have favorable global health applications where medical access is limited or when pathology bottlenecks challenge prompt diagnostic readouts.

cancer diagnostics | smartphone | molecular sensing | point-of-care diagnostics | cervical cancer

he rapid dissemination of electronic communication devices such as smartphones, tablets, and wearable electronics, all with integrated sensors, creates new possibilities for inexpensive point-of-care (POC) diagnostics and care delivery. One example is detecting cancer in low- and middle-income countries where limited resources and geographical constraints often lead to missed opportunities for intervention, resulting in mortalities even with treatable cancers (1). Current efforts to control cancer thus focus on implementing population-based early screening programs; a key element for success is a cost-effective, robust diagnostic platform that can be readily deployed into POC settings (2). Whereas conventional microscopy of human samples (smears, aspirates, biopsies, blood) is the most widely used to diagnose cancer, its POC adaptation is limited by inherent drawbacks such as bulky optics, requirements for trained microscopists, and operatordependent variability.

Recent advances in digital sensors and computational approaches have introduced new microscopy techniques. Digital holography, in particular, has emerged as one alternative to conventional bright-field microscopy. Following the initial description of lens-free holography by Kreuzer's group (3), various diffractionbased imaging systems have been developed (4–8). The majority of recent work, however, is based on identifying targets by their inherent morphology (e.g., blood cells, bacteria, Caenorhabditis elegans) (4, 9–14). We reasoned that it would be possible to impart molecular specificity to improve disease detection and phenotyping akin to other molecular profiling strategies (15, 16).

Here we describe a digital diffraction diagnostics (D3)—a computational analysis of distinct diffraction patterns generated by microbeads that bind to biological target of interest. The strategy can detect a broad range of targets (SI Appendix, Table S1): soluble proteins, nucleic acids, or cellular proteins. To provide effective

POC operation at remote sites, we adopted a client-server model: the data acquired by a smartphone were digitally processed by a remote parallel-computing server. We tested the approach by exploring cancer cell profiling with immunomicrobeads. Diffraction patterns generated by microbeads were detected with a smartphone camera in a bright-field setting, and digital processing reconstructed the images of bead-bound cells to retrieve molecular information. The assay protocol enabled molecular analyses on $>10^4$ individual cells in a single still image, with the entire assav complete in 45 min. As an initial proof-of-principle in human clinical samples, we used D3 to screen for cervical cancer, the third most prevalent cancer in women worldwide, with 80% of cases occurring in resource-limited countries (16). Cellular analyses using the D3 assay reliably identified patients at high clinical risk for malignancy. To show its versatility, we further extended the D3 assay to other disease targets, including human papillomavirus (HPV) DNA and lymphoma cell detection in fine-needle aspirates.

Results

D3 Platform. The D3 assay for cell detection is illustrated in Fig. 1.4. Specimens are obtained from minimally invasive procedures (e.g., smears, brushings, fine-needle aspiration, blood draw), and

Significance

Smartphones and wearable electronics have advanced tremendously over the last several years but fall short of allowing their use for molecular diagnostics. We herein report a generic approach to enable molecular diagnostics on smartphones. The method utilizes molecular-specific microbeads to generate unique diffraction patterns of "blurry beads" which can be recorded and deconvoluted by digital processing. We applied the system to resolve individual precancerous and cancerous cells as well as to detect cancer-associated DNA targets. Because the system is compact, easy to operate, and readily integrated with the standard, portable smartphone, this approach could enable medical diagnostics in geographically and/or socioeconomically limited settings with pathology bottlenecks.

Author contributions: R.W. and H.L. oversaw all research studies; H.I., C.M.C., R.W., and H.L. designed individual projects; C.M.C., M.A.-W., O.Z., and R.W. designed clinical studies and obtained samples; H.I., H.S., J.S., D.P., C.M., O.Z., J.R., and B.M. performed research; C.M.C., H.S., M.L., D.P., and J.R. contributed new reagents/analytic tools; H.I., C.M.C., H.S., M.L., J.S., D.P., L.F., C.M., M.A.-W., O.Z., J.R., B.M., R.H.T., M.P., R.W., and H.L. analyzed data; and H.I., C.M.C., R.W., and H.L. wrote the paper

The authors declare no conflict of interest.

This article is a PNAS Direct Submission.

¹H.I. and C.M.C. contributed equally to this work.

²Present address: Cardno ChemRisk, San Francisco, CA 94105.

³To whom correspondence may be addressed. Email: rweissleder@mgh.harvard.edu or hlee@mgh.harvard.edu.

This article contains supporting information online at www.pnas.org/lookup/suppl/doi:10. 1073/pnas.1501815112/-/DCSupplemental

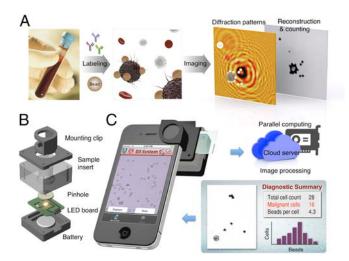


Fig. 1. D3 platform. (A) Assay schematic for cellular detection. Target cells in patient samples (e.g., blood or biopsy) are immunolabeled with microbeads, and their diffraction patterns are recorded. The diffraction images are then digitally reconstructed into object images wherein bead-labeled target cells are identified. For the detection of other types of targets, see SI Appendix, Table S1. (B) The snap-on module for a smartphone consists of an LED powered by a coin battery, a pinhole for uniform illumination with partial coherence, and a sample mount. (C) The D3-mounted smartphone's embedded phone camera is used to record the diffraction images of the specimen. The recorded images are transferred to a server via the cloud service for real-time image reconstruction and analyses, which can be returned to the smartphone in less than 2 min.

cells are labeled with molecular-specific microbeads. Labeled samples are placed directly on the imaging device. Interference patterns between scattered light from the specimen and the reference light are recorded (17, 18). Digital signal processing then recovers and analyzes object images. Because individual cells are spatially resolved and only target-cell-associated beads are counted, there is no need for washing steps, leading to simplified assays. Selective microbead binding is critical to distinguishing target cells from other host cells and quantitatively profiling protein markers in individual cells.

To perform the D3 assay in POC settings, we implemented a portable sensing terminal that uses the embedded optics and communication functions of a smartphone (Fig. 1B). We constructed a snap-on module, containing both a light source and sample insert, to mount over the phone camera (SI Appendix, Fig. S1). The acquired diffraction patterns were transferred to a dedicated server for postprocessing (SI Appendix, Fig. S2). Following this step, the analytical readouts (e.g., target cell counts, bead counts per cell) and reconstructed images were sent back to the smartphone for display. This scheme frees the sensing terminals from heavy computation load, thereby making their implementation simple and cost-effective. All data were communicated through a secure cloud service, and we programmed a user-friendly interface to streamline the process (SI Appendix, Movie S1). The system had a wide field-of-view (FOV), whereas microscopic resolution could be achieved through numerical reconstruction. The FOV and the spatial resolution for iPhone 4S were 14 mm² and 2 μm, respectively. Alternatively, a miniaturized imager connected to a local computer can be used (e.g., MT9P031, Aptina Imaging Inc.; SI Appendix, Fig. S3), which had an FOV and spatial resolution of 24 mm² and 2 µm, respectively.

D3 Processing. To accurately detect bead-bound target cells, we formulated a processing algorithm for image reconstruction and postanalysis (Fig. 2A). The reconstruction was based on the Rayleigh–Sommerfeld diffraction principle but was extended to digitally retrieve both transmittance and phase shift of objects

through an iterative optimization (19–21). In each iteration, the routine applied physical constraints (i.e., light transmittance and object supports) to a reconstructed object image and updated the corresponding diffraction patterns with retrieved phase information (see *Materials and Methods* for details). The method provided high phase contrast between cells and microbeads (Fig. 2B). Each type could be easily distinguished, even when the size was similar (*SI Appendix*, Fig. S4).

Following reconstruction, images were processed by the detection routine. The algorithm generated transmittance and phase-correlation maps by scanning a microbead reference image over the reconstructed images (*SI Appendix*, Fig. S5). Cells and microbeads could be differentiated from the transmittance and phase correlations, respectively. Subsequently, cells labeled with microbeads were automatically identified, and their individual bead counts were recorded.

To accelerate imaging analyses, we used a server equipped with a graphics processing unit (GPU). The code executed massively parallel image processing threads (>5,000) using its multicore processors, which permitted near-instantaneous image reconstruction and postanalyses (SI Appendix, Table S2). For instance, using a 448-core GPU (Tesla C-2070), a 16-bit 1024×1024 diffraction pattern could be analyzed within 90 ms, ~3,000-fold faster than relying on a conventional central processing unit (4 cores 2.4 GHz; Fig. 2C).

We adopted an encrypted cloud storage for data transfer. The scheme provides a buffer for asynchronous communication between smartphones and the server, and is readily scalable to global networks. To minimize data transfer time, especially from

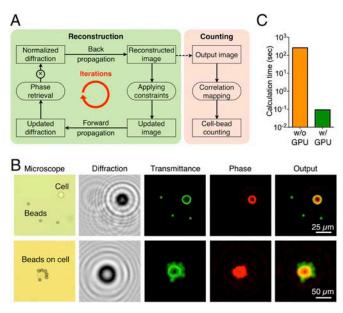


Fig. 2. Real-time reconstruction and counting process. (*A*) Diagram of reconstruction and counting algorithm. A diffraction image, normalized by a reference image obtained in the absence of specimens, is reconstructed through an iterative process. Following the image reconstruction, cells and beads are detected using a counting algorithm, which scanned a reference image of a microbead over the reconstructed image. (*B*) Examples of the image reconstruction. Raw diffraction patterns of cancer cells and 7-μm microbeads show undecipherable patterns. The reconstruction algorithm recovers both transmittance and phase information. Cells and microbeads can be differentiated from their high phase contrast. The bead-bound cells are automatically identified, and the bead numbers are counted. The transmittance (green) and phase contrast (red) images are pseudocolored to better visualize optical properties of cells and beads. (*C*) Computational time for image reconstruction and cell/bead counting (1-MB pixel image) with and without GPU-implemented systems.

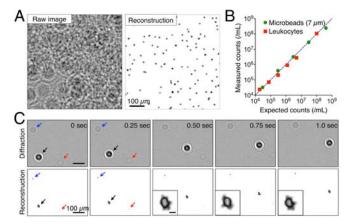


Fig. 3. High-throughput cell and bead identification. (*A*) Diffraction and reconstructed images of 7-μm microbeads at a concentration of 5×10^7 beads per mL. More than 10^5 objects can be detected at microscopic resolution from a single image (also see *SI Appendix*, Fig. S7). (*B*) Comparison between the D3-counted microbeads and leukocytes and their expected counts. Note the linearity ($R^2 > 0.97$) even at very high bead or cell concentrations (4×10^8 beads per mL and 1×10^8 cells per mL). (*C*) Temporal image reconstruction of cells in flow. Diffraction images were recorded at 4 frames per s and reconstructed in real time by the D3 server. A bead-labeled cancer cell (black arrow), a nontargeted cell (red), and a free-floating microbead (blue) are automatically identified. (*Inset*) High-resolution details of the bead-labeled cell undergoing rotational motion in the flow stream.

smartphones to a cloud storage, we converted original uncompressed color images (24 MB) into lossless gray-scale images (2.9 MB, Portable Network Graphics/PNG format). When microbeads with the diameter of >5 µm were used, the file could be further compressed (0.4 MB, Joint Photographic Experts Group/JPEG format) without affecting bead counts (*SI Appendix*, Fig. S6). These final images can be transferred to the cloud storage within 3 min, even through legacy 2G cellular network (transfer speed, 20 kbps).

High-Throughput D3 Assay for Cell Detection. With its large FOV (14 mm² for iPhone 4S and 24 mm² for the image sensor) and rapid image processing, the D3 platform enabled high-throughput cellular analyses. In a single image acquisition, more than 100,000 individual objects can be detected at microscopic resolution (Fig. 3A and SI Appendix, Fig. S7). The dynamic range of detection spanned over 4 orders of magnitude (Fig. 3B), with the object concentration reaching up to $\sim 10^8$ microbeads or cells per milliliter of sample (SI Appendix, Figs. S7–S9). The capacity for high-density imaging, combined with the recognition of beadbound cells, made it possible to detect target cells in the presence of abundant host cells (e.g., leukocytes) and unbound microbeads. Importantly, this eliminated the need for external washing and purification steps. The assay throughput could be further increased by flowing target cells through a microfluidic channel and imaging in real-time (FOV, $2.5 \times 2.5 \text{ mm}^2$; 10 frames per s) (Fig. 3C and SI Appendix, Fig. S10 and Movie S2). This is akin to a flow cytometer with imaging capabilities for quantitative analysis (22), but in a miniaturized system.

Quantitative Profiling. We next applied the D3 assay to cell profiling (Fig. 4*A*). Human cancer cell lines were immunolabeled with microbeads to generate specific diffraction signatures. Whereas it is possible to use antibody-coated microbeads directly on cells, we found that a two-step approach increased bead binding (23). We thus opted for highly efficient bioorthogonal [e.g., between transcyclooctene and tetrazine (24)] or streptavidin/biotin approaches. For example, using the latter, cells were first targeted by biotinylated antibodies and subsequently incubated with

streptavidin-coated microbeads. We further tested commercially available microbeads in different sizes (diameter 3–22 μ m). A bead diameter between 5 and 7 μ m was found to optimize accurate bead counting while minimizing cell clustering (*SI Appendix*, Fig. S11).

To validate D3-based cellular profiling, we measured the expression of three protein markers, human epidermal growth factor receptor 2 (HER2)/neu, epithelial cell adhesion molecule (EpCAM), and epidermal growth factor receptor (EGFR), on human cells (SkBr3, human breast carcinoma). Samples were immunolabeled with 7-µm microbeads and analyzed using the D3 system (Fig. 4A and SI Appendix, Fig. S12). The average bead count per cell was highest for HER2/neu targeting (8.0 beads per cell), followed by EpCAM (3.9 beads per cell) and EGFR (0.5 beads per cell); these results were consistent with immunofluorescence microscopy. Unlike microscopy, however, the D3 assay enabled simultaneous analyses of far greater numbers of cells (>10,000 cells) because of its wide FOV. The cellular bead counts generated with automated D3 analyses were statistically identical with those from manual microscopy enumeration (P = 0.43; paired t test; Fig. 4B and SI Appendix, Fig. S13). Further comparison with flow cytometry validated D3 assay's analytically capacity (Fig. 4C). The number of beads per cell correlated linearly with levels of marker expression ($R^2 = 0.99$). Similar D3 profiling on a different cell line (A431, human epidermoid carcinoma) also matched well with immunofluorescence microscopy and flow cytometry results (SI Appendix, Fig. S14).

Whereas the above examples used parallel profiling of separate images, it is also possible to perform multiplexing within the same sample using microbeads of different optical signatures. For instance, we tested three bead sizes and three different materials (e.g., polystyrene, silica, silica coated with silver) that can be effectively distinguished through nominal size and transmittance, respectively. Combining these sets could provide nine-channel multiplexing (*SI Appendix*, Fig. S15).

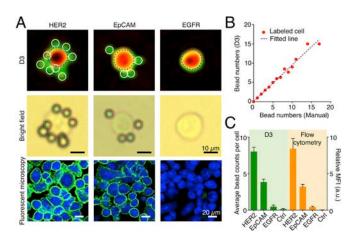


Fig. 4. Detecting cancer cell markers with immunobead labeling. (A) Cancer cells (SkBr3, human breast carcinoma) were immunobead-labeled for HER2, EpCAM, and EGFR. ($Top\ Row$) Representative reconstructed images in pseudocolor (green, transmittance; red, phase). (Middle Row) Corresponding bright-field micrographs. ($Bottom\ Row$) Cells labeled with fluorescent antibodies for comparison. HER2, human epidermal growth factor receptor 2; EpCAM, epithelial cell adhesion molecule; EGFR, epidermal growth factor receptor. (B) The bead numbers on labeled cells, determined automatically by D3, were in good agreement ($R^2=0.97$) with those counted manually from microscope images. (C) The average bead count per cell correlated with the expression level of a target marker as determined by flow cytometry ($R^2=0.99$). MFI, mean fluorescence intensity. a.u., arbitrary unit.

Im et al. PNAS Early Edition | 3 of 6

Clinical Applications of D3. We evaluated the clinical utility of D3 by first focusing on cervical cancer surveillance. Cervical cancer maintains high incidence rates in resource-poor countries (16) where the availability of objective early screening systems is limited. We reasoned that the portable D3 system could be used as a first-line diagnostic tool without subjective readouts to promptly triage suspicious or high-risk cases. The strategy could potentially offset pathology bottlenecks and reduce repeated patient visits to central clinics, which are often complicated by geographical and/or socioeconomic constraints (25, 26).

We obtained cervical specimens through brushing, loop electrosurgical excision procedure (LEEP), or biopsies during colposcopic evaluation. Twenty-five patients with previously abnormal Pap smear results were recruited. Cellular samples were labeled with a mixture of tagged antibodies against EpCAM, CD44, or tumor-associated calcium signal transducer2 (TACD2/Trop2). These cancer markers were chosen for their elevated expression in cervical cancer as described in literature (27-29). We counted the total number of bead-bound cells as well as the number of microbeads per cell. Blinded to D3 results, patient specimens were separately examined through conventional pathology, and classified into three risk classes: "high risk," "low risk," or "benign" (Fig. 5A) The D3 analyses showed that bead counts among targeted cells increased along the clinical risk (Fig. 5B). The mean bead counts (n_{bead}) per targeted cell were significantly different among the clinical risk classifications (P < 0.05, Tukey multiple comparison test), indicating that n_{bead} could serve as a single diagnostic measure (Fig. 5C). The class boundaries, determined

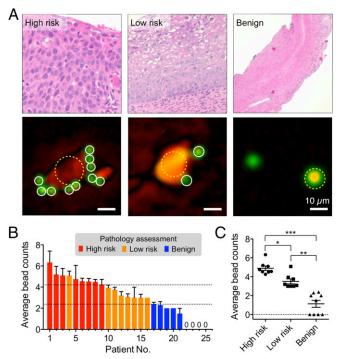


Fig. 5. Cervical cancer diagnosis with the D3 platform. (A) Histology (Top) and representative reconstructed image of cells (Bottom) from high-risk (cervical intraepithelial neoplasia/CIN 2, 3), low-risk (CIN 1), and benign patient samples. Samples were targeted with a mixture of EpCAM. CD44, and Trop2 antibodies, followed by microbead labeling. More beads were bound to cells in higher risk patient samples. The transmittance (green) and the phase (red) were pseudocolored for clarification. (B and C) The profiling result of patient samples (n = 25). The average numbers of beads per labeled cell were significantly different among high-risk, low-risk, and benign groups. The dotted lines indicate the class boundaries. *P = 0.035; **P < 0.001; ****P* < 0.001.

from multiclass logistic regression, were $n_{bead} > 4.2$ between high risk and low risk; and $n_{bead} > 2.4$ between low risk and benign. We further dichotomized the patients into two groups, high risk versus low risk/benign, to reflect the conventional clinical process for intervention and/or follow-up. In our limited data set, the detection sensitivity was 100% and the specificity 92% (high risk vs. low risk/benign).

We also adopted the same D3 platform for the HPV-DNA detection (SI Appendix, Fig. S16A), given its high relevance in cervical cancer diagnostics. We applied the bead-dimer assay format: a pair of oligonucleotides, whose sequences were complementary to that of target DNA, were conjugated to silica and polystyrene microbeads, respectively. The target DNA was captured on polystyrene (PS) beads and sequentially labeled with silica beads. The hybridization yielded PS-silica bead dimers with unique diffraction signature (SI Appendix, Fig. S16B). The number of PS-silica hybrids was then counted to quantify the amount of target DNA. The D3 assay was highly sensitive; HPV 16 and 18 DNA targets could be detected down to atto-mole range without PCR amplification (SI Appendix, Fig. S16 C and D). Compared with fluorescent detection, the bead-based D3 assay benefited from simpler optics (i.e., no filter sets) and stronger light signal (bright field).

Extending the clinical utility of D3 to other malignancies, we conducted a pilot study to detect lymphoma cells in fine-needle aspirates (FNA) of lymph nodes in patients with lymphadenopathy. POC lymphoma diagnostics would be of particular interest in sub-Saharan Africa plagued by a high prevalence of AIDSrelated cancers and lymphoma (the "second wave of AIDS") (25, 30, 31). Freshly harvested FNA samples were incubated with immunobeads specific to CD20, one lymphoma marker (SI Appendix, Fig. S17). Subsequent D3 analysis allowed the correct diagnosis of four patients with pathology confirmed lymphoma and also excluded the diagnosis in another four patients with confirmed benign lymphadenopathy.

Discussion

Global cancer rates continue to increase, and the World Health Organization predicts new cases to rise to 19.3 million by 2025 as the world's population grows, ages, and gains access to antiretroviral drugs (1, 32-35). Rapid cancer screening, however, remains an unmet clinical need. The D3 strategy reported here could address some of the diagnostic challenges in resourcelimited areas. It capitalizes on the already widespread distribution of smartphones and allows fast (minutes-hours for a final answer), very low cost (compared with sectioning, microscopes, and flow cytometers), and simple diagnostics. Molecular diagnoses are achieved by integrating immunolabeling assays, cloud computing, and digital processing. The resulting system enables quantitative and operator-independent cellular analysis and reports not only cancer cell counts but also the expression levels of molecular markers. In a pilot study of cervical cancer screening, we used three molecular markers to define risk categories based on invasiveness. The D3 assay was fast (40 min for immunolabeling, most of which is "hands-off" time and 3 min for data processing; SI Appendix, Table S3) and cost-effective (\$1.80 per assay; SI Appendix, Table S4). We expect that the assay costs will ultimately be much cheaper once scaled up and further optimized.

We anticipate further improvements in some analytical capabilities of D3. First, a next-generation system would incorporate multiplexed cellular detection based on different optical properties of microbeads. We have shown that microbeads can be differentiated based on their size and absorbance (SI Appendix, Fig. S15). Applying these signatures would enable multiplexed molecular profiling of the same cells to improve detection accuracy. In parallel, superresolution approaches could be used to improve the spatial resolution (6, 14, 36–38), and thereby further boost D3's multiplexing capacity. Compressive sensing is particularly appealing (39, 40), as it can numerically reconstitute high-frequency information (i.e., small features in images) with no modification in the current D3 setup. By incorporating compressive sensing, we expect to reconstruct images with submicrometer resolution ($\sim 0.6 \mu m$), which would allow analyses of all types of mammalian cells. Second, DNA detection should be further developed for POC operation. This would require implementing disposable cartridges (41, 42) and portable systems (43, 44) for DNA extraction and amplification. Finally, the platform should be tested for robust field operation. We plan to establish a lyophilization protocol for transport and storage of reagents (e.g., antibodies, microbeads) (45). The validation tests will be extended using larger cohorts, variably skilled operators, and diverse environment settings to obtain better statistical power (reproducibility, accuracy, diagnostic performance). In this light, the work presented here has catalyzed two larger clinical trials focused, respectively, on cervical cancer (including HPV testing) and lymphoma detection (FNAs of enlarged lymph nodes). We envision that these advances will position D3 as a versatile screening tool for various cancer types (e.g., cervix, breast, lymphoma) and infectious diseases (e.g., Ebola, HIV, tuberculosis) with applications in field work, mobile clinics, and home care settings.

Materials and Methods

D3 Imaging Terminal. Electrical components [e.g., light-emitting diode (LED), battery socket, switch] were purchased (Digi-Key) and mounted on a custom-designed printed circuit board. The main body of the snap-on module was machined out of black acrylic plastic, and housed the light source (590 nm), a 100-µm pinhole, and a minilens. The focal length (4 mm) of the lens was similar to that of the embedded lens (4.2 mm) in the phone camera (*SI Appendix*, Fig. 51). By pairing these two lenses, we achieved a unit magnification to maximize the FOV, and used the phone camera without any modification. The size of the snap-on was 4 × 4 × 5.5 cm³.

D3 App. The D3 app was programmed with user-friendly interfaces for operation in iOS 6 or higher version. The app has three main screens: (i) image capturing and processing, (ii) reconstruction parameters settings, and (iii) data communication with a cloud service. The images captured by a phone camera module were saved as uncompressed data (PNG) or compressed image (JPEG), and uploaded along with other imaging information (e.g., wavelength, diagnosis location, time, patient data) into a dedicated folder in a cloud storage (Dropbox). The uploaded images were processed by a D3 image GPU server (see below), and the results were saved into a subfolder. The D3 app subsequently downloaded reconstructed images and analysis results. All data were encrypted according to the 256-bit Advanced Encryption Standard. The application program interface library from the vendor (Dropbox) was used to implement the data transfer routine.

D3 Imaging Server. The D3 server (HP xw4600 workstation, Hewlett Packard) had the following system specifications (SI Appendix, Table S2): CPU, Core2 Duo E8500 3.16 GHz (Intel); memory, 8-GB DDR2 (double data rate2); GPU, Tesla C-2070 (Nvidia); operating system, Ubuntu 12.04 64-bit. The GPU had 448 CUDA (Compute Unified Device Architecture) cores and 6 GB memory. The signal processing program was written in C++ language and used vendor-provided modules (CUDA extensions, CUDA driver 5.0, CUFFT library). The image analysis workflow is shown in SI Appendix, Fig. S2. The imaging server cyclically polled a dedicated folder in a cloud storage (Dropbox). When new images and image information were uploaded, the imaging server executed image reconstruction and postimaging analyses (cell and bead counting). The reconstructed images and counting statistics were then saved into a subfolder. When synchronized in the cloud storage, the image and data files could be accessed by users.

Image Reconstruction. The size of an uncompressed image file on the iPhone 4S was \sim 24 MB (2,448 \times 3,264 pixels, 24-bit RGB). This raw image file was converted to gray-scale PNG (\sim 2.9 MB) or JPEG (\sim 0.4 MB) files (SI Appendix, Fig. S6), and normalized by a reference image recorded without samples. The normalization removed intrinsic defects and accurately calculated object transmittance (21). The normalized diffraction images were up-sampled four times through linear interpolation and used as input data for reconstruction. The reconstruction was based on phase retrieval algorithms, which can recover phase information from intensity-based diffraction patterns through iterative

processes (4, 18, 19). The algorithm has four steps: (i) back-propagate an input image, (ii) apply constraints, (iii) forward-propagate updated image, and (iv) update retrieved phase information. First, the normalized diffraction image was numerically back-propagated by an optical distance between the object and the imager. We calculated the optimal optical distance by finding a focal depth with the sharpest object boundary (46). Calculating field propagation was based on the Rayleigh-Sommerfeld diffraction integral in a convolution approach, where the propagated field was calculated by the inverse Fourier transform of the multiplication between the Fourier transform of field and the transfer function (20). During the first iteration, object supports were defined using a segmentation method, where object boundaries were found by thresholding intensity variances (46). For the back-propagated image, pixels outside the object supports were regarded as background, and their transmittance values (i.e., the modulus of field) were set to unity. If a pixel inside the object support had a transmittance value larger than unity due to artificial twinimage superimposition, its transmittance value was also forced to unity. After applying the constraints, the updated image was propagated to the image plane, where the forward-propagated field had nonzero phase information. The phase information was added to the measured diffraction image as a new input. The process was usually repeated $10\sim30$ times until the reconstructed image with retrieved phase information converged.

Counting Algorithm. For detecting beads and cells, a microbead reference image was scanned over the reconstructed images to generate modulus and phase correlation maps as shown in SI Appendix, Fig. S5. The reference microbead image was obtained by averaging microbead images in a pure bead solution. The correlation coefficients for modulus and phase were calculated from pixel-to-pixel comparison between reference and reconstructed images. Cells were first detected when a local maximum phase correlation coefficient was larger than the threshold value of phase correlation coefficient, which was obtained from images of pure cell population. For each cell detected, microbeads within the object support were detected from the local maxima of the modulus correlation coefficients. Microbeads within a distance of 10 pixels (or 22 μm) from a center of cells were considered bound to cells. This search radius was experimentally determined for 7-µm beads. The detection algorithm was validated by comparing bead counts with manual counting using a conventional microscopy. The microscope was equipped with a 10x objective (N.A. = 0.17) and a cooled CCD camera (7.4 \times 7.4- μm^2 pixel size; Spot RT3, Diagnostic Instruments Inc.), and produced images with 1.4 pixel/µm resolution.

Clinical Samples. The clinical study was approved by the Partners Healthcare Institutional Review Board (Massachusetts General Hospital/Brigham and Women's Hospital). Informed consent was obtained from adult women who were referred to the Colposcopy Clinic for previously abnormal Pap smears. Samples were obtained by brushing, cervical biopsy, or LEEP. One clinical provider (M.A.-W.) performed all cervical procedures and provided excess or otherwise discarded ectocervical or endocervical specimens. Biopsies entailed visualizing the exocervix and bathing with 5% acetic acid using clinically standard procedures. Suspicious aceto-white epithelial changes were identified with a colposcope (Foto Optik; Leisegang Medical Inc.) followed by punch biopsies. Before the use of acetic acid, brushing samples were collected with surgical brushes (Surgipath C-E Brush, Leica Microsystems; Cytobrush Plus GT Gentle Touch, BD Surepath). Samples were suspended in sterile PBS (1 mL), and incubated (30 min, 20 °C) with a mixture of antibodies against EpCAM (clone MAB9601, R&D Systems), CD44 (clone IM7, Biolegend), and Trop2 (Clone 162-46.2, Abcam). The antibody concentration was 5 µg/mL for each. Targeted samples were then incubated with streptavidin-coated polystyrene microbeads (0.5 mg, $7\text{-}\mu\text{m}$ diameter, Spherotech) for 10 min at room temperature and analyzed using the D3 platform. Here, the sample volume examined was 10 μ L; the number of microbeads per cell was automatically counted using D3 software. All experiments were conducted blind to pathology results and clinical interpretation of risk. Please see SI Appendix for cell preparation, fluorescence measurements, HPV-DNA detection, and clinical lymph node samples.

ACKNOWLEDGMENTS. The authors thank M. Birrer, D. Dizon, and M. Del Carmen for many helpful suggestions; Melina Pectasides for assistance with clinical sample collection; and K. Joyes for reviewing the manuscript. This work was supported in part by US NIH Grants R01-HL113156 (to H.L.), R01-EB010011 (to R.W.), R01-EB00462605A1 (to R.W.), T32CA79443 (to R.W.), K12CA087723-11A1 (to C.M.C.), Massachusetts General Hospital Physician Scientist Development Award (to C.M.C.), National Heart, Lung, and Blood Institute Contract HHSN268201000044C (to R.W.), and Department of Defense Ovarian Cancer Research Program Award W81XWH-14-1-0279 (to H.L.)

Im et al. PNAS Early Edition | **5 of 6**

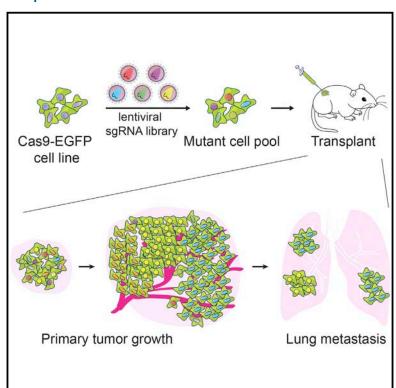
- 1. Varmus H, Trimble EL (2011) Integrating cancer control into global health. Sci Transl Med 3(101):01cm28.
- 2. Chin CD, Linder V, Sia SK (2012) Commercialization of microfluidic point-of-care diagnostic devices. Lab Chip 12(12):2118-2134.
- 3. Xu W, Jericho MH, Meinertzhagen IA, Kreuzer HJ (2001) Digital in-line holography for biological applications. Proc Natl Acad Sci USA 98(20):11301-11305.
- 4. Garcia-Sucerquia J, et al. (2006) Digital in-line holographic microscopy. Appl Opt 45(5):836-850.
- 5. Gurkan UA, et al. (2011) Miniaturized lensless imaging systems for cell and microorganism visualization in point-of-care testing. Biotechnol J 6(2):138-149.
- 6. Zheng G, Lee SA, Antebi Y, Elowitz MB, Yang C (2011) The ePetri dish, an on-chip cell imaging platform based on subpixel perspective sweeping microscopy (SPSM). Proc Natl Acad Sci USA 108(41):16889-16894.
- 7. Kim SB, et al. (2011) A cell-based biosensor for real-time detection of cardiotoxicity using lensfree imaging. Lab Chip 11(10):1801-1807.
- 8. Greenbaum A, et al. (2012) Imaging without lenses: Achievements and remaining challenges of wide-field on-chip microscopy. Nat Methods 9(9):889–895.
- 9. Seo S, et al. (2010) High-throughput lens-free blood analysis on a chip. Anal Chem 82(11):4621-4627.
- 10. Mudanyali O, Bishara W, Ozcan A (2011) Lensfree super-resolution holographic microscopy using wetting films on a chip. Opt Express 19(18):17378-17389.
- 11. Lee SA, et al. (2011) Color capable sub-pixel resolving optofluidic microscope and its application to blood cell imaging for malaria diagnosis. PLoS ONE 6(10):e26127.
- 12. Greenbaum A, Akbari N, Feizi A, Luo W, Ozcan A (2013) Field-portable pixel superresolution colour microscope. PLoS ONE 8(9):e76475.
- 13. Su T-W, Choi I, Feng J, Huang K, McLeod E, Ozcan A (2013) Sperm trajectories form chiral ribbons. Sci Rep 3:1664.
- 14. Zheng G, Horstmeyer R, Yang C (2013) Wide-field, high-resolution Fourier ptychographic microscopy. Nat Photonics 7(9):739–745.
- Ojesina AI, et al. (2014) Landscape of genomic alterations in cervical carcinomas. Nature 506(7488):371-375
- 16. Schiffman M, Solomon D (2013) Clinical practice. Cervical-cancer screening with human papillomavirus and cytologic cotesting. N Engl J Med 369(24):2324–2331.
- 17. Fung J, et al. (2011) Measuring translational, rotational, and vibrational dynamics in colloids with digital holographic microscopy. Opt Express 19(9):8051-8065.
- 18. Mudanyali O, et al. (2010) Compact, light-weight and cost-effective microscope based on lensless incoherent holography for telemedicine applications. Lab Chip 10(11):
- 19. Fienup JR (1982) Phase retrieval algorithms: A comparison. Appl Opt 21(15):2758-2769.
- 20. Kreis TM (2002) Frequency analysis of digital holography with reconstruction by convolution. Opt Eng 41(8):1829-1839.
- Latychevskaia T, Fink H-W (2007) Solution to the twin image problem in holography. Phys Rev Lett 98(23):233901.
- 22. Basiji DA, Ortyn WE, Liang L, Venkatachalam V, Morrissey P (2007) Cellular image analysis and imaging by flow cytometry. Clin Lab Med 27(3):653-670, viii
- Agasti SS, et al. (2012) Supramolecular host-guest interaction for labeling and detection of cellular biomarkers. Angew Chem Int Ed Engl 51(2):450-454.
- 24. Haun JB, Devaraj NK, Hilderbrand SA, Lee H, Weissleder R (2010) Bioorthogonal chemistry amplifies nanoparticle binding and enhances the sensitivity of cell detection. Nat Nanotechnol 5(9):660-665.
- 25. Chabner BA, Efstathiou J, Dryden-Peterson S (2013) Cancer in Botswana: The second wave of AIDS in Sub-Saharan Africa. Oncologist 18(7):777-778.

- 26. Ramogola-Masire D, et al. (2012) Cervical cancer prevention in HIV-infected women using the "see and treat" approach in Botswana. J Acquir Immune Defic Syndr 59(3): 308-313.
- 27. Dall P, et al. (1994) Surface protein expression and messenger RNA-splicing analysis of CD44 in uterine cervical cancer and normal cervical epithelium. Cancer Res 54(13):
- 28. Varughese J, et al. (2011) Cervical carcinomas overexpress human trophoblast cellsurface marker (Trop-2) and are highly sensitive to immunotherapy with hRS7, a humanized monoclonal anti-Trop-2 antibody. Am J Obstet Gynecol 205(6):e1-e7.
- 29. Went PTH, et al. (2004) Frequent EpCam protein expression in human carcinomas. Hum Pathol 35(1):122-128.
- 30. Varmus H, Kumar HS (2013) Addressing the growing international challenge of cancer: A multinational perspective. Sci Transl Med 5(175):cm2.
- 31. Livingston J (2013) Cancer in the shadow of the AIDS epidemic in southern Africa. Oncologist 18(7):783-786
- 32. Beaglehole R, et al.; Lancet NCD Action Group (2011) UN High-Level Meeting on Non-Communicable Diseases: Addressing four questions. Lancet 378(9789):449-455.
- 33. Daar AS, et al. (2007) Grand challenges in chronic non-communicable diseases. Nature 450(7169):494-496.
- 34. Narayan KMV, Ali MK, del Rio C, Koplan JP, Curran J (2011) Global noncommunicable diseases—lessons from the HIV-AIDS experience, N Engl J Med 365(10):876-878.
- 35. Trimble EL (2010) Global cooperation in gynecologic cancer. J Gynecol Oncol 21(1):
- 36. Gazit S, Szameit A, Eldar YC, Segev M (2009) Super-resolution and reconstruction of sparse sub-wavelength images. Opt Express 17(26):23920-23946.
- 37. Bishara W, et al. (2011) Holographic pixel super-resolution in portable lensless on-chip microscopy using a fiber-optic array. Lab Chip 11(7):1276-1279.
- 38. Mudanyali O, et al. (2013) Wide-field optical detection of nanoparticles using on-chip microscopy and self-assembled nanolenses. Nat Photonics 7(3):247-254
- 39. Brady DJ, Choi K, Marks DL, Horisaki R, Lim S (2009) Compressive holography. Opt Express 17(15):13040-13049.
- 40. Rivenson Y, Stern A, Javidi B (2013) Overview of compressive sensing techniques applied in holography [Invited]. Appl Opt 52(1):A423-A432.
- 41. Hoffmann J, Mark D, Lutz S, Zengerle R, von Stetten F (2010) Pre-storage of liquid reagents in glass ampoules for DNA extraction on a fully integrated lab-on-a-chip cartridge, Lab Chip 10(11):1480-1484.
- 42. Liu C, Mauk MG, Hart R, Qiu X, Bau HH (2011) A self-heating cartridge for molecular diagnostics. Lab Chip 11(16):2686-2692.
- 43. Huang S, et al. (2013) Low cost extraction and isothermal amplification of DNA for infectious diarrhea diagnosis. PLoS ONE 8(3):e60059.
- 44. Jiang L. Mancuso M. Lu Z. Akar G. Cesarman E. Erickson D (2014) Solar thermal polymerase chain reaction for smartphone-assisted molecular diagnostics. Sci Rep 4:
- 45. Bhambhani A, Blue JT (2010) Lyophilization strategies for development of a highconcentration monoclonal antibody formulation: Benefits and pitfalls. Am Pharm Rev
- 46. McElhinney CP, et al. (2007) Depth-independent segmentation of macroscopic threedimensional objects encoded in single perspectives of digital holograms. Opt Lett 32(10):1229-1231.



Genome-wide CRISPR Screen in a Mouse Model of **Tumor Growth and Metastasis**

Graphical Abstract



Authors

Sidi Chen, Neville E. Sanjana, ..., Feng Zhang, Phillip A. Sharp

Correspondence

zhang@broadinstitute.org (F.Z.), sharppa@mit.edu (P.A.S.)

In Brief

Using an in vivo genome-wide CRISPR/ Cas9 screen, loss-of-function mutations that drive tumor growth and metastasis to the lung have been identified, demonstrating Cas9-based screening as a robust method to systematically assay gene phenotypes in cancer evolution.

Highlights

- Genome-wide in vivo CRISPR-Cas9 screen in mice reveals genes regulating lung metastasis
- Screen identifies loss-of-function mutations in known tumor suppressors and novel genes
- Candidate metastasis genes are validated using a pooled competition assay
- Effect of mutations on primary tumor growth positively correlates with metastasis





Genome-wide CRISPR Screen in a Mouse Model of Tumor Growth and Metastasis

Sidi Chen, 1,2,3,10 Neville E. Sanjana, 3,4,5,6,7,10 Kaijie Zheng, 3,4 Ophir Shalem, 3,4 Kyungheon Lee, 8 Xi Shi, 3,4 David A. Scott, 3,4 Jun Song, 8 Jen Q. Pan, 3,4 Ralph Weissleder, 8,9 Hakho Lee, 8 Feng Zhang, 3,4,5,6,7,* and Phillip A. Sharp^{1,2,*}

Massachusetts Institute of Technology, Cambridge, MA 02139, USA

SUMMARY

Genetic screens are powerful tools for identifying genes responsible for diverse phenotypes. Here we describe a genome-wide CRISPR/Cas9-mediated loss-of-function screen in tumor growth and metastasis. We mutagenized a non-metastatic mouse cancer cell line using a genome-scale library with 67,405 single-guide RNAs (sgRNAs). The mutant cell pool rapidly generates metastases when transplanted into immunocompromised mice. Enriched sgRNAs in lung metastases and late-stage primary tumors were found to target a small set of genes, suggesting that specific loss-of-function mutations drive tumor growth and metastasis. Individual sgRNAs and a small pool of 624 sgRNAs targeting the top-scoring genes from the primary screen dramatically accelerate metastasis. In all of these experiments, the effect of mutations on primary tumor growth positively correlates with the development of metastases. Our study demonstrates Cas9-based screening as a robust method to systematically assay gene phenotypes in cancer evolution in vivo.

INTRODUCTION

Cancer genomes have complex landscapes of mutations and diverse types of genetic aberrations (Lawrence et al., 2013; Weinberg, 2007). A major challenge in understanding the cancer genome is to disentangle alterations that are driving the processes of tumor evolution from passenger mutations (Garraway and Lander, 2013). Primary tumor growth and metastasis are distinct yet linked processes in the progression of solid tumors (Nguyen et al., 2009; Valastyan and Weinberg, 2011; Vanharanta and Massagué, 2013). It has been observed in the clinic that the

probability of detecting metastases in a patient correlates positively with the size of a primary tumor (Heimann and Hellman, 1998). Several possible explanations have been suggested: metastatic properties may only be acquired in late-stage tumors, larger tumors may seed proportionally more cells into circulation that eventually migrate to other sites, or cells with a strong ability to proliferate may also have enhanced ability to metastasize (Weinberg, 2007). In early studies using random insertional mutagenesis, it was observed that metastatic cell subpopulations overgrow to complete dominance in the primary tumor, suggesting progressive selection at both sites (Korczak et al., 1988; Waghorne et al., 1988).

Genetic screens are powerful tools for assaying phenotypes and identifying causal genes in various hallmarks of cancer progression (Hanahan and Weinberg, 2011). RNAi and overexpression of open reading frames (ORFs) have been utilized for screening cancer genes in several models of oncogenesis in mice (Schramek et al., 2014; Shao et al., 2014; Zender et al., 2008). Recently, the Cas9 nuclease (Barrangou et al., 2007; Bolotin et al., 2005; Chylinski et al., 2013, 2014; Deltcheva et al., 2011; Garneau et al., 2010; Gasiunas et al., 2012; Jinek et al., 2012; Sapranauskas et al., 2011) from the microbial type II CRISPR (clustered regularly interspaced short palindromic repeats) system has been harnessed to facilitate loss-of-function mutations in eukaryotic cells (Cong et al., 2013; Mali et al., 2013). When the Cas9 nuclease is targeted to specific locations in the genome, DNA cleavage results in double-stranded breaks (DSBs), which are repaired via non-homologous endjoining (NHEJ) (Rouet et al., 1994). NHEJ repair results in insertion or deletion (indel) mutations that can cause loss of function if the DSB occurs in a coding exon. The Cas9 nuclease can be guided to its DNA target by a single-guide RNA (sgRNA) (Jinek et al., 2012), a synthetic fusion between the CRISPR RNA (crRNA) and trans-activating crRNA (tracrRNA) (Deltcheva et al., 2011). In cells, Cas9-mediated gene disruption requires the full-length tracrRNA (Cong et al., 2013; Mali et al., 2013), in which secondary structures at the 3' end of tracrRNA are



¹David H. Koch Institute for Integrative Cancer Research, Cambridge, MA 02139, USA

²Department of Biology, Massachusetts Institute of Technology, Cambridge, MA 02139, USA

³Broad Institute of MIT and Harvard, Cambridge, MA 02142, USA

⁴Stanley Center for Psychiatric Research, Cambridge, MA 02142, USA

⁵McGovern Institute for Brain Research

⁶Department of Brain and Cognitive Sciences

⁷Department of Biological Engineering

⁸Center for Systems Biology, Massachusetts General Hospital, Boston, MA 02114, USA

⁹Department of Systems Biology, Harvard Medical School, Boston, MA 02115, USA

¹⁰Co-first author

^{*}Correspondence: zhang@broadinstitute.org (F.Z.), sharppa@mit.edu (P.A.S.) http://dx.doi.org/10.1016/j.cell.2015.02.038

critical for Cas9-mediated genome modification (Cong et al., 2013; Hsu et al., 2013).

Screens utilizing Cas9 have identified genes that are essential for cell survival and genes involved in drug resistance in various cell lines (Shalem et al., 2014; Wang et al., 2014; Koike-Yusa et al., 2014; Zhou et al., 2014). In vivo pooled screens are challenging due to many factors, such as the complexity of the library, limitations of virus delivery and/or cell transplantation, uniformity of viral transduction at a low MOI, and the complex dynamics and interactions of cells in animals. In this study, we report a genome-wide Cas9 knockout screen in a mouse model of tumor evolution. This screen provides a systematic phenotypic measurement of loss-of-function mutations in primary tumor growth and metastasis.

RESULTS

CRISPR/Cas9 Library-Mediated Mutagenesis Promotes Metastasis

We derived and cloned a cell line (Chen et al., 2014) from a mouse non-small-cell lung cancer (NSCLC) (Kumar et al., 2009). This cell line possesses an oncogenic *Kras* in conjunction with homozygous *p53* and heterozygous *Dicer1* loss of function (*Kras*^{G12D/+};*p53*^{-/-};*Dicer1*^{+/-}, denoted KPD) and is capable of inducing tumors when transplanted into immunocompromised mice (Chen et al., 2014; Kumar et al., 2009). We transduced this cell line with a lentivirus carrying a Cas9 transgene fused to a GFP and generated clonal cell lines (Cas9-GFP KPD) (Experimental Procedures) (Figures S1A and S1B). A clonal Cas9-GFP KPD cell line (clone 5) was selected to provide genetic and cellular homogeneity for subsequent screens.

We utilized a pooled genome-wide mouse sgRNA library (termed mouse genome-scale CRISPR knockout library A, or mGeCKOa) containing 67,405 sgRNAs targeting 20,611 protein-coding genes and 1,175 microRNA precursors in the mouse genome (Sanjana et al., 2014). The library also contains 1,000 control sgRNAs (termed non-targeting sgRNAs) designed to have minimal homology to sequences in the mouse genome (Sanjana et al., 2014; Shalem et al., 2014). We transduced the Cas9-GFP KPD cell line with the mGeCKOa library in three independent infection replicate experiments; for each replicate, the library representation (cells per lentiviral CRISPR construct) was greater than 400× (Figure 1A) (Experimental Procedures).

After in vitro culture for 1 week, we subcutaneously transplanted 3×10^7 cells into the flanks of immunocompromised Nu/Nu mice (Figure 1A). We transplanted the cells from each infection replicate into four mice, using one mouse for early tumor sequencing and three mice for sequencing of late-stage primary tumor and metastases (Figure 1A). Both mGeCKOatransduced and untransduced Cas9-GFP KPD cells formed tumors at the injection site (Figure 1B). Like most subcutaneously transplanted tumors, these tumors were poorly differentiated. The primary tumors induced by mGeCKOa-transduced cells grew slightly faster than tumors from the untransduced cells at an early stage (Figure 1C) (2 weeks post-transplantation) (paired two-tailed t test, p = 0.18 for data at 4 weeks, p = 0.6 for data at 6 weeks) (Figure 1C).

At 6 weeks post-transplantation, we imaged the mice using micro-computed tomography (μCT) and found tumors in the lungs of the mice transplanted with mGeCKOa-transduced Cas9-GFP KPD cells (mGeCKOa mice), but not in the mice transplanted with untransduced Cas9-GFP KPD cells (control mice) (Figure 1D, Figure S1C). Mice were sacrificed and examined for metastases in various organs. Under a fluorescent stereoscope at 6× magnification, metastases were visually detected in the lung in 89% (8/9) of the mGeCKOa mice (Figure S1D). The mGeCKOa mice on average had 80% of their lung lobes positive for metastases (Figure 1E). In contrast, none (0/3) of the control mice developed detectable metastases in the lung (Figure 1E). At this time, metastases were not detected in the liver, kidney, or spleen in either group (Figure 1F). These data indicated that mGeCKOa library transduction enhanced the ability of the Cas9-GFP KPD cells to form metastases in the lung.

Dynamic Evolution of sgRNA Library Representation during Tumor Growth and Metastasis

To investigate the sgRNA representation through different stages of tumor evolution and to identify genes where loss of function confers a proliferative or metastatic phenotype, we used deep sequencing to readout the sgRNA representation (see Data S1 in Dataset S1). At 6 weeks post transplantation, we sequenced the late-stage primary tumor and three random lobes from the lung of each of the nine mGeCKOa mice (Figure 1A) (Experimental Procedures). In parallel, we also sequenced the mGeCKOa input plasmid library, the pre-transplantation mGeCKOa-transduced Cas9-GFP KPD cells (cultured in vitro for 7 days after transduction), and early-stage primary tumors (2 weeks post transplantation, one mouse from each infection replicate). In the cell samples, the sgRNA representations showed high concordance between technical replicates (correlation, $\rho = 0.95$ on average, n = 3) and biological infection replicates (correlation, ρ = 0.84 on average, n = 3) (Figures 2A, S2A, S2B, and S2E). The sgRNA representation of cell samples correlates highly with the plasmid representation (correlation, $\rho = 0.93$ on average, n = 3) (Figures 2A, S2C, and S2E). Furthermore, different sgRNAs that target the same gene are correlated in terms of rank change (correlation, ρ = 0.49 on average, n = 3) (Figure S2D). Using gene set enrichment analysis (GSEA), we found that the sgRNAs with significantly decreased abundance in cells compared to plasmid are enriched for genes involved in fundamental cellular processes, such as ribosomal proteins, translation factors, RNA splicing factors, and RNA processing factors, indicating selection against the loss of these genes after 1 week in culture (Figure S2F).

To investigate the sgRNA library dynamics in different sample types (plasmid, pre-transplantation cells, early primary tumor, late primary tumor, and lung metastases), we compared the overall distributions of sgRNAs from all samples sequenced. Cell samples clustered tightly with each other and the plasmid, forming a cell-plasmid clade (Figures 2A and S2E). Early primary tumor samples also clustered with each other and then with the cell-plasmid clade, whereas late tumors and lung metastases clustered together in a distinct group (Figures 2A and S2E). The overlap of detected sgRNAs between different pre-transplantation infection replicates is over 95% (Figure S3A). The detected sgRNAs in the three infection replicates of early tumor

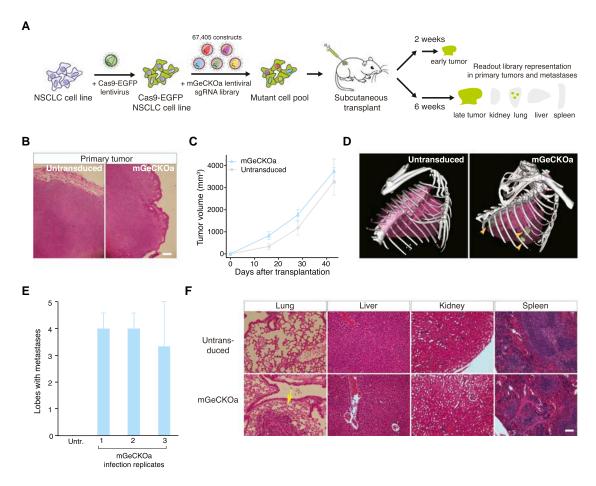


Figure 1. Tumor Growth and Metastasis in Transplanted Cas9-GFP KPD Cells with mGeCKOa Library

- (A) Schematic representation of the loss-of-function metastasis screen using the mouse genome-scale CRISPR/Cas9 knockout library (mGeCKOa).
- (B) Representative H&E stains of primary tumor from *Nu/Nu* mice subcutaneously transplanted with a Cas9-GFP *Kras*^{G12D/+};*p*53^{-/-};*Dicer1*^{+/-} (KPD) NSCLC cell line that was either untransduced or transduced with the mGeCKOa lentiviral library. Scale bar, 200 μm.
- (C) Primary tumor growth curve of Nu/Nu mice transplanted with untransduced cells (n = 3 mice) or mGeCKOa-transduced Cas9-GFP KPD cells (n = 9 mice). Error bars indicate SEM.
- (D) MicroCT 3D reconstruction of the lungs of representative mice transplanted with control (untransduced) and mGeCKOa-transduced (mGeCKOa) cell pools. Lung metastases were identified and traced in each 2D section (green).
- (E) Percent of lobes with metastases visible after dissection under a fluorescence stereoscope in *Nu/Nu* mice transplanted with untransduced Cas9-GFP KPD cells (n = 3 mice) or mGeCKOa-transduced Cas9-GFP KPD cells with three independent infection replicate experiments (1, 2, and 3; n = 3 mice per replicate). Error bars indicate SEM.
- (F) Representative H&E stains from various organs of *Nu/Nu* mice subcutaneously transplanted with untransduced and mGeCKOa-transduced Cas9-GFP KPD cells. Yellow arrow indicates a lung metastasis. Scale bar, 40 μm. See also Figure S1.

samples overlap 63%–76% with each other (Figure S3B). Early primary tumors retained less than half (32%–49%) of the sgRNAs found in the transplanted cell populations (Figures 2B, 2C, S3C, and S3D). Compared to the cell populations, sgRNAs whose targets are genes involved in fundamental cellular processes are further depleted in early tumors (Table S1).

Interestingly, only a small fraction of sgRNAs (less than 4% of all sgRNAs, or less than 8% of sgRNAs in the early primary tumor of the corresponding replicate) were detected in the late-stage primary tumor samples (Figures 2B, 2C, S3C, and S3D). The sgRNA diversity (i.e., number of different sgRNAs detected) further decreased in samples from lung metastases (Figures

2B, 2C, S3C, and S3D). The lung samples retained \leq 0.4% of all sgRNAs in the mGeCKOa library, or \leq 1.1% of sgRNAs found in the early primary tumor of the corresponding replicate, with a subset of highly enriched sgRNAs (Figures 2B, 2C, S3C, and S3D). The global patterns of sgRNA distributions in different sample types are distinct, as is evident in the strong shifts in the respective cumulative distribution functions (Kolmogorov-Smirnov [KS] test, p < 10 $^{-15}$ for all pairwise comparisons) (Figure 2D).

Enriched sgRNAs in Primary Tumors

Late primary tumors retain few sgRNAs (on average 813 ± 264 sgRNAs, n = 9 mice), with even fewer at high frequencies

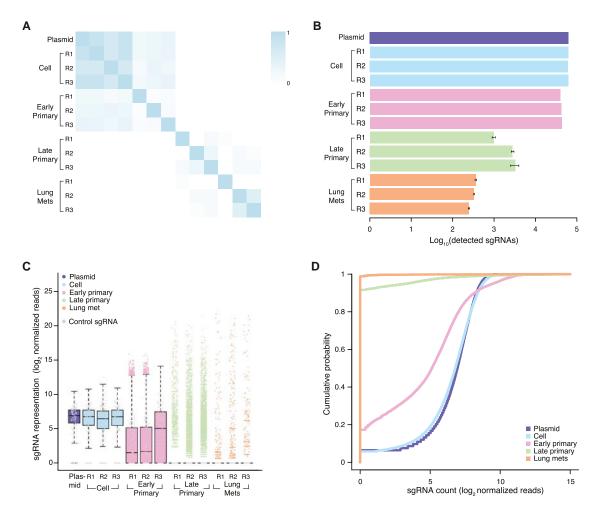


Figure 2. Representation of mGeCKOa Library at Different Stages of Tumor Growth and Metastasis

(A) Pearson correlation coefficient of the normalized sgRNA read counts from the mGeCKOa plasmid library, transduced cells before transplantation (day 7 after spinfection), early primary tumors (~2 weeks after transplantation), late primary tumors (~6 weeks after transplantation), and lung metastases (~6 weeks after transplantation). For each biological sample type, three independent infection replicates (R1, R2, and R3) are shown. n = 1 mouse per infection replicate for early primary tumors; n = 3 mice per infection replicate for late primary tumors and lung samples.

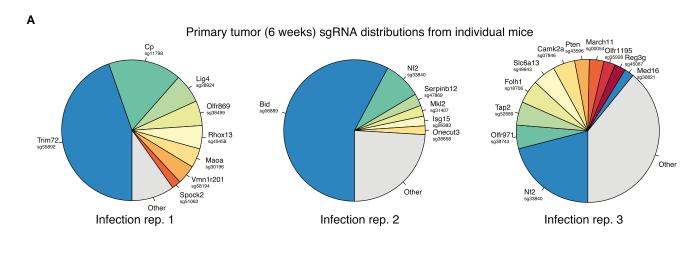
(B) Number of unique sgRNAs in the plasmid, cells before transplantation, early and late primary tumors, and lung metastases as in (A). Error bars for late primary tumors and lung metastases denote SEM for n = 3 mice per infection replicate.

(C) Boxplot of the sgRNA normalized read counts for the mGeCKOa plasmid pool, cells before transplantation, early and late primary tumors, and lung metastases as in (A). Outliers are shown as colored dots for each respective sample. Gray dots overlaid on each boxplot indicate read counts for the 1,000 control (non-targeting) sgRNAs in the mGeCKOa library. Distributions for late primary tumors and lung metastases are averaged across individual mice from the same infection replication.

(D) Cumulative probability distribution of library sgRNAs in the plasmid, cells before transplantation, early and late primary tumors, and lung metastases as in (A). Distributions for each sample type are averaged across individual mice and infection replications. See also Figures S2 and S3.

(4 \pm 1 sgRNAs with >5% of total reads) in each mouse (Figures 2B, 2C, S2C, S2D, 3A, and S4H). We used three methods to identify enriched sgRNAs in late primary tumors: (1) sgRNAs above a certain threshold, (2) top-ranked sgRNAs in the tumor of each mouse, and (3) using false discovery rate (FDR), i.e., sgRNAs enriched compared to the distribution of the 1,000 non-targeting sgRNAs. All three methods generated similar results (Figure S4A). Taking the results from (3) as an example, a total of 935 sgRNAs (targeting 909 genes) are enriched over the non-targeting controls (FDR cutoff = 0.2%) in the late primary tumor of one or more mice (Figures 3B and 3C). These sgRNAs are targeting genes highly enriched in apoptosis pathways (Table S2), with many of them being pro-apoptotic, such as BH3 interacting-domain death agonist (Bid), phosphatase and tensin homolog (Pten), cyclin-dependent kinase inhibitor 2a (Cdkn2a), and O-6-methylguanine-DNA methyltransferase (Mgmt), suggesting strong selection for mutations that inactivate apoptosis in primary tumor cells.

We identified 24 candidate genes that were targeted by two or more independent sgRNAs enriched in late primary tumors



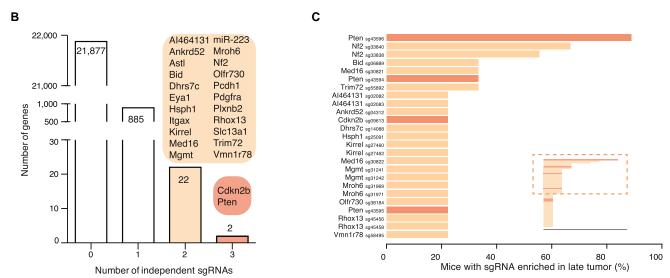


Figure 3. Enriched sgRNAs from the mGeCKOa Screen in Primary Tumors

(A) Pie charts of the most abundant sgRNAs in the primary tumors (at \sim 6 weeks post-transplantation) of three representative mice (one from each replicate mGeCKOa infection). The area for each sgRNA corresponds to the fraction of total reads from the primary tumor for the sgRNA. All sgRNAs with \geq 2% of total reads are plotted individually.

(B) Number of genes with 0, 1, 2, or 3 significantly enriched (FDR < 0.2% for at least one mouse) mGeCKOa sgRNAs targeting that gene. For genes/miRs with 2 or more enriched sgRNAs, genes/miRs are categorized by how many sgRNAs targeting that gene/miR are enriched as indicated in the colored bubbles adjacent to each bar.

(C) Inset: waterfall plot of sgRNAs where multiple sgRNAs targeting the same gene are significantly enriched in primary tumors. Each sgRNA is ranked by the percent of mice in which it is enriched. Only sgRNAs enriched in two or more mice are shown in the main panel. Main panel: enlargement and gene labels for sgRNAs at the top of the list from the inset (boxed region).

See also Figures S3, S4, and S5.

(Figures 3B and 3C). These genes were found to be mutated in patients in many previously reported cancer sequencing studies curated by cBioPortal (Cerami et al., 2012; Gao et al., 2013) (Figure S5A). For example, in somatic mutations identified by The Cancer Genome Atlas (TCGA) for NSCLC, including adenocarcinoma (LUAD) (Cancer Genome Atlas Research Network, 2014) and lung squamous cell carcinoma (LUSC) (Cancer Genome Atlas Research Network, 2012), 36% (107/407) of patients have one or more of these 24 genes mutated (Figures S5B and S5C). Several candidates were well-known tumor suppressors,

such as *Pten*, cyclin-dependent kinase inhibitor 2b (*Cdkn2b*), neurofibromin 2 (*Nf2/Merlin*), alpha-type platelet-derived growth factor receptor (*Pdgfra*), and integrin alpha X (*Itgax*).

Enriched sgRNAs in Metastases

We also sequenced the sgRNA distributions from three lung lobes for each mouse transplanted with mGeCKOa-transduced Cas9-GFP KPD cells. In each lobe, the sgRNA representation is dominated by one or a few sgRNAs (Figures 4A, S3D, and S4I). In each mouse, the lung sgRNA representation (average of

normalized sgRNA representations from three lobes) is also dominated by a small number of sgRNAs (on average, 3.4 ± 0.4 sgRNAs with >5% of total reads) (Figure 4B), suggesting that metastases were seeded by a small set of cells, which grew to dominance over this timescale. Non-targeting sgRNAs were occasionally detected in the metastases but were never observed at high frequency (<0.1% of total reads in any lobe; Figures 2C, 4A and 4B, and S4I). These observations are consistent with our finding that untransduced tumors are not metastatic (Figure 1E), suggesting that specific sgRNA-mediated mutations led to metastasis.

The sgRNA representations in the lung metastases are similar to those in the late-stage primary tumors in several ways. First, the detected sgRNAs in lung samples overlap significantly with those in late tumor samples (chi-square test, $p < 10^{-15}$) (Figure S3E). Second, the number of sgRNAs detected in lung samples correlates, albeit weakly, with the number of sgRNAs detected in late primary tumor samples (ρ = 0.42, F test, p = 0.097) (Figure S3F). Third, the abundance (number of reads) of sgRNAs in the lung correlates positively with that in the late primary tumors of the same mouse (correlation, $\rho = 0.18$ on average, F test, p < 0.01, n = 9) (Figure S3G). Fourth, in most mice (8/9), the lung metastasis enriched sgRNAs also occupy a large fraction of reads in the late primary tumor of the same mouse (Figure 4C, left panel), significantly larger than a random sampling of the same number of sgRNAs from the mGeCKOa library (Figure 4C, right panel). These data indicate that mutants with preferential ability to proliferate in late primary tumors are more likely to dominate the metastases.

The three methods (threshold, rank, or FDR) of finding enriched sgRNAs in the lung metastases yield similar results (Figure S4B). Using the non-targeting sgRNA distribution to set a FDR-based cutoff for enrichment, the enriched sgRNAs in different lobes of the same mouse overlap with each other by $62\% \pm 5\%$ (chi-square test, p < 10^{-15}) (Figure S4C), while different mice show greater variability while still overlapping significantly (29% \pm 3%, chi-square test, p < 10⁻¹⁵) (Figure S4D). The overlap between sgRNAs in different biological/infection replicate experiments when pooling enriched sgRNAs from all mice in the same replicate is 54% (chi-square test, p < 10^{-15}) (Figure S4E), suggesting that pooling sgRNAs from mice in the same experiment facilitates the identification of shared hits. These data suggest that the three independent experiments reproducibly captured a common set of hits and provide a picture for in vivo experimental variation between different lobes, different animals, and different infection replicates.

We found 147 sgRNAs enriched in more than one lobe, and 105 sgRNAs enriched in the lung of more than one mouse (Figures 4D and 4E). These include sgRNAs targeting Nf2, Pten, tripartite motif-containing protein 72 (Trim72), fibrinogen alpha chain (Fga), Bid, cyclin-dependent kinase inhibitor 2a (Cdkn2a), zinc finger FYVE domain-containing 28 (Zfyve28), reproductive homeobox 13 (Rhox13), and BRISC and BRCA1 A complex member 1 (Babam1), as well as microRNA genes miR-152 and miR-345. Intriguingly, a few sgRNAs targeting the Pol II subunits and olfactory receptor are also enriched in the lung, possibly due to off-target effects or unknown roles of these genes. For most sgRNAs detected in lung metastases, the relative abundance in metastases is lower than that in the late primary tumor of the

same mouse, with a metastasis-primary ratio (MPR) less than 1 (Figure S4F), likely due to more skewed distributions of sgRNAs in the metastases compared to those in the late primary tumors. A small subset of sgRNAs, however, are more abundant in metastases than in primary tumors (MPR > 1) in multiple mice, e.g., sgRNAs targeting Nf2, Trim72, prostaglandin E synthase 2 (Ptges2), or ubiquitin-conjugating enzyme E2G 2 (Ube2g2) (Figure 4F).

For four genes, Nf2, Pten, Trim72, and Zfyve28, two independent sgRNAs targeting different regions of the same gene were enriched in lung metastases (Figure 4G). One of the Zfyve28-targeting sgRNAs, however, is enriched in only one mouse, whereas Nf2, Pten, and Trim72 all have two sgRNAs enriched in multiple mice (Figure 4H). These three genes, several representative genes with one frequently enriched sgRNA (Cdkn2a, Fga, and Cryba4), and the two top-scoring microRNAs (miR-152 and miR-345) were chosen to assay individually for primary tumor growth and metastases formation.

Validation In Vivo Using Individual sgRNAs

For these eight genes (Nf2, Pten, Trim72, Cdkn2a, Fga, Cryba4, miR-152, and miR-345), we cloned multiple sgRNAs targeting each of them into the lentiGuide-Puro vector and transduced them into the Cas9-GFP KPD cell line (Figure 5A) (Experimental Procedures). As expected, these sgRNAs generated a broad distribution of NHEJ-mediated indels at the target site when examined 3 days post-transduction, with a bias toward deletions (Figure 5B). For protein-coding genes, the majority (>80%) of indels are out of frame, which potentially disrupts the protein functions. For miR-152 and miR-345, the sqRNAs generated mostly deletions (>90% of indels are deletions, average indel size -7 bp) (Figure 5B), overlapping with the loop or mature microRNA sequences in the hairpins, which are structures required for maturation of microRNAs. For proteins where specific antibodies are available (Nf2 and Pten), we found that the majority of the protein products were significantly reduced 1 week after lentiviral sgRNA infection (Figure S6A).

When these single-sgRNA-transduced cells were transplanted into the flanks of immunocompromised mice, they all formed tumors in situ. With two mice injected per sgRNA and three sgRNAs per gene, all genes tested showed increased lung metastasis formation compared to controls (untransduced and non-targeting sgRNAs), with the most significant ones being *Nf2*, *Pten*, and *Cdkn2a* (Fisher's exact test, one-tailed, $p < 10^{-3}$) (Figures 5C and 5D). Fga and Trim72 also have effects on metastasis acceleration (Fga p = 0.001, Trim72 p = 0.046). Cryba4 is not statistically different from controls (p = 0.1). sgRNAs targeting miR-345 or miR-152 significantly increased the rate of metastasis (miR-345 p = 0.01, miR-152 p = 0.046). These data suggest that loss-of-function mutations in any of Nf2, Pten, Cdkn2a, Trim72, Fga, miR345, or miR-152 are sufficient to accelerate the rate of metastasis formation in this genetic background.

Most genes targeted by single sgRNAs also contributed to accelerated primary tumor growth compared to controls (Figure 5E). Nf2 and Pten loss of function dramatically speed up tumor growth (KS test, p < 0.001) (Figure 5E); Cdkn2a-, Trim72-, and Fga-targeting sgRNAs slightly accelerate primary tumor growth (KS test, p = 0.003-0.01); Cryba4 has a marginal effect

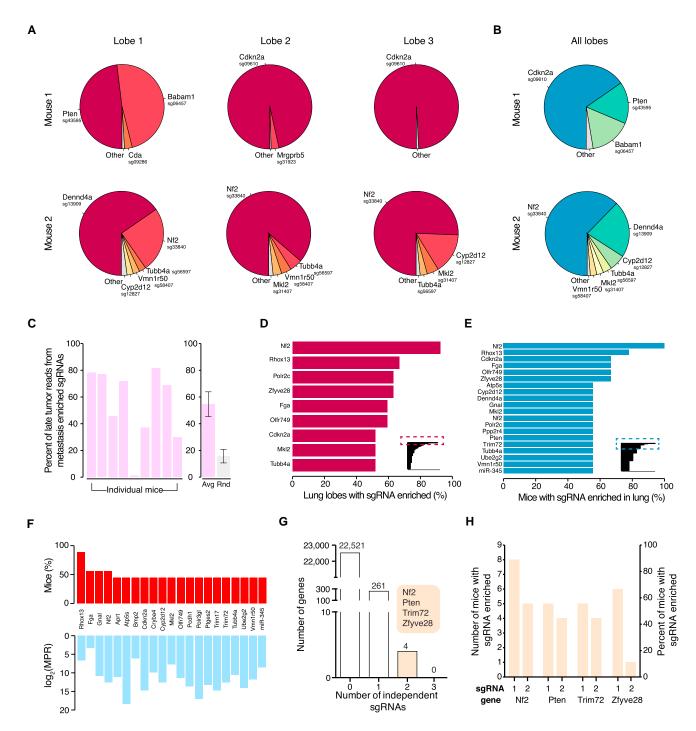


Figure 4. Enriched sgRNAs from the mGeCKOa Screen in Lung Metastases

(A) Pie charts of the most abundant sgRNAs in three individual lobes of the lungs of two representative mice transplanted with mGeCKOa-transduced cells. The area for each sgRNA corresponds to the fraction of total reads from the lobe for the sgRNA. All sgRNAs with $\geq 2\%$ of total reads are plotted individually. (B) Pie charts of the most abundant sgRNAs in the lung (averaged across three individual lobes) for the two mice shown in (A). All sgRNAs with $\geq 2\%$ of average reads are plotted individually.

(C) Left: percentage of late tumor reads for the significantly enriched (FDR < 0.2%) mGeCKOa sgRNAs found in the lung metastases (averaged across three dissected lobes). Right: in purple, the percentage of late tumor reads for the significantly enriched (FDR < 0.2%) mGeCKOa sgRNAs found in the lung metastases (average across all mice, n = 9 mice). In gray, the percentage of late tumor reads for random, size-matched samplings of sgRNAs present in the late tumor (n = 100 samplings). Error bars indicate SD.

(legend continued on next page)

(KS test, p = 0.08); and neither miR-152- nor miR-345-targeting sgRNAs promote primary tumor growth (KS test, p > 0.1). Overall, for the targets we examined using individual sgRNAs, the number of lobes with lung metastases strongly correlates with the terminal volume of the late primary tumor (or average primary tumor growth rate) (correlation, $\rho = 0.83$, F test, p < 0.01) (Figure 5F), indicating at a single-gene level that mutant cells with a stronger ability to promote primary tumor growth generate metastases faster.

To analyze blood samples for the presence of circulating tumor cells (CTCs), we designed a microfluidic device based on the physical size of the Cas9-GFP KPD cells (Figures S6B and S6C). We performed CTC capture with terminal blood samples from mice injected with Cas9-GFP KPD cells transduced with sgRNAs targeting Nf2, Pten, Trim72, Cdkn2a, and miR-152 and from mice injected with Cas9-GFP KPD control cells (untransduced or non-targeting sgRNA) (Figures S6C and S6D). Mice transplanted with cells transduced with sgRNAs targeting Nf2, Pten, Trim72, or Cdkn2a had a higher concentration of CTCs as compared to controls (Figures S6D-S6G), consistent with the higher rate of lung metastasis formation.

Competitive Dynamics of Top Hits Assessed Using an sgRNA Minipool

To better understand the relative metastatic potential of multiple genes from our genome-wide screen, we designed a targeted pooled screen with a smaller library. This small library (termed validation minipool) contains 524 sgRNAs targeting 53 genes that had highly enriched sgRNAs in lung metastases in the genome-wide screen (ten sgRNAs per gene for most genes) plus 100 non-targeting sgRNAs. We also created a size-matched library containing 624 non-targeting sgRNAs (termed control minipool) (Figure 6A). Lentiviruses from these two pools were used to transduce the Cas9-GFP KPD cells, which were cultured in vitro for 1 week and then transplanted into Nu/Nu mice (Figure 6A). Both validation minipool- and control minipool-transduced cells induced primary tumor growth at a similar rate (Figure 6B). However, mice transplanted with validation minipool cells had a dramatically elevated rate of lung metastasis formation (Figure 6C).

We sequenced the validation minipool plasmid library and the transduced cells pre-transplantation, as well as the late-stage primary tumors and whole lungs of the mice at 5 weeks posttransplantation (see Data S2 in Dataset S1). The sgRNA representations correlate strongly between technical replicates of the transduced cell pool, late primary tumors, and lung metastases (Figures S7A and S7D). The sgRNA representation in the cell sample strongly correlated with the plasmid (correlation, $\rho = 0.91$) (Figures S7B and S7D). Almost all (99.4%) sgRNAs were recovered in the plasmid and the cell population (Figure S7C). The late primary tumors retained less than half of the sgRNAs, and the metastases in the whole lung retained only a small fraction (2%-7%) of all sgRNAs (Figure S7C). Enriched sgRNAs from lung metastases clustered with each other and with late primary tumors (Figure S7D). Similar to the genome-wide library, in this validation minipool, the plasmid and cell samples had a unimodal distribution of sgRNAs, whereas the late primary tumors and lung metastases contained a bimodal distribution, with the majority of sgRNAs being absent and a small fraction spanning a large range of non-zero read counts (Figure 6D). Intriguingly, two mice retained relatively high sgRNA diversity in late primary tumors (Figure 6D), likely due to dormant or slowly proliferating cells that remained in low numbers during tumor growth. Similar to the genome-wide library, large shifts in the sgRNA distribution exist between different sample types (KS test, p $< 10^{-15}$ for pairwise comparisons between the cell, primary tumor, and lung metastases, p = 0.02 between plasmid and cell) (Figure 6E).

In the validation minipool, the sgRNAs detected in the late primary tumors or the lungs of five different mice significantly overlap with each other (Figures S7E and S7F). The late primary tumors and lung metastases are dominated by a few sgRNAs (Figures 7A and S7G-S7I), suggesting that these sgRNAs outcompete others during tumor growth and metastasis. With the validation library, the sgRNA representations are highly correlated between late primary tumors and lung metastases (correlation, $\rho = 0.55$ on average, F test, p < 0.01, n = 5) (Figure 7B). The late primary tumors and lung metastases have dozens of sgRNAs at moderate to high frequencies (Figures 7B and 7C). Several genes have multiple independent sgRNAs that are enriched in the lung over the primary tumor (MPR > 1), such as Nf2 (eight sgRNAs), Pten (four sgRNAs), Trim72 (three sgRNAs), Ube2g2 (three sgRNAs), Ptges2 (two sgRNAs), and ATP-dependent DNA ligase IV (Lig4) (two sgRNAs) (Figures 7C and 7D). Two Cdkn2a sgRNAs were present in both late primary tumors and lung metastases in two mice, but with MPR < 1. Fga-, Cryba4-, miR-152-, and miR-345-targeting sgRNAs were not found at high frequency in either late primary tumors or lung metastases, suggesting that they are outcompeted by other loss-of-function mutations (such as Nf2), which agrees with the relatively reduced metastasis formation of these genes in the

⁽D) Inset: all sgRNAs found in individual lung lobes, ordered by the percent of lobes in which a particular sgRNA was among the significantly enriched (FDR < 0.2%) sgRNAs for that lobe. Only sgRNAs enriched in two or more lobes are shown. Main panel: enlargement and gene labels for sgRNAs at the top of the list from the inset (boxed region).

⁽E) Inset: all sgRNAs found in individual mice (averaged across three dissected lobes), ordered by the percent of mice in which a particular sgRNA was among the significantly enriched (FDR < 0.2%) sgRNAs for that mouse. Only sgRNAs enriched in two or more mice are shown. Main panel: enlargement and gene labels for sqRNAs at the top of the list from the inset (boxed region).

⁽F) Bottom: metastasis primary ratio (MPR) for the sgRNAs in mGeCKOa with enrichment in metastases over late tumors (MPR > 1) observed in at least three mice. The sgRNAs are sorted by the number of mice in which the MPR for the sgRNA is greater than 1. Top: number of mice in which the MPR for this sgRNA is greater than 1. In both panels, individual sgRNAs are labeled by gene target.

⁽G) Number of genes with 0, 1, 2, or 3 significantly enriched (FDR < 0.2% for at least one mouse) mGeCKOa sgRNAs in the lung metastases. For genes with 2 enriched sqRNAs, gene names are indicated in the colored bubble adjacent to the bar.

⁽H) Number of mice and percentage of mice in which each sgRNA was enriched in the lung metastases for all genes with multiple enriched sgRNAs. See also Figures S4 and S5.

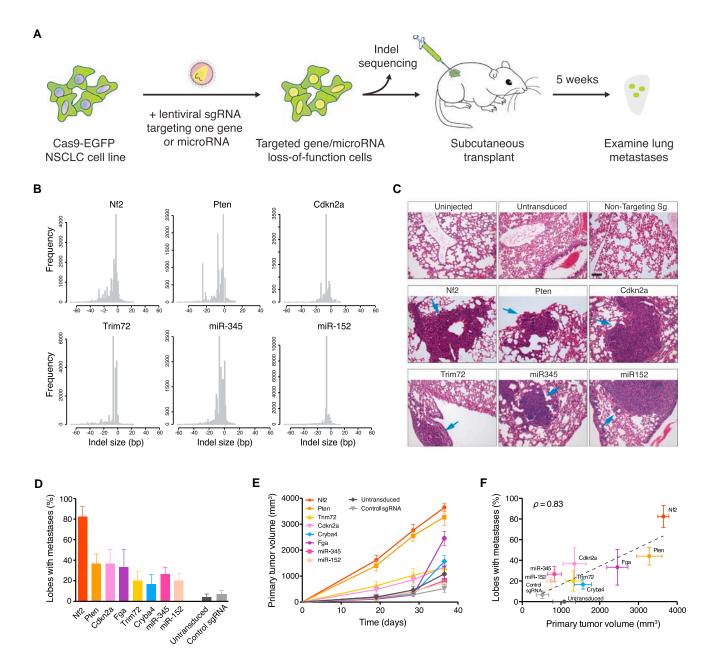
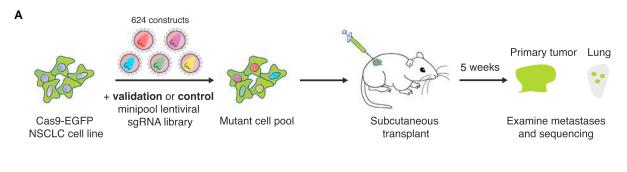


Figure 5. Validation of Target Genes and MicroRNAs from mGeCKOa Screen Using Individual sgRNAs

(A) Schematic representation of lentiviral transduction of Cas9-GFP KPD cells with single sgRNAs designed to target one gene or miR. After puromycin selection, the cell population was transplanted into *Nu/Nu* mice and also deep sequenced to examine the distribution of indels at the target site. After 5 weeks, the primary tumor and lungs were examined.

- (B) Histograms of indel sizes at the genomic locus targeted by a representative sgRNA for each gene/miR after 3 days of puromycin selection. Indels from sgRNAs targeting the same gene were pooled (6 sgRNAs for each protein-coding gene; 4 sgRNAs for each miR).
- (C) Representative H&E staining of lung lobes from uninjected mice (n = 3 mice), mice transplanted with cells transduced with Cas9 only (n = 5), and mice transplanted with cells containing Cas9 and a single sgRNA (n = 6). Single sgRNAs are either control/non-targeting sgRNAs (n = 6 mice for control sgRNAs, 3 distinct control sgRNAs with 2 mice each) or targeting sgRNAs (n = 6 mice for each gene/miR target, 3 sgRNAs per target with 2 mice each). Blue arrows indicate lung metastases. Scale bar, 10 μ m.
- (D) Percent of lung lobes with metastases after 6 weeks for the mice in (C). Error bars indicate SEM.
- (E) Primary tumor growth curve of Nu/Nu mice transplanted with NSCLC cells transduced with Cas9 only (n = 5) or single sgRNAs (n = 6 mice per gene/miR target, 3 sgRNAs per target with 2 mice each; n = 6 mice for control sgRNAs, 3 control sgRNAs with 2 mice each). Error bars indicate SEM.
- (F) Correlation between primary tumor volume and percent of lobes with metastases for each gene in (D) and (E). Error bars indicate SEM. See also Figure S6.



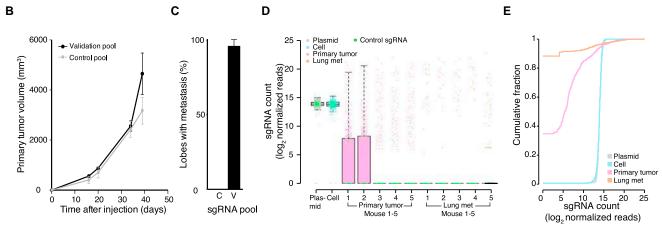


Figure 6. Tumor Evolution and Library Representation in Transplanted Cas9-GFP KPD Cells with Minipool Libraries

(A) Schematic representation of the loss-of-function metastasis minipool screen. Briefly, Cas9-GFP KPD cells were transduced with either validation minipool (524 gene-targeting + 100 non-targeting sgRNAs) or control minipool (624 non-targeting sgRNAs). After puromycin selection, the cell pools were transplanted into Nu/Nu mice. After 5 weeks, validation minipool sgRNAs were sequenced from primary tumor and lung samples.

(B) Primary tumor growth curve of Nu/Nu mice transplanted with Cas9 vector + validation minipool cells (n = 5 mice) or Cas9 + control minipool cells (n = 5 mice). Error bars indicate SEM.

- (C) Percent of lung lobes with metastases after 6 weeks for the mice in (B). C, control minipool; V, validation minipool. Error bars indicate SEM.
- (D) Boxplot of the sgRNA normalized read counts for the plasmid library, cells before transplantation, primary tumors, and lung metastases using the validation
- (E) Cumulative probability distribution of library sgRNAs in the validation plasmid pool, cells before transplantation, primary tumors, and lung metastases. Distributions of primary tumor and lung metastases are averaged across five mice. See also Figure S7.

individual sgRNA validation. These results further validate several of the top hits from the primary screen, using either sgRNA dominance (e.g., Nf2, Pten, Trim72) or MPR (e.g., Nf2, Trim72, Ube2g2, Ptges2). This validation minipool reveals the dynamics of multiple competing mutants chosen from the primary screen hits and indicates that mutants with strong progrowth effects tend to enhance metastasis (Figure 7E).

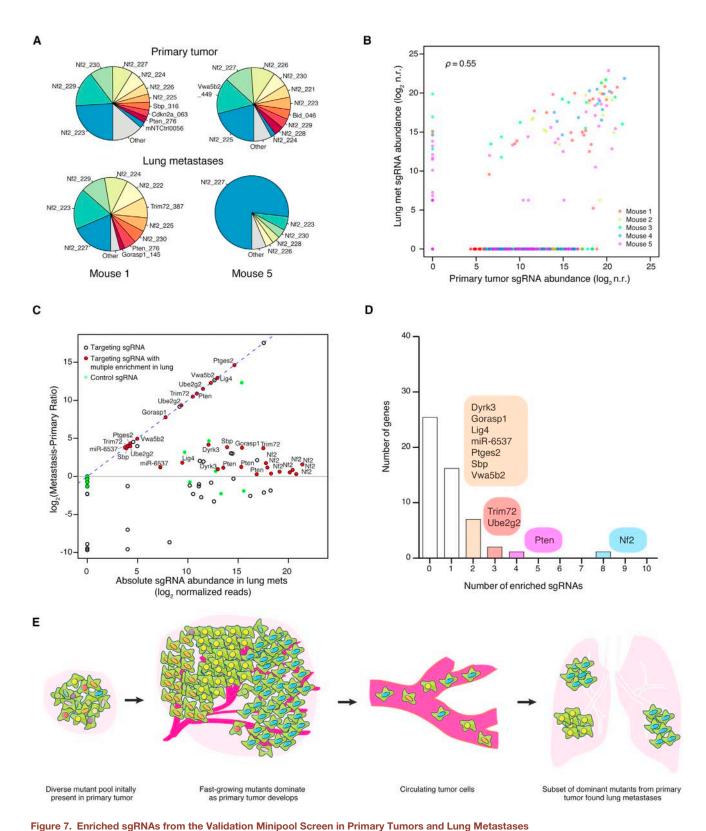
TCGA Gene Expression of Screen Hits in Human Lung Cancer

To assess the relevance of our mGeCKOa and validation minipool screen hits (genes targeted by sgRNAs enriched in lung metastases) to pathological metastasis in human cancer, we performed gene expression analysis of the human orthologs of these genes. We compared mRNA levels in metastatic compared to non-metastatic primary tumors in patient samples using TCGA mRNA sequencing data. We found that most (61%-75%) of these genes are downregulated in metastatic tumors in NSCLC patients (Figures S5D and S5E; Table S6). These data suggest that downregulation of these genes is selected for in metastatic tumors from patients.

DISCUSSION

Pooled Mutagenesis in a Metastasis Model

Distal metastases develop as primary tumors shed CTCs into the circulation, from which CTCs travel to the destination site, move out of the blood or lymphatic vessels, and initiate clonal growth (Valastyan and Weinberg, 2011; Vanharanta and Massagué, 2013; Weinberg, 2007). In this study, cancer cells transplanted into the flanks of mice form primary tumors in situ, and cells from this mass undergo the intravasation-circulation-extravasation-clonal growth cascade to form distal metastases (Francia et al., 2011). The initial lung cancer cell line has little capacity to form metastases; in contrast, after being mutagenized with the mGeCKOa genome-scale Cas9 knockout library, the cell



(A) Pie charts of the most abundant sgRNAs in the primary tumor and the whole lung of two representative mice transplanted with validation minipool-transduced Cas9-GFP KPD cells. The area for each sgRNA corresponds to the fraction of total reads from the tissue (primary tumor or lung metastases) for the sgRNA. All sgRNAs with ≥2% of total reads are plotted individually.

population forms highly metastatic tumors. Thus, these mutations, acting in simple or complex pleiotropic ways, accelerate metastasis. In this model, the effect of mutations on metastasis strongly correlates with their abundance in late-stage primary tumors.

sgRNA Dynamics during Tumor Evolution

The dynamics of the sgRNA population changed dramatically over the course of tumor development and metastasis, reflecting the selection and bottlenecks of cellular evolution in vitro and in vivo. After a week in culture, cells retained most of the sgRNAs present in the plasmid library, with decreases in sgRNAs targeting genes involved in fundamental cellular processes. The distribution of non-targeting control sgRNAs is almost identical to those targeting genes, suggesting that the selective pressure of in vitro culture alone does not radically alter sgRNA representation, similar to previous observations in human melanoma cells (Shalem et al., 2014).

In contrast, less than half of the sgRNAs survive in an earlystage primary tumor. This loss of representation occurs with both gene-targeting sgRNAs and non-targeting control sgRNAs. suggesting that random sampling influences sgRNA dynamics during the transplantation and tumor initiation processes, although we cannot exclude that some of the non-targeting sgRNAs might have detrimental or pro-growth effects. We also detected further dropout of genes involved in fundamental cellular processes in early tumor samples compared to cell samples. Thus, it is likely that the sgRNA dynamics are influenced by a combination of selection and random sampling during transplantation and tumor initiation.

As primary tumors grow, the mutant cells proliferate and compete as a pool. This creates strong selection for sgRNAs targeting anti-apoptotic genes and other tumor suppressors. The majority of the genetic diversity in early tumors is lost during the subsequent 4 weeks of primary tumor growth in mice. Accordingly, sequencing revealed a smaller set of dominant sgRNAs, usually on the order of hundreds to a few thousand per mouse. In addition, almost all of non-targeting sgRNAs are lost during primary tumor growth, which is consistent with selection for cells with special growth and survival properties. This observation is also consistent with earlier transplantation studies by Kerbel and colleagues using small pools of randomly mutagenized cells, which found that the majority of clonal variants detectable by Southern blot disappeared within 6 weeks of primary tumor growth, leaving one dominant clone (Korczak et al., 1988; Waghorne et al., 1988).

Each step toward metastasis has a bottleneck effect. In the lung metastases, we detected very few sgRNAs at high abundance. As with the primary tumor, we found only a few non-targeting sgRNAs at low frequencies in metastases. Their presence could be due to unknown off-target effects of these sgRNAs, random shedding of CTCs in the primary tumor, or clustering together with other strongly selected CTCs during metastasis (Aceto et al., 2014).

Relevance of Screen Hits to Human Cancer

Several of the genes enriched in late-stage primary tumors are associated with cancer, but their functions in tumor growth are poorly understood. For example, Mgmt, a gene with two enriched sgRNAs, is required for DNA repair and is thus crucial for genome stability (Tano et al., 1990). Mutation, silencing, or promoter methylation of MGMT is associated with primary glioblastomas (Jesien-Lewandowicz et al., 2009). Med16, another gene with two enriched sgRNAs, encodes a subunit of the mediator complex of transcription regulation, which has been recently implicated in cancer (Huang et al., 2012; Schiano et al., 2014).

We found that the genes that are significantly enriched in lung metastases largely overlap with those found in abundance in the late primary tumor. Several of these hits were validated in vivo using multiple individual sgRNAs, including Nf2, Pten, Cdkn2a, Trim72, Fga, miR-152, and miR-345. Nf2, Pten, and Cdkn2a are well-known tumor suppressor genes. Intriguingly, the NF2 locus is mutated at only 1% frequency in primary tumors of human NSCLC patients (LUAD and/or LUSC) (Cancer Genome Atlas Research Network, 2012, 2014). Nf2 mutant mice develop a range of highly metastatic tumors (McClatchey et al., 1998). It is possible that NF2 mutations influence metastases to a greater degree than primary tumor growth, but this awaits metastasis genomics from patient samples. Pten mutations are also associated with advanced stages of tumor progression in a mouse model of lung cancer (McFadden et al., 2014), and PTEN was found to be mutated at 8% in adenocarcinoma patients (LUAD). CDKN2A has been shown to be often inactivated in lung cancer (Kaczmarczyk et al., 2012; Yokota et al., 2003). Fga encodes fibrinogen, an extracellular matrix protein involved in blood clot formation. Fga mutations have been found in various cancer types in TCGA (Lawrence et al. 2013), as well as circulating tumor cells (Lohr et al., 2014). Trim72 is an E3 ubiquitin ligase, and its role in cancer metastasis is largely unknown. Studies have shown that miR-152 and miR-345 are associated with cancer and metastasis (Cheng et al., 2014; Tang et al., 2011). FGF2 and BAG3, which promote metastasis, were predicted targets of miR-152 and miR-345; thus, loss of these

See also Figure S7.

⁽B) Scatterplot of normalized sgRNA read counts in primary tumor and lung metastases for all sgRNAs in the validation minipool for each mouse (different color dots indicate sgRNAs from different mice). log₂ n.r., log₂ normalized reads.

⁽C) log₂ ratio of sgRNA abundance in the lung metastases over the primary tumor (MPR) plotted against the abundance in the lung metastases (n = 5 mice per sgRNA). Green dots are the 100 control sgRNAs. Dots with black outlines are non-control sgRNAs that target genes or miRs. Red dots indicate non-control sgRNAs for which more than one sgRNA targeting the same gene/miR is enriched in the lung metastases over the primary tumor (i.e., log₂(MPR) > 0) and are labeled with the gene/miR targeted. The lung-primary ratio is calculated for individual mice, and these quantities are averaged across mice.

⁽D) Number of genes with 0 to 10 significantly enriched validation minipool sgRNAs in lung metastases. For genes/miRs with 2 or more enriched sgRNAs, genes/ miRs are categorized by how many sgRNAs targeting that gene/miRs are enriched, as indicated in the colored bubbles adjacent to each bar.

⁽E) Schematic illustration of tumor growth and metastasis in the library-transduced NSCLC transplant model. The initially diverse set of loss-of-function mutations in the subcutaneously transplanted pool is selected over time for mutations that promote growth of the primary tumor. A subset of these mutants also dominate lung metastases.

microRNAs may lead to acceleration of metastases, likely due to de-repression of these genes (Cheng et al., 2014; Tang et al., 2011).

In our own analysis of TCGA samples from lung cancer patients, we observed downregulation of the human orthologs of the genes identified in the genome-wide and validation minipool screens at the mRNA level in metastatic tumors compared to non-metastatic tumors, suggesting that these genes may also be inactivated during pathological metastasis. Human orthologs of these genes are often found to be mutated in cancers. Moreover, these genes have been implicated in various pathways and biological processes in tumorigenesis and/or metastasis in human cancer (Tables S7A–S7C). However, most cancer sequencing studies involve samples from primary tumors of patients. In the clinic, metastases are rarely sampled. Future patient sequencing directly from metastases may further connect genes identified in the mouse model to those mutated or silenced in clinical metastases.

Future In Vivo Functional Genomic Screens

Our study provides a roadmap for in vivo Cas9 screens, and future studies can take advantage of this model to explore other oncogenotypes, delivery methods, or metastasis target organs. Genome-scale CRISPR screening is feasible using a transplant model with virtually any cell line or genetic background (e.g., mutations in *EGFR*, *KRAS*, *ALK*, etc.), including a large repertoire of human cell lines from diverse cancer types (Barretina et al., 2012). Other cell delivery methods, such as intravenous injection or orthotopic transplantation, may help identify genes regulating extravasation and clonalization. Examining samples from other stages or sites, such as CTCs or metastases to other organs, can provide a more refined picture of tumor evolution.

In addition to these parameters, several aspects of the screen perturbations themselves can also be modified. Targeted drug therapies or immunotherapies can be applied in conjunction with the in vivo screening strategy to identify genes involved in acquired resistance. Other screening technologies, such as Cas9-mediated activation (Gilbert et al., 2014; Konermann et al., 2015), can identify metastasis-regulating factors that act in a gain-of-function manner. Activation screens that identify oncogenes, as well as dropout screens that identify genetic dependencies, may facilitate identification of novel therapeutic targets. Targeted subpool strategies can be used to reduce the library size and facilitate further confirmation of primary screens. In a customized library, genes can be chosen based on genomic analysis, pathways, or clinical relevance for focused screening libraries. Additionally, application of pooled sgRNA libraries using individually barcoded cells will allow quantitative assessment of the robustness and significance of each candidate hit and will enable analysis of the competitive dynamics among different perturbations. With these promising future directions and the results of our study, Cas9-based in vivo screening establishes a new platform for functional genomics discovery.

EXPERIMENTAL PROCEDURES

Generation of Cas9-GFP Expression Vector

A lentiviral vector, lenti-Cas9-NLS-FLAG-2A-EGFP (lentiCas9-EGFP), was generated by subcloning Cas9 into a lentiviral vector.

Pooled Guide-Only Library Cloning and Viral Production

The Cas9-GFP KPD cell line was transduced at a MOI of \sim 0.4 with lentivirus produced from a genome-wide lentiviral mouse CRISPR knockout guide-only library (Sanjana et al., 2014) containing 67,405 sgRNAs (mGeCKOa, Addgene 1000000053) with at least 400-fold representation (cells per construct) in each infection replicate. A detailed viral production and infection protocol can be found in Extended Experimental Procedures.

Animal Work Statement

All animal work was performed under the guidelines of the MIT Division of Comparative Medicine, with protocols (0411-040-14, 0414-024-17, 0911-098-11, 0911-098-14, and 0914-091-17) approved by the MIT Committee for Animal Care, and were consistent with the Guide for the Care and Use of Laboratory Animals, National Research Council, 1996 (institutional animal welfare assurance no. A-3125-01).

Mice, Tumor Transplant, and Metastasis Analysis in the Primary Screen

Untransduced or mGeCKOa-transduced Cas9-GFP KPD cells were injected subcutaneously into the right side flank of Nu/Nu mice at 3 \times 10 7 cells per mouse. Transplanted primary tumor sizes were measured by caliper. At 6 weeks post-transplantation, mice were sacrificed and several organs (liver, lung, kidney, and spleen) were dissected for examination of metastases under a fluorescence stereoscope.

Mouse Tissue Collection

Primary tumors and other organs were dissected manually. For molecular biology, tissues were flash frozen with liquid nitrogen and ground in 24-well polyethylene vials with metal beads in a GenoGrinder machine (OPS Diagnostics). Homogenized tissues were used for DNA/RNA/protein extractions using standard molecular biology protocols. Tissues for histology were then fixed in 4% formaldehyde or 10% formalin overnight, embedded in paraffin, and sectioned at $6\,\mu m$ with a microtome as described previously (Chen et al., 2014). Slices were subjected to H&E staining as described previously (Chen et al., 2014).

Genomic DNA Extraction from Cells and Mouse Tissues

Genomic DNA from cells and tissues (primary tumors and lungs) was extracted using a homemade modified salt precipitation method similar to the Puregene (QIAGEN/Gentra) procedure. The sgRNA cassette was amplified and prepared for Illumina sequencing as described previously (Shalem et al., 2014). A detailed readout protocol can be found in Extended Experimental Procedures.

Individual Gene and MicroRNA Validation

Six sgRNAs per protein-coding gene and four sgRNAs per microRNA gene were chosen for validation using individual sgRNAs (Table S4). For protein-coding genes, we cloned both the three sgRNAs from the mGeCKOa library and three additional sgRNAs to target each gene. For microRNAs, we used all four sgRNAs from the mGeCKOa library.

Validation and Control Minipool Synthesis and In Vivo Transplantation

Validation and control minipools (Table S5) were synthesized using array oligonucleotide synthesis (CustomArray) and transduced at >1,000-fold representation in Cas9-GFP KPD cells. After 7 days in culture, Cas9-GFP KPD cells transduced with the validation minipool or control minipool were injected subcutaneously into the right side flank of Nu/Nu mice at 3 \times 10 7 cells per mouse with five replicate mice. After 5 weeks, mice were sacrificed, and primary tumors and lungs were dissected.

ACCESSION NUMBERS

Genomic sequencing data have been deposited in the NCBI Sequence Read Archive under accession number PRJNA273894. Plasmids and pooled libraries have been deposited in Addgene (LentiCas9-EGFP: 63592, Metastasis Validation Minipool library: 63594, Mouse Non-targeting Control Minipool: 63595).

SUPPLEMENTAL INFORMATION

Supplemental Information includes Extended Experimental Procedures, seven figures, seven tables, and a dataset and can be found with this article online at http://dx.doi.org/10.1016/j.cell.2015.02.038.

AUTHOR CONTRIBUTIONS

S.C, N.E.S., O.S., F.Z., and P.A.S. conceived and designed the study. S.C., N.E.S., and K.Z. performed all screening and validation experiments. S.C., N.E.S., O.S., and D.A.S. analyzed the data. K.L., J.S., R.W., and H.L. designed the CTC chip and performed CTC analysis. X.S. and J.Q.P. performed western blots. S.C., N.E.S., F.Z., and P.A.S. wrote the manuscript with the input from all authors. P.A.S. and F.Z. supervised the work.

ACKNOWLEDGMENTS

We thank R. Weinberg and R. Kerbel for critically reading the manuscript; the entire P.A.S. lab and F.Z. lab, L. Cong, T. Kelly, X. Ni, M. Nobel, J. Boehm, A. Tsherniak, S. Levine, M. Cornwall-Brady, S. Malstrom, M. Jennings, E. Vasile, C. Whittaker, K. Cormier, R. Bronson, and colleagues at the Koch Institute, Broad Institute, McGovern Institute, and Department of Biology for technical assistance and/or discussion; the Swanson Biotechnology Center for technical support (Genomics, Animal Imaging and Preclinical Testing, Bioinformatics and Computing, Microscopy, Flow Cytometry, Microscopy, and Histology, in particular). This work is supported by grants to P.A.S., including a United States Public Health Service grant R01-CA133404 from the NIH, an MIT-Harvard Center for Cancer Nanotechnology Excellence Grant U54 CA151884 from the National Cancer Institute, a generous gift from the Marie D. and Pierre Casimir-Lambert Fund, an SkTech/MIT Initiative Grant from the Skolkovo Foundation, and the Koch Institute Support (core) grant P30-CA14051 from the National Cancer Institute. F.Z. is supported by the NIH through NIMH grant 5DP1-MH100706) and NIDDK grant 5R01-DK097768; a Waterman Award from the National Science Foundation; the Keck, New York Stem Cell, Damon Runyon, Searle Scholars, Merkin, and Vallee foundations; and Bob Metcalfe. F.Z. is a New York Stem Cell Foundation Robertson Investigator. S.C. is a Damon Runyon Cancer Research Fellow (DRG-2117-12) and also supported by the Dale Frey Award for Breakthrough Scientists. N.E.S. is supported by a Simons Center for the Social Brain Postdoctoral Fellowship and NIH NHGRI award K99-HG008171. O.S. is a fellow of the Klarman Cell Observatory. R.W. is supported by NIH grant U54 CA151884. D.A.S. is supported by a NSF Graduate Research Fellowship. H.L. is supported by Department of Defense grant OCRP W81XWH-14-1-0279. CRISPR reagents (plasmids and libraries) are available to the academic community through Addgene. F.Z. is a co-founder of Editas Medicine and a scientific advisor for Editas Medicine and Horizon Discovery.

Received: December 30, 2014 Revised: February 3, 2015 Accepted: February 18, 2015 Published: March 5, 2015

REFERENCES

Aceto, N., Bardia, A., Miyamoto, D.T., Donaldson, M.C., Wittner, B.S., Spencer, J.A., Yu, M., Pely, A., Engstrom, A., Zhu, H., et al. (2014). Circulating tumor cell clusters are oligoclonal precursors of breast cancer metastasis. Cell 158. 1110-1122.

Barrangou, R., Fremaux, C., Deveau, H., Richards, M., Boyaval, P., Moineau, S., Romero, D.A., and Horvath, P. (2007). CRISPR provides acquired resistance against viruses in prokaryotes. Science 315, 1709-1712.

Barretina, J., Caponigro, G., Stransky, N., Venkatesan, K., Margolin, A.A., Kim, S., Wilson, C.J., Lehár, J., Kryukov, G.V., Sonkin, D., et al. (2012). The Cancer Cell Line Encyclopedia enables predictive modelling of anticancer drug sensitivity. Nature 483, 603-607.

Bolotin, A., Quinquis, B., Sorokin, A., and Ehrlich, S.D. (2005). Clustered regularly interspaced short palindrome repeats (CRISPRs) have spacers of extrachromosomal origin. Microbiology 151, 2551–2561.

Cancer Genome Atlas Research Network (2012). Comprehensive genomic characterization of squamous cell lung cancers. Nature 489, 519-525.

Cancer Genome Atlas Research Network (2014). Comprehensive molecular profiling of lung adenocarcinoma. Nature 511, 543-550.

Cerami, E., Gao, J., Dogrusoz, U., Gross, B.E., Sumer, S.O., Aksoy, B.A., Jacobsen, A., Byrne, C.J., Heuer, M.L., Larsson, E., et al. (2012). The cBiol. cancer genomics portal: an open platform for exploring multidimensional cancer genomics data. Cancer Discovery 2, 401-404.

Chen, S., Xue, Y., Wu, X., Le, C., Bhutkar, A., Bell, E.L., Zhang, F., Langer, R., and Sharp, P.A. (2014). Global microRNA depletion suppresses tumor angiogenesis. Genes Dev. 28, 1054-1067.

Cheng, Z., Ma, R., Tan, W., and Zhang, L. (2014). MiR-152 suppresses the proliferation and invasion of NSCLC cells by inhibiting FGF2. Exp. Mol. Med. 46,

Chylinski, K., Le Rhun, A., and Charpentier, E. (2013). The tracrRNA and Cas9 families of type II CRISPR-Cas immunity systems. RNA Biol. 10, 726-737.

Chylinski, K., Makarova, K.S., Charpentier, E., and Koonin, E.V. (2014). Classification and evolution of type II CRISPR-Cas systems. Nucleic Acids Res. 42, 6091-6105.

Cong, L., Ran, F.A., Cox, D., Lin, S., Barretto, R., Habib, N., Hsu, P.D., Wu, X., Jiang, W., Marraffini, L.A., and Zhang, F. (2013). Multiplex genome engineering using CRISPR/Cas systems. Science 339, 819-823.

Deltcheva, E., Chylinski, K., Sharma, C.M., Gonzales, K., Chao, Y., Pirzada, Z.A., Eckert, M.R., Vogel, J., and Charpentier, E. (2011). CRISPR RNA maturation by trans-encoded small RNA and host factor RNase III. Nature 471,

Francia, G., Cruz-Munoz, W., Man, S., Xu, P., and Kerbel, R.S. (2011). Mouse models of advanced spontaneous metastasis for experimental therapeutics. Nat. Rev. Cancer 11, 135-141.

Gao, J., Aksoy, B.A., Dogrusoz, U., Dresdner, G., Gross, B., Sumer, S.O., Sun, Y., Jacobsen, A., Sinha, R., Larsson, E., et al. (2013). Integrative analysis of complex cancer genomics and clinical profiles using the cBioPortal. Sci. Signal. 6, p11.

Garneau, J.E., Dupuis, M.E., Villion, M., Romero, D.A., Barrangou, R., Boyaval, P., Fremaux, C., Horvath, P., Magadán, A.H., and Moineau, S. (2010). The CRISPR/Cas bacterial immune system cleaves bacteriophage and plasmid DNA. Nature 468, 67-71.

Garraway, L.A., and Lander, E.S. (2013). Lessons from the cancer genome. Cell 153, 17-37.

Gasiunas, G., Barrangou, R., Horvath, P., and Siksnys, V. (2012). Cas9-crRNA ribonucleoprotein complex mediates specific DNA cleavage for adaptive immunity in bacteria. Proc. Natl. Acad. Sci. USA 109, E2579-E2586.

Gilbert, L.A., Horlbeck, M.A., Adamson, B., Villalta, J.E., Chen, Y., Whitehead, E.H., Guimaraes, C., Panning, B., Ploegh, H.L., Bassik, M.C., et al. (2014). Genome-scale CRISPR-mediated control of gene repression and activation. Cell 159, 647-661.

Hanahan, D., and Weinberg, R.A. (2011). Hallmarks of cancer: the next generation. Cell 144, 646-674.

Heimann, R., and Hellman, S. (1998). Aging, progression, and phenotype in breast cancer. J. Clin. Oncol. 16, 2686-2692.

Hsu, P.D., Scott, D.A., Weinstein, J.A., Ran, F.A., Konermann, S., Agarwala, V., Li, Y., Fine, E.J., Wu, X., Shalem, O., et al. (2013). DNA targeting specificity of RNA-guided Cas9 nucleases. Nat. Biotechnol. 31, 827-832.

Huang, S., Hölzel, M., Knijnenburg, T., Schlicker, A., Roepman, P., McDermott, U., Garnett, M., Grernrum, W., Sun, C., Prahallad, A., et al. (2012). MED12 controls the response to multiple cancer drugs through regulation of TGF-β receptor signaling. Cell 151, 937–950.

Jesien-Lewandowicz, E., Jesionek-Kupnicka, D., Zawlik, I., Szybka, M., Kulczycka-Wojdala, D., Rieske, P., Sieruta, M., Jaskolski, D., Och, W., Skowronski, W., et al. (2009). High incidence of MGMT promoter methylation in primary glioblastomas without correlation with TP53 gene mutations. Cancer Genet. Cytogenet, 188, 77-82.

Jinek, M., Chylinski, K., Fonfara, I., Hauer, M., Doudna, J.A., and Charpentier, E. (2012). A programmable dual-RNA-guided DNA endonuclease in adaptive bacterial immunity. Science 337, 816-821.

Kaczmarczyk, G., Lewandowski, R., Trautsolt, W., Ziółkowski, A., and Kozielski, J. (2012). Cytological examination of pleural cavity lavage accompanied by the study of gene promoter hypermethylation of p16 and O6methylguanine-DNA-methyltransferase genes in diagnostics of non-small cell lung cancer metastatic changes into pleura. Contemp Oncol (Pozn) 16, 322-327.

Koike-Yusa, H., Li, Y., Tan, E.P., Velasco-Herrera, Mdel.C., and Yusa, K. (2014). Genome-wide recessive genetic screening in mammalian cells with a lentiviral CRISPR-guide RNA library. Nat. Biotechnol. 32, 267-273.

Konermann, S., Brigham, M.D., Trevino, A.E., Joung, J., Abudayyeh, O.O., Barcena, C., Hsu, P.D., Habib, N., Gootenberg, J.S., Nishimasu, H., et al. (2015). Genome-scale transcriptional activation by an engineered CRISPR-Cas9 complex. Nature 517, 583-588.

Korczak, B., Robson, I.B., Lamarche, C., Bernstein, A., and Kerbel, R.S. (1988). Genetic tagging of tumor cells with retrovirus vectors: clonal analysis of tumor growth and metastasis in vivo. Mol. Cell. Biol. 8, 3143-3149.

Kumar, M.S., Pester, R.E., Chen, C.Y., Lane, K., Chin, C., Lu, J., Kirsch, D.G., Golub, T.R., and Jacks, T. (2009). Dicer1 functions as a haploinsufficient tumor suppressor. Genes Dev. 23, 2700-2704.

Lawrence, M.S., Stojanov, P., Polak, P., Kryukov, G.V., Cibulskis, K., Sivachenko, A., Carter, S.L., Stewart, C., Mermel, C.H., Roberts, S.A., et al. (2013). Mutational heterogeneity in cancer and the search for new cancerassociated genes. Nature 499, 214-218.

Lohr, J.G., Adalsteinsson, V.A., Cibulskis, K., Choudhury, A.D., Rosenberg, M., Cruz-Gordillo, P., Francis, J.M., Zhang, C.Z., Shalek, A.K., Satija, R., et al. (2014). Whole-exome sequencing of circulating tumor cells provides a window into metastatic prostate cancer. Nat. Biotechnol. 32, 479-484.

Mali, P., Yang, L., Esvelt, K.M., Aach, J., Guell, M., DiCarlo, J.E., Norville, J.E., and Church, G.M. (2013). RNA-guided human genome engineering via Cas9. Science 339, 823-826.

McClatchey, A.I., Saotome, I., Mercer, K., Crowley, D., Gusella, J.F., Bronson, R.T., and Jacks, T. (1998). Mice heterozygous for a mutation at the Nf2 tumor suppressor locus develop a range of highly metastatic tumors. Genes Dev. 12, 1121-1133.

McFadden, D.G., Papagiannakopoulos, T., Taylor-Weiner, A., Stewart, C., Carter, S.L., Cibulskis, K., Bhutkar, A., McKenna, A., Dooley, A., Vernon, A., et al. (2014). Genetic and clonal dissection of murine small cell lung carcinoma progression by genome sequencing. Cell 156, 1298-1311.

Nguyen, D.X., Bos, P.D., and Massagué, J. (2009). Metastasis: from dissemination to organ-specific colonization. Nat. Rev. Cancer 9, 274-284.

Rouet, P., Smih, F., and Jasin, M. (1994). Introduction of double-strand breaks into the genome of mouse cells by expression of a rare-cutting endonuclease. Mol. Cell. Biol. 14, 8096-8106.

Sanjana, N.E., Shalem, O., and Zhang, F. (2014). Improved vectors and genome-wide libraries for CRISPR screening. Nat. Methods 11, 783-784.

Sapranauskas, R., Gasiunas, G., Fremaux, C., Barrangou, R., Horvath, P., and Siksnys, V. (2011). The Streptococcus thermophilus CRISPR/Cas system provides immunity in Escherichia coli. Nucleic Acids Res. 39, 9275-9282.

Schiano, C., Casamassimi, A., Rienzo, M., de Nigris, F., Sommese, L., and Napoli, C. (2014). Involvement of Mediator complex in malignancy. Biochim. Biophys. Acta 1845, 66-83.

Schramek, D., Sendoel, A., Segal, J.P., Beronja, S., Heller, E., Oristian, D., Reva, B., and Fuchs, E. (2014). Direct in vivo RNAi screen unveils myosin Ila as a tumor suppressor of squamous cell carcinomas. Science 343, 309-313.

Shalem, O., Sanjana, N.E., Hartenian, E., Shi, X., Scott, D.A., Mikkelsen, T.S., Heckl, D., Ebert, B.L., Root, D.E., Doench, J.G., and Zhang, F. (2014). Genome-scale CRISPR-Cas9 knockout screening in human cells. Science 343, 84-87,

Shao, D.D., Xue, W., Krall, E.B., Bhutkar, A., Piccioni, F., Wang, X., Schinzel, A.C., Sood, S., Rosenbluh, J., Kim, J.W., et al. (2014). KRAS and YAP1 converge to regulate EMT and tumor survival. Cell 158, 171-184.

Tang, J.T., Wang, J.L., Du, W., Hong, J., Zhao, S.L., Wang, Y.C., Xiong, H., Chen, H.M., and Fang, J.Y. (2011). MicroRNA 345, a methylation-sensitive microRNA is involved in cell proliferation and invasion in human colorectal cancer. Carcinogenesis 32, 1207-1215.

Tano, K., Shiota, S., Collier, J., Foote, R.S., and Mitra, S. (1990). Isolation and structural characterization of a cDNA clone encoding the human DNA repair protein for O6-alkylguanine. Proc. Natl. Acad. Sci. USA 87, 686-690.

Valastyan, S., and Weinberg, R.A. (2011). Tumor metastasis: molecular insights and evolving paradigms. Cell 147, 275-292.

Vanharanta, S., and Massagué, J. (2013). Origins of metastatic traits. Cancer Cell 24, 410-421.

Waghorne, C., Thomas, M., Lagarde, A., Kerbel, R.S., and Breitman, M.L. (1988). Genetic evidence for progressive selection and overgrowth of primary tumors by metastatic cell subpopulations. Cancer Res. 48, 6109-6114.

Wang, T., Wei, J.J., Sabatini, D.M., and Lander, E.S. (2014). Genetic screens in human cells using the CRISPR-Cas9 system. Science 343, 80-84.

Weinberg, R.A. (2007). The Biology of Cancer (Garland Science).

Yokota, J., Nishioka, M., Tani, M., and Kohno, T. (2003). Genetic alterations responsible for metastatic phenotypes of lung cancer cells. Clin. Exp. Metastasis 20, 189-193

Zender, L., Xue, W., Zuber, J., Semighini, C.P., Krasnitz, A., Ma, B., Zender, P., Kubicka, S., Luk, J.M., Schirmacher, P., et al. (2008), An oncogenomics-based in vivo RNAi screen identifies tumor suppressors in liver cancer. Cell 135,

Zhou, Y., Zhu, S., Cai, C., Yuan, P., Li, C., Huang, Y., and Wei, W. (2014). Highthroughput screening of a CRISPR/Cas9 library for functional genomics in human cells. Nature 509, 487-491.

Expert Reviews

Nano-plasmonic exosome diagnostics

Expert Rev. Mol. Diagn. 15(6), 725-733 (2015)

Hyungsoon Im¹, Huilin Shao^{1,2}, Ralph Weissleder^{1,3}, Cesar M Castro*^{1,4} and Hakho Lee*¹

¹Center for Systems Biology, Massachusetts General Hospital, Harvard Medical School, Boston, MA 02114. USA ²Institute of Molecular and Cell Biology, Agency for Science, Technology and Research, Singapore 138673, Singapore ³Department of Systems Biology, Harvard Medical School, Boston, MA 02114, USA ⁴Massachusetts General Hospital Cancer Center, Harvard Medical School, Boston, MA 02114, USA *Authors for correspondence: Tel.: +1 617 726 8226 cmcastro@mgh.harvard.edu

hlee@mgh.harvard.edu

Exosomes have emerged as a promising biomarker. These vesicles abound in biofluids and harbor molecular constituents from their parent cells, thereby offering a minimally-invasive avenue for molecular analyses. Despite such clinical potential, routine exosomal analysis, particularly the protein assay, remains challenging, due to requirements for large sample volumes and extensive processing. We have been developing miniaturized systems to facilitate clinical exosome studies. These systems can be categorized into two components: microfluidics for sample preparation and analytical tools for protein analyses. In this report, we review a new assay platform, nano-plasmonic exosome, in which sensing is based on surface plasmon resonance to achieve label-free exosome detection. Looking forward, we also discuss some potential challenges and improvements in exosome studies.

Keywords: cancer • exosome • extracellular vesicles • molecular diagnosis • surface plasmon resonance

The growing emphasis on targeted and personalized therapy concomitantly increases the need to analyze and monitor key cancer proteins and pathway activation [1–3]. Although tissue biopsies remain the gold standard, their invasiveness and limited sampling often present practical challenges with patient management [4].

Exosomes have emerged as a new class of cancer biomarker for clinical diagnostics [5,6]. Exosomes are membrane-bound phospholipid vesicles (50-200 nm in diameter) that are actively secreted by cancer cells (Figure 1). These vesicles carry cellular constituents of their originating cells, including transmembrane and intracellular proteins [7], mRNA [8], DNA [9], miRNA [10], lipids and metabolites and can serve as cellular surrogates [11]. Combined with their large abundance and ubiquitous presence in bodily fluids (e.g., blood, ascites, urine) [5,12,13], exosomes offer significant advantages for cancer monitoring [14-16]. Namely, an exosomal assay can be robust and minimally invasive for repeated tests. As most tumor cells shed exosomes, the assay can also report relatively unbiased readouts of the whole tumor burden, less affected by the scarcity of the samples (e.g., circulating tumor cells to circulating DNAs) or intra-tumoral heterogeneity (e.g., fine-needle aspiration) [17]. Furthermore, the amount and molecular profile of cancer exosomes have been shown to correlate with tumor burden as well as treatment efficacy [17,18]. A number of recent

review articles have highlighted exosomes' role in diagnostics, cell-to-cell interactions and therapeutic opportunities [5,6,19-23]. Despite such clinical potential, routine exosome analysis is still a challenging task. Conventional methods (e.g., Western blotting, ELISA) require large sample volumes (>500 µl per biomarker) and extensive processing (e.g., 3 h with ultracentrifugation) [6,24]. Such assays become impractical when multiple markers need to be profiled or the sample volume is inherently limited (e.g., cerebrospinal fluid)

Various exosome detection platforms have been introduced to overcome these challenges (Figure 2 & Table 1) [17,18,25-30]. Integration with microfluidics allows for exosome analyses in small volumes; adoption into novel sensing methods (e.g., surface plasmon resonance, magnetic resonance) generated exosomal assays with shorter assay time, higher sensitivity and higher throughput. Commercialized nucleic acid sensing technologies (e.g., RainDrop) have been adapted for a variety of exosomal RNA components with high sensitivity. With their high sensitivity and throughput, these new technologies have shown great promise for both exosomal RNA and protein detection over conventional analytical methods.

We have been advancing miniaturized systems to facilitate exosome studies (FIGURE 3). These systems are comprised of two components: microfluidics to facilitate sample preparation and

informahealthcare.com 10.1586/14737159.2015.1041378 © 2015 Informa UK Ltd ISSN 1473-7159 **725**

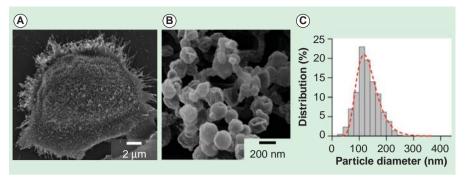


Figure 1. Exosomes shed from ovarian cancer cell. (A) Electron microscopy image of a primary human ovarian cancer cell (CaOV3) confirms the avid release of membrane vesicles by the cell. **(B)** High magnification image shows that the vesicles on the cell surface assumed typical saucer-shaped characteristics of exosomes. **(C)** The size distribution of the exosomes, as characterized by the nanoparticle tracking analysis, ranges from 20 to 250 nm.

Reproduced with permission from [18] © Nature Publishing Group (2014).

analytical tools for protein analyses. The microfluidic devices are designed to collect intact exosomes directly from biological samples, replacing ultracentrifugation or proprietary precipitation methods. The first developed device used a detachable membrane filter (1 µm pore) to sizeselectively enrich exosomes from large sample volumes [31]; the next developed system was based on acoustic actuation, which enabled controllable size-cutoff and continuous, inflow filtration [32]. For protein analyses, we initially adopted the µNMR technology to magnetically profile exosomal proteins [17]. In μNMR, target proteins were labeled with magnetic nanoparticles, and changes in transverse relaxation of the samples were measured. The signal

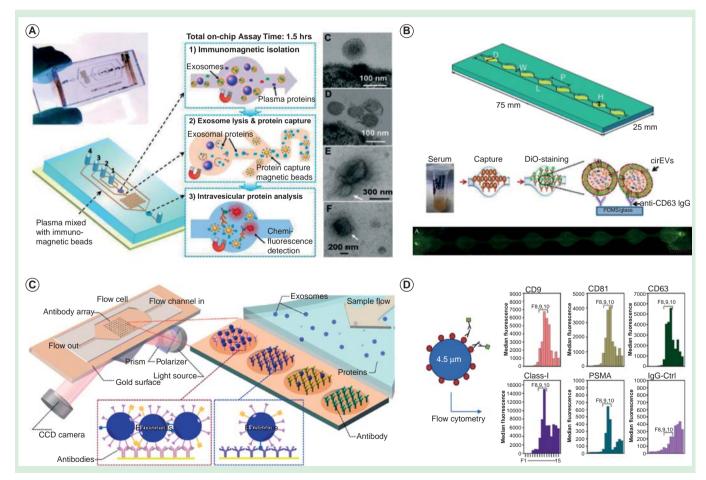


Figure 2. New exosome sensing platforms. (A) An integrated microfluidic chip for exosome isolation, chemical lysis and exosomal protein analysis. Reproduced with permission from [26] published by The Royal Society of Chemistry. **(B)** A microfluidic device (ExoChip) for on-chip exosome capture and analysis. Reproduced from [27] with permission of The Royal Society of Chemistry. **(C)** A surface plasmon resonance imaging (SPRi) system for label-free exosome detection. Reprinted with permission from [29] © American Chemical Society (2014). **(D)** Aptamer-based platform (SOMAscanTM) for proteomic analysis of cancer exosomes. Reproduced with permission from [28].

726Expert Rev. Mol. Diagn. 15(6), (2015)

Table 1. Comparison of exosomal sensing platforms.					
Method	Sensing principle	Target	Sensitivity	Throughput	Ref.
nPLEX	SPR	Protein	~10 ³ exosomes	High (>100 arrays)	[18]
μ NMR	Magnetic resonance	Protein	~10 ⁴ exosomes	Low (single channel)	[17]
ExoChip	Fluorescence	CD63+/Rab5 + EVs	0.5 pM	Low (three channels)	[27]
SOMAscan	Fluorescence	Protein	100 fM	Very high (1129)	[28]
Microfluidic chip	Fluorescence	Protein	0.3 pg/ml	Low (single channel)	[26]
SPRi	SPR	Protein	5×10^7 exosomes/cm ²		[29]
BEAMing & digital PCR	Fluorescence	RNA	0.01% (mutant detection)	High	[25]
miRNA microarray/NanoString	Fluorescence	miRNA		Very high (>1000)	[30]
nPLEX: Nano-plasmonic exosome; SPR: Surface plasmon resonance.					

detection is robust against biological background, and the assay was demonstrated to benefit from such a well-established platform [33–36]. The μNMR assay, however, was difficult to scale up for high-throughput detection. The task requires a large NMR-grade magnet to accommodate multiple NMR probes, and also entails labeling with magnetic nanoparticles. Recently, we developed a new assay system, termed nano-plasmonic exosome (nPLEX) [18] that could overcome these challenges. The nPLEX sensing is based on surface plasmon resonance (SPR) through periodic nanohole arrays, wherein target-specific exosome binding on the array causes significant SPR signal changes. The system is scalable with a large number of sensing units (>100) integrated into a single chip, and the assay is label-free (i.e., no need for secondary labeling with nanoparticles) [37,38].

This special report will review this nascent nPLEX technology, assessing its sensor design, assay protocols, and clinical applications. We will specifically focus on nPLEX's capacity for fast, high-throughput exosome analyses and also discuss directions to further improvements.

nPLEX Technology Sensing principle

The nPLEX system comprises of periodic nanohole arrays made in an opaque gold (Au) film (Figure 4A). Light illumination to the nanohole arrays can excite strong electromagnetic fields, called surface plasmons on the surface (Figure 4B), which lead to SP-mediated extraordinary optical transmission [39,40]. The transmission spectral peak positions are highly sensitive to the refractive index on the nanohole surface, and exosome binding to the nanohole surface (via affinity ligands) would red-shift the optical transmission peaks (Figure 4C). The amount of spectral shift correlates with the molecular mass density [41], which enables quantification of captured exosomes on the sensing surface. Because exosome binding itself induces a spectral shift, the nPLEX can detect exosomes in a label-free manner.

The nanohole-based plasmonic detection has unique advantages over conventional SPR systems (e.g., Kretschmann configuration [42]). First, a simple, collinear optical setup can be used for signal measurements [38,43], and the system can be readily

miniaturized [18,44]. Second, the system is scalable for high-throughput detection. The minimal array size for the extraordinary optical transmission could be as small as 5-by-5 periodic nanoholes (foot print < $10~\mu m^2$) [45], which allows for the integration of high density arrays (> 10^6 detection sites per cm²) [46–48]. Such high density is difficult to achieve with the Kretschmann configuration. The large tilt angle of incidence

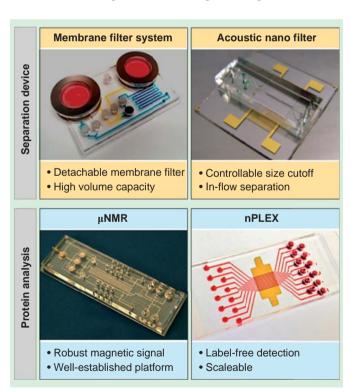


Figure 3. Miniaturized devices developed for exosome separation (top) and its protein profiling (bottom).

Images are adapted with permission from [17,18] © Nature Publishing Group (2014).

Adapted with permission from [31] © American Chemical Society

Adapted with permission from [32] © American Chemical Society (2015).

informahealthcare.com 727

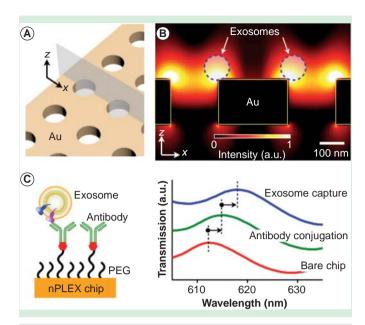


Figure 4. Nano-plasmonic exosome sensing principle. (A) A sensing site comprises a periodic nanohole array patterned in a gold film. (B) Finite-difference time-domain simulation shows the enhanced electromagnetic fields tightly confined near a periodic nanohole surface. The field distribution overlaps with the size of exosomes captured onto the sensing surface. (C) Antibodies were immobilized on the nPLEX chip, and exosomes were captured based on their expression of extravesicular markers (left). Antibody conjugation and exosome binding were monitored by measuring spectral shifts via the nPLEX sensor (right). a.u.: Arbitrary unit; nPLEX: Nano-plasmonic exosome. Reproduced with permission from [18] © Nature Publishing Group (2014).

could lead to optical aberration when a numerical aperture is used to increase spatial resolution or defocusing when imaging arrays in a large area.

System design

The geometry of the nanoholes was optimized through three-dimensional simulation to match the sensing range with the mean diameter of exosomes (~100 nm; Figure 5A). The nPLEX signal was measured by monitoring the transmission spectrum via a spectrometer setup. In this mode, individual arrays are sequentially scanned, and a spectral shift of resonance peak from exosome binding is detected. Although the spectrum-based measurements provide comprehensive information of the nanohole's optical characteristics, it could be time-consuming with large sensing arrays. For faster readout, we alternatively measured changes in transmission intensity at an excitation wavelength (Figure 5B). This intensity-based method could monitor multiple sensing arrays simultaneously, enabling high-throughput parallel measurements.

FIGURE 6A shows the first nPLEX prototype. The structure was patterned in a 200 nm-thick Au film on a glass substrate. We laid out a 12 × 3 array of sensing units with multichannel microfluidics placed on top (FIGURE 6B). Each channel spanned over three sensing units for triplicate measurements. The sample volume per channel was ~1 µl. For parallel measurements of nPLEX arrays, an intensity-based detection system integrated with miniaturized optics consisting of a laser diode and an image sensor was also developed (FIGURE 6C). This system can simultaneously monitor changes in the transmitted light intensities of 36 arrays for high-throughput parallel measurements.

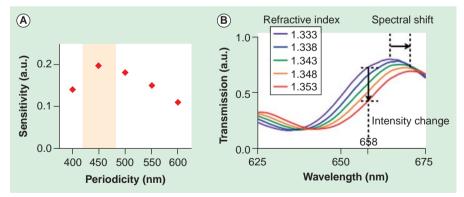


Figure 5. Device design optimization. (A) The sensitivity of the nPLEX sensor was defined as $\Delta\lambda/w$, where $\Delta\lambda$ and w are the shift and the width of SPR spectrum, respectively. The nanohole array with 450-nm hole-pitch showed the highest sensitivity for the detection of 100 nm exosomes. **(B)** Increase in the refractive index on the nPLEX surface induces a spectral shift $(\Delta\lambda)$ of resonance peak to a longer wavelength. The increase of refractive index also causes intensity changes (Δp) at a given wavelength (e.g., at 658 nm). Therefore, exosome binding can be detected by either tracking $\Delta\lambda$ by spectrometry or Δp by imaging.

a.u.: Arbitrary unit; nPLEX: Nano-plasmonic exosome.

Reproduced with permission from [18] © Nature Publishing Group (2014).

Analytical nPLEX assay for molecular profiling

To impart molecular specificity, the nanohole surface was coated with different antibodies in each channel. Following antibody conjugation, exosomes were introduced and spectral shifts were measured before and after exosome binding. An IgG control channel was incorporated to measure the contribution from nonspecific binding and its signal was subtracted from each target channel.

To determine the detection sensitivity, we functionalized the sensor surface with antibodies against CD63, a type III lysosomal membrane protein enriched in exosomes. Alternatively, other exosomespecific lysosomal membrane proteins (e.g., CD9, CD81) were also used [49]. Samples were prepared from CaOV3 (human ovarian carcinoma) cell lines, and their initial exosome concentrations were estimated by nanoparticle-tracking

analysis. A pair of nPLEX sensors, functionalized with CD63 and control IgG antibodies, respectively, were used to measure the relative spectral ($\Delta\lambda^{\text{CD63}}$) or intensity (Δp^{CD63}) changes against known exosome counts. The titration experiments established the limit of detection of ~ 3000 exosomes (670 aM) with the label-free nPLEX assay (FIGURE 7A). The observed sensitivity based on the limit of detection was 10^4 - and 10^2 -fold higher than Western blotting and chemiluminescence ELISA, respectively.

To quantitatively detect exosome proteins, we functionalized the nPLEX sensors with antibodies against target markers and measured associated signals $(\Delta \lambda^{\text{target}})$ or Δp^{target} from exosome capture. Next, we defined the expression level (ξ^{target}) of the target marker by scaling the marker-associated changes to those of CD63 (i.e., $\xi^{\text{target}} = \Delta \lambda^{\text{target}}/\Delta \lambda^{\text{CD63}} \approx \Delta p^{\text{target}}/\Delta p^{\text{CD63}}$). Such normalization accounted for differences in exo-

some counts among samples and thereby reported the average expression level of a target marker per exosome [17,18]. This method was applied to profile exosomes from different cell lines (CaOV3, OV90) for various extravesicular markers (FIGURE 7B). Expression levels were well-matched ($R^2 > 98\%$) between nPLEX and ELISA, verifying the accuracy of the developed nPLEX assay. In addition, the nPLEX assay could be adapted for downstream genetic analyses by releasing

captured exosomes from the device using surface regeneration protocols [17,18].

Clinical potential of exosomes

We first explored the correlation between exosomes and their parental cells. Multiplexed *in vitro* nPLEX screening showed good agreement of protein expression between exosomes and their parental cells across different ovarian cancer cell lines (FIGURE 8A). Such close matching of molecular profiles between exosome and cells was previously identified in glioblastoma multiforme cell lines using μNMR [17]. In addition, our nPLEX screening showed that EpCAM and CD24 were highly expressed in tested ovarian cancer cell lines.

Based on these results, the nPLEX system was applied to detect ovarian cancer exosomes in patient-derived ascites (Figure 8B). Thirty ascites samples were obtained: 20 patients were diagnosed with Stage 3 (n=10) and 4 (n=10) ovarian

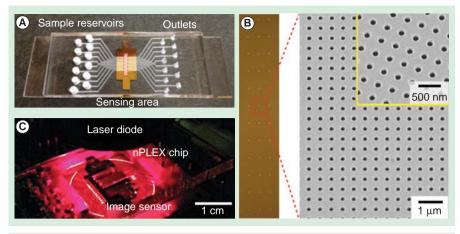


Figure 6. First nano-plasmonic exosome. prototype. (A) A photograph of the nanohole device integrated with microfluidics. A 12-channel fluidic cell was placed on top of a glass slide containing nanohole arrays. **(B)** A total of 36 measurement sites were arranged into a 12×3 array. Each measurement site had periodic nanoholes (right). The structure was patterned in a gold film (200 nm thick) deposited on a glass substrate. **(C)** A photograph of the miniaturized nPLEX imaging system. The nPLEX chip was located directly on an image sensor, which measured transmitted light intensities of the 36 sites simultaneously.

nPLEX: Nano-plasmonic exosome.

Reproduced with permission from [18] © Nature Publishing Group (2014).

cancer and 10 control ascites patients were diagnosed with liver cirrhosis [18]. The study demonstrated that unprocessed ascites contained large quantities (>10⁹ per ml) of exosomes; nPLEX was sensitive enough to detect exosomes directly isolated from ascites by simple syringe membrane filtration; and the levels of EpCAM and CD24 per exosome were significantly higher in ovarian cancer patient samples than in control groups. For 30 samples tested, the detection accuracy was 97% using

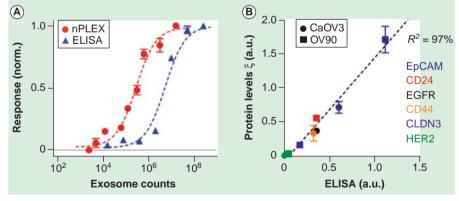


Figure 7. Exosome quantification and protein profiling with nano-plasmonic exosome. (A) Exosomes isolated from human ovarian cancer cell line were introduced onto a nPLEX sensor functionalized with CD63 antibody for exosomal capture. The nPLEX platform showed considerably higher sensitivity than ELISA. (B) Comparison between nPLEX and ELISA measurements. Exosomes isolated from human ovarian cancer cell lines were used. The expression level (ξ) was determined by normalizing the marker signal with that of CD63, which accounted for variation in exosomal counts across samples. All measurements were in triplicate and the data is displayed as mean \pm s.d. nPLEX: Nano-plasmonic exosome.

Reproduced with permission from [18] © Nature Publishing Group (2014).

informahealthcare.com 729

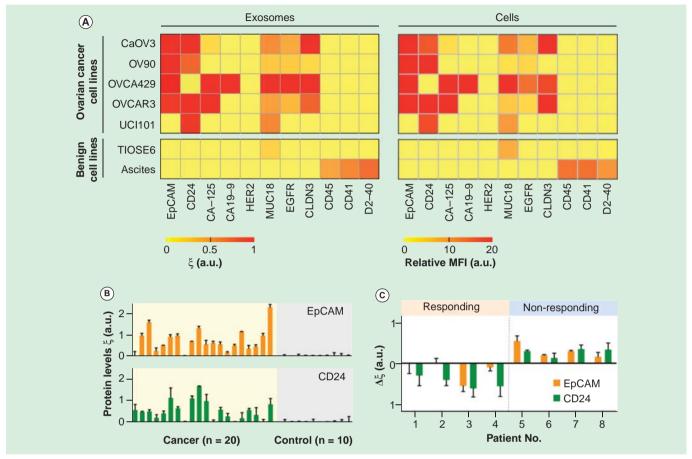


Figure 8. Molecular profiling of ovarian cancer exosomes. (A) *In-vitro* study. Ovarian cancer associated markers (EpCAM, CD24, CA-125, CA19-9, HER2, MUC18, EGFR, Claudin3), immune host cell markers (CD41, CD45) and a mesothelial marker (D2-40) were profiled on both parental ovarian cells (right, using flow cytometry) and their derived exosomes (left, using nPLEX sensor). Exosomal protein profiles showed an excellent match with those of originating cells. A two-marker combination comprising EpCAM and CD24 could effectively distinguish cancer exosomes from benign exosomes. (B) Ascites exosomes from ovarian cancer and non-cancer patients were evaluated by the nPLEX sensor. Cancer exosomes were captured on EpCAM and CD24-specific sensor sites, and the exosomal expression levels of these markers were measured. Ovarian cancer patients (n = 20) were associated with elevated EpCAM and CD24 expression, while non-cancer patients (n = 10) showed negligible signals. (C) Longitudinal nPLEX assays. Ascites samples were collected sequentially from ovarian cancer patients undergoing chemotherapy (n = 8). Measuring temporal changes in exosomal expressions of EpCAM and CD24 could distinguish treatment response.

MFI: Mean fluorescence intensity; nPLEX: Nano-plasmonic exosome.

Reproduced with permission from [18] © Nature Publishing Group (2014).

EpCAM and CD24 as diagnostic markers. The nPLEX screening was further used to evaluate the prognostic values of exosomes for treatment monitoring (Figure 8C). For ovarian cancer patients (n = 8) undergoing standard chemotherapy, the study demonstrated that the levels of exosomal EpCAM, CD24 or both decreased among responding patients, whereas levels of these markers increased in non-responding patients.

Expert commentary

Exosomes present new opportunities for cancer diagnoses and treatment monitoring. These vesicles abound in biological fluids and carry cell-specific cargos (lipids, proteins and genetic materials), which can be harnessed as a minimally invasive means to probe the molecular status of tumors. Significant technical developments are underway to channel exosome

analysis into clinical settings: fluidic-based tools have been devised to facilitate sample preparation, and analytical platforms have been adapted to detect exosomes in clinical samples. Such efforts have started to unveiling tumor-associated exosomal fingerprints, particularly in RNA profiles (both coding and noncoding).

Exosomal protein analysis, on the other hand, still remains challenging. With the lack of universal amplification strategy (e.g., PCR), protein analysis generally requires large quantities of exosomes and often involves extensive sample processing. The nPLEX technology was developed to address these issues. The nPLEX's high sensitivity allows for quantitative measurements on small sample amounts; the detection is label-free to minimize assay time and potential sample loss/degradation; and the system is scalable to a large array for high-throughput assays.

Extended insight into exosomal proteins could help capture dynamic snapshots of tumors, which are hard to detect with genetic assays. Aberrant changes in cancer cells, in response to microenvironmental stress, are reflected in protein levels and its post-translational modification, which have significant effects on disease progression and therapeutic response. As such, the improved exosomal proteomic analyses, proffered by nPLEX, could pave the way for the potential use of exosomes as companion diagnostics and pharmacodynamic readouts.

We identify two immediate directions to further improve the nPLEX technology. First, the assay format needs to be developed to measure both extra- and intravesicular proteins. The initial nPLEX studies were limited to detecting transmembrane or lipid-bound proteins, since the assay was based on capturing whole exosomes on the device surface. Devising a new assay for intravesicular proteins is critical to probe the activation status of proteins as well as to measure cytosolic protein targets. Second, the clinical utility of nPLEX requires further validation under the auspices of larger clinical trials. The large datasets thus generated would aid in identifying key exosomal finger-prints for cancer. These efforts would establish nPLEX as a transformative platform facilitating cancer research and clinical practice.

Five-year view

The trajectories undertaken by the exosome field's development of first-generation analytical tools parallel those of the more mature circulating tumor cell research. Exosomes are abundant and stable in circulation. These advantages impart significant practical value on exosomes as noninvasive and unbiased surrogates for tissue-based biomarkers. As seen in cellular analyses, we envision that more advanced technologies for exosome

enrichment and detection will be developed to ultimately enable high-throughput profiling of single exosomes. This will potentially lead to the identification of exosome subpopulations, highly specific to cancer, which could be prospectively explored in cancer clinical trials. Additional investigations will focus on whether testing of cancer exosomes could generate pharmacodynamic readouts. Coupled with the ready access of liquid biopsies, earlier 'go-no go' decisions could inform drug development. Improved understanding of the mechanisms driving exosomal signaling will accelerate the efforts to exploit exosomal targeting to deliver therapeutic payloads. This transition to theranostics could be a key step for the exosome field and usher in further attention from pharmaceutical stakeholders, among others. Such diverse opportunities create an exciting venue for exosome research - we anticipate an expanding pipeline of committed and accomplished junior and seasoned investigators across disciplines, along with increased funding opportunities for the next 5 years and beyond.

Acknowledgement

The authors thank XO Breakefield (Massachusetts General Hospital, Boston, MA, USA) for help with discussion.

Financial & competing interests disclosure

This work was supported in part by NIH grants R01 HL113156 to H Lee; NIH grants P01 CA069246, U54 CA151884 and T32-CA79443 to R.Weissleder; and DoD OCRP Award W81XWH-14-1-0279 to H Lee. H Shao acknowledges financial support from the B.S.-Ph.D. National Science Scholarship awarded by the Agency for Science, Technology and Research, Singapore. The authors have no other relevant affiliations or financial involvement with any organization or entity with a financial interest in or financial conflict with the subject matter or materials discussed in the manuscript apart from those disclosed.

Key issues

- Exosomes are membrane-bound vesicles that contain molecular constituents of their cell of origin, including proteins, nucleic acids, lipids and metabolites.
- Exosomes can serve as a minimally invasive biomarker for cancer diagnosis and treatment monitoring.
- Miniatured devices are being developed to expedite exosome isolation and its downstream analyses. These devices could shorten the hands-on assay time and minimize required samples volumes.
- The surface plasmon resonance -based nano-plasmonic exosome (nPLEX) technology enables rapid, sensitive, label-free profiling of exosomal proteins.
- The nPLEX assay is quantitative, reporting the average expression level of target protein markers per exosomes.
- The detection platform is scalable for high-throughput, automated detection.
- By changing the affinity ligands, the nPLEX platform could be used to detect exosomes from virtually any cell type, and hence could serve as a universal platform for exosome analyses.
- Intra-exosomal biology remains an area of active interest given its potential to generate novel pharmacodynamic readouts or therapeutic approaches.

informahealthcare.com 731

References

Papers of special note have been highlighted as:
• of interest

- of considerable interest
- Bidard FC, Weigelt B, Reis-Filho JS. Going with the flow: from circulating tumor cells to DNA. Sci Transl Med 2013;5:207ps14
- Pantel K, Alix-Panabieres C. Real-time liquid biopsy in cancer patients: fact or fiction? Cancer Res 2013;73:6384-8
- Basik M, Aguilar-Mahecha A, Rousseau C, et al. Biopsies: next-generation biospecimens for tailoring therapy. Nat Rev Clin Oncol 2013;10:437-50
- Gerlinger M, Rowan AJ, Horswell S, et al. Intratumor heterogeneity and branched evolution revealed by multiregion sequencing. N Engl J Med 2012;366: 883-92
- Thery C, Ostrowski M, Segura E. Membrane vesicles as conveyors of immune responses. Nat Rev Immunol 2009;9:581-93
- Simpson RJ, Lim JW, Moritz RL, Mathivanan S. Exosomes: proteomic insights and diagnostic potential. Expert Rev Proteomics 2009;6:267-83
- Graner MW, Alzate O, Dechkovskaia AM, et al. Proteomic and immunologic analyses of brain tumor exosomes. FASEB J 2009;23:1541-57
- Skog J, Wurdinger T, van Rijn S, et al. Glioblastoma microvesicles transport RNA and proteins that promote tumour growth and provide diagnostic biomarkers. Nat Cell Biol 2008;10:1470-6
- First paper reporting the role of microvesicles in tumor growth and the potential use as diagnostic biomarkers for glioblastoma.
- Balaj L, Lessard R, Dai L, et al. Tumour microvesicles contain retrotransposon elements and amplified oncogene sequences. Nat Commun 2011;2:180
- Valadi H, Ekström K, Bossios A, et al. Exosome-mediated transfer of mRNAs and microRNAs is a novel mechanism of genetic exchange between cells. Nat Cell Biol 2007;9:654-9
- Kalra H, Simpson RJ, Ji H, et al. Vesiclepedia: a compendium for extracellular vesicles with continuous community annotation. PLoS Biol 2012;10:e1001450
- Raimondo F, Morosi L, Chinello C, et al. Advances in membranous vesicle and exosome proteomics improving biological understanding and biomarker discovery. Proteomics 2011;11:709-20

- Thery C, Zitvogel L, Amigorena S. Exosomes: composition, biogenesis and function. Nat Rev Immunol 2002;2:569-79
- Andre F, Schartz NEC, Movassagh M, et al. Malignant effusions and immunogenic tumour-derived exosomes. Lancet 2002;360: 295-305
- Peinado H, Alečković M, Lavotshkin S, et al. Melanoma exosomes educate bone marrow progenitor cells toward a pro-metastatic phenotype through MET. Nat Med 2012;18:883-91
- Grange C, Tapparo M, Collino F, et al. Microvesicles released from human renal cancer stem cells stimulate angiogenesis and formation of lung premetastatic niche. Cancer Res 2011;71:5346-56
- Shao H, Chung J, Balaj L, et al. Protein typing of circulating microvesicles allows real-time monitoring of glioblastoma therapy. Nat Med 2012;18:1835-40
- Original paper reporting exosome detection in glioblastoma multiforme patients using a miniaturized NMR system.
- Im H, Shao H, Park YI, et al. Label-free detection and molecular profiling of exosomes with a nano-plasmonic sensor. Nat Biotechnol 2014;32:490-5
- Original paper reporting the nPLEX technology; SPR systems were optimized for the exosome analysis.
- Colombo M, Raposo G, Thery C. Biogenesis, secretion, and intercellular interactions of exosomes and other extracellular vesicles. Annu Rev Cell Dev Biol 2014;30:255-89
- Kooijmans SA, Vader P, van Dommelen SM, et al. Exosome mimetics: a novel class of drug delivery systems. Int J Nanomedicine 2012;7: 1525-41
- Kourembanas S. Exosomes: vehicles of intercellular signaling, biomarkers, and vectors of cell therapy. Annu Rev Physiol 2015;77:13-27
- Thery C. Exosomes: secreted vesicles and intercellular communications. F1000 Biol Rep 2011;3:15
- Vlassov AV, Magdaleno S, Setterquist R, Conrad R. Exosomes: current knowledge of their composition, biological functions, and diagnostic and therapeutic potentials. Biochim Biophys Acta 2012;1820:940-8
- Taylor DD, Zacharias W, Gercel-Taylor C. Exosome isolation for proteomic analyses and RNA profiling. Methods Mol Biol 2011;728:235-46

- Chen WW, Balaj L, Liau LM, et al. BEAMing and Droplet Digital PCR Analysis of Mutant IDH1 mRNA in Glioma Patient Serum and Cerebrospinal Fluid Extracellular Vesicles. Mol Ther-Nucl Acids 2013:2
- He M, Crow J, Roth M, et al. Integrated immunoisolation and protein analysis of circulating exosomes using microfluidic technology. Lab Chip 2014;14:3773-80
- Kanwar SS, Dunlay CJ, Simeone DM, Nagrath S. Microfluidic device (ExoChip) for on-chip isolation, quantification and characterization of circulating exosomes. Lab Chip 2014;14:1891-900
- Webber J, Stone TC, Katilius E, et al. Proteomics analysis of cancer exosomes using a novel modified aptamer-based array (SOMAscanTM) Platform. Mol Cell Proteomics 2014;13:1050-64
- Zhu L, Wang K, Cui J, et al. Label-free quantitative detection of tumor-derived exosomes through surface plasmon resonance imaging. Anal Chem 2014;86: 8857-64
- Donker RB, Mouillet JF, Chu T, et al. The expression profile of C19MC microRNAs in primary human trophoblast cells and exosomes. Mol Hum Reprod 2012;18: 417-24
- Rho J, Chung J, Im H, et al. Magnetic Nanosensor for Detection and Profiling of Erythrocyte-Derived Microvesicles. ACS Nano 2013;7:11227-33
- Original paper describing a membrane-based microfluidic devices for vesicle isolation.
- Lee K, Shao H, Weissleder R, Lee H. Acoustic purification of extracellular microvesicles. ACS Nano 2015;9:2321-7
- Original paper reporting the acoustic-wave microfluidic system that performs in-flow separation of microvesicles.
- Lee H, Sun E, Ham D, Weissleder R. Chip-NMR biosensor for detection and molecular analysis of cells. Nat Med 2008;14:869-74
- •• First demonstration of miniaturized NMR system for molecular analysis.
- Haun JB, Castro CM, Wang R, et al. Micro-NMR for rapid molecular analysis of human tumor samples. Sci Transl Med 2011;3:71ra16
- Lee H, Yoon TJ, Figueiredo JL, et al. Rapid detection and profiling of cancer cells in fine-needle aspirates. Proc Natl Acad Sci USA 2009;106:12459-64

732 Expert Rev. Mol. Diagn. 15(6), (2015)

- Issadore D, Min C, Liong M, et al. Miniature magnetic resonance system for point-of-care diagnostics. Lab Chip 2011;11:2282-7
- Im H, Wittenberg NJ, Lesuffleur A, et al. Membrane protein biosensing with plasmonic nanopore arrays and pore-spanning lipid membranes. Chem Sci 2010;1:688-96
- Brolo AG. Plasmonics for future biosensors.
 Nat Photonics 2012;6:709-13
- Ebbesen TW, Lezec HJ, Ghaemi HF, et al. Extraordinary optical transmission through sub-wavelength hole arrays. Nature 1998;391:667-9
- Dahlin AB. Sensing applications based on plasmonic nanopores: The hole story.
 Analyst. 2015. [Epub ahead of print]
- A recent review paper discussing the development of nanopore-based plasmonic nanosensors and their applications.
- 41. Jung LS, Campbell CT, Chinowsky TM, et al. Quantitative interpretation of the

- response of surface plasmon resonance sensors to adsorbed films. Langmuir 1998;14:5636-48
- 42. Homola J. Present and future of surface plasmon resonance biosensors. Anal Bioanal Chem 2003;377:528-39
- Im H, Sutherland JN, Maynard JA, Oh SH. Nanohole-based surface plasmon resonance instruments with improved spectral resolution quantify a broad range of antibody-ligand binding kinetics. Anal Chem 2012;84:1941-7
- Cetin AE, Coskun AF, Galarreta BC, et al. Handheld high-throughput plasmonic biosensor using computational on-chip imaging. Light-Sci Appl 2014;3:e122
- Przybilla F, Degiron A, Genet C, et al. Efficiency and finite size effects in enhanced transmission through subwavelength apertures. Opt Express 2008;16:9571-9
- Im H, Lesuffleur A, Lindquist NC, Oh SH. Plasmonic nanoholes in a multichannel microarray format for parallel kinetic assays

- and differential sensing. Anal Chem 2009:81:2854-9
- Lindquist NC, Lesuffleur A, Im H, Oh SH. Sub-micron resolution surface plasmon resonance imaging enabled by nanohole arrays with surrounding Bragg mirrors for enhanced sensitivity and isolation. Lab Chip 2009;9:382-7
- Escobedo C, Chou YW, Rahman M, et al. Quantification of ovarian cancer markers with integrated microfluidic concentration gradient and imaging nanohole surface plasmon resonance. Analyst 2013;138: 1450-8
- Lotvall J, Hill AF, Hochberg F, et al. Minimal experimental requirements for definition of extracellular vesicles and their functions: a position statement from the International Society for Extracellular Vesicles. J Extracell Vesicles 2014;3:26913
- A recent report describing molecular characteristics of extracellular vesicles.

informahealthcare.com 733



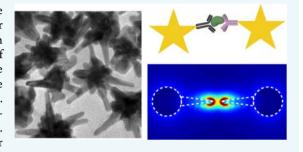
Nanostar Clustering Improves the Sensitivity of Plasmonic Assays

Yong Il Park, † Hyungsoon Im, † Ralph Weissleder, **,†,‡ and Hakho Lee*,†

[†]Center for Systems Biology, Massachusetts General Hospital, Harvard Medical School, Boston, Massachusetts 02114, United States [‡]Department of Systems Biology, Harvard Medical School, Boston, Massachusetts 02115, United States

Supporting Information

ABSTRACT: Star-shaped Au nanoparticles (Au nanostars, AuNS) have been developed to improve the plasmonic sensitivity, but their application has largely been limited to single-particle probes. We herein describe a AuNS clustering assay based on nanoscale self-assembly of multiple AuNS and which further increases detection sensitivity. We show that each cluster contains multiple nanogaps to concentrate electric fields, thereby amplifying the signal via plasmon coupling. Numerical simulation indicated that AuNS clusters assume up to 460fold higher field density than Au nanosphere clusters of similar mass. The results were validated in model assays of protein biomarker detection. The AuNS clustering assay showed higher sensitivity than Au



nanosphere. Minimizing the size of affinity ligand was found important to tightly confine electric fields and improve the sensitivity. The resulting assay is simple and fast and can be readily applied to point-of-care molecular detection schemes.

ocalized surface plasmon resonance (LSPR) is a promising biosensing strategy for molecular detection. 1-4 Based on surface plasmons that are tightly confined on metallic nanoparticles, LSPR is highly sensitive to changes in dielectric environment surrounding the particles. This unique property has been exploited to detect molecular targets upon their binding to a nanoparticle surface.⁵⁻⁸

The most widely used LSPR materials are noble metal (Ag, Au) nanospheres; their synthetic methods are well established, and these particles show plasmon resonance in visible wavelengths. Recently, star-shaped nanoparticles (nanostars) have been explored as an alternative substate to improve the LSPR sensitivity. Nanostars have multiple branches with sharp tips that generate more localized electromagnetic fields than do spherical nanoparticles and thereby produce larger spectral changes upon molecular binding. Indeed, Au nanostars have shown >5-fold higher sensitivity than Au nanospheres in LSPR sensing. Most previous studies, however, used nanostars as single-particle LSPR probes. 10,13 Namely, the analytical signal was generated when individual nanostars were labeled with target molecules. We hypothesized that the plasmonic signal could be further amplified by inducing the formation of nanostar clusters. This configuration would create multiple nanogaps between nanostars, where electric fields are concentrated and plasmons are coupled.

We herein report on the development and the optimization of such a clustering assay. Using Au nanostars (AuNS) as a substrate, we designed an assay wherein target molecules assemble AuNS into nanoscale-clusters with nanogap junctions. Small AuNS (70 nm in size) with a thiolated ligand were found optimal for sensitive and stable plasmonic sensing. Numerical simulation (finite-difference time-domain/FDTD) showed that a cluster of AuNS can concentrate up to 460-fold higher energy

density than an Au nanosphere cluster. We then experimentally verified the results using different molecular interactions (i.e., biotin-avidin and antigen-antibody). The AuNS clustering assay produced much larger spectral shifts than AuNS-ligand alone. Notably, the signal improvement inversely depended on the interparticle distance, which highlighted the importance of minimizing the size of the capturing ligand. The developed assay benefits from fast binding kinetics (<30 min) and a simple signal readout (colorimetry) and could be a potential tool for point-of-care molecular detection.

To synthesize AuNS, we adopted a seed-mediated growth method (see Experimental Procedures in the Supporting Information). Spherical Au nanoparticles (AuNP) with a mean diameter of 13 nm were prepared as a seed (Figure 1a, left) and dispersed in an Au precursor (HAuCl₄) solution. Starshaped Au nanoparticles with multiple branches were formed when ascorbic acid and silver nitrate were injected into the seed solution (Figure 1a, right). The reaction was rapid (<1 min for completion) and produced AuNS with size variations of <30% (Figure S1). We further controlled the overall size of AuNS by changing the molar concentration ratio between Au3+ and AuNP seeds ($[Au^{3+}]/[AuNP]$). Higher $[Au^{3+}]/[AuNP]$ ratios led to the synthesis of larger AuNS (Figures 1b and S2). When the ratio was $>2 \times 10^7$, Au precursors spontaneously nucleated, resulting in a mixed phase of AuNP and AuNS (Figure S2). Larger AuNS exhibited a LSPR peak at longer wavelength (Figure 1c and d), because they support more extended longitudinal plasmon resonance along their branches.²¹ The peak width also broadened with the particle size (Figure S3),

Received: June 17, 2015 Revised: June 23, 2015

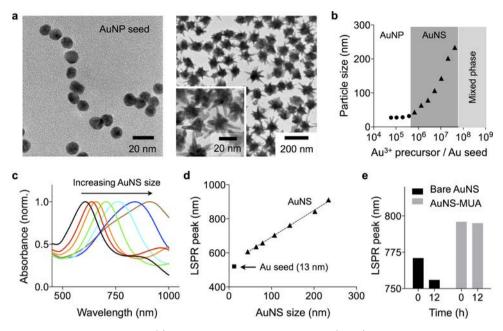


Figure 1. Synthesis and characterization of AuNS. (a) Transmission electron microscopy (TEM) images of AuNP and AuNS. Spherical particles (diameter 13 nm, left) were used as a seed to grow AuNS (right). (b) The size of AuNS was controlled by changing the ratio between AuNP seed and Au³⁺ precursor concentrations. (c, d) Absorbance spectra of AuNS. Increasing the particle size led to shifts of the LSPR peaks to longer wavelengths. (e) Bare AuNS showed a drift in LSPR peak over time. Passivating the AuNS with a thiol ligand (11-mercaptoundecanoic acid/MUA) stabilized the LSPR spectra.

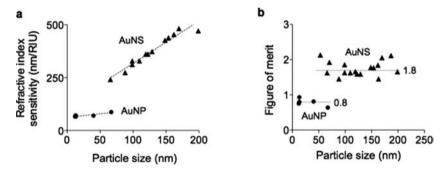


Figure 2. Detection sensitivities of AuNP and AuNS. (a) The refractive index sensitivity (RIS) of AuNS and AuNP of different sizes was measured. The RIS linearly increased with the overall size of the particles. (b) The figure of merit (FOM) was obtained by dividing the RIS with the corresponding full width at half-maximum of the LSPR peak. AuNS assumed higher FOM than AuNP. For a given particle type (i.e., AuNS or AuNP), the FOM values were found similar, independent of the particle size (P = 0.87, AuNS; P = 0.18, AuNP).

which was likely due to the increasing polydispersity (different branch length and number of branches per particle).

As-synthesized bare AuNS were found spectrally unstable; the sharp tips with high surface energy were susceptible to atomic reorganization, which resulted in the shift of the LSPR peaks to shorter wavelengths (Figure 1e). We reasoned that thiol-based ligands could stabilize AuNP by forming a covalent bond with surface Au atoms. Indeed, when AuNS were coated with thiol ligands (e.g., lipoic acid, 11-mercaptoundecanoic acid/MUA, thiolated-polyethylene glycol/PEG), the particles maintained their LSPR peak positions (>12 h in phosphate-buffered saline) (Figures 1e and S4).

We next characterized the LSPR properties of individual AuNS. The refractive index sensitivity (RIS) was determined by measuring spectral shifts of particles suspended in solutions of different refractive indices. Water and dimethyl sulfoxide were mixed at varying volume ratios to control the refractive index (see Experimental Procedures in the Supporting Information). The measured RIS of AuNS increased with the overall particle

size, ranging from 250 to 500 nm/RIU (refractive index unit, Figure 2a). With similar particle volume, AuNS showed higher RIS than AuNP, validating the advantage of forming sharp branches. For example, the sensitivity of 66 nm AuNS (241 nm/RIU) was 3-fold higher than that of 40 nm spherical AuNP (70 nm/RIU). We also compared the figure of merit (FOM) of particles, that was defined as RIS divided by the full width at half-maximum of the LSPR peak (Figure 2b). Particles with high FOM are preferred as they improve the LSPR detection sensitivity. Overall, AuNS had higher FOM (~1.8) than spherical AuNP (~0.8). For a given shape, however, the FOM remained similar (coefficient of variation <12%), because both the RIS and peak-width increased with the particle size. For clustering assays, we thus used small AuNS (~70 nm) for their superior colloidal stability, compared to larger particles.

For molecular sensing with AuNS, we adopted a clustering assay format: AuNS coated with affinity ligands self-assemble into nanoscale clusters in the presence of target molecules (Figure 3a). Such clustering could produce strong plasmonic

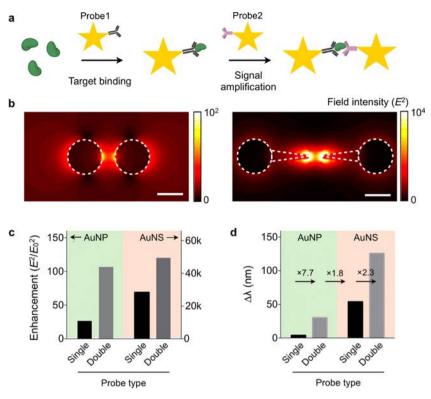


Figure 3. Electromagnetic simulation of the clustering assay. (a) Schematic of the AuNS clustering assay. The target molecule bridges the metal tips of AuNS probes to concentrate electrical fields. (b) Simulated electric field intensity (E^2) surrounding a particle pair. The field magnitude is 460 times higher in the AuNS dimer (right) than in the AuNP dimer (left). Scale bar, 50 nm. (c) The field intensity (E^2) relative to that of the incident light (E_0^2) was compared for different assay configurations. The clustering assay amplifies the signal from the single-probe assay. (d) The spectral shift $(\Delta \lambda)$ for each assay type was calculated from the E-field data. The overall sensitivity improved by >32 fold with the AuNS-clustering assay.

coupling among AuNS to increase the spectral shift. We first performed a three-dimensional finite-difference time-domain (FDTD) simulation (Figure S5). We calculated the electricfield (E-field) of AuNP and AuNS dimers, a simplified version of clusters. The map showed the field intensity (E^2) concentrated at the junction of two metal particles (Figure 3b). The AuNS dimer showed up to 460-fold higher enhancement than the AuNP dimer (Figure 3c), with E-field more efficiently concentrated between tips. The maximum enhancement was observed when two tips of AuNS aligned in a line. Even with misaligned tips, however, the AuNP dimer still showed higher field intensity than the AuNP dimer (Figure S5). The simulation also confirmed that signal amplification could be achieved though particle clustering. Forming a particle-dimer increased the field intensity by 1.7-fold for AuNS (4-fold for AuNP; Figure 3c). Such increases resulted in larger spectral shift $(\Delta \lambda)$. The $\Delta \lambda$ for the AuNS dimer, as estimated from the field information, was 2.3-fold larger than AuNS single particle

We applied the AuNS clustering assay to detect protein targets. As a model system, we used avidin—biotin interaction and first compared the detection sensitivity between AuNS and AuNP. Biotinylated particles with similar volumes (AuNP, 40 nm in diameter; AuNS, 70 nm in overall size) were prepared and concentration-matched (see Experimental Procedures in the Supporting Information for details). Varying concentrations of avidin were added to particle solutions, and resulting spectral shifts ($\Delta\lambda$) were measured. In the presence of avidin, the particles clustered and their spectral peaks red-shifted (Figure 4a). Dynamic light scattering measurements confirmed the avidin-specific clustering; the hydrodynamic diameter increased

with avidin concentration (Figure S6). Dark-field microscopy could also detect AuNS clustering. The aggregated particles appeared brighter than individual particles due to the increased scattering cross-section (Figure S7). The microscopy, however, has a limited assay speed and throughput and requires fine-tuning of particle concentrations to obtain optimal particle numbers in a field-of-view. In all concentrations tested, AuNS showed larger $\Delta \lambda$ than AuNP. For instance, with the addition of 16 nM of avidin, $\Delta \lambda = 19$ nm for AuNS, and $\Delta \lambda = 1.5$ nm for AuNP. Titration measurements further confirmed the superiority of AuNS over AuNP (Figure 4b), with AuNS displaying a 7-fold lower limit of detection (LOD = 3.4 nM) than AuNP (LOD = 23.4 nM).

We next examined the effect of the interparticle distance on the clustering assay sensing. Reducing the interparticle distance (d_{vv}) is crucial in improving the detection sensitivity, since the field enhancement between the tips decreases exponentially with d_{pp} (Figure S8). As a model detection target, we used the kidney injury molecule-1 (KIM1), a urinary protein marker for kidney injury.²⁷ To control the particle distance, we prepared two types of probes (see Experimental Procedures in the Supporting Information): AuNS conjugated with full polyclonal antibodies (Ab-AuNS) and AuNS with half antibody fragments (A $b_{1/2}$ -AuNS). As a control, we prepared AuNS conjugated with isotype-matched IgG antibodies. The KIM1 titration experiments showed dose-dependent spectral shifts (Figure 4c), with the half antibody configuration displaying larger spectral shifts than that with the full-antibody probes. When BSA was used as a control analyte, we observed negligible signal changes (Figure S9); this confirmed that the signal changes were due to antibody-antigen specific aggregation. The LOD for $Ab_{1/2}$ -

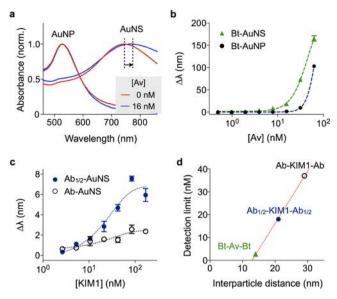


Figure 4. Protein detection with AuNS. (a) Biotinylated AuNP (Bt-AuNP) and AuNS (Bt-AuNS) with similar particle volumes were incubated with avidin, and the corresponding spectral changes were monitored. With the addition of 16 nM of avidin, Bt-AuNS displayed more pronounced spectral shifts ($\Delta \lambda = 19 \text{ nm}$) than Bt-AuNP ($\Delta \lambda = 19 \text{ nm}$) than Bt-AuNP ($\Delta \lambda = 19 \text{ nm}$) 1.5 nm). (b) Avidin-titration experiments confirmed the superior sensitivity of the AuNS system. The limit of detection (LOD) of Bt-AuNS was 7 times lower than that of Bt-AuNP. (c) The effect of the interparticle distance on the assay sensitivity was studied. Kidney injury molecule-1 (KIM1) was used as the detection target. To change the interparticle distance, AuNS was conjugated with either full antibody against KIM1 (Ab-AuNS) or half antibody fragments (Ab_{1/2}-AuNS). The shorter probe (Ab_{1/2}-AuNS) produced larger LSPR spectral shifts in KIM1 titration measurements. AuNS conjugated with isotype-matched goat IgG was used as control. (d) The detection limits of the three systems in (b) and (c) were compared. The detection sensitivity was found to be inversely proportional to the interparticle distance.

AuNS was 2-fold lower than that of Ab-AuNS. We further compared the detection sensitivity as a function of the interparticle distance (Figure 4d, Table S1). The LOD values were obtained from the titration experiments (Figure 4b and 4c), and d_{pp} was estimated from the lengths of the passivation layer, affinity ligands, and target molecules. The avidin—biotin system ($d_{pp} \approx 12$ nm) showed the lowest detection limit (the highest sensitivity), followed by the half antibody—antigen ($d_{pp} \approx 19$ nm) and the full-antibody—antigen ($d_{pp} \approx 33$ nm) systems. The improved sensitivity (2-fold) with a shorter interparticle distance is consistent with our numerical simulation data (Figure S8).

In summary, AuNS are promising nanoprobes for plasmonic biosensing. With multiple branched tips at their surface, AuNS can concentrate electromagnetic fields more efficiently compared to spherical particles and thereby generate larger plasmonic spectral shifts upon molecular binding. In this study, we found three key aspects to improve sensitive biosensing with AuNS, namely 1) a covalent surface coating to maintain particle morphology and its resonance spectra; 2) AuNS clustering to more strongly concentrate electromagnetic energy; and 3) minimizing the interparticle distance in AuNS clusters. The resulting AuNS assay was simple and fast, as the reaction occurs in bulk solution and the signals can be read out from visual color changes. Compared to the microscopic observation of individual AuNS, the method is also scalable for high

throughput detection. We envision that this assay could have potential applications in point-of-care molecular detection.

ASSOCIATED CONTENT

S Supporting Information

Experimental procedures, Figures S1–S9, and Table S1. The Supporting Information is available free of charge on the ACS Publications website at DOI: 10.1021/acs.bioconjchem.5b00343.

AUTHOR INFORMATION

Corresponding Authors

*Phone: 617-726-8226. E-mail: rweissleder@mgh.harvard.edu. Corresponding author address: Center for Systems Biology, Massachusetts General Hospital, 185 Cambridge St, CPZN 5206, Boston, MA 02114 (R.W.).

*E-mail: hlee@mgh.harvard.edu. Corresponding author address: Center for Systems Biology, Massachusetts General Hospital, 185 Cambridge St, CPZN 5206, Boston, MA 02114 (H.L.).

Notes

The authors declare no competing financial interest.

ACKNOWLEDGMENTS

We thank K. Lee for microscopy imaging and H. Shao and H. J. Chung for helpful discussions. This work was supported in part by NIH Grants R01HL113156, R01EB004626, R01EB010011, HHSN268201000044C, U54-CA119349, and T32-CA79443 and Department of Defense OCRP Program Award W81XWH-14-1-0279.

■ REFERENCES

- (1) Hutter, E., and Fendler, J. H. (2004) Exploitation of localized surface plasmon resonance. *Adv. Mater.* 16, 1685–1706.
- (2) Anker, J. N., Hall, W. P., Lyandres, O., Shah, N. C., Zhao, J., and Van Duyne, R. P. (2008) Biosensing with plasmonic nanosensors. *Nat. Mater.* 7, 442–453.
- (3) Jain, P. K., Huang, X., El-Sayed, I. H., and El-Sayed, M. A. (2008) Noble metals on the nanoscale: optical and photothermal properties and some applications in imaging, sensing, biology, and medicine. *Acc. Chem. Res.* 41, 1578–1586.
- (4) Sepulveda, B., Angelome, P. C., Lechuga, L. M., and Liz-Marzan, L. M. (2009) LSPR-based nanobiosensors. *Nano Today* 4, 244–251.
- (5) Haes, A. J., and Van Duyne, R. P. (2002) A nanoscale optical blosensor: Sensitivity and selectivity of an approach based on the localized surface plasmon resonance spectroscopy of triangular silver nanoparticles. *J. Am. Chem. Soc.* 124, 10596–10604.
- (6) Sherry, L. J., Jin, R., Mirkin, C. A., Schatz, G. C., and Van Duyne, R. P. (2006) Localized surface plasmon resonance spectroscopy of single silver triangular nanoprisms. *Nano Lett.* 6, 2060–2065.
- (7) Mayer, K. M., and Hafner, J. H. (2011) Localized surface plasmon resonance sensors. *Chem. Rev.* 111, 3828–3857.
- (8) Gao, B., Rozin, M. J., and Tao, A. R. (2013) Plasmonic nanocomposites: polymer-guided strategies for assembling metal nanoparticles. *Nanoscale 5*, 5677–5691.
- (9) Lu, X., Rycenga, M., Skrabalak, S. E., Wiley, B., and Xia, Y. (2009) Chemical synthesis of novel plasmonic nanoparticles. *Annu. Rev. Phys. Chem.* 60, 167–192.
- (10) Nehl, C. L., Liao, H., and Hafner, J. H. (2006) Optical properties of star-shaped gold nanoparticles. *Nano Lett.* 6, 683–688.
- (11) Hao, F., Nehl, C. L., Hafner, J. H., and Nordlander, P. (2007) Plasmon resonances of a gold nanostar. *Nano Lett.* 7, 729–732.
- (12) Senthil, K., Pandian, Pastoriza-Santos, I., Rodriguez-Gonzalez, B., Garcia, d. A., Javier, F., and Liz-Marzan, L. M. (2008) High-yield

synthesis and optical response of gold nanostars. Nanotechnology 19, 015606.

- (13) Dondapati, S. K., Sau, T. K., Hrelescu, C., Klar, T. A., Stefani, F. D., and Feldmann, J. (2010) Label-free biosensing based on single gold nanostars as plasmonic transducers. *ACS Nano* 4, 6318–6322.
- (14) Barbosa, S., Agrawal, A., Rodriguez-Lorenzo, L., Pastoriza-Santos, I., Alvarez-Puebla, R. A., Kornowski, A., Weller, H., and Liz-Marzan, L. M. (2010) Tuning size and sensing properties in colloidal gold nanostars. *Langmuir* 26, 14943—14950.
- (15) Guerrero-Martinez, A., Barbosa, S., Pastoriza-Santos, I., and Liz-Marzan, L. M. (2011) Nanostars shine bright for you Colloidal synthesis, properties and applications of branched metallic nanoparticles. *Curr. Opin. Colloid Interface Sci. 16*, 118–127.
- (16) Vo-Dinh, T., Fales, A. M., Griffin, G. D., Khoury, C. G., Liu, Y., Ngo, H., Norton, S. J., Register, J. K., Wang, H. N., and Yuan, H. (2013) Plasmonic nanoprobes: from chemical sensing to medical diagnostics and therapy. *Nanoscale* 5, 10127–10140.
- (17) Webb, J. A., Erwin, W. R., Zarick, H. F., Aufrecht, J., Manning, H. W., Lang, M. J., Pint, C. L., and Bardhan, R. (2014) Geometry-Dependent Plasmonic Tunability and Photothermal Characteristics of Multibranched Gold Nanoantennas. *J. Phys. Chem. C* 118, 3696–3707.
- (18) Solis, D. M., Taboada, J. M., Obelleiro, F., Liz-Marzan, L. M., and Garcia de Abajo, F. J. (2014) Toward ultimate nanoplasmonics modeling. *ACS Nano* 8, 7559–7570.
- (19) Lu, W., Singh, A. K., Khan, S. A., Senapati, D., Yu, H., and Ray, P. C. (2010) Gold nano-popcorn-based targeted diagnosis, nanotherapy treatment, and in situ monitoring of photothermal therapy response of prostate cancer cells using surface-enhanced Raman spectroscopy. J. Am. Chem. Soc. 132, 18103–18114.
- (20) Yuan, H., Liu, Y., Fales, A. M., Li, Y. L., Liu, J., and Vo-Dinh, T. (2013) Quantitative surface-enhanced resonant Raman scattering multiplexing of biocompatible gold nanostars for in vitro and ex vivo detection. *Anal. Chem.* 85, 208–212.
- (21) Khoury, C. G., and Vo-Dinh, T. (2008) Gold Nanostars For Surface-Enhanced Raman Scattering: Synthesis, Characterization and Optimization. *J. Phys. Chem. C* 2008, 18849—18859.
- (22) Im, H., and Oh, S. H. (2014) Oxidation sharpening, template stripping, and passivation of ultra-sharp metallic pyramids and wedges. *Small* 10, 680–684.
- (23) Malinsky, M. D., Kelly, K. L., Schatz, G. C., and Van Duyne, R. P. (2001) Chain length dependence and sensing capabilities of the localized surface plasmon resonance of silver nanoparticles chemically modified with alkanethiol self-assembled monolayers. *J. Am. Chem. Soc.* 123, 1471–1482.
- (24) Vega, M. M., Bonifacio, A., Lughi, V., Marsi, S., Carrato, S., and Sergo, V. (2014) Long-term stability of surfactant-free gold nanostars. *J. Nanopart. Res.* 16, 2729.
- (25) Joshi, G. K., McClory, P. J., Muhoberac, B. B., Kumbhar, A., Smith, K. A., and Sardar, R. (2012) Designing Efficient Localized Surface Plasmon Resonance-Based Sensing Platforms: Optimization of Sensor Response by Controlling the Edge Length of Gold Nanoprisms. *J. Phys. Chem. C* 116, 20990–21000.
- (26) Bu, T., Zako, T., Fujita, M., and Maeda, M. (2013) Detection of DNA induced gold nanoparticle aggregation with dark field imaging. *Chem. Commun.* 49, 7531–7533.
- (27) Waanders, F., van Timmeren, M. M., Stegeman, C. A., Bakker, S. J., and van Goor, H. (2010) Kidney injury molecule-1 in renal disease. *J. Pathol.* 220, 7–16.



Integrated Magneto-Electrochemical Sensor for Exosome Analysis

Sangmoo Jeong,^{†,⊥} Jongmin Park,[†] Divya Pathania,[†] Cesar M. Castro,^{†,‡} Ralph Weissleder,^{†,‡,§} and Hakho Lee*,[†]

Supporting Information

ABSTRACT: Extracellular vesicles, including exosomes, are nanoscale membrane particles that carry molecular information on parental cells. They are being pursued as biomarkers of cancers that are difficult to detect or serially follow. Here we present a compact sensor technology for rapid, on-site exosome screening. The sensor is based on an integrated magneto-electrochemical assay: exosomes are immunomagnetically captured from patient samples and profiled through electrochemical reaction. By combining magnetic enrichment and enzymatic amplification, the approach enables (i) highly sensitive, cell-specific exosome detection and (ii) sensor miniaturization and scale-up for high-throughput measurements. As a proof-of-concept, we implemented a portable, eight-channel device and applied it to screen extracellular vesicles in plasma



samples from ovarian cancer patients. The sensor allowed for the simultaneous profiling of multiple protein markers within an hour, outperforming conventional methods in assay sensitivity and speed.

KEYWORDS: extracellular vesicles, electrochemical sensing, cancer, diagnostics, point-of-care

rowing evidence has positioned extracellular vesicles (EVs) as an effective readout of cancer management.¹⁻⁶ Exosomes, in particular, have emerged as a potent biomarker. Exosomes are nanoscale vesicles actively secreted by cells. These vesicles carry molecular constituents of their originating cells, including transmembrane and cytosolic proteins, 7 mRNA, 8 DNA, 9 and microRNA, 10 and can thus serve as cellular surrogates. 11 Combined with their relative abundance and ubiquitous presence in bodily fluids (e.g., serum, ascites, urine, cerebrospinal fluid), 12-14 exosomes can offer unique advantages for longitudinal monitoring. 15-17 Exosome analyses are minimally invasive and afford relatively unbiased readouts of the entire tumor burden, less affected by the scarcity of the samples or intratumoral heterogeneity.⁵

Analyzing extracellular vesicles in routine clinical settings, however, still remains a difficult task, mainly due to the lack of adequately sensitive and fast assay platforms, particularly for protein analyses. Flow cytometry provides high-throughput detection¹⁸ yet tends to miss small vesicles (<200 nm) because of weak light scattering.¹⁹ New counting approaches based on particle tracking or dynamic light scattering can offer more accurate particle counts, >103-fold higher than those reported by flow cytometry,²⁰ but yield limited molecular information. Conversely, conventional molecular assays (e.g., Western blot, ELISA) require large amounts of samples and become impractical for clinical research needs, notably serial analyses, large patient cohorts, or limited specimens in biorepositories.

We have previously developed miniaturized systems to facilitate EV analyses in clinical environments. These systems include microfluidic devices for sample preparation 21,22 and analytical tools for protein analyses.^{3,5} Ensuing clinical studies with patient samples established EVs' clinical utility for cancer diagnosis and treatment monitoring:3,5 tumor-specific exosomes could be identified based on their unique transmembrane protein signature, and exosomal protein changes could be correlated with treatment responses. Translating these systems into routine clinical tests, however, is still limited by (i) separate procedures and devices required for exosome isolation and detection, (ii) technical complexities involved in device fabrication and operation, and (iii) relatively high costs of analytical instruments (e.g., NMR detector, spectral microscope).

We reasoned that electrochemical sensing could be an effective detection modality that is easily applicable to clinical settings. Electrochemical sensing could achieve high sensitivity through signal amplification with redox-active reporters. 23-28 The readout system measures electrical currents and can be

Received: December 1, 2015 Accepted: January 25, 2016 Published: January 25, 2016

[†]Center for Systems Biology, Massachusetts General Hospital, 185 Cambridge Street, CPZN 5206, Boston, Massachusetts 02114, United States

^{*}Massachusetts General Hospital Cancer Center, Boston, Massachusetts 02114, United States

Department of Systems Biology, Harvard Medical School, 200 Longwood Avenue, Boston, Massachusetts 02115, United States

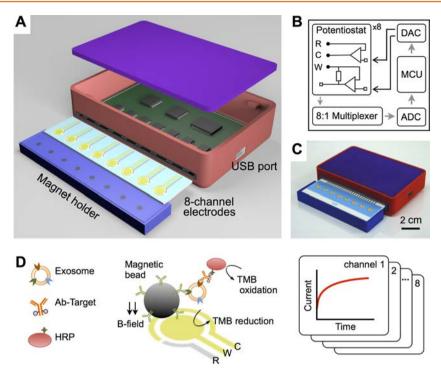


Figure 1. Integrated magnetic—electrochemical exosome (iMEX) platform. (A) Sensor schematic. The sensor can simultaneously measure signals from eight electrodes. Small cylindrical magnets are located below the electrodes to concentrate immunomagnetically captured exosomes. (B) Circuit diagram. The sensor system has eight potentiostats, an 8-to-1 multiplexer, an analog-to-digital converter (ADC), a digital-to-analog converter (DAC), and a microcontroller unit (MCU). Each potentiostat has three electrodes: reference (R), counter (C), and working (W). (C) Packaged device. The device has a small form factor $(9 \times 6 \times 2 \text{ cm}^3)$. (D) Schematic of iMEX assay. Exosomes are captured on magnetic beads directly in plasma and labeled with HRP enzyme for electrochemical detection. The magnetic beads are coated with antibodies against CD63, an enriched surface marker in exosomes. The working (W) and the counter (C) electrodes are made of gold (Au), and the reference electrode (R) is made of silver/silver chloride (Ag/AgCl). Eight channels are simultaneously monitored for high-throughput analysis. HRP, horseradish peroxidase; TMB, 3,3',5,5'-tetramethylbenzidine.

realized as a compact and low-power device.^{29,30} Harnessing electrochemical sensing for exosome analyses, however, is challenged by both assay design and hardware development: (i) combining exosome isolation and detection in a single platform; (ii) providing fast, high-throughput assays for multiplexed screening; and (iii) making the system affordable and easy to use.

We herein report on a new integrated approach, iMEX (integrated magnetic-electrochemical exosome), for fast, streamlined exosome analyses. The iMEX combines two orthogonal modalities, magnetic selection and electrochemical detection. Magnetic beads are used for exosome capture and labeling; captured exosomes are detected via electrochemical sensing. The iMEX offers distinct advantages: (i) cell-specific exosomes can be isolated directly from complex media without need for extensive filtration or centrifugation; (ii) the assay can achieve high detection sensitivity through magnetic enrichment and enzymatic amplification; (iii) through the electrical detection scheme, sensors can be miniaturized and expanded for parallel measurements. To prove the concept, we implemented a portable iMEX platform with eight detection channels. The iMEX was able to detect exosomes at a sensitivity of $<10^5$ vesicles. Importantly, it only used 10 μ L of samples and generated readouts within 1 h. We further explored iMEX's potential clinical utility by profiling EVs collected from ovarian cancer patients. With its capacities for fast, high-throughput, and on-spot analysis, the iMEX could accelerate the transition of EV and exosome analyses toward routine clinical testing.

RESULTS AND DISCUSSION

iMEX Platform. The miniaturized iMEX system had eight independent channels (Figure 1A). Each channel was equipped with a potentiostat capable of measuring a wide range of current ($\pm 7.5 \mu A$). The input signal was conditioned by a lowpass filter (cutoff frequency, 5 Hz) to suppress high-frequency noise (Figure S1). The eight potentiostats were connected to a digital-to-analog converter for potential control, an analog-todigital converter for signal digitization, a multiplexer for channel selection, and a microcontroller unit for system operation (Figure 1B and Figure S2). We packaged the device as a handheld unit (Figure 1C). A card-edge connector was used for the quick attachment of the electrode cartridge. A magnet holder, containing eight cylindrical magnets, was placed underneath the electrode cartridge. These magnets were used to concentrate magnetic beads to the sensor surface. The overall device cost was <\$50. The system performance was comparable to that of commercial equipment (SP-200, Bio-Logic; Figure S1BB), but the iMEX device was much smaller and cost-effective. Furthermore, the iMEX effectively provided a simultaneous readout from all electrodes through rapid polling of each channel (50 ms per channel). All data were monitored and analyzed by custom-designed software (Figure S3).

Figure 1D summarizes the iMEX assay scheme. Exosomes are first captured onto immunomagnetic beads. Targeting antibodies with an oxidizing enzyme (horseradish peroxidase, HRP) are then used, followed by mixing the beads with chromogenic electron mediators (3,3′,5,5′-tetramethylbenzidine, TMB), which generate electrical current when HRP is

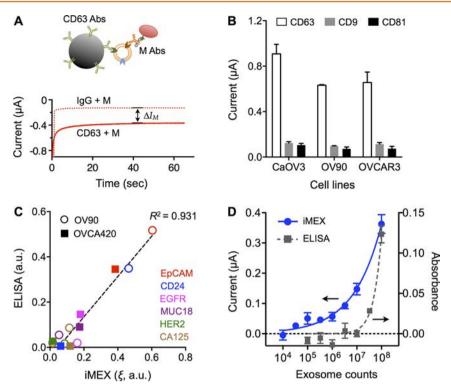


Figure 2. Characteristics of the iMEX diagnostic platform. (A) Schematic of the electrochemical measurement in the iMEX assay. With -100 mV reduction potential, the current level reached a plateau within 1 min. The current difference between the CD63 bead and IgG bead samples ($\Delta I_{\rm M}$) was used as a representative value of a target protein marker. Abs, antibodies. M, marker. (B) Signal comparison of three tetraspanin markers (CD63, CD9, and CD81) in cancer exosomes. Signals from CD63 were much higher than those from other markers in exosomes collected from ovarian cancer cell lines (CaOV3, OV90, and OVCAR3). (C) Comparison between iMEX and ELISA. Six surface proteins were profiled in two ovarian cancer cell lines (OV90 and OVCA420). The results showed high correlation ($R^2 = 0.931$); a.u., arbitrary unit. (D) Varying number of exosomes were spiked into human plasma and assayed by iMEX and ELISA. The detection limits were 3 \times 10⁴ (iMEX) and 3 \times 10⁷ (ELISA). All measurements were performed in triplicate, and the data are displayed as mean \pm SD.

encountered (Figure S4; see Materials and Methods for details). Using magnetic beads significantly simplifies the assay procedures: excess agents (e.g., antibodies, enzymes) can be removed via magnetic washing, and captured exosomes can be magnetically concentrated on the electrodes to improve the detection sensitivity.

Assay Optimization. We optimized the iMEX assay protocol. We applied the chronoamperometry method for signal detection: the electrical current generated from TMB reduction was monitored, while a reduction potential (-100 mV *versus* Ag/AgCl reference electrode) was applied to a working electrode. The current level (*I*) reached a plateau within 1 min after the reduction potential was applied (Figure 2A). We averaged the current level (*I*) from 40 to 45 s as a representative value.

To capture exosomes, we used magnetic beads that were coated with antibodies against tetraspanin, transmembrane proteins enriched in exosomes. 5,31,32 We first compared signal levels with differently sized beads (diameters = 2.7 and 8.8 μ m). When the total surface area of beads was matched to capture a similar amount of exosomes, the measured signal levels were nearly identical (Figure SSA). This result can be explained by estimating a diffusivity in porous media: The effective diffusivity (D_e) for stacked beads can be expressed as $D_e = D_0 \times e^m$, where D_0 is the diffusivity in free media and e is the porosity of the structure. In the case of uniformly sized beads, both e (\leq 0.47) and e (e0.47) are bead-size-independent; the iMEX signals are thus expected to remain constant. We opted to use 2.7 e10 beads; bigger beads tended to sediment, requiring

frequent shaking of samples. Compared to the no-enrichment scheme, magnetic enrichment led to \sim 72% increase in the analytical signal (Figure SSB).

We next tested three representative tetraspanin proteins (CD63, CD9, CD81) as a target; these markers are reportedly enriched in exosomes. $^{13,33-39}$ We prepared 2.7 μ m magnetic beads specific to each marker (see Materials and Methods for details). When applied to exosomes from different cell lines, CD63-based capture showed consistently high signal (Figure 2B); we thus opted to use CD63 as a marker for exosome enrichment.

For each target marker (M), we prepared a pair of magnetic beads: one conjugated with antibodies against CD63 (CD63 beads) and the other with antibodies against iso-type matched IgG (IgG beads). Exosomes were mixed with each bead type and subsequently labeled with antibodies against a target marker; the net signal difference $\Delta I_{\rm M}$ ($I_{\rm CD63+M}-I_{\rm IgG+M}$; Figure 2A) was then obtained. We used $\Delta I_{\rm CD63}$ to estimate the total exosome load, and defined a normalized metric $\xi_{\rm M}$ ($\Delta I_{\rm M}/\Delta I_{\rm CD63}$) as the expression level of a target marker (M). Note that such scaling would compensate for variations in exosome numbers among samples.

iMEX Validation. We applied the developed iMEX protocol to profile exosomes for transmembrane proteins. For this validation study, we harvested exosomes from cell culture (OV90, OVCA420) through a conventional method (see Materials and Methods for details) and spiked them into phosphate buffered saline (PBS) solution (~10⁹ exosomes/mL). Samples were aliquoted and processed by iMEX and

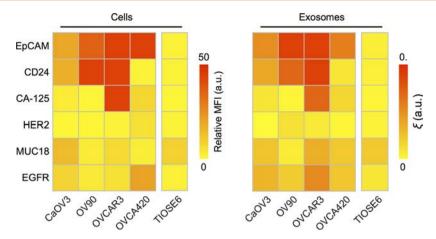


Figure 3. Profiling of surface proteins in ovarian cancer cells and their secreting exosomes. Four ovarian cancer cell lines (CaOV3, OV90, OVCAR3, and OVCA420) and one normal cell line (TIOSE6) were screened for six putative cancer markers (*via* flow cytometry, left panel). Cell-derived exosomes were immunomagnetically captured (CD63-specific) and assayed by iMEX (right panel). The profiling data showed a good match between cells and CD63-positive exosomes. The iMEX assay was duplicated, and the mean values are displayed.

ELISA. Comparative analysis showed high correlation between two methods (Figure 2C; $R^2 = 0.931$), confirming iMEX's analytical capacity. The iMEX assay, however, was faster (1 h) and consumed smaller amounts of samples (10 μ L) than ELISA (5 h, 100 μ L).

We further tested iMEX for detecting exosomes in biofluids. Cancer exosomes were collected from cell culture (OV90), and varying numbers of exosomes were spiked into undiluted human plasma. Titration experiments established the limit of detection of 3×10^4 exosomes, with the dynamic ranges spanning 4 orders of magnitude (Figure 2D). Similar measurements with ELISA required more than 10^7 exosomes for reliable detection. Using matched controls (IgG beads) was important to compensate for background signals from sample-dependent, nonspecific exosome binding.

Profiling of Protein Markers in Cell-Derived Exosomes. We applied the iMEX to screen exosomal surface markers from a panel of ovarian cancer cell lines. Because iMEX enriches CD63-positive (CD63+) exosomes and labels them for target proteins, we were able to examine how closely CD63+ exosomes reflect their cells of origin. We chose six representative surface markers based on prior studies: epithelial cell adhesion molecule (EpCAM),40 CD24,41 cancer antigen 125 (CA125), 42,43 human epidermal growth factor 2 (HER2), 44,45 mucin 18 (MUC18), 46 and epidermal growth factor receptor 2 (EGFR).⁴⁷ The cellular expression levels of these markers were measured with flow cytometry; exosomes were harvested from the conditioned cell culture media and profiled with iMEX. The molecular profiles of cells and CD63+ exosomes were highly correlated (Figure 3), which supported the use of exosomes as cellular surrogates.

Clinical: Direct Analyses of Plasma from Patients with Ovarian Cancer. The iMEX assay isolates EVs directly from plasma or serum and allows for profiling in a rapid, high-throughput manner—key for successful integration into the clinical workflow. To demonstrate clinical feasibility, we customized the iMEX assay for ovarian cancer EV detection in blood (Figure 4A). Clinical plasma samples were aliquoted without any purification, and each aliquot (10 μ L per marker) was incubated with magnetic beads for EV capture (15 min), followed by magnetic washing. The bead-bound EVs were consecutively labeled for target markers (15 min) and HRP (15

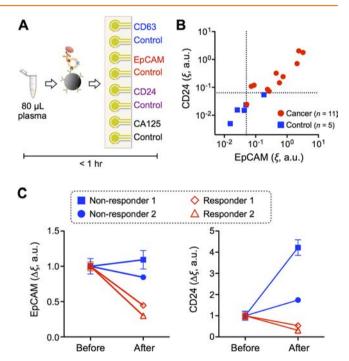


Figure 4. iMEX for clinical applications. (A) iMEX assay for clinical sample analysis. Ten microliters of plasma per marker was used, and the entire assay was completed within 1 h without filtration and centrifugation processes. (B) Plasma samples from ovarian cancer patients (n=11) and healthy controls (n=5) were analyzed with the iMEX assay. EpCAM and CD24 levels were much higher in cancer patients. The EpCAM and CD24 expression levels ($\xi_{\rm EpCAM}$ νs $\xi_{\rm CD24}$) were highly correlated ($R^2=0.870$). (C) Longitudinal monitoring of drug treatment responses. Plasma samples from four ovarian cancer patients were analyzed with the iMEX assay. EpCAM and CD24 levels in responders were decreased significantly, but their levels in nonresponders were stable (EpCAM) or increased (CD24) after treatment. All measurements were duplicated; a.u., arbitrary unit.

min) and loaded onto the device. With the eight electrodes independently operated, we were able to simultaneously measure four different markers (CD63, EpCAM, CD24, and CA125) along with their respective IgG controls. The IgG

controls were beneficial for specific detection of target molecules among nonpurified clinical samples.

We tested single-time-point plasma samples from 11 ovarian cancer patients and five healthy controls. The expression levels of EpCAM and CD24 in EVs were much higher in ovarian cancer patients than in healthy controls, and both metrics showed high correlation (Figure 4B and Figure S6). We next examined iMEX's potential for serial EV testing by measuring EpCAM and CD24 in plasma collected at two time points (2 months apart) from four ovarian cancer patients undergoing drug treatment. The iMEX assays were conducted blinded to treatment response. For "nonresponding" patients, expression levels of EpCAM and CD24 increased while "responding" patients displayed a significant decrease in both markers (Figure 4C). For nonresponders, the level of CD24 showed steeper increases than that of EpCAM.

CONCLUSION

We developed the iMEX technology to aid the translation of exosome analysis into clinical settings. A unique feature of iMEX is the integration of vesicle isolation and detection into a single platform. The use of magnetic actuation simplifies vesicle isolation and subsequent assay steps, and the electrochemical sensing facilitates high-throughput screening and sensor miniaturization. The current study validated these concepts: (i) a portable detection system was implemented with the capacity for parallel measurements; (ii) the iMEX enriched exosomes directly from blood and profiled them for molecular information; (iii) the entire iMEX assay (*i.e.*, exosome isolation, labeling, detection) was completed within 1 h while consuming only 10 μ L of plasma per marker. We also demonstrated iMEX's clinical potential by profiling EVs within blood collected from ovarian cancer patients.

The bead-based magnetic enrichment brings several advantages in the iMEX measurement. First, the method provides a convenient way of concentrating signal sources on the electrodes, which enhances the detection sensitivity. Second, compared to the surface-based capture wherein antibodies are immobilized on the chip surface, the bead-based method is amenable to reliable and simpler conjugation chemistry and benefits from faster binding kinetics between antibodies and exosomes. Third, the bead-bound vesicles could be readily recovered for downstream molecular analyses in tandem with iMEX. For instance, bead-bound EVs can be eluted³¹ or lysed³ to profile their nucleic acid contents.

The iMEX system can complement other exosome analysis platforms we have developed (Table S1), particularly the nanoplasmonic exosome (nPLEX) sensor. The nPLEX is well-suited to conduct massively parallel exosome screening, potentially for central clinical laboratories; it has high detection sensitivity, down to $\sim 10^3$ exosomes, and is equipped with >1000 detection sites. The system complexity and the requirement for nanofabrication, however, are limiting factors for nPLEX's routine clinical applications. The iMEX system has lower sensitivity and throughput than nPLEX but is affordable and miniaturized for on-site exosome detection.

In the current work, we focused on profiling CD63-positive EV population (exosomes), which was motivated by two factors: (i) the signal from CD63 capture was the highest (Figure 2B) among the tetraspanin markers tested; and (ii) we and others have previously shown that ovarian cancer exosomes are enriched with CD63. The iMEX profiling found a high correlation in protein expression between CD63-positive

exosomes and their parent cells (Figure 3); this result validated the potential use of CD63-positive exosomes as cellular surrogates. However, we note the need to extend the exosome capture strategy, considering that diverse EV types (e.g., CD63-negative) may exist in patient samples. Examining these populations could yield more precise information to capture tumor heterogeneity. The iMEX method can be readily adopted for such purposes by changing capture antibodies.

We envision multiple directions to further advance the iMEX technology. First, the assay throughput can be improved by increasing the number of detection sites. Electrochemical sensing is ideally suited for such a scale-up: the sensing elements (electrodes) can be readily microfabricated into a large array format, and signals (electrical currents) can be read out by compact electronics with high-speed multiplexing. Second, the detection sensitivity could be improved by exploring new designs for electrochemical signal detection. The signal level is correlated with the surface area of a sensor and the amount of enzyme bound to target entities; thus, higher sensitivity can be achieved by using a nanostructured sensor surface or multilabel nanoparticles. 24,49,50 Third, detection targets can be expanded to include other exosomal constituents. For example, exosomes carry various nucleic acids (e.g., mRNA, microRNA); analyzing nucleic acids along with exosomal proteins would provide a more accurate snapshot of tumor states. 6,8,9,51 Electrochemical sensing has been applied to detect a trace amount of nucleic acids (<1 pM) without PCR amplification.^{23,28,52} We expect that similar approaches could be adopted to profile exosomal nucleic acids. The resulting iMEX could be a powerful clinical tool for affordable, scalable, and comprehensive exosome analyses, thereby deepening our insights into tumor biology and accelerating effective cancer management.

MATERIALS AND METHODS

Fabrication of the iMEX System. The device consists of a microcontroller (Atmega328, Atmel Corporation), a digital-to-analog converter (DAC8552, Texas Instruments), an analog-to-digital converter (ADC161S626, Texas Instruments), a multiplexer (ADG708, Analog Devices), and eight potentiostats. Each potentiostat consists of two operational amplifiers (AD8606, Analog Devices): one amplifier maintains the potential difference between a working electrode and a reference electrode, and the other one works as a transimpedance amplifier to convert a current to a voltage signal. The current measuring range of the transimpedance amplifier was $\pm 7.5~\mu A$. The eight-channel electrodes are commercially available (DropSens, Spain).

Preparation of Immunomagnetic Beads. Five milligrams of magnetic beads coated with epoxy groups (Dynabeads M-270 Epoxy, Invitrogen) was suspended in 1 mL of 0.1 M sodium phosphate solution at room temperature for 10 min. The magnetic beads were separated from the solution with a permanent magnet and resuspended in 100 μ L of the same solution. One hundred micrograms of antibodies against CD63 (Ancell) or respective IgG (Ancell) was added and mixed thoroughly. One hundred microliters of 3 M ammonium sulfate solution was added, and the whole mixture was incubated overnight at 4 °C with slow tilt rotation. The beads were washed twice with PBS solution and finally resuspended in 2 mL of PBS with 1% bovine serum albumin (BSA).

Biotinylation of Labeling Antibodies. Sulfo-NHS-biotin (10 mM, Pierce) solution in PBS was incubated with antibodies for 2 h at room temperature. Unreacted sulfo-NHS-biotin was removed using Zeba spin desalting column, 7K MWCO (Thermo Scientific). Antibodies were kept at 4 $^{\circ}\text{C}$ until use.

iMEX Assay. Ten microliters of exosome-spiked PBS solution (or plasma) was mixed with 50 μ L of the immunomagnetic bead solution

for 15 min at room temperature. The bead concentration was determined according to the following criterion: $[C_b \times V_b \times 4\pi R_b^2]/$ $[C_e \times V_e \times \pi R_e^2] > 100$, where C_b and C_e are the bead and the exosome concentrations, respectively; $V_{\rm b}$ and $V_{\rm e}$ are the volume of the bead solution and the exosome-spiked solution (or plasma), respectively; R_b and R_e are the mean radius of beads and exosomes, respectively. This requirement ensured that sufficient bead surface was available for exosome capture. In our experiment condition, $R_{\rm e}\sim 50$ nm, $R_{\rm b}=1.4~\mu{\rm m}$, and $C_{\rm e}\sim 10^{10}$ /mL. Therefore, we adjusted the bead concentration to $\sim 10^8$ /mL. The magnetic beads were separated from the solution with a permanent magnet and resuspended in 80 μ L of PBS (1% BSA). After 5 s of vortexing, the beads were separated and resuspended in 80 μ L of PBS (1% BSA). Ten microliters of antibodies of interest (2.2 μ g/mL in PBS) was mixed with the beads for 15 min at room temperature. The magnetic beads were separated and washed as described before, and they were resuspended in 50 µL of PBS (1% BSA). Five microliters of streptavidin-conjugated HRP enzymes (1:100 diluted in PBS) was mixed with the beads for 15 min at room temperature. The magnetic beads were separated and washed as described before, and they were resuspended in 7 μ L of PBS. The prepared bead solution and 20 µL of UltraTMB solution (Thermo-Fisher Scientific) were loaded on top of the screen-printed electrode. After 3 min, chronoamperometry measurement was started with the electrochemical sensor. The current levels in the range of 40-45 s were averaged.

Enzyme-Linked Immunosorbent Assay. CD63 antibody (Ancell) and IgG1 antibody (Ancell) were diluted to 5 μ g/mL concentration in PBS and added to the Maxisorp 96-well plate (Nunc) for overnight incubation at 4 °C. After being washed with PBS, 2% BSA in PBS blocking solution was added to the plate for 1 h incubation at room temperature. Subsequently, 10^8 exosomes in 100 μ L pf PBS were added to each well for 1 h incubation at room temperature. After the blocking solution was discarded, antibodies (1 μ g/mL) against various markers were added to each well and incubated at room temperature for 1 h. Unbound antibodies were washed with PBS three times. Streptavidin—HRP molecules were added to the each well for 1 h at room temperature. After being washed out with PBS, the chemiluminescence signal was measured.

Flow Cytometry. We used 5×10^5 cells per antibody for flow cytometry experiments. Cells were fixed with 4% paraformaldehyde for 10 min at room temperature and then washed with PBS (0.5% BSA). Subsequently, cells were blocked with BSA (0.5% in PBS) and then incubated with primary antibodies (4 μ g/mL). After primary antibody incubation, cells were washed, incubated with fluorophore-conjugated secondary antibody (2 μ g/mL; Abcam), and washed. The fluorescence signals from the labeled cells were measured using BD LSRII flow cytometer (BD Biosciences). Mean fluorescent intensities recorded were normalized using the following formula [(signal – IgG isotype control)/secondary]. Blocking and incubation with antibodies (primary and secondary) were preformed for 30 min each at room temperature. Every washing step comprised three 5 min washes at 300g with PBS (0.5% BSA).

Cell Culture. OV90, OVCAR3, OCVA420, and TIOSE6 cells were grown in RPMI-1640 medium (Cellgro). CaOV3 were cultured in Dulbecco's modified essential medium (Cellgro). All media were supplemented with 10% fetal bovine serum (FBS) and penicillin—streptomycin (Cellgro). All cell lines were tested and were free of mycoplasma contamination (MycoAlert mycoplasma detection kit, Lonza, LT07-418).

Exosome Isolation from Cultured Cells. We used a conventional method to harvest exosomes from cell culture media. Cells at passages 1–15 were cultured in vesicle-depleted medium (with 5% depleted FBS) for 48 h. Conditioned medium from $\sim 10^7$ cells was collected and centrifuged at 300g for 5 min. Supernatant was filtered through a 0.2 μ m membrane filter (Millipore) and concentrated by 100 000g for 1 h. After the supernatant was removed, the exosome pellet was washed with PBS and centrifuged at 100 000g for 1 h. The exosome pellet was resuspended in PBS.

Clinical Sample Preparation. The study was approved by the Institutional Review Board at the Dana-Farber/Harvard Cancer

Center (PI: Castro), and the procedures followed were in accordance with institutional guidelines. Informed consent was obtained from all subjects (n = 11). Peripheral blood was withdrawn (\sim 15 mL) from patients with ovarian cancer and centrifuged at 400g for 15 min to separate plasma from red blood cells and buffy coat. Ten microliters of plasma was used for each surface marker analysis.

ASSOCIATED CONTENT

S Supporting Information

The Supporting Information is available free of charge on the ACS Publications website at DOI: 10.1021/acsnano.5b07584.

Additional figures and supporting details (PDF)

AUTHOR INFORMATION

Corresponding Author

*E-mail: hlee@mgh.harvard.edu.

Present Address

¹Department of Radiology, Memorial Sloan-Kettering Cancer Center, New York, NY 10065.

Author Contributions

S.J., J.P., D.P., C.M.C., R.W., and H.L. designed the study, analyzed data, prepared figures, and wrote the manuscript. S.J., J.P., and D.P. performed the research.

Notes

The authors declare no competing financial interest.

ACKNOWLEDGMENTS

The authors thank Dr. Breakefield (Massachusetts General Hospital) for many helpful discussions and granting the use of laboratory resources, and Dr. Birrer (Massachusetts General Hospital) for the gift of the OVCA420 cells. This work was supported in part by U.S. NIH Grants R01-HL113156 (to H.L.), R01-EB00462605 (to R.W.), P01CA069246 (to R.W.), T32CA79443 (to R.W.), K12CA087723-11A1 (to C.M.C.), Ovarian Cancer Research Fund Liz Tilberis Early Career Award (to C.M.C.), DOD Ovarian Cancer Research Program Award W81XWH-14-1-0279 (to H.L. and C.M.C.), and Basic Science Research Program (NRF-2014R1A6A3A03060030 to J.P.) funded by the Ministry of Education, South Korea.

REFERENCES

- (1) Costa-Silva, B.; Aiello, N. M.; Ocean, A. J.; Singh, S.; Zhang, H.; Thakur, B. K.; Becker, A.; Hoshino, A.; Mark, M. T.; Molina, H.; Xiang, J.; Zhang, T.; Theilen, T. M.; Garcia-Santos, G.; Williams, C.; Ararso, Y.; Huang, Y.; Rodrigues, G.; Shen, T. L.; Labori, K. J.; et al. Pancreatic Cancer Exosomes Initiate Pre-Metastatic Niche Formation in the Liver. *Nat. Cell Biol.* **2015**, *17*, 816–826.
- (2) Hoshino, A.; Costa-Silva, B.; Shen, T. L.; Rodrigues, G.; Hashimoto, A.; Tesic Mark, M.; Molina, H.; Kohsaka, S.; Di Giannatale, A.; Ceder, S.; Singh, S.; Williams, C.; Soplop, N.; Uryu, K.; Pharmer, L.; King, T.; Bojmar, L.; Davies, A. E.; Ararso, Y.; Zhang, T.; et al. Tumour Exosome Integrins Determine Organotropic Metastasis. *Nature* **2015**, *527*, *329*–*335*.
- (3) Im, H.; Shao, H.; Park, Y. I.; Peterson, V. M.; Castro, C. M.; Weissleder, R.; Lee, H. Label-free Detection and Molecular Profiling of Exosomes With a Nano-Plasmonic Sensor. *Nat. Biotechnol.* **2014**, 32, 490–495.
- (4) Melo, S. A.; Luecke, L. B.; Kahlert, C.; Fernandez, A. F.; Gammon, S. T.; Kaye, J.; LeBleu, V. S.; Mittendorf, E. A.; Weitz, J.; Rahbari, N.; Reissfelder, C.; Pilarsky, C.; Fraga, M. F.; Piwnica-Worms, D.; Kalluri, R. Glypican-1 Identifies Cancer Exosomes and Detects Early Pancreatic Cancer. *Nature* 2015, 523, 177–182.
- (5) Shao, H.; Chung, J.; Balaj, L.; Charest, A.; Bigner, D. D.; Carter, B. S.; Hochberg, F. H.; Breakefield, X. O.; Weissleder, R.; Lee, H.

Protein Typing of Circulating Microvesicles Allows Real-time Monitoring of Glioblastoma Therapy. *Nat. Med.* **2012**, *18*, 1835–1840. (6) Shao, H.; Chung, J.; Lee, K.; Balaj, L.; Min, C.; Carter, B. S.; Hochberg, F. H.; Breakefield, X. O.; Lee, H.; Weissleder, R. Chipbased Analysis of Exosomal mRNA Mediating Drug Resistance in

- Glioblastoma. *Nat. Commun.* **2015**, *6*, 6999.

 (7) Graner, M. W.; Alzate, O.; Dechkovskaia, A. M.; Keene, J. D.; Sampson, I. H.; Mitchell, D. A.; Bigner, D. D. Proteomic and
- (7) Graner, M. W.; Alzate, O.; Dechkovskaia, A. M.; Keene, J. D.; Sampson, J. H.; Mitchell, D. A.; Bigner, D. D. Proteomic and Immunologic Analyses of Brain Tumor Exosomes. *FASEB J.* **2009**, 23, 1541–1557.
- (8) Skog, J.; Wurdinger, T.; van Rijn, S.; Meijer, D. H.; Gainche, L.; Sena-Esteves, M.; Curry, W. T. J.; Carter, B. S.; Krichevsky, A. M.; Breakefield, X. O. Glioblastoma Microvesicles Transport RNA and Proteins That Promote Tumour Growth and Provide Diagnostic Biomarkers. *Nat. Cell Biol.* **2008**, *10*, 1470–1476.
- (9) Balaj, L.; Lessard, R.; Dai, L.; Cho, Y. J.; Pomeroy, S. L.; Breakefield, X. O.; Skog, J. Tumour Microvesicles Contain Retrotransposon Elements and Amplified Oncogene Sequences. *Nat. Commun.* **2011**, *2*, 180.
- (10) Valadi, H.; Ekstrom, K.; Bossios, A.; Sjostrand, M.; Lee, J. J.; Lotvall, J. O. Exosome-mediated Transfer of mRNAs and microRNAs is a Novel Mechanism of Genetic Exchange Between Cells. *Nat. Cell Biol.* **2007**, *9*, 654–659.
- (11) Kalra, H.; Simpson, R. J.; Ji, H.; Aikawa, E.; Altevogt, P.; Askenase, P.; Bond, V. C.; Borras, F. E.; Breakefield, X.; Budnik, V.; Buzas, E.; Camussi, G.; Clayton, A.; Cocucci, E.; Falcon-Perez, J. M.; Gabrielsson, S.; Gho, Y. S.; Gupta, D.; Harsha, H. C.; Hendrix, A.; et al. Vesiclepedia: A Compendium for Extracellular Vesicles With Continuous Community Annotation. *PLoS Biol.* **2012**, *10*, e1001450.
- (12) Raimondo, F.; Morosi, L.; Chinello, C.; Magni, F.; Pitto, M. Advances in Membranous Vesicle and Exosome Proteomics Improving Biological Understanding and Biomarker Discovery. *Proteomics* **2011**, *11*, 709–720.
- (13) Théry, C.; Zitvogel, L.; Amigorena, S. Exosomes: Composition, Biogenesis and Function. *Nat. Rev. Immunol.* **2002**, *2*, 569–579.
- (14) Théry, C.; Ostrowski, M.; Segura, E. Membrane Vesicles as Conveyors of Immune Responses. *Nat. Rev. Immunol.* **2009**, *9*, 581–593.
- (15) Andre, F.; Schartz, N. E.; Movassagh, M.; Flament, C.; Pautier, P.; Morice, P.; Pomel, C.; Lhomme, C.; Escudier, B.; Le Chevalier, T.; Tursz, T.; Amigorena, S.; Raposo, G.; Angevin, E.; Zitvogel, L. Malignant Effusions and Immunogenic Tumour-derived Exosomes. *Lancet* 2002, 360, 295–305.
- (16) Peinado, H.; Aleckovic, M.; Lavotshkin, S.; Matei, I.; Costa-Silva, B.; Moreno-Bueno, G.; Hergueta-Redondo, M.; Williams, C.; Garcia-Santos, G.; Ghajar, C.; Nitadori-Hoshino, A.; Hoffman, C.; Badal, K.; Garcia, B. A.; Callahan, M. K.; Yuan, J.; Martins, V. R.; Skog, J.; Kaplan, R. N.; Brady, M. S.; et al. Melanoma Exosomes Educate Bone Marrow Progenitor Cells Toward a Pro-metastatic Phenotype Through Met. *Nat. Med.* **2012**, *18*, 883–891.
- (17) Grange, C.; Tapparo, M.; Collino, F.; Vitillo, L.; Damasco, C.; Deregibus, M. C.; Tetta, C.; Bussolati, B.; Camussi, G. Microvesicles Released From Human Renal Cancer Stem Cells Stimulate Angiogenesis and Formation of Lung Premetastatic Niche. *Cancer Res.* 2011, 71, 5346–5356.
- (18) Rubin, O.; Crettaz, D.; Canellini, G.; Tissot, J. D.; Lion, N. Microparticles in Stored Red Blood Cells: an Approach Using Flow Cytometry and Proteomic Tools. *Vox Sang.* **2008**, *95*, 288–297.
- (19) van der Pol, E.; van Gemert, M. J.; Sturk, A.; Nieuwland, R.; van Leeuwen, T. G. Single vs Swarm Detection of Microparticles and Exosomes By Flow Cytometry. *J. Thromb. Haemostasis* **2012**, *10*, 919–930.
- (20) Lawrie, A. S.; Albanyan, A.; Cardigan, R. A.; Mackie, I. J.; Harrison, P. Microparticle Sizing By Dynamic Light Scattering in Fresh-frozen Plasma. *Vox Sang.* **2009**, *96*, 206–212.
- (21) Rho, J.; Chung, J.; Im, H.; Liong, M.; Shao, H.; Castro, C. M.; Weissleder, R.; Lee, H. Magnetic Nanosensor for Detection and Profiling of Erythrocyte-derived Microvesicles. *ACS Nano* **2013**, *7*, 11227–11233.

(22) Lee, K.; Shao, H.; Weissleder, R.; Lee, H. Acoustic Purification of Extracellular Microvesicles. ACS Nano 2015, 9, 2321–2327.

- (23) Wei, F.; Patel, P.; Liao, W.; Chaudhry, K.; Zhang, L.; Arellano-Garcia, M.; Hu, S.; Elashoff, D.; Zhou, H.; Shukla, S.; Shah, F.; Ho, C. M.; Wong, D. T. Electrochemical Sensor for Multiplex Biomarkers Detection. *Clin. Cancer Res.* **2009**, *15*, 4446–4452.
- (24) Munge, B. S.; Coffey, A. L.; Doucette, J. M.; Somba, B. K.; Malhotra, R.; Patel, V.; Gutkind, J. S.; Rusling, J. F. Nanostructured Immunosensor for Attomolar Detection of Cancer Biomarker Interleukin-8 Using Massively Labeled Superparamagnetic Particles. *Angew. Chem., Int. Ed.* **2011**, *50*, 7915–7918.
- (25) Wen, Y.; Pei, H.; Shen, Y.; Xi, J.; Lin, M.; Lu, N.; Shen, X.; Li, J.; Fan, C. DNA Nanostructure-based Interfacial Engineering for PCR-free Ultrasensitive Electrochemical Analysis of microRNA. *Sci. Rep.* **2012**. *2*. 867.
- (26) Hsieh, K.; Patterson, A. S.; Ferguson, B. S.; Plaxco, K. W.; Soh, H. T. Rapid, Sensitive, and Quantitative Detection of Pathogenic DNA at the Point of Care Through Microfluidic Electrochemical Quantitative Loop-mediated Isothermal Amplification. *Angew. Chem., Int. Ed.* **2012**, *51*, 4896–4900.
- (27) Campuzano, S.; Torrente-Rodriguez, R. M.; Lopez-Hernandez, E.; Conzuelo, F.; Granados, R.; Sanchez-Puelles, J. M.; Pingarron, J. M. Magnetobiosensors Based on Viral Protein p19 for MicroRNA Determination in Cancer Cells and Tissues. *Angew. Chem., Int. Ed.* **2014**, *53*, 6168–6171.
- (28) Das, J.; Ivanov, I.; Montermini, L.; Rak, J.; Sargent, E. H.; Kelley, S. O. An Electrochemical Clamp Assay for Direct, Rapid Analysis of Circulating Nucleic Acids in Serum. *Nat. Chem.* **2015**, *7*, 569–575.
- (29) Nemiroski, A.; Christodouleas, D. C.; Hennek, J. W.; Kumar, A. A.; Maxwell, E. J.; Fernandez-Abedul, M. T.; Whitesides, G. M. Universal Mobile Electrochemical Detector Designed for Use in Resource-limited Applications. *Proc. Natl. Acad. Sci. U. S. A.* **2014**, *111*, 11984—11989.
- (30) Rowe, A. A.; Bonham, A. J.; White, R. J.; Zimmer, M. P.; Yadgar, R. J.; Hobza, T. M.; Honea, J. W.; Ben-Yaacov, I.; Plaxco, K. W. Cheapstat: an Open-source, "do-it-yourself" Potentiostat for Analytical and Educational Applications. *PLoS One* **2011**, *6*, e23783.
- (31) Jorgensen, M.; Baek, R.; Pedersen, S.; Sondergaard, E. K.; Kristensen, S. R.; Varming, K. Extracellular Vesicle (EV) Array: Microarray Capturing of Exosomes and Other Extracellular Vesicles for Multiplexed Phenotyping. *J. Extracell. Vesicles* **2013**, *2*, 20920.
- (32) Yang, J.; Wei, F.; Schafer, C.; Wong, D. T. Detection of Tumor Cell-specific miRNA and Protein in Exosome-like Microvesicles From Blood and Saliva. *PLoS One* **2014**, *9*, e110641.
- (33) Chen, C.; Skog, J.; Hsu, C. H.; Lessard, R. T.; Balaj, L.; Wurdinger, T.; Carter, B. S.; Breakefield, X. O.; Toner, M.; Irimia, D. Microfluidic Isolation and Transcriptome Analysis of Serum Microvesicles. *Lab Chip* **2010**, *10*, 505–511.
- (34) Gercel-Taylor, C.; Atay, S.; Tullis, R. H.; Kesimer, M.; Taylor, D. D. Nanoparticle Analysis of Circulating Cell-derived Vesicles in Ovarian Cancer Patients. *Anal. Biochem.* **2012**, 428, 44–53.
- (35) Kobayashi, M.; Salomon, C.; Tapia, J.; Illanes, S. E.; Mitchell, M. D.; Rice, G. E. Ovarian Cancer Cell Invasiveness is Associated With Discordant Exosomal Sequestration of Let-7 miRNA and miR-200. *J. Transl. Med.* **2014**, *12*, 4.
- (36) Logozzi, M.; De Milito, A.; Lugini, L.; Borghi, M.; Calabro, L.; Spada, M.; Perdicchio, M.; Marino, M. L.; Federici, C.; Iessi, E.; Brambilla, D.; Venturi, G.; Lozupone, F.; Santinami, M.; Huber, V.; Maio, M.; Rivoltini, L.; Fais, S. High Levels of Exosomes Expressing CD63 and Caveolin-1 in Plasma of Melanoma Patients. *PLoS One* **2009**, *4*, e5219.
- (37) Lotvall, J.; Hill, A. F.; Hochberg, F.; Buzas, E. I.; Di Vizio, D.; Gardiner, C.; Gho, Y. S.; Kurochkin, I. V.; Mathivanan, S.; Quesenberry, P.; Sahoo, S.; Tahara, H.; Wauben, M. H.; Witwer, K. W.; Thery, C. Minimal Experimental Requirements for Definition of Extracellular Vesicles and Their Functions: a Position Statement from the International Society for Extracellular Vesicles. *J. Extracell. Vesicles* 2014, 3, 26913.

(38) Melo, S. A.; Sugimoto, H.; O'Connell, J. T.; Kato, N.; Villanueva, A.; Vidal, A.; Qiu, L.; Vitkin, E.; Perelman, L. T.; Melo, C. A.; Lucci, A.; Ivan, C.; Calin, G. A.; Kalluri, R. Cancer Exosomes Perform Cell-Independent microRNA Biogenesis and Promote Tumorigenesis. *Cancer Cell* **2014**, *26*, 707–721.

- (39) Paggetti, J.; Haderk, F.; Seiffert, M.; Janji, B.; Distler, U.; Ammerlaan, W.; Kim, Y. J.; Adam, J.; Lichter, P.; Solary, E.; Berchem, G.; Moussay, E. Exosomes Released By Chronic Lymphocytic Leukemia Cells Induce the Transition of Stromal Cells Into Cancerassociated Fibroblasts. *Blood* **2015**, *126*, 1106–1117.
- (40) Runz, S.; Keller, S.; Rupp, C.; Stoeck, A.; Issa, Y.; Koensgen, D.; Mustea, A.; Sehouli, J.; Kristiansen, G.; Altevogt, P. Malignant Ascitesderived Exosomes of Ovarian Carcinoma Patients Contain CD24 and EpCAM. *Gynecol. Oncol.* 2007, 107, 563–571.
- (41) Kristiansen, G.; Denkert, C.; Schluns, K.; Dahl, E.; Pilarsky, C.; Hauptmann, S. CD24 is Expressed in Ovarian Cancer and is a New Independent Prognostic Marker of Patient Survival. *Am. J. Pathol.* **2002**, *161*, 1215–1221.
- (42) Bast, R. C. J.; Xu, F. J.; Yu, Y. H.; Barnhill, S.; Zhang, Z.; Mills, G. B. CA 125: the Past and the Future. *Int. J. Biol. Markers* 1998, 13, 179–187.
- (43) Mandeville, H.; Rustin, G. J. The Role of CA 125 in Epithelial Ovarian Carcinoma. *J. BUON.* **2002**, *7*, 13–17.
- (44) Meden, H.; Kuhn, W. Overexpression of the Oncogene c-erbB-2 (HER2/neu) in Ovarian Cancer: a New Prognostic Factor. Eur. J. Obstet. Gynecol. Reprod. Biol. 1997, 71, 173–179.
- (45) Verri, E.; Guglielmini, P.; Puntoni, M.; Perdelli, L.; Papadia, A.; Lorenzi, P.; Rubagotti, A.; Ragni, N.; Boccardo, F. HER2/neu Oncoprotein Overexpression in Epithelial Ovarian Cancer: Evaluation of Its Prevalence and Prognostic Significance. Clinical Study. *Oncology* **2005**, *68*, 154–161.
- (46) Aldovini, D.; Demichelis, F.; Doglioni, C.; Di Vizio, D.; Galligioni, E.; Brugnara, S.; Zeni, B.; Griso, C.; Pegoraro, C.; Zannoni, M.; Gariboldi, M.; Balladore, E.; Mezzanzanica, D.; Canevari, S.; Barbareschi, M. M-CAM Expression as Marker of Poor Prognosis in Epithelial Ovarian Cancer. *Int. J. Cancer* **2006**, *119*, 1920–1926.
- (47) Psyrri, A.; Kassar, M.; Yu, Z.; Bamias, A.; Weinberger, P. M.; Markakis, S.; Kowalski, D.; Camp, R. L.; Rimm, D. L.; Dimopoulos, M. A. Effect of Epidermal Growth Factor Receptor Expression Level on Survival in Patients With Epithelial Ovarian Cancer. *Clin. Cancer Res.* **2005**, *11*, 8637–8643.
- (48) Coutelieris, F. A.; Delgado, J. M. P. Q. Transport Processes in Porous Media; Springer: Berlin, 2012.
- (49) Ambrosi, A.; Airo, F.; Merkoci, A. Enhanced Gold Nanoparticle Based ELISA for a Breast Cancer Biomarker. *Anal. Chem.* **2010**, 82, 1151–1156.
- (50) Das, J.; Kelley, S. O. Tuning the Bacterial Detection Sensitivity of Nanostructured Microelectrodes. *Anal. Chem.* **2013**, *85*, 7333–7338
- (51) Wei, F.; Lin, C. C.; Joon, A.; Feng, Z.; Troche, G.; Lira, M. E.; Chia, D.; Mao, M.; Ho, C. L.; Su, W. C.; Wong, D. T. Noninvasive Saliva-based EGFR Gene Mutation Detection in Patients With Lung Cancer. *Am. J. Respir. Crit. Care Med.* **2014**, *190*, 1117–1126.
- (52) Li, X. M.; Wang, L. L.; Luo, J.; Wei, Q. L. A Dual-amplified Electrochemical Detection of mRNA based on Duplex-specific Nuclease and Bio-Bar-Code Conjugates. *Biosens. Bioelectron.* **2015**, 65, 245–250.

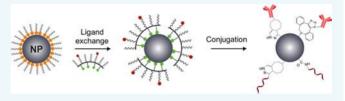


Facile Coating Strategy to Functionalize Inorganic Nanoparticles for Biosensing

Yong Il Park, $^{\dagger,\ddagger,\perp}$ Eunha Kim, $^{\dagger,\ddagger,\#}$ Chen-Han Huang, †,‡ Ki Soo Park, †,‡ Cesar M. Castro, Hakho Lee, *,†,‡ and Ralph Weissleder $^{*,\dagger,\ddagger,\parallel}$

Supporting Information

ABSTRACT: The use of inorganic nanoparticles (NPs) for biosensing requires that they exhibit high colloidal stability under various physiological conditions. Here, we report on a general approach to render hydrophobic NPs into hydrophilic ones that are ready for bioconjugation. The method uses peglyated polymers conjugated with multiple dopamines, which results in multidentate coordination. As proof-of-



concept, we applied the coating to stabilize ferrite and lanthanide NPs synthesized by thermal decomposition. Both polymer-coated NPs showed excellent water solubility and were stable at high salt concentrations under physiological conditions. We used these NPs as molecular-sensing agents to detect exosomes and bacterial nucleic acids.

I norganic nanoparticles (NPs) often exhibit interesting properties that can be exploited for sensitive and robust biomedical sensing. Examples include superparamagnetic NPs for magnetic sensing, 4,5 quantum dots detectable with photoluminescence, bhosphorescent nanoparticles, 11-13 These unique physical properties exist at room temperature, obviating the need for expensive detectors and specialized systems. Furthermore, chemical and other amplification strategies have been devised to amplify analytical signals for ultrasensitive and miniaturized detection schemes. 14,15

One challenging aspect of rendering NPs truly useful for biosensing has been the need to stabilize NP's surface with biocompatible and nonreactive coating materials. This task is particularly difficult not only for injectable materials (e.g., superparamagnetic NPs) but also for agents intended for diagnostic in vitro use. The surface coating should allow NPs to stay in solution, react with hydrophilic components, provide functional groups to attach affinity ligands, and passivate the metal surface. Without such stabilizing coatings, proteins often absorb nonspecifically to the surface, leading to diagnostic interference, high noise levels, or low reactivity. Surface modifications can be particularly challenging for inorganic NPs synthesized via nonhydrolytic thermal decomposition in hydrophobic conditions. 16,17 A variety of hydrophilic coating strategies have been described for metal oxides but most of these strategies have drawbacks under rigorous biological conditions or where long-term stability (months to years) is required. Furthermore, under stress conditions (high temperature, high salinity, and non-neutral pH), these effects are exacerbated. A simple yet reliable coating strategy for metal

oxides is thus needed to convert "pure" core crystals synthesized under thermal conditions.

Here, we report on a generalized coating protocol to convert hydrophobic NPs into hydrophilic ones that can be further modified for molecular sensing. We reasoned that using dopamine as an anchoring group would form stable polymercoated NPs because dopamine can bind to the NP surface with high affinity. We tested the method using two representative particles, namely ferrite NPs and lanthanide NPs. We prepared dopamine-based polyethylene glycol (PEG) polymer and coated hydrophobic NPs with polymer through ligand exchange. The polymer-coated NPs displayed excellent colloidal stability at high temperatures and under a wide range of physiological buffer conditions. Furthermore, the conjugates provided facile chemical functionalities with which to graft various affinity ligands. We used the prepared NPs as sensing agents for two different types of biosensors. The ferrite NPs were used to detect exosomes using a miniaturized nuclear magnetic resonance (NMR) system. Lanthanide NPs maintained their optical properties (i.e., no quenching in luminescence emission) and was used to detect bacterial nucleic acids through time-gated imaging.

RESULTS

Generalized Coating Scheme. Figure 1 shows the developed NP-coating and bioconjugation strategy. We used

Special Issue: Interfacing Inorganic Nanoparticles with Biology

Received: September 15, 2016 Revised: October 25, 2016 Published: October 28, 2016



[†]Center for Systems Biology, [‡]Department of Radiology, and [§]Department of Medicine, Massachusetts General Hospital, Harvard Medical School, Boston, Massachusetts 02114, United States

Department of Systems Biology, Harvard Medical School, Boston, Massachusetts 02115, United States

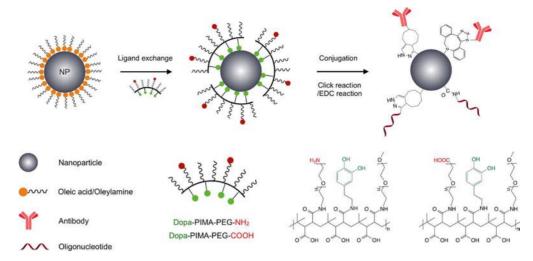


Figure 1. Generalized coating and bioconjugation strategy for nanoparticles. Multiple dopamine-containing PEG polymers are used to increase the binding affinity between the polymer and the NP. The dopamine-based polymers replace the hydrophobic capping agent on the NP surface. For the subsequent introduction of affinity ligands for molecular recognition, various bioconjugation strategies (e.g., bioorthogonal click reaction and EDC coupling) can be chosen depending on the affinity ligands.

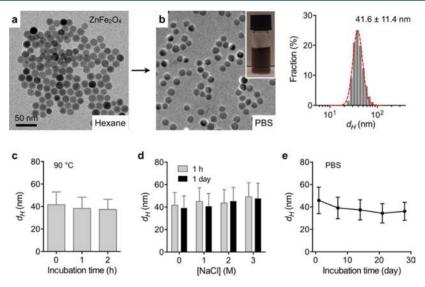


Figure 2. Polymer-coated magnetic nanoparticles (MNPs). (a) Zn-doped ferrite (ZnFe $_2$ O $_4$) MNPs were produced via the thermal decomposition method. As-synthesized particles were hydrophobic and dispersed in organic solvent. The core size was 16 nm. (b) MNPs were transferred to the aqueous phase through the polymer (PEG length 5000) coating. The particles were well-dispersed without aggregation. The mean hydrodynamic diameter (d_H) was 41.6 nm. The insert is photograph of MNP aqueous solution. (c–e) Coating stability. The polymer-coated MNPs were challenged either by (c) heating, (d) high salt concentrations, or (e) long-term storage in PBS. No significant changes in particle size were observed, confirming the high stability of the polymer coating.

dopamine (DOPA) as the affinity ligand because DOPA can readily attach to metal surface through adsorption. This process, however, is reversible; DOPA can be dissociated from NPs under physiological conditions. To improve coating stability, we synthesized PEG polymers containing multiple DOPAs. Specifically, we grafted DOPA and PEG on a polymer backbone, poly(isobutylene-alt-maleic anhydride) (PIMA), through reaction with maleic anhydride, creating DOPA—PIMA—PEG. This method did not need additional cross-linkers and facilitated the creation of DOPA—PIMA—PEG with different PEG length and various functional groups for specific bioconjugation (e.g., EDC coupling and bioorthogonal click reaction).

As proof of principle, we synthesized four kinds of polymers with varying PEG lengths (2000 and 5000) and functional

groups (amine and carboxylic acid). The successful polymer synthesis was confirmed by ¹H NMR (Figure S1). Different PEG lengths were tested to determine the effect of chain length on long-term colloidal stability. We used DOPA–PIMA–PEG to replace hydrophobic capping agents (e.g., oleic acid and oleylamine) on the NP surface. We then conjugated affinity ligands for molecular recognition. Antibody conjugation was performed with a bioorthogonal reaction using tetrazine and trans-cyclooctene (TCO); ¹⁹ oligonucleotides were attached to carboxylic groups using an EDC reaction.

Application to Ferrite Nanoparticles. We applied the developed coating strategy to stabilize magnetic nanoparticles (MNPs). Among the various NP compositions, we chose Zndoped ferrite $(ZnFe_2O_4)$ for its high saturation magnetization and chemical stability. ²⁰ The particles were first synthesized via

nonhydrolytic thermal decomposition (see the experimental procedures in the Supporting Information for details), which produced monodisperse NPs (core diameter: 16 nm) with high crystallinity (Figure 2a). The measured magnetization ($M_{\rm s}$) was 177 emu/g [metal] (Figure S2), close to that of bulk material (200 emu/g). Following the polymer-coating with DOPA–PIMA–PEG₅₀₀₀, the MNPs were well dispersed in aqueous media, and no aggregation was observed (Figure 2b, left). The hydrodynamic diameter ($d_{\rm H}$) of polymer-coated MNPs was 41.6 nm, implying a polymer thickness of ~13 nm (Figure 2b, right). The hydrodynamic diameter was reduced to 32.2 nm with DOPA–PIMA–PEG₂₀₀₀ coating (Figure S3).

We next tested the colloidal stability of polymer-coated MNPs by subjecting them to heat stress or high salt concentrations. The particles maintained colloidal stability against such challenges. No significant changes in particle distribution were observed after continuous heating at 90 °C for 2 h (Figure 2c) or immersion in 3 M of NaCl (Figure 2d), which confirmed the stable attachment of polymers to the particle surface. We also assessed long-term stability by storing particles in PBS buffer (Figure 2e). Longer PEG chains resulted in better stability; MNPs coated with PEG $_{2k}$ produced large-sized aggregates within 3 weeks, and MNPs with PEG $_{5000}$ showed no aggregation (Figure S4).

Stabilization of Lanthanide Nanoparticles. Lanthanide NPs can be used as luminescent labels for optical imaging and sensors. The luminescence remains highly stable without photobleaching or blinking, and colors can be tuned by varying dopant ions. We synthesized NaGdF₄ NPs co-doped with Ce³⁺, Tb³⁺ via thermal decomposition (see the experimental procedures in the Supporting Information). The composition allowed the particles to have long luminescence lifetime, which would benefit time-gated luminescent imaging. The synthesized NPs were highly crystalline with a narrow size distribution (core size of 13 nm; Figure 3a). As in MNPs, the polymercoated lanthanide NPs were well-dispersed in aqueous media without aggregation (Figure 3b). Furthermore, we observed negligible differences in overall particle size and distribution at different NP concentrations (Figure S5).

We next measured the luminescence properties of watersoluble lanthanide NPs. Both particles, either with PEG₂₀₀₀ or PEG₅₀₀₀ polymers, exhibited characteristic green emission peaks of Tb³⁺ ions (mainly 546 nm emission assigned due to the transition from ⁵D₄ to ⁷F₅) under 254 nm excitation (Figure 3c). Emission intensity was slightly higher with PEG_{5000} coating, presumably because longer PEGs can better protect Tb3+ from vibrational quenching by solvents (Figure S6). The polymercoated lanthanide NPs showed high colloidal stability under various buffer conditions (HEPES, MES, and NaOH) and in high salt concentrations (NaCl, 3 M). However, the particles were found unstable in PBS. Phosphate ions tend to strongly coordinate to the surface of lanthanide NPs, and excess phosphate ions in PBS can remove the polymer by ligand exchange.²³ Although lanthanide NPs are coated with phosphate polymer, excess phosphate ions from PBS could still hamper their long-term dispersibility. Therefore, the use of PBS should be avoided for lanthanide NPs.

Biosensing Applications. We applied the polymer-coated ZnFe₂O₄ MNPs to microNMR-based magnetic sensing. This detection modality is favorable when samples are in complex media (e.g., blood). Because biological samples have negligible magnetic background, microNMR sensing can be highly sensitive in turbid samples. We first measured the transverse

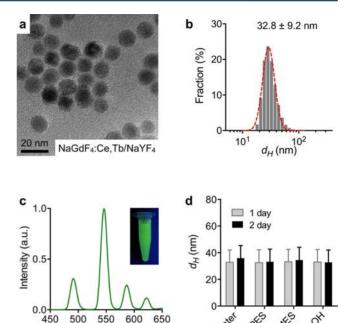


Figure 3. Polymer-coated lanthanide nanoparticles. (a) Lanthanide NPs co-doped with Ce^{3+} , Tb^{3+} were synthesized via thermal decomposition and rendered water-soluble through the polymer coating. (b) The initial core size of the lanthanide NPs was 13 nm; following the polymer coating, the hydrodynamic diameter was 32.8 nm, as measured by dynamic light scattering. (c) Emission spectrum from aqueous suspensions of lanthanide NPs. The particles were excited at 254 nm. The main emission peak was at 546 nm, which is characteristic of Tb^{3+} . The insert is a photograph of colloidal solution under a 254 nm UV lamp. (d) The polymer-coated lanthanide NPs were subject to various stress tests. For example, the particle size was unaffected under different buffer conditions. Other test results are available in the Supporting Information.

Wavelength (nm)

relaxivity (r_2) of the MNPs (Figure 4a). Owing to their high magnetic moments, ZnFe₂O₄ MNPs, even with a small core size (13 nm), exhibited higher r_2 values (313 s⁻¹ mM⁻¹) than did Fe₃O₄ MNPs (core size of 25 nm; 279 s⁻¹ mM⁻¹). For the given particle composition, the r_2 values increased with the particle size (574 s⁻¹ mM⁻¹ for 17 nm ZnFe₂O₄ MNPs). We used the particles to detect exosomes, nanoscale vesicles secreted from cells. MNPs were conjugated with anti-EGFR antibodies via tetrazine-TCO bioorthogonal chemistry; aminefunctionalized MNPs were labeled with tetrazine-NHS, and antibodies were reacted with TCO-NHS. Mixing two agents grafted antibodies on MNP surface through the fast and highly selective click reaction (see the experimental procedures in the Supporting Information). Exosomes were collected from culture media of a human glioblastoma multiforme cell line (SkMG3), and serially diluted. The titration experiments (Figure 4b) established the detection limit of $\sim 10^7$ exosomes.

We used lanthanide NPs for time-gated imaging-based sensing. In time-gated imaging, particles are first excited with a short light pulse. Detection starts after a short (~1 ms) delay to exclude short-lived fluorescence and to integrate long-lived luminescence only. This scheme removes autofluorescence and interference from excitation light, enhancing overall detection sensitivity and simplifying the optical setup (no optical filters needed). The luminescence decay lifetime of polymer coated lanthanide NPs was ~2.3 ms (Figure 4c). A long decay time in the range of milliseconds allowed for control of time gating

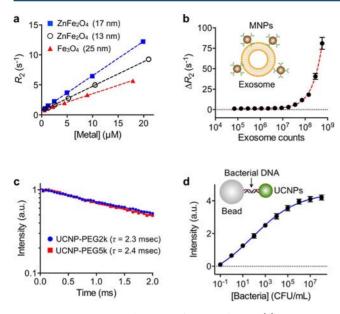


Figure 4. Biosensing applications of prepared NPs. (a) MicroNMR assays with MNPs. Transverse relaxation rate (R_2) of watersoluble MNPs with different sizes and compositions was measured. Due to their superior magnetic moments, ZnFe₂O₄ MNPs showed higher R₂ than Fe₃O₄ MNPs. Among ZnFe₂O₄ MNPs, the R₂ values increased with the particle size. (b) The MNPs were used to detect exosomes. MNPs were conjugated with antibodies against EGFR to label exosomes from a human glioblastoma multiforme cell line (SkMG3). The detection threshold was approximately 10⁷ exosomes. (c) Timegated detection with lanthanide NPs. After the excitation light was turned off, the luminescence from Tb3+ persisted with the typical decay time of 2.3 ms. This property was exploited for time-gated detection; UCNPs were pulse-excited, and the resulting luminescence light was detected. The method minimizes background signal coming from autofluorescence. (d) Lanthanide NPs were used to detect bacterial nucleic acids. Microbeads (diameter 10 μ m) and NPs were conjugated with oligonucleotides complementary to target bacteria DNA. The limit of detection was close to single bacteria.

with electronics (without mechanical chopper). We devised an assay protocol for detecting bacterial DNA using the lanthanide NPs. Carboxylated microbeads (diameter 10 μ m) and carboxylated lanthanide NPs were conjugated with oligonucleotides complementary to target DNA (Table S1). The microbeads were used to capture target DNA and subsequently labeled with lanthanide NPs. The resulting luminescence signal from microbeads was then measured via time-gated imaging. Figure 4d shows a proof-of-concept example. Bacterial RNA from a *Staphyllococcus aureus* culture was extracted and PCR-amplified to prepare single-stranded DNA. Titration experiments showed that sensitivity was close to reaching single-bacteria detection.

In summary, we developed a generalized polymer-coating scheme to prepare hydrophilic NPs for biosensing. The polymer contained multiple dopamine molecules for firm attachment to NP surfaces as well as multiple PEGs to achieve hydrophilicity. When applied to ferrite and lanthanide NPs, polymer coating resulted in excellent colloidal stability. Thus, coated NPs were stable at high temperatures and in physiological buffers. Furthermore, the coating provided various functional groups to further conjugate affinity ligands for molecular sensing.

ASSOCIATED CONTENT

S Supporting Information

The Supporting Information is available free of charge on the ACS Publications website at DOI: 10.1021/acs.bioconjchem.6b00524.

Additional experimental details. Figures showing NMR spectra, M—H curve, size distributions, colloidal stability, emission spectra, and dual filtration. A table showing DNA sequences used for bacterial detection. (PDF)

AUTHOR INFORMATION

Corresponding Authors

*E-mail: rweissleder@mgh.harvard.edu. Phone: 617-726-8226.

*E-mail: hlee@mgh.harvard.edu.

Present Addresses

¹Y.I.P.: School of Chemical Engineering, Chonnam National University, 77 Yongbong-ro, Buk-gu, Gwangju 61186, Republic of Korea.

*E.K.: Department of Molecular Science and Technology, Ajou University, Suwon 16499, Republic of Korea.

Notes

The authors declare no competing financial interest.

ACKNOWLEDGMENTS

This work was supported in part by NIH Grants R01HL113156, R21CA205322, R01EB004626, R01EB010011, HHSN268201000044C, U54-CA119349, and T32-CA79443 and by the Department of Defense OCRP Program Award W81XWH-14-1-0279.

■ REFERENCES

- (1) Song, Y., Wei, W., and Qu, X. (2011) Colorimetric biosensing using smart materials. *Adv. Mater.* 23, 4215–4236.
- (2) Wang, J., and Qu, X. (2013) Recent progress in nanosensors for sensitive detection of biomolecules. *Nanoscale* 5, 3589–3600.
- (3) Yakoh, A., Pinyorospathum, C., Siangproh, W., and Chailapakul, O. (2015) Biomedical Probes Based on Inorganic Nanoparticles for Electrochemical and Optical Spectroscopy Applications. *Sensors* 15, 21427–21477.
- (4) Wang, Y., Ju, Z., Cao, B., Gao, X., Zhu, Y., Qiu, P., Xu, H., Pan, P., Bao, H., Wang, L., and Mao, C. (2015) Ultrasensitive rapid detection of human serum antibody biomarkers by biomarker-capturing viral nanofibers. *ACS Nano 9*, 4475–4483.
- (5) Lee, H., Shin, T. H., Cheon, J., and Weissleder, R. (2015) Recent Developments in Magnetic Diagnostic Systems. *Chem. Rev.* 115, 10690–10724.
- (6) Lowe, S. B., Dick, J. A., Cohen, B. E., and Stevens, M. M. (2012) Multiplex sensing of protease and kinase enzyme activity via orthogonal coupling of quantum dot-peptide conjugates. *ACS Nano* 6, 851–857.
- (7) Xiong, L. H., Cui, R., Zhang, Z. L., Yu, X., Xie, Z., Shi, Y. B., and Pang, D. W. (2014) Uniform fluorescent nanobioprobes for pathogen detection. *ACS Nano* 8, 5116–5124.
- (8) Hildebrandt, N., Spillmann, C. M., Algar, W. R., Pons, T., Stewart, M. H., Oh, E., Susumu, K., Díaz, S. A., Delehanty, J. B., and Medintz, I. L. (2016) Energy Transfer with Semiconductor Quantum Dot Bioconjugates: A Versatile Platform for Biosensing, Energy Harvesting, and Other Developing Applications. *Chem. Rev.*, DOI: 10.1021/acs.chemrev.6b00030.
- (9) Miao, Y., Zhang, Z., Gong, Y., and Yan, G. (2014) Phosphorescent quantum dots/doxorubicin nanohybrids based on photoinduced electron transfer for detection of DNA. *Biosens. Bioelectron.* 59, 300–306.

(10) Zheng, W., Tu, D., Huang, P., Zhou, S., Chen, Z., and Chen, X. (2015) Time-resolved luminescent biosensing based on inorganic lanthanide-doped nanoprobes. *Chem. Commun.* 51, 4129–4143.

- (11) Dondapati, S. K., Sau, T. K., Hrelescu, C., Klar, T. A., Stefani, F. D., and Feldmann, J. (2010) Label-free biosensing based on single gold nanostars as plasmonic transducers. *ACS Nano* 4, 6318–6322.
- (12) Park, Y. I., Im, H., Weissleder, R., and Lee, H. (2015) Nanostar Clustering Improves the Sensitivity of Plasmonic Assays. *Bioconjugate Chem.* 26, 1470–1474.
- (13) Focsan, M., Campu, A., Craciun, A. M., Potara, M., Leordean, C., Maniu, D., and Astilean, S. (2016) A simple and efficient design to improve the detection of biotin-streptavidin interaction with plasmonic nanobiosensors. *Biosens. Bioelectron.* 86, 728–735.
- (14) Cao, Y. C., Jin, R., and Mirkin, C. A. (2002) Nanoparticles with Raman spectroscopic fingerprints for DNA and RNA detection. *Science* 297, 1536–1540.
- (15) Liong, M., Tassa, C., Shaw, S. Y., Lee, H., and Weissleder, R. (2011) Multiplexed magnetic labeling amplification using oligonucleotide hybridization. *Adv. Mater.* 23, H254–7.
- (16) Nam, J., Won, N., Bang, J., Jin, H., Park, J., Jung, S., Jung, S., Park, Y., and Kim, S. (2013) Surface engineering of inorganic nanoparticles for imaging and therapy. *Adv. Drug Delivery Rev.* 65, 622–648.
- (17) Palui, G., Aldeek, F., Wang, W., and Mattoussi, H. (2015) Strategies for interfacing inorganic nanocrystals with biological systems based on polymer-coating. *Chem. Soc. Rev.* 44, 193–227.
- (18) Wang, W., Ji, X., Na, H. B., Safi, M., Smith, A., Palui, G., Perez, J. M., and Mattoussi, H. (2014) Design of a multi-dopamine-modified polymer ligand optimally suited for interfacing magnetic nanoparticles with biological systems. *Langmuir* 30, 6197–6208.
- (19) Haun, J. B., Devaraj, N. K., Hilderbrand, S. A., Lee, H., and Weissleder, R. (2010) Bioorthogonal chemistry amplifies nanoparticle binding and enhances the sensitivity of cell detection. *Nat. Nanotechnol.* 5, 660–665.
- (20) Jang, J. T., Nah, H., Lee, J. H., Moon, S. H., Kim, M. G., and Cheon, J. (2009) Critical enhancements of MRI contrast and hyperthermic effects by dopant-controlled magnetic nanoparticles. *Angew. Chem., Int. Ed.* 48, 1234–1238.
- (21) Noh, S. H., Na, W., Jang, J. T., Lee, J. H., Lee, E. J., Moon, S. H., Lim, Y., Shin, J. S., and Cheon, J. (2012) Nanoscale magnetism control via surface and exchange anisotropy for optimized ferrimagnetic hysteresis. *Nano Lett.* 12, 3716–3721.
- (22) Zheng, W., Zhou, S., Chen, Z., Hu, P., Liu, Y., Tu, D., Zhu, H., Li, R., Huang, M., and Chen, X. (2013) Sub-10 nm lanthanide-doped CaF2 nanoprobes for time-resolved luminescent biodetection. *Angew. Chem., Int. Ed.* 52, 6671–6676.
- (23) Boyer, J. C., Manseau, M. P., Murray, J. I., and van Veggel, F. C. (2010) Surface modification of upconverting NaYF4 nanoparticles with PEG-phosphate ligands for NIR (800 nm) biolabeling within the biological window. *Langmuir* 26, 1157–1164.